

Title	Atomic layer deposition of metal oxides for photovoltaic applications
Authors	Ryan, Louise P.
Publication date	2020-01-05
Original Citation	Ryan, L. P. 2020. Atomic layer deposition of metal oxides for photovoltaic applications. PhD Thesis, University College Cork.
Type of publication	Doctoral thesis
Rights	© 2020, Louise P. Ryan. - https://creativecommons.org/licenses/by-nc-nd/4.0/
Download date	2023-05-08 02:20:30
Item downloaded from	http://hdl.handle.net/10468/10486

Ollscoil na hÉireann, Corcaigh

NATIONAL UNIVERSITY OF IRELAND, CORK



Atomic Layer Deposition of Metal Oxides for Photovoltaic Applications

A thesis presented to

The National University of Ireland

For the degree of Doctor of Philosophy

by

Louise P. Ryan B.Sc.

Department of Chemistry,

Tyndall National Institute,

University College Cork.

Head of Department: Dr Humphrey Moynihan

January 2020

Supervised by Dr Ian M. Povey, Dr Shane O'Brien and Professor Martyn E. Pemble

Table of Contents

<i>List of Acronyms</i>	<i>v</i>
<i>Declaration</i>	<i>viii</i>
<i>Acknowledgements</i>	<i>ix</i>
<i>Abstract</i>	<i>xi</i>
<i>Overview of Thesis</i>	<i>xiii</i>
<i>Chapter 1: Overview of Atomic Layer Deposition</i>	<i>1</i>
1.1 History of Atomic Layer Deposition	1
1.2 Principles of ALD	3
1.3 Growth per Cycle	4
1.4 Self-Limiting Regime	6
1.5 ALD Temperature Window	8
1.6 ALD Processes	9
1.6.1 Thermal ALD	9
1.6.2 Plasma-Assisted ALD	9
1.7 ALD of Zinc Oxide as a Transparent Conducting Oxide (TCO)	11
1.7.1 Deposition of ZnO using Diethylzinc	14
1.8 ALD of Doped ZnO for Transparent Conducting Oxides	18
1.8.1 ALD of Al-doped ZnO	21
1.8.2 ALD of Ti-doped ZnO	25
1.8.3 ALD of Hf-doped ZnO	26
1.9 Atomic Layer Deposition of V₂O₅	27
Bibliography	31
<i>Chapter 2: Introduction to Perovskite Solar Cells</i>	<i>47</i>
2.1 History of Perovskite Solar Cells	47
2.2 Operating Principle of Solar Cell Devices	49
2.3 Electrical Characteristics of Solar Cell Devices	50
2.4 Working Mechanism of Perovskite Solar Cells	54
2.5 Device Architecture	57
2.5.1 Conventional <i>n-i-p</i> Configuration	59
2.5.2 Inverted <i>p-i-n</i> Configuration	59
2.6 Challenges	60

2.6.1 Stability	60
2.6.2 Hysteresis	62
2.7 Perovskite Tandem Devices	64
Bibliography	68
<i>Chapter 3: Experimental Instrumentation</i>	73
3.1 Deposition Systems	73
3.1.2 Cambridge Nanotech Fiji 200LLC ALD System	73
3.1.2 Picosun R200 ALD System	74
3.2 Instrumentation for Analysis and Characterisation of Thin Films	76
3.2.1 X-ray Diffraction (XRD)	76
3.2.2 X-ray Photoelectron Spectroscopy	78
3.2.3 Four Point Probe	80
3.2.4 Hall Effect Measurement	82
3.2.5 Transmission Electron Microscopy (TEM)	85
3.2.6 Scanning Electron Microscopy (SEM)	86
3.2.7 UV/Visible/NIR Spectroscopy	88
Bibliography	91
<i>Chapter 4: Fundamental Study of Atomic Layer Deposited ZnO and Doped ZnO</i>	92
4.0 Experimental Details	92
4.1 Thermal ALD Processes	92
4.2 Results	96
4.2.1 Electrical Properties	96
4.2.2 Optical Properties	98
4.2.3 X-ray Diffraction	102
4.2.4 X-ray Photoelectron Spectroscopy	105
4.3 Discussion	106
4.4 Conclusion	109
Bibliography	110
<i>Chapter 5: Optimisation of Transparent Conducting Oxide Layer for Incorporation into Perovskite Solar Cells</i>	112
5.1 Experimental Details	112
5.1.1 ALD of ZnO and Doped ZnO: Picosun R200	112
5.2 Results	112
5.2.1 Surface Morphology	112
5.2.2 X-ray Diffraction	115
5.2.3 Optical Properties	116
5.2.4 Electrical Properties	117
5.3 Discussion	121

5.4 Conclusion	123
Bibliography	124
<i>Chapter 6: Incorporation of Atomic Layer Deposited Ti-doped ZnO into Perovskite Solar Cells</i>	126
6.1 Experimental Details	126
6.2 Results and Discussion	130
6.3 Conclusion	137
Bibliography	139
<i>Chapter 7: Atomic Layer Deposition of Hole Transport Material, VO_x and Incorporation into Perovskite Solar Cells</i>	140
7.0 Introduction	140
7.1 Experimental Details	141
7.1.1 Thermal ALD of VO _x	141
7.1.2 Plasma-Enhanced ALD VO _x	141
7.2 Results and Discussion	143
7.2.1 As grown VO _x	143
7.2.2 Annealed VO _x	145
7.2.3 Surface Morphology of as grown and annealed samples	146
7.3 Incorporation of VO_x into perovskite solar cells as a hole transport layer	148
7.3.1 Experimental Details	148
7.4 Results and Discussion	150
7.5 Conclusion	152
Bibliography	154
<i>Chapter 8: Low Temperature Atomic Layer Deposited Ti-doped ZnO for incorporation into Tandem Solar Cells</i>	155
8.0 Introduction	155
8.1 Experimental	156
8.2 Results and Discussion	156
8.2.1 Electrical Properties	156
8.2.2 X-ray Diffraction	158
8.2.3 Surface Morphology	160
8.2.4 Optical Properties	164
8.3 Discussion	166
8.4 Conclusion	169
Bibliography	170

<i>Chapter 9: Conclusions and Future Work</i>	<i>171</i>
9.1 Overall Conclusions	171
9.2 Future Work	175
<i>Appendix I</i>	<i>177</i>
<i>Publications and Conference Presentations</i>	<i>177</i>
<i>Appendix II</i>	<i>179</i>
<i>Additional Data</i>	<i>179</i>

List of Acronyms

2T	Two-Terminal
4T	Four-Terminal
ALD	Atomic Layer Deposition
ALE	Atomic Layer Epitaxy
AZO	Al-doped ZnO
c-Si	Crystalline Silicon
CIGS	Copper Indium Gallium Selenide
CMOS	Complementary Metal-Oxide Semiconductor
CVD	Chemical Vapour Deposition
DEZ	Diethylzinc
DMAI	Dimethylaluminium isopropoxide
DMZ	Diemethylzinc
DSSC	Dye Sensitised Solar Cell
EQE	External Quantum Efficiency
ETL	Electron Transport Layer
ETM	Electron Transport Material
FABr	Formamidinium Bromide
FAI	Formamidinium Iodide
FF	Fill Factor
FTO	Fluorine Tin Oxide
GPC	Growth per Cycle
HTL	Hole Transport Layer
HTM	Hole Transport Material
HZO	Hf-doped ZnO
IC	Integrated Circuit

IR	Infrared
I_{sc}	Short Circuit Current
ITO	Indium Tin Oxide
J_{dark}	Dark Current
J_{mp}	Short Circuit Density – Maximum Power Point
J_{sc}	Short Circuit Density
K_b	Boltzmann's Constant
MFC	Mass Flow Controller
MOCVD	Metal-Organic Chemical Vapour Deposition
MOSFETS	Metal Oxide Semiconductor Field Effect Transistors
PCBM	Phenyl-C61-Butyric Acid Methyl Ester
PCE	Power Conversion Efficiency
PEALD	Plasma Enhanced Atomic Layer Deposition
PK	Perovskite
PLD	Pulsed Layer Deposition
P_{mp}	Maximum Power Output
PSC	Perovskite Solar Cell
QE	Quantum Efficiency
SAM	Self-Assembled Monolayer
SEM	Scanning Electron Microscopy
TCO	Transparent Conducting Oxide
TDMAT	Tetrakis Dimethylamido Titanium
TDMAV	Tetrakis Dimethylamino Vanadium
TEM	Transmission Electron Microscopy
TEMAH	Tetrakis Ethylmethyldamido Hafnium
TEMAV	Tetrakis Ethylmethyldamino Vanadium
TFEL	Thin Film Electroluminescence

TMA	Trimethylaluminium
TmPyPB	1,3,5 – tri-(m-pyrid-3-yl phenyl) Benzene
TTIP	Titanium Isopropoxide
TZO	Ti-doped ZnO
V_{mp}	Voltage – Maximum Power Point
V_{oc}	Open Circuit Voltage
VTOP	Vanadium Oxy-tri-isopropoxide
XPS	X-ray Photoelectron Spectroscopy
XRD	X-ray Diffraction

Declaration

This is to certify that the work I am submitting is my own and has not been submitted for another degree, either at University College Cork or elsewhere. All external references and sources are clearly acknowledged and identified within the contents. I have read and understood the regulations of University College Cork concerning plagiarism.



Louise Ryan

15 January 2020

Date

Acknowledgements

I would like to sincerely thank my supervisor Dr Ian Povey for giving me the opportunity to pursue a PhD in his research group in Tyndall National Institute. His advice, generosity and patience throughout this whole journey has been indispensable. To my co-supervisors Dr Shane O'Brien and Prof Martyn Pemble I extend my thanks for their encouragement and positivity throughout the course of my studies. I want to express my gratitude to members of the Advanced Materials and Surfaces Group both past and present in particular Dr Adrian Walsh and Dr Melissa McCarthy without whom the PhD experience wouldn't have been the same.

I would like to acknowledge all the help given from those in Tyndall National Institute and University College Cork; Dr Brendan Sheehan for performing TEM, Scott Monaghan for use and training of the Hall effect measurement system, Vince Lodge for SEM, Krime Khalifi, Dr Mircea Modreanu, Dr James Connolly, Paul Tassie and Dan O'Connell. I would also like to thank Dr Fathima Laffir of University of Limerick for performing XPS on my samples. I would like to thank Arnaud Walter, Matthias Bräuninger and Florent Sahli of EPFL and CSEM for processing some of my samples on top of their own workload.

To my friends outside my research group and outside Tyndall namely, Emma Coleman, Darragh Cronin, Ruaidhri Murphy, Eoin Walsh, Michael Dillane, Anya Curran, Declan Jordan, Damien Nolan and Damien Randles who I have gotten the chance to know during my studies and who have always offered encouragement and entertainment.

To all the members of the tea table, including Dermot, Tom, John, JJ, Don Jon, Boot and Fred I extend my sincere thanks for welcoming me to Tyndall and giving me sound advice at every turn.

A massive thank you to my parents and family for their guidance, patience and listening ear throughout my time in education. Lastly, to my grandfather, Joe for encouraging me to pursue a PhD in the first place.

Abstract

Organic-inorganic halide perovskite solar cells have gained a lot of traction in recent years due to their high power conversion efficiencies (PCE), >20%, tunable band gap and low fabrication costs. However, as the maximum theoretical efficiency outlined by the Shockley-Queisser model for a single-junction perovskite solar cell is close to being reached, researchers have begun fabricating tandem solar cells to ensure the continued improvements in PCEs. Tandem solar cells require the stacking of two solar devices such as c-Si and perovskite solar cells, the PCEs of each device is additive thus exceeding the theoretical limit.

Transferring from a single junction perovskite device to a tandem device comes with its own challenges. The sensitive nature of the perovskite material requires changes to be made in the fabrication process of the cell to ensure that all layers are deposited using a low-energy process at low temperatures to prevent the degradation of the underlying layers. The changes in the fabrication processes must also not affect the electrical, optical and morphological properties of the materials which in turn could reduce the PCE of the device.

To date, indium-tin oxide (ITO) is the commercial standard for use as the transparent conducting oxide (TCO) in perovskite solar cells. Although ITO has low sheet resistance values (8-100 Ω/\square) the material is deposited using sputtering methods and undergoes high temperature (>400°C) heat treatments. When incorporating this material into a tandem solar device such a high temperature process is not viable as it can affect the integrity of the device. As a result an alternative material of similar properties is required to replace ITO in tandem solar cells.

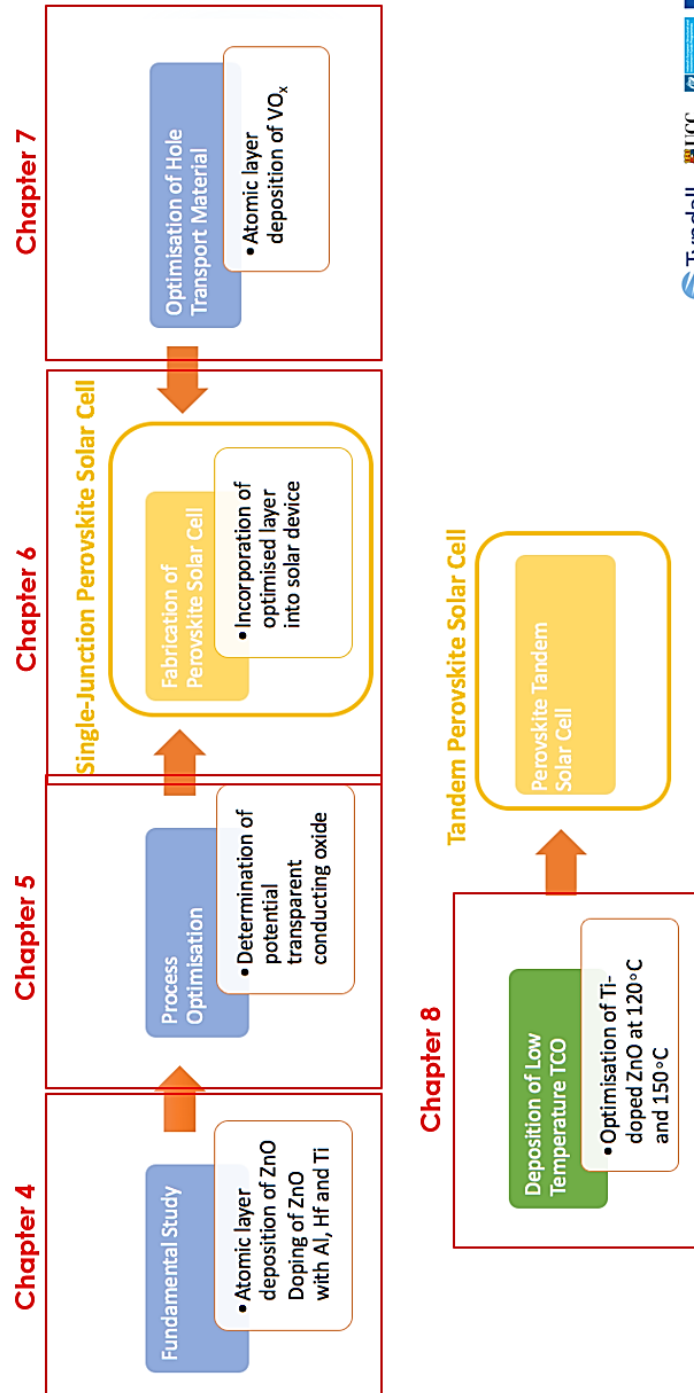
This thesis focuses on the deposition of ZnO and doped ZnO by atomic layer deposition (ALD), a scalable industry relevant technology, to replace ITO in tandem solar cells. To begin, a fundamental study of ZnO and its doped counterparts were deposited at the optimum temperature, 200°C and characterized. Ti-doped ZnO

(TZO) was shown to have the most potential for replacing ITO in a single-junction perovskite solar cell. The optimized TZO was then incorporated into a single-junction perovskite solar cell in the p-i-n configuration and compared to the state-of-the-art perovskite solar devices as proof of concept.

TZO was then deposited at low temperatures by the same methodology to evaluate its potential for incorporation into a tandem solar device. Low temperature deposition of TZO resulted in significantly higher sheet resistance values compared to values of the material deposited at the optimum temperature. Although the material maintained good optical properties the electrical properties could not compete with those of commercial ITO.

The hole transport layer (HTL) in perovskite solar cells has, to date, focused on organic thin films, however due to instabilities and parasitic optical absorptions there has been a drive for an inorganic alternative. In this thesis, as a proof of concept, vanadium oxide is investigated as a possible hole transport medium. ALD grown VOx was directly incorporated into a perovskite solar device in the p-i-n configuration that was demonstrated to generate a photocurrent. However, further work is required to develop this device and determine the viability of a vanadium based HTL.

Overview of Thesis



Chapter 1: Overview of Atomic Layer Deposition

1.1 History of Atomic Layer Deposition

Atomic layer deposition (ALD) is a chemical vapour deposition method that allows for low temperature deposition of thin films with excellent conformality and thickness control enabling deposition of continuous thin films even at high aspect ratios. Atomic layer deposition was first reported as “molecular layering” in the Soviet Union by Russian scientists in the 1960’s.¹⁻³ Numerous papers were subsequently published on this technique by Kol’tsov and his co-workers.⁴⁻¹⁰ This method was later introduced and patented in Finland by Suntola and Anston in the late 1970’s under the more commonly acknowledged name atomic layer epitaxy.¹¹ The technique was originally developed in order to meet the requirements of improving thin films for electroluminescent display devices. The first patent describes a method of depositing highly conformal thin films by introducing reactive precursors into the chamber sequentially to form a thin film on a substrate surface. The patent outlines an apparatus consisting of a vacuum chamber, a stage for the test substrates and a source that facilitates two precursors. It describes how ZnS, SnO₂ and GaP layers were deposited by this method onto glass substrates.¹² Later a second patent was submitted in 1983 which included changes to the apparatus design to counter leaks in the reactor chamber.¹³ Improvements in ALE techniques aided in the development of polycrystalline luminescent ZnS:Mn materials which were used for electroluminescent displays in the 1980’s.^{14, 15}

There have since been large advancements in the materials deposited by ALD and in the ALD kits commercially available. As a result, there has been a dramatic increase in the interest of ALD in a range of industries.^{16, 17, 18} To date, ALD has been used for the fabrication of microelectronics, where the miniaturisation of devices requires the use of high aspect ratio structures to reduce the size of devices such as complementary metal-oxide-semiconductor (CMOS) integrated circuits (IC) and dual-gate metal-oxide-semiconductor field effect transistors (MOSFETs), diffusion

barriers and interconnects in ICs.^{16, 19, 20} ALD has the capability to deposit thin films on these structures with good conformality while maintaining its electrical properties more reliably compared to other deposition methods. ALD has also been used to deposit transparent conducting oxides for flat panel displays such as thin film electroluminescence (TFEL) displays.^{21, 22, 23} ALD has also been reported as being used for battery applications such as Li-batteries.²⁴⁻²⁷ It was shown that the use of ALD in the fabrication of the batteries have improved the energy efficiency of the battery. ALD has been used for many years in the fabrication of medical devices where ALD TiO_2 and Al_2O_3 have been ALD coated onto implants as an alternative to stainless steel due to the reduction in weight and anti-microbial characteristics.²¹⁰⁻²¹³ Certain materials have also been deposited by ALD and used as a photocatalyst in the purification of air and waste water.³²

In particular, ALD has been utilized to deposit transport layers, barrier layers and transparent conducting layers for a wide range of solar cells such as crystalline-Si (c-Si), copper indium gallium selenide solar cells, (CIGS), CdTe and dye-sensitised solar cells (DSSC).³³⁻³⁹

In this thesis, the application of ALD to the field of solar cells is explored, in particular the charge transport and contact layers in perovskite (PK) solar cells. Although there are still issues with the stability and cost of ownership, relative to silicon technology, PK solar cells are reaching power conversion efficiencies (PCE) in excess of 20%, approaching the Shockley–Queisser limit for a single junction solar cell.⁴⁰ To counter this theoretical limitation, and cost of ownership issues, research is focusing towards multi-junction systems where a further enhancement of the PCE may make PK based cells viable. As a result, further challenges are now being faced, in the delicate PK based heterostructures stringent thermal budgets and non-destructive deposition techniques are vital to maintain the integrity of devices. Atomic layer deposition can deposit a wide range of materials at low temperature to ensure minimal damage to the underlying layers, this in conjunction with its compatibility with technology

scaling has identified it as one potential method for the fabrication of PK based solar cells.

1.2 Principles of ALD

ALD is a modified chemical vapour deposition (CVD) technique which proceeds via alternating pulses of reactants separated by a gas purge where in principle one atomic layer is deposited after each pulse cycle. Gas phase reactants sequentially enter the chamber and chemisorb onto the heated substrates surface. Any molecules physisorbed onto the surface are then removed using a gas purge to prevent the build-up of unwanted by-products and surplus precursor. As a consequence, the thickness of thin films grown can be controlled due to a fixed deposited rate per cycle. ALD is a self-limiting deposition method whereby molecules only adsorb onto an unoccupied reaction site. One monolayer is formed once all available sites are full and the reaction has ceased. The self-limiting mechanism results in conformal films as each reaction cycle is driven to completion. As no available surface sites remain after film growth the thin films tend to be continuous and pinhole-free.¹⁶

Figure 1.2.1 outlines the four steps for ALD growth for a binary metal oxide. The mechanism proceeds via two half-reaction cycles which include a self-terminating reaction of the first precursor followed by a purge of inert gas. This is then followed by another self-terminating reaction of the co-reactant and further purge of inert gas.

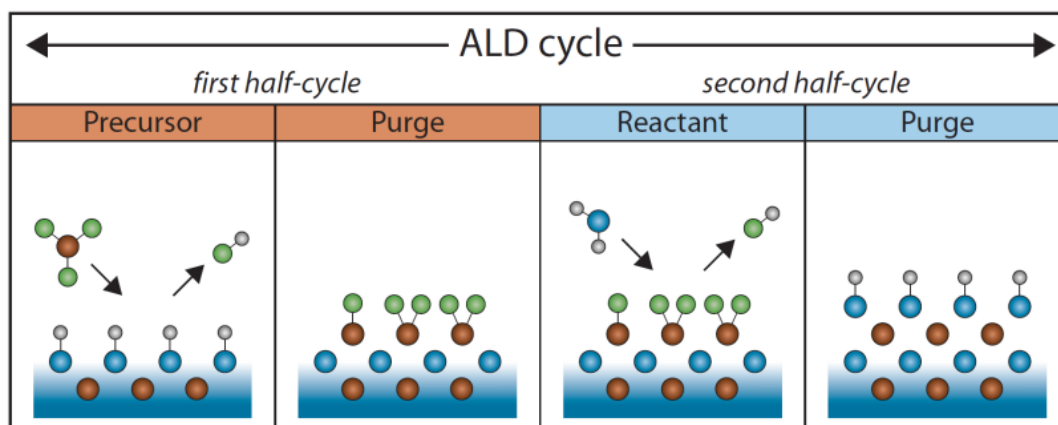


Figure 1.2.1: Schematic of one ALD reaction cycle mechanism⁴¹

From figure 1.2.1, a substrate terminated with hydroxyl or oxygen groups is placed inside the chamber. Reactant A, usually the metal-based precursor, is pulsed into the chamber in the gaseous phase and reacts with the surface hydroxyl groups but not with itself to form a chemisorbed surface species. The self-terminating feature ensures that once all available reaction sites are full the reaction ceases. A purge step of inert gas ensures any physisorbed surface species or any by-products are evacuated from the chamber. Reactant B is then pulsed into the chamber and reacts with the chemisorbed species on the surface to form the desired product. As the cycle results in an oxygen species terminating the surface the reaction cycle can begin again and be cycled until the desired layer thickness has been reached.⁴²

1.3 Growth per Cycle

Each ALD cycle deposits a given amount of material known as the growth per cycle (GPC). This is generally measured in nanometers per cycle, (nm/cycle) or Angstroms per cycle, (Å/cycle). To deposit a desired film thickness reaction cycles must be repeated until the desired thickness has been obtained. Growth per cycle assumed linearity in growth rate and is calculated by dividing the thickness of the film (nm) by the number of ALD cycles (equation 1.1).

$$GPC = \frac{\text{Thickness of Film (Å or nm)}}{\text{Number of ALD Cycles}} \quad 1.1$$

In order to deposit one full monolayer of material each cycle, the substrates surface must be saturated with precursor to ensure all available reaction sites are filled after each half-cycle. Although for ALD the growth rate is determined by self-limiting reactions partial pressure of the precursors used, the number of reaction sites available, exposure time and purge times need to be sufficient to ensure coverage is controlled.

Several models have been theorized to explain the steric effects on the precursor molecule and how these affect the GPC of the material. These models estimate the GPC taking into account: (i) the size of the reactant ML_n ⁴³, (ii) the size and geometry of the adsorbed species⁴⁴ and (iii) the size and number of adsorbed ligands.^{45, 46} Thus the GPC of a material increases with decreasing size of the reactant molecule. In complex ALD systems the GPC is usually less than one monolayer of deposited material.

Full monolayer coverage is not always achieved due to steric hindrance caused by bulky ligands of the reactant precursors preventing all reaction sites being filled. Large ligands chemisorbed to the surface can block part of the surface from being accessible from further reactant molecules. This in turn preventing further reactions with neighbouring reactive sites resulting in a discontinuous layer.

Alkyl groups are widely used in ALD precursors. The ligands are small enough so you see little steric hindrance effects and thus the GPC is quite high. However, these ligands can leave carbon and hydrogen contamination in the films due to the low decomposition temperatures of the precursors.

Several growth regimes have been reported for ALD-grown materials. The most commonly known is the layer-by-layer growth or two-dimensional growth where the precursor molecules always react with lowest unfilled reactive site resulting in a full monolayer of growth each ALD cycle. Alternatively, the material does not nucleate well on the substrate material and deposits preferentially on ALD-grown material causing island growth on the substrate.⁴⁷ It is possible for the islands to develop into a continuous film after further ALD cycles. However, generally for uniform thin film growth the precursor molecules should react with the substrate surface species on the first ALD cycle.

1.4 Self-Limiting Regime

As previously mentioned, atomic layer deposition proceeds using a self-terminating reaction mechanism whereby once the substrate surface is saturated with precursor the reaction ceases. The self-limiting mechanism allows us to control the thickness of the thin films accurately by removing the influence, within limits, of variations in precursor flux that determine the uniformity in traditional CVD methodologies. Process design with sufficiently long exposure and purge times allow the precursor and co-reactants time to react with all available reaction sites driving each cycle to completion even in high aspect structures. As all surface sites have then been filled one obtains conformal, pinhole-free films.¹⁶ The limiting chemistry can be controlled by optimizing the growth conditions such a deposition temperature.

The self-limiting regime operates via three different mechanisms; (i) Ligand exchange, (ii) Dissociation and (iii) association.^{46, 47}

(i) Ligand Exchange

The reactant molecule splits and reacts with the surface species. The remaining ligands react with the surface site and combine with the remaining surface species in the gaseous phase. This by-product is then removed during purging. The resultant molecule is then chemisorbed onto the substrate surface (see figure 1.2.2 (a)).

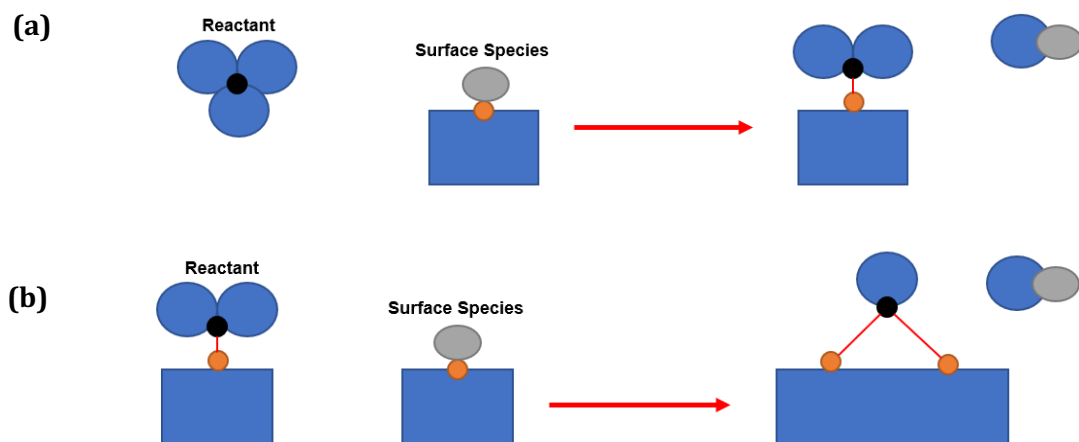


Figure 1.4.1: Schematic illustrating ligand exchange reactions of atomic layer deposition

Ligand exchange has been also known to occur between a surface bound species and surface species. Here reaction occurs between both surface bound species releasing a by-product in the gas phase but does not result in a new metal species being bound (see figure 1.2.2 (b)).

(ii) *Dissociation*

Dissociation occurs when the reaction molecule is split and combines with surface reaction sites as outlined in figure 1.2.3.

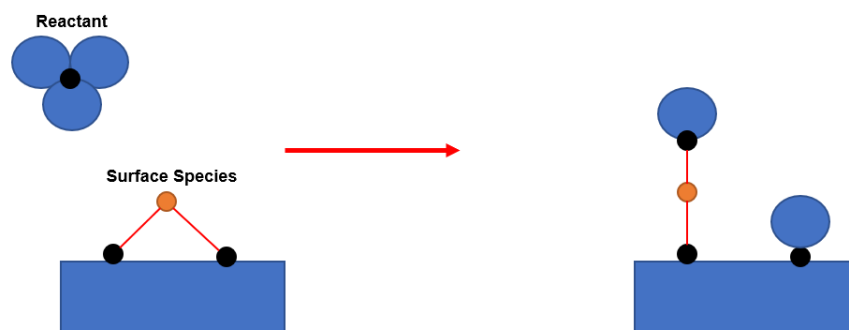


Figure 1.4.2: Schematic illustrating dissociation reaction of atomic layer deposition

(iii) *Association*

An association mechanism proceeds by the reactant molecule reacting and chemisorbing to the surface of the substrate without the release of ligands as a gaseous by-product.

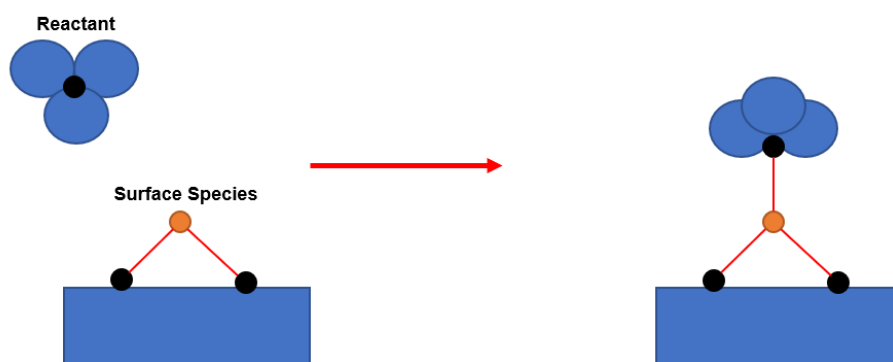


Figure 1.4.3: Schematic illustrating association reaction of atomic layer deposition

Ligand exchange is widely thought to be the preferred reaction method as the reaction equilibrium can be reached by removing gaseous by-products during a purge step.

1.5 ALD Temperature Window

ALD deposits thin films at low temperatures (typically 50-300°C).^{48, 49} The growth per cycle of deposited materials is often dependent on the growth temperatures used.⁵⁰ The temperature range in which ALD meets the requirements for self-limiting growth is known as the “ALD window”.⁵¹ Here, the growth rate is constant with temperature and deposits one monolayer per cycle. Figure 1.5.1 illustrates the ALD temperature window and how physical processes can limit its range.

From figure 1.5.1 it can be seen that the growth rate can increase, decrease or remain constant depending on the temperature. At high temperatures the first incoming precursor can desorb from the surface of the substrate prior to the second precursor entering the chamber causing a reduction in the growth rate. Alternatively, the first precursor can adsorb to the surface and the second precursor may decompose in the gas phase before the subsequent reaction can occur, resulting in the first stable precursor depositing onto the surface without being under self-limiting regime thus increasing the growth rate.⁴⁷

Low temperatures can reduce the growth rate due to insufficient activation energy to bring the reaction to completion. As a result, the precursors desorb from the surface reducing the growth rate. Conversely, low temperatures can cause the desorbed molecules to condense as a liquid or a solid on the substrates surface causing an increase in the growth rate.⁵¹⁻⁵³

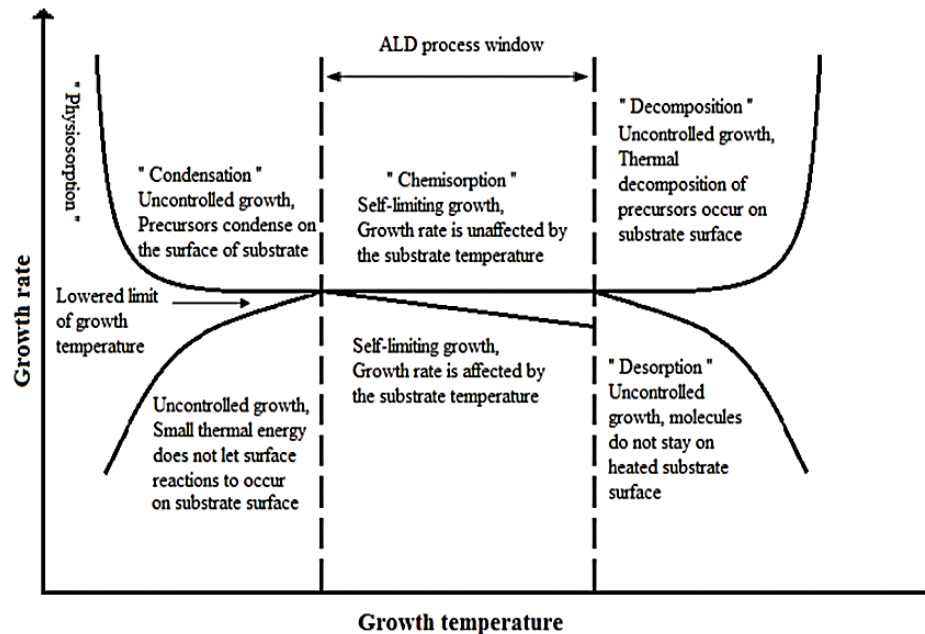


Figure 1.5.1: Image representing the ALD temperature window and how physical processes limit the ideal growth behavior and influence the growth per cycle ²²⁵

1.6 ALD Processes

1.6.1 Thermal ALD

The most commonly used ALD process to deposit metal oxides. These processes are driven solely by thermal energy (figure 1.6.1). Thermal ALD requires the substrate and the reactor to be heated to sufficient growth temperature in order to provide the necessary activation energy for the reaction to occur to completion. It is a common choice for precursors of high reactivity that need little additional activation energy. Thermal ALD processes are typically carried out using a binary reaction and generally require a co-reactant to proceed.¹⁶ This reactant is usually H_2O , O_2 or O_3 to produce metal oxides.⁵⁴⁻⁵⁸ However, H_2 has also been used in order to reduce metals or semiconductor materials.¹⁶

1.6.2 Plasma-Assisted ALD

Some processes are difficult to complete using a thermal ALD mechanism. For example, single-element films are becoming more commonly deposited by ALD and

these are challenging to deposit by thermal ALD and H_2O . As a result, a plasma is implemented to deposit these materials. Plasma produces radicals that enable reactions that otherwise would not go to completion using thermal ALD.¹⁶

Plasma-assisted ALD is often adopted when using precursors with low reactivity. They require a plasma to supply the activation energy required for the reaction to proceed that it cannot get from thermal ALD. As a result, a wider range of precursors are available to choose from that can deposit using plasma-assisted ALD. It has been shown that plasma-enhanced ALD produces dense films of low impurity leading to films with good electrical characteristics. In addition, plasma-enhanced processes often have deposit materials at a higher growth rate and require shorter purge times than thermal ALD processes reducing the overall deposition time required.^{48, 59} The increased growth rate has been attributed to the increased number of reactive sites produced by the plasma which are available for precursor adsorption.⁵⁹⁻⁶¹

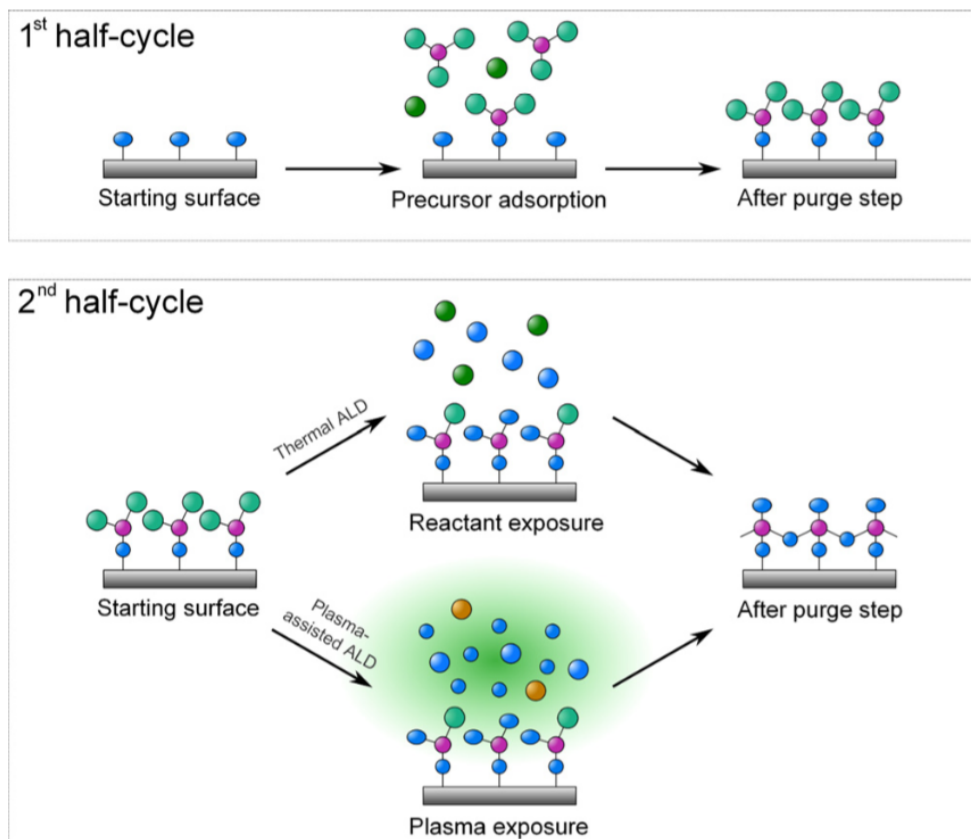


Figure 1.6.1: Image outlining the reaction mechanism of thermal ALD and plasma-enhanced ALD. The 2nd half-cycle involves a co-reactant such as H₂O or O₂ to provide to oxygen source⁴⁸

1.7 ALD of Zinc Oxide as a Transparent Conducting Oxide (TCO)

Transparent conducting oxides have been extensively researched for applications such as 3D electronics and flat panel displays. Common TCOs include indium-tin oxide (ITO), zinc oxide (ZnO) and gallium nitride (GaN). Currently ITO is the most commonly used TCO in perovskite solar cells as a transparent contact layer.⁶² In recent years, ZnO has seen an increase in interest as a replacement TCO for ITO in solar cells due to its optical and electrical properties.⁶³

ZnO can be deposited by various methods including; chemical spray pyrolysis⁶⁴⁻⁶⁶, sol-gel⁶⁷⁻⁶⁹, sputtering⁷⁰⁻⁷², chemical vapour deposition (CVD)^{73, 74}, pulsed laser

deposition (PLD)⁷⁵⁻⁷⁷, metalorganic chemical vapour deposition (MOCVD)⁷⁸⁻⁸⁰ and atomic layer deposition (ALD).⁸¹

For this thesis, ZnO has been studied with the intention of replacing ITO in perovskite solar cells. Low energy deposition processes are required for incorporation into perovskite solar cells or tandem solar cells. Atomic layer deposition was the chosen method for depositing ZnO due to its ability to produce conformal, pinhole-free thin films at low temperature.

ZnO is a wide band-gap semiconductor (3.37 eV) with a large exciton binding energy of 60 meV.⁸² The band gap of any TCO is very important as it determines whether the material is transparent to visible light (400-800 nm). The ZnO wide band gap allows it to be transparent across the entire visible spectrum. ZnO is also a conducting material and it has been shown that doping with other elements such as Al³⁺ can further improve the resistivity of the material.

ZnO is known to crystallise in a cubic rocksalt, wurtzite or zinc blende crystal phase (see figure 1.7.1). The wurtzite crystal structure is the most commonly seen for ZnO as it is thermodynamically stable at standard temperature and pressure in this form. The zinc blende structure can be obtained by growing ZnO on cubic substrates and ZnO can achieve the rocksalt crystal structure when put under pressures of >95 kbar. As a result, wurtzite and zinc blende structures are more commonly seen in ZnO materials. Wurtzite and zinc blende are very similar in structure with the main difference being the angles of the adjacent tetrahedral unit being different. The values for zinc blende and wurtzite are 60° and 0° respectively.⁸³

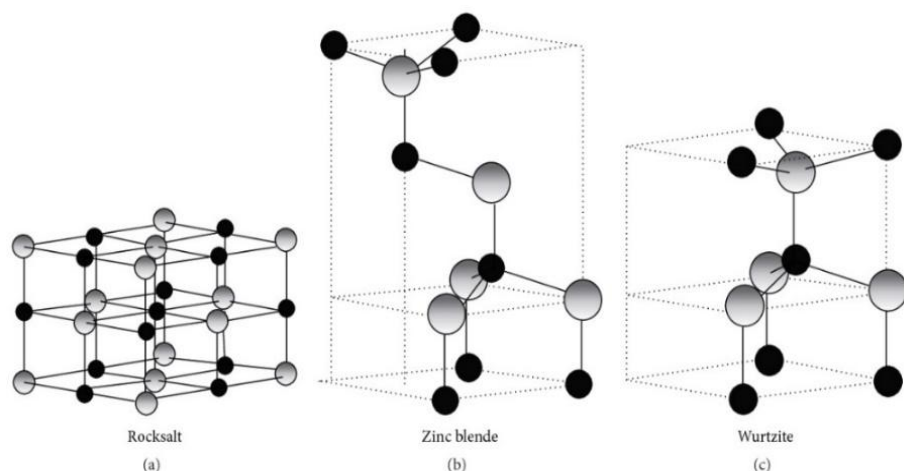


Figure 1.7.1: Schematic of possible crystal structures of ZnO (a) cubic rocksalt and (b) zinc blende and (c) wurtzite structure with the O atoms in grey and the Zn in black⁸³

It has been reported that generally the more dominant crystalline growth is in the [002] direction for wurtzite structures and [004] for zinc blende structures.⁸⁴ Here we focus on the expected crystalline orientations of wurtzite structure by XRD due to the predominantly [002] crystalline orientation obtained in the experimental ZnO data discussed in chapter 4.

The wurtzite phase is reported to have two primary growth directions. The a-axis (002) plane is a charged, polar surface due to the alternating layers of Zn^{2+} and O^{2-} and alternatively the c-axis (100) plane has a neutral surface with alternating rows of Zn^{2+} and O^{2-} . It has been observed that the [100] direction is preferred when ZnO is deposited at low temperatures and alternatively the [002] direction is more prevalent at higher deposition temperatures.^{85, 86}

ZnO deposition was first reported by ALD in the 1980s using zinc acetate and H_2O as co-reactants.^{87, 88} Since then large advancements in Zn-based precursors have been made, with dimethylzinc, $(\text{Zn}(\text{CH}_3)_2)$ and diethylzinc, $(\text{Zn}(\text{C}_2\text{H}_5)_2)$ being the most commonly used.

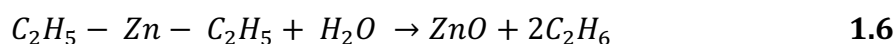
Other less reactive precursors include zinc propionate $(\text{Zn}(\text{C}_3\text{H}_5\text{O}_2)_2)$ and zinc acetylacetonate $(\text{Zn}(\text{C}_5\text{H}_7\text{O}_2)_2)$. However, these often require high deposition

temperatures. Besides H₂O, other oxidants such as O₂, H₂O₂, NO₂ and CO₂ have been used to deposit ZnO by thermal ALD. Oxygen and water have also been used extensively as co-reactants for plasma-enhanced ALD (PEALD) (see section 1.6.2).⁸⁹⁻⁹² The high reactivity of the plasma contributes to a reduction in the deposition temperature of the ZnO and produces thin films of high stoichiometry.⁸¹ However, as the ZnO is intended for replacing ITO in a perovskite solar cell, the high energy plasma can cause damage to the underlying layers of the solar cell. As a result, we focus on thermal ALD using H₂O as a co-reactant for the purpose of this study.

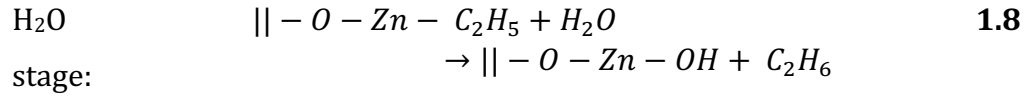
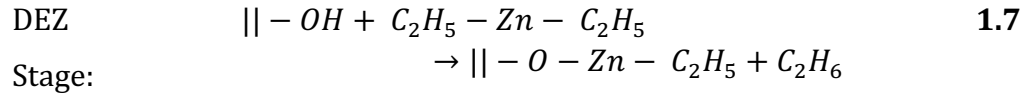
1.7.1 Deposition of ZnO using Diethylzinc

The two most commonly used ALD precursors for ZnO are diethylzinc (DEZ) and dimethylzinc (DMZ). The main difference between the precursors is their composition, where DEZ is made up of Zn atoms bonded to ethyl groups whereas Zn atoms are bonded to methyl groups in DMZ. It has been reported that both precursors have similar deposition temperature ranges and in some cases DMZ has been reported to deposit at slightly lower temperatures at higher growth rates. Although both precursors have similar properties and yield films of equal quality, DEZ has been reported on more frequently in the literature than DMZ and therefore is the more popular choice of Zn precursor. This has been attributed to the controllability of the electrical properties of the ZnO films produced by DEZ/H₂O.^{93, 94} It was reported that DEZ produces films of lower resistivity than DMZ and therefore remains the more popular choice.

DEZ has a high vapour pressure at room temperature making it simple to transport in the ALD reactor and it is also extremely reactive. Due to the high reactivity with H₂O, DEZ reacts readily to form ZnO. Equation 1.6 outlines the overall reaction with H₂O.



The reaction mechanism proceeds via two stages; DEZ stage and water stage where $||$ - represents the substrate surface (equations 1.7, 1.8).^{87, 95}



ZnO can be deposited by ALD across a wide temperature range. The ideal range at which self-limiting deposition of ZnO occurs (ALD window) has been reported by various authors as being, 105-165°C⁹⁶, 100-180°C⁹⁷, 130-180°C^{98, 99}, 70-200°C¹⁰⁰ and 200-268°C.^{101, 102} Table 1.1 outlines the literature values for the ALD windows of thermal ALD processes of DEZ and H₂O. The table highlights that there is a wide range where ZnO is deposited as a conformal thin film using DEZ and H₂O.

Substrate	Dep. Temp (°C)	ALD Window (°C)	Growth Rate (Å/cycle)	Ref
Si (100)	70-350	-	1.9	[103]
Glass	120-350	-	0.5-2.5	[64]
Glass	91-180	105-165	2.7	[104,105]
Glass	105-235	105-165	-	[106]
Sapphire (0001)	100-250	130-180	2.7	[107]
Glass, Si (100)	90-200	100-180	1.8-1.9	[97]
Glass	140	-	2.5-2.7	[108]
Si (100)	60-300	125-150	1.94	[109]
Glass	60-300	130-170	1.3	[110]

Glass, Sapphire, Si, GaAs	60-250	110-180	1.8-1.9	[111]
Glass, Si	120-240	120-150	1.8	[63]
Glass, Si, GaAs/Al₂O₃	100-300	100-200	-	[112]
PVP/Si	80-140	-	2.0	[113]
Glass	100-250	-	1.2	[114]
Si, SiO₂/Si	150-400	-	0.5-2.0	[115]
Si (100)	25-200	-	-	[116]
Glass, Si (100)	100-200	120-170	2.1	[117]
GaAs	180	-	1.8	[118]
Si (100)	RT-140	-	0.8-2.2	[102]
Glass, Si (100)	100-240	-	-	[119]
Si (100)	80-240	100-160	2.0	[120]
SiO₂/Si, MgO	70-190	130-170	2.3	[121]
Si (111)	200	-	-	[122]
Glass, c-Si (100)	200-250	-	1.8	[123]
SiO₂/Si	40-210	110-160	1.7-2.5	[124]
Si(111)	150-300	-	1.8-2.1	[125]
GaN, Graphene Sapphire, Si (100)	150-300	-	0.9-1.9	[126]
Glass	50-200	-	0.7-1.9	[127]
-	150	-	1.8	[128]
Glass, Si, SiO₂/Si	170	-	2.1-2.2	[129]

Si (100)	75-300	-	0.96-1.8	[130]
Si (100)	200	-	2.2	[131]
Glass, Si	100-200	-	1.8-2.0	[132]
Si, N-doped Graphene, N-doped carbon nanotubes	30-250	-	1.8-2.6	[133]

Table 1.1: ALD processes reported for thermal ALD of ZnO using diethylzinc and H₂O as co-reactants⁸¹

ZnO has also been reported to deposit at low temperatures by ALD with the lowest reporting temperature at 25°C. This is due to the volatility of the Zn precursor. Although this is outside the ALD window experiment design enabled the material to maintain a constant growth rate between 120-200°C and reducing slightly at temperatures below 120°C.¹³⁴ It was also reported that changing the growth mechanism to PEALD did not improve the growth rate significantly at lower temperatures.¹³⁵

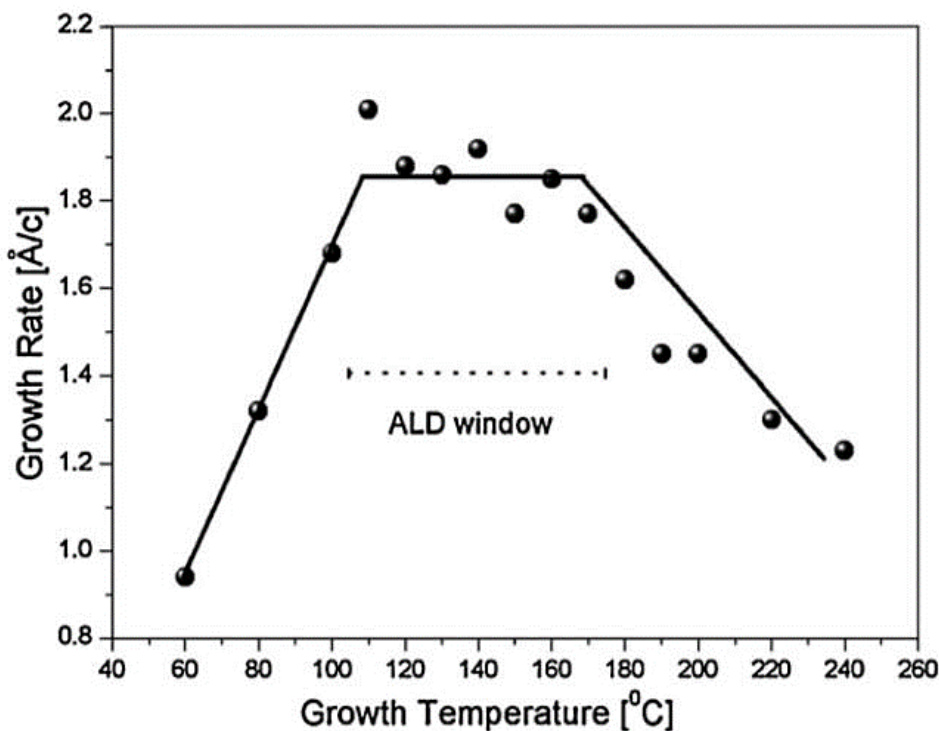


Figure 1.7.2: Represents the growth rate ($\text{\AA}/\text{cycle}$) as a function of temperature and, outlines the ALD window of ZnO 90-170°C¹⁰⁸

The average growth rate of ZnO was reported as being 0.18-0.2 nm/cycle within the ALD window. Depositing above and below the ALD window resulted in a reduction in the growth rate due to thermal decomposition at high temperatures and reduced surface reactions at low temperatures.

1.8 ALD of Doped ZnO for Transparent Conducting Oxides

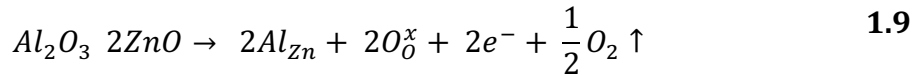
As a semiconductor material, ZnO has the ability to create excess charges by doping the material with elements with a higher number of valence electrons than Zn. Doing so has been shown to enhance the electrical properties of the ZnO. Using this method ZnO can be doped using elements from group III, IV and V to create excess charges in the lattice. Banerjee *et al* summarizes the elements reported in the literature that have been used to dope ZnO by ALD (see figure 1.8.1).⁸⁵

Elements used for doping ALD ZnO

1 1A 1A 1 H Hydrogen 1.008	2 2A 2A 4 Be Beryllium 9.012																	13 3A 3A 5 B Boron 10.811	14 4A 4A 6 C Carbon 12.011	15 5A 5A 7 N Nitrogen 14.007	16 6A 6A 8 O Oxygen 15.999	17 7A 7A 9 F Fluorine 18.998	18 8A 8A 10 Ne Neon 20.180																																		
3 1A 1A 3 Li Lithium 6.941	4 2A 2A 4 Be Beryllium 9.012	11 1A 1A 11 Na Sodium 22.990	12 2A 2A 12 Mg Magnesium 24.305	13 3A 3A 13 Al Aluminum 26.982	14 4A 4A 14 Si Silicon 28.086	15 5A 5A 15 P Phosphorus 30.974	16 6A 6A 16 S Sulfur 32.065	17 7A 7A 17 Cl Chlorine 35.453	18 8A 8A 18 Ar Argon 39.948											19 1A 1A 19 K Potassium 39.098	20 2A 2A 20 Ca Calcium 40.078	21 3A 3A 21 Sc Scandium 44.956	22 4A 4A 22 Ti Titanium 47.867	23 5A 5A 23 V Vanadium 50.942	24 6A 6A 24 Cr Chromium 51.996	25 7A 7A 25 Mn Manganese 54.938	26 8A 8A 26 Fe Iron 55.845	27 9A 9A 27 Co Cobalt 58.933	28 10A 10A 28 Ni Nickel 58.693	29 11A 11A 29 Cu Copper 63.546	30 12A 12A 30 Zn Zinc 65.38	31 13A 13A 31 Ga Gallium 69.723	32 14A 14A 32 Ge Germanium 72.631	33 15A 15A 33 As Arsenic 74.922	34 16A 16A 34 Se Selenium 78.971	35 17A 17A 35 Br Bromine 79.904	36 18A 18A 36 Kr Krypton 83.798																				
37 1A 1A 37 Rb Rubidium 85.468	38 2A 2A 38 Sr Strontium 87.62	39 3A 3A 39 Y Yttrium 88.906	40 4A 4A 40 Zr Zirconium 91.224	41 5A 5A 41 Nb Niobium 92.906	42 6A 6A 42 Mo Molybdenum 95.95	43 7A 7A 43 Tc Technetium 98.907	44 8A 8A 44 Ru Ruthenium 101.07	45 9A 9A 45 Rh Rhodium 102.905	46 10A 10A 46 Pd Palladium 106.42	47 11A 11A 47 Ag Silver 107.868	48 12A 12A 48 Cd Cadmium 112.414	49 13A 13A 49 In Indium 114.818	50 14A 14A 50 Sn Tin 118.711	51 15A 15A 51 Sb Antimony 121.760	52 16A 16A 52 Te Tellurium 127.6	53 17A 17A 53 I Iodine 126.905	54 18A 18A 54 Xe Xenon 131.29											55 1A 1A 55 Cs Cesium 132.905	56 2A 2A 56 Ba Barium 137.328	57-71 3A 3A 57-71 La Lanthanum 138.905	72 4A 4A 72 Hf Hafnium 178.49	73 5A 5A 73 Ta Tantalum 180.948	74 6A 6A 74 W Tungsten 183.84	75 7A 7A 75 Re Rhenium 186.207	76 8A 8A 76 Os Osmium 190.23	77 9A 9A 77 Ir Iridium 192.222	78 10A 10A 78 Pt Platinum 195.084	79 11A 11A 79 Au Gold 196.967	80 12A 12A 80 Hg Mercury 200.592	81 13A 13A 81 Tl Thallium 204.383	82 14A 14A 82 Pb Lead 207.2	83 15A 15A 83 Bi Bismuth 208.980	84 16A 16A 84 Po Polonium (209)	85 17A 17A 85 At Astatine (210)	86 18A 18A 86 Rn Radon (222)												
87 1A 1A 87 Fr Francium 223.020	88 2A 2A 88 Ra Radium 226.025	89-103 3A 3A 89-103 La Lanthanum 138.905	104 4A 4A 104 Rf Rutherfordium (261)	105 5A 5A 105 Db Dubnium (262)	106 6A 6A 106 Sg Seaborgium (266)	107 7A 7A 107 Bh Bohrium (264)	108 8A 8A 108 Hs Hassium (277)	109 9A 9A 109 Mt Meitnerium (276)	110 10A 10A 110 Ds Darmstadtium (281)	111 11A 11A 111 Rg Roentgenium (280)	112 12A 12A 112 Cn Copernicium (285)	113 13A 13A 113 Nh Nihonium (284)	114 14A 14A 114 Fl Flerovium (289)	115 15A 15A 115 Mc Moscovium (288)	116 16A 16A 116 Lv Livermorium (293)	117 17A 17A 117 Ts Tennessine (294)	118 18A 18A 118 Og Oganesson (294)											104 4A 4A 104 Rf Rutherfordium (261)	105 5A 5A 105 Db Dubnium (262)	106 6A 6A 106 Sg Seaborgium (266)	107 7A 7A 107 Bh Bohrium (264)	108 8A 8A 108 Hs Hassium (277)	109 9A 9A 109 Mt Meitnerium (276)	110 10A 10A 110 Ds Darmstadtium (281)	111 11A 11A 111 Rg Roentgenium (280)	112 12A 12A 112 Cn Copernicium (285)	113 13A 13A 113 Nh Nihonium (284)	114 14A 14A 114 Fl Flerovium (289)	115 15A 15A 115 Mc Moscovium (288)	116 16A 16A 116 Lv Livermorium (293)	117 17A 17A 117 Ts Tennessine (294)	118 18A 18A 118 Og Oganesson (294)															
																		57 3A 3A 57 La Lanthanum 138.905	58 4A 4A 58 Ce Cerium 140.12	59 5A 5A 59 Pr Praseodymium 140.908	60 6A 6A 60 Nd Neodymium 144.24	61 7A 7A 61 Pm Promethium 144.913	62 8A 8A 62 Sm Samarium 150.36	63 9A 9A 63 Eu Europium 151.964	64 10A 10A 64 Gd Gadolinium 157.25	65 11A 11A 65 Tb Terbium 158.925	66 12A 12A 66 Dy Dysprosium 162.50	67 13A 13A 67 Ho Holmium 164.930	68 14A 14A 68 Er Erbium 167.259	69 15A 15A 69 Tm Thulium 168.934	70 16A 16A 70 Yb Ytterbium 173.054	71 17A 17A 71 Lu Lutetium 174.967											89 3A 3A 89 Ac Actinium 227.028	90 4A 4A 90 Th Thorium 232.038	91 5A 5A 91 Pa Protactinium 231.036	92 6A 6A 92 U Uranium 238.029	93 7A 7A 93 Np Neptunium 237.048	94 8A 8A 94 Pu Plutonium 244.064	95 9A 9A 95 Am Americium 243.061	96 10A 10A 96 Cm Curium 247.070	97 11A 11A 97 Bk Berkelium 247.070	98 12A 12A 98 Cf Californium 251.080	99 13A 13A 99 Es Einsteinium (252)	100 14A 14A 100 Fm Fermium 257.105	101 15A 15A 101 Md Mendelevium (258)	102 16A 16A 102 No Nobelium 259.108	103 17A 17A 103 Lr Lawrencium (260)

Figure 1.8.1: Elements reported by literature that have been used to dope ZnO by ALD⁸⁵

Equation 1.9 outlines the mechanism of how using Al₂O₃ to dope ZnO can improve its electrical conductivity by producing two free electrons into the conduction band of ZnO.⁸⁵



Atomic layer deposition is one of the most commonly used methods for depositing conformal, uniform doped ZnO thin films. ALD can be used to produce a range of doped ZnO by changing the doping element and the dopant concentration in the film. Due to its layer-by-layer deposition mechanism ZnO is not doped in the conventional sense. Instead, ALD grows the thin films by alternating pulses of DEZ/H₂O and dopant/H₂O which result in a nanolaminate. Figure 1.8.2 outlines how the dopant concentration can be varied in the films using a super cycle mechanism using Al-doped ZnO as an example. To deposit a 19:1 ratio of ZnO:Al₂O₃ 19 cycles of DEZ/H₂O are deposited followed by 1 cycle of TMA (trimethylaluminium)/ H₂O. This is equivalent to one super cycle.

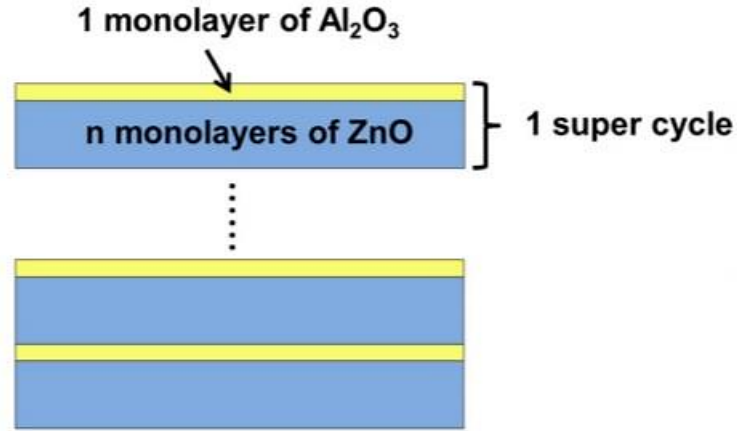


Figure 1.8.2: Illustration of the deposition mechanism of Al-doped ZnO outlining the individual monolayers of ZnO and Al_2O_3 which make up one super cycle¹³⁶

The product of the number of super cycles and the number of layers deposited in each super cycle results in the total number of ALD cycles. The desired thickness of the film can then be achieved by altering the number of super cycles depending on the growth rate of the desired material.

The atomic percent (atomic %) of the dopant incorporated into the ZnO is generally calculated using the formula outlined below¹³⁷ (Equation 1.10).

$$\text{atomic \%} = \frac{GPC_{\text{dopant}}}{GPC_{\text{dopant}} + nGPC_{\text{ZnO}}} \times 100 \quad 1.10$$

Where, GPC_{dopant} is the deposition rate of the dopant oxide, GPC_{ZnO} is the deposition rate of the ZnO and n is the number of monolayers of ZnO deposited per super cycle.

This is just one reported method of how to calculate the atomic % of a dopant in ZnO thin films. Other methods have been reported in the literature. Lee *et al* use information reported on by Elam and co-workers¹³⁸ which state that during the deposition of Al-doped ZnO, the first ALD cycles, the growth rate of Al_2O_3 on ZnO is 72% of ZnO when deposited on Al_2O_3 . They also reported that when ZnO is deposited

on Al₂O₃, ZnO requires a stabilization time for the first 4 ALD cycles. As a result, only 81% of Zn atoms were deposited on Al₂O₃ surface compared to when ZnO is deposited on a ZnO surface. A slightly lower growth per cycle thus is expected from this laminate growth method. Using these values, the atomic % of Al was calculated using equation 1.11 below:

$$atomic \% = \frac{0.72 \times N_{Al}}{0.72 \times N_{Al} + 0.81 \times 4 \times N_{Zn} + (R_{ALD} - 4) \times N_{Zn}} \quad 1.11$$

Where 4, 0.72 and 0.81 take into account the stabilization time required by Zn or Al atoms and R_{ALD} represents the number of ALD cycles.¹³⁸

Hou *et al* based their calculations on the assumption that the real Al concentration was more similar to the “rule of mixtures” formula and therefore incorporated the densities of Zn and Al to obtain atomic % of Al in the ZnO films.

$$atomic \% = \frac{\rho_{Al} C_{Al_2O_3}}{\rho_{Al} C_{Al_2O_3} + \rho_{Zn} (1 - C_{Al_2O_3})} \quad 1.12$$

Where $C_{Al_2O_3}$ is the percent of Al cycles and ρ_{Al} and ρ_{Zn} are the density values of Al and Zn respectively.¹⁴⁰

1.8.1 ALD of Al-doped ZnO

Small amounts of Al³⁺ has been known to improve ZnO conductivity and Al-doped ZnO (AZO) has been widely reported in literature.^{86, 141} Trimethylaluminium (TMA) is the preferred choice of Al-based precursor as its deposition mechanism has been shown to be close to ideal. This means that the surface reactions are truly self-limiting and any by-products formed as a result of the reactions are inert.⁴⁷ As TMA is the most reported on Al-based precursor here we focus reviewing the prominent reports on AZO using TMA/H₂O by thermal ALD.

Due to the layer-by-layer super cycle growth method of AZO, the even distribution of Al^{3+} atoms in the ZnO lattice is difficult to achieve in the resultant nanolaminate structure. Instead, lamellar distribution of Al^{3+} atoms occur in the thin film structure. Kessels *et al* proposed that the lateral distance between the Al_2O_3 dopant layers affected the doping efficiency and as a consequence the electrical properties of the material. Al doping of ZnO is most efficient when the lateral distance is higher than the critical value ($l_c = 3.8 \text{ nm}$).^{142, 143} In this case the conductivity of the films increases with increasing cycles of ZnO. However, if the lateral distance is much below l_c the conductivity of the films decreases with increasing cycles of ZnO. A similar hypothesis was reported by Lee *et al* where the l_c was in the range of 2.3-2.6 nm. Lee *et al* proposed that Al-doping occurs mainly at the interface between the ZnO and Al_2O_3 dopant layers. Here, the Al^{3+} atoms create an electric field at the interface. The electric fields caused by the dopant atoms result in Coulombic forces between the Al^{3+} atoms which prevent further doping within each field. If the interspacing between the dopant layers is too small the electric fields can overlap. The repulsive forces between the electric field reduces the doping efficiency of Al in the subsequent layers.^{144, 145}

When the interspacing between the dopants is far below l_c clustering of Al dopants can occur at the interface. In this case stoichiometric Al_2O_3 can form at the interface.¹⁴⁵ Al_2O_3 can act as scattering centres in the lattice rather than added to the number of free electrons thus reducing the carrier concentration and a higher resistivity.¹⁴⁶ In order to prevent clustering the dopant layers are generally kept well separated in the films.

Several methods have been tested to improve the Al distribution in thin films. Wu *et al* began by replacing the Al precursor TMA with dimethylaluminium isopropoxide (DMAI). They showed that by replacing the methyl groups with a bulky isopropoxide group the steric hindrance effects promoted Al^{3+} separation in the film improving the Al distribution in the film. They proved that by improving the distribution in the film similarly improve the conductivity of the material.¹⁴⁷

Na and co-workers altered the DEZ/ TMA pulsing sequence where TMA is introduced directly after DEZ pulse without water exposure. They proved that changing the pulse sequence reduced the Al incorporation making the Al atoms more homogeneously distributed throughout the lattice.¹⁴⁸ Lee *et al* reported that reducing the pulse time of the TMA left unreacted sites on the surface of the substrate where the ZnO could fill first. This in turn increased the doping efficiency of Al³⁺ increasing the electron concentration by improving the distribution of Al atoms in the film.¹⁴⁴

In order to get good electrical properties from AZO films Al concentration of 2-5 atomic % (eqn. 1.10) have been studied. The bulk of the literature has suggested that Al concentration of 1.9-2.5 atomic % equivalent to 19:1 or 20:1 ratio ZnO:dopant is the optimum concentration for low resistivity and good carrier concentrations in the temperature range 200-250°C.¹⁴⁴⁻¹⁵⁷ These values of Al content are not all verified by XPS and are a guideline only. It was observed that when the Al concentration exceeded 2 atomic % the carrier concentration, mobility and resistance worsened significantly. Early stages of ALD growth of AZO films begin as island growth on the substrate surface. As a result, conductance of the films are generally low during nucleation and increased significantly once the film begins to form a complete layer. Complete coverage has been reported to begin after 50 ALD cycles.¹²⁴ Because of this nucleation delay the growth rate of AZO films varies in the literature and is highly dependent on the growth temperature. The growth per cycle has been reported to range from 0.13-0.125 nm/cycle between 200-325°C^{144, 145, 154, 158} with the growth rate increasing with increasing temperature. In this case, it is important to determine from the literature the optimum temperature at which the electrical properties of ZnO are at their best. In this case, several papers determined that depositing AZO films using a 19:1 ratio (~2 atomic %) at 200°C gave the lowest resistance values while maintaining good optical properties.^{144, 159-162} Although the GPC of ZnO and Al₂O₃ remain constant at 150-200°C and 200-250°C respectively.¹⁶³

There is some variance from paper to paper regarding the morphological properties such as the crystalline orientation of AZO films. Kim *et al* report that thin films grow

in a way that minimized the surface energy of the substrates and grow in the lowest energy phase parallel to the substrate (epitaxial growth). In some cases, the substrate is amorphous and thus there is no influence on the crystal orientation from the substrate. As a result, the ZnO will grow in the low energy planes, (002), (110) and (100).¹⁵¹ Doping ZnO with Al will influence the crystal orientation of the ZnO lattice as atoms Zn^{2+} are substituted by Al^{3+} atoms. The preferred orientation post Al^{3+} incorporation varies across the literature. In some cases undoped ZnO reveals a preferred orientation in the [100] direction and the (002) peak disappears entirely once doped with Al.^{151, 164, 165} On the other hand several papers report that the (002) peak increases in intensity and becomes preferred over (100) peak once Al^{3+} is incorporated.^{154, 156, 159, 162} In some cases the undoped ZnO was deposited with a preferred crystalline orientation of (002) and the dominant orientation changed to (100) when Al^{3+} was incorporated.^{136, 137, 149, 164-166}

In general AZO dominantly changes from c-axis (001) to a-axis orientation (110) with increasing temperature. A theory proposed by Banerjee *et al* suggests that undoped ZnO films are made up of alternating rows of Zn^{2+} and O^{2-} atoms resulting in a neutrally charged surface in the (100) direction. As Al^{3+} atoms are incorporated the positively charged atoms upsets the neutral surface of the (100) plane. As a result, the surface energy changes causing a change in orientation to the (002) plane.¹³⁷

The opposite has also been reported for AZO films with high Al concentrations where AZO dominantly changes from a-axis (002) to c-axis (100) orientation with increasing temperature.^{105, 167} Where (100) is preferred at 150°C and (002) is preferred at higher temperatures of 250°C.^{152, 163, 168, 169}

ZnO has been doped with various other elements using the same layer-by-layer methodology and some of the hypotheses proposed for AZO films can similarly be applied to other dopant elements. With the vast numbers of papers published on Al-doped ZnO using TMA as Al-precursor it can be said that TMA is the preferred choice for use in thermal ALD.

1.8.2 ALD of Ti-doped ZnO

Doping ZnO with transition metals is not widely studied or reported in the literature. Ti is one of the more reactive transition metals with oxygen and can grow TiO₂ effectively using H₂O or O₂ as a co-reactant by ALD. TiO₂ has been reported in the literature as being deposited using TiCl₃^{168, 170}, titanium isopropoxide, Ti (OCH (CH₃)₂)₄, (TTIP)¹⁷¹⁻¹⁷⁴, and tetrakis (dimethylamido) titanium, Ti (N (CH₃)₂)₄, (TDMAT)¹⁷⁵⁻¹⁷⁷, TiCl₄¹⁷⁸ with H₂O or O₂. As seen with AZO films, dopant elements with slow growth rates can be advantageous when trying to improve the doping efficiency and dopant distribution throughout the thin film. Due to the suppression of dopant clustering from higher doping efficiencies the electrical properties of the films can be improved. Ti-based precursors deposit TiO₂ in the range of 0.02-0.05 nm/cycle much lower than ZnO or Al₂O₃ (0.2 nm/cycle and 0.1 nm/cycle respectively).¹⁷⁹

Doping mechanisms of Ti-doped ZnO (TZO) films have not been extensively studied. The most common method reported in literature to deposit TZO films is TTIP/H₂O¹⁸⁰⁻¹⁸⁴. The authors corroborate that the optimum temperature for TZO deposition is 200°C. In addition, all studies showed that the incorporation of low concentrations of Ti improved the conductivity of the ZnO films. Lee *et al*¹⁸¹ comment that the best TZO films demonstrate better conductivity than optimized AZO films suggesting that Ti had a higher doping efficiency than Al. General trends indicate that the resistance, mobility and carrier concentration of TZO films improve with increasing Ti concentration. Lee *et al*¹⁸¹ also explain how Ti is incorporated into the films as a Ti⁴⁺ ion by ALD. When the Zn²⁺ ion is substituted for Ti⁴⁺ ions there are two free electrons to contribute to the conductivity.¹⁸¹ However, when the Ti concentration exceeds the optimum the electrical properties degrade. As more dopant atoms are incorporated, the Ti atoms group near the grain boundaries forming TiO_x depleting the number of free carriers in the thin film. There is then a knock-on effect on the mobility as a result of carrier scattering at the grain boundaries.¹⁸¹ Wan *et al* reported that the films changed from polycrystalline to amorphous as the Ti concentration increased which could indicate the formation of the TiO_x molecules forming at high concentrations.¹⁸³

In general, TZO grows initially as c-axis orientated grains as the c-orientated grains have been reported to have a higher nucleation rate to the perpendicular a-axis orientated grains. As the film increases in thickness the a-axis orientation grains then become dominant in the film resulting in a preferential change from [100] to [002] crystal orientation. There has been some disagreement between authors regarding the preferred orientation of the TZO films with Bergum *et al* reporting (100) peak decreasing in intensity with Ti concentration whereas Ye *et al* report the opposite as (002) decreases in intensity with Ti concentration.^{180, 181}

TiCl₄ has also been used to dope ZnO with Ti. However, the ALD window for the precursor was reported as 200-400°C. Even at such high temperatures the growth rate of TiO₂ was low indicating surface-hindered growth.¹⁷⁸ For the application here with prerequisites such as low deposition temperatures and low energy processes TiCl₄ is not viable.

To date there has been no work done on doping ZnO with Ti using TDMAT and H₂O as co-reactants by thermal ALD. The small ligands attached to the titanium metal could assist in more efficient adsorption to the substrate increasing the growth rate of TZO while still gaining from the improvements in electrical properties of ZnO. TDMAT has been shown to deposit TiO₂ at 0.041-0.054 nm/cycle which implies that the doping distribution of Ti⁴⁺ in the ZnO lattice should be sufficiently efficient to prevent clustering of Ti⁴⁺ atoms and thereby increasing the resistance of the films.^{185,}

186

1.8.3 ALD of Hf-doped ZnO

In general little research has been done on doping ZnO with group IV elements. Geng *et al* describe the deposition of Hf-doped ZnO (HZO) films using tetrakis (ethylmethylamido) hafnium (IV), Hf(N(CH₃)(C₂H₅)₄), (TEMAH) and H₂O by thermal ALD. The growth per cycle of HfO₂ was measured to be 0.1 nm/cycle similar to values obtained for Al₂O₃. Similar to AZO and TZO films a deviation from the theoretical thickness value of HZO films was observed with the deviation increasing as the Hf concentration increased. This implies that there is a nucleation delay of DEZ on HfO₂

hindering the adsorption of the DEZ molecules on the surface. The incorporation of Hf into the ZnO lattice occurs in a similar way to Ti doping. Hf deposits by ALD in the 4+ state and thus Zn^{2+} is substituted for Hf^{4+} atoms supplying the material with an additional two free electrons.

Geng *et al*¹⁸⁷ observe a rapid decrease in resistivity as Hf is incorporated into the film with the lowest value being achieved when using a 10:1 ratio ZnO:dopant. However, at high concentrations the resistivity begins to rise again. As the concentration of the Hf increases amorphous HfO_x aggregates in the grain boundaries of the thin film resulting in an increase in carrier scattering causing a decrease in mobility and carrier concentration.

HZO films grow preferentially in the [100] direction at low Hf concentrations. As the Hf content increases the crystalline orientation changes from [100] to [002]. Additionally, the (100) peak seen at 31.8° is shifted to 31.5° at high Hf concentrations. This shift is attributed to the difference in ionic radius of Zn^{2+} and Hf^{4+} (0.74 Å and 0.78 Å respectively) when ZnO is doped causes an expansion of the crystal lattice and thus the lattice parameter.

1.9 Atomic Layer Deposition of V_2O_5

Vanadium oxide has been deposited by a range of methods including magnetron sputtering¹⁸⁸⁻¹⁹², pulsed laser deposition¹⁹³⁻¹⁹⁶, electron-beam evaporation¹⁹⁷⁻¹⁹⁹, chemical vapour deposition (CVD)²⁰⁰⁻²⁰⁵, spray pyrolysis²⁰⁶⁻²⁰⁹ and sol-gel techniques²¹⁰⁻²¹². For this work, the deposition of V_2O_5 by ALD was studied.

Vanadium oxide can exist in oxidation states from V^{2+} to V^{5+} as VO, V_2O_3 , VO_2 and V_2O_5 . However, mixed valence states of vanadium oxide also exist as other oxides such as range of oxides between VO_2 and V_2O_3 which contain both V^{4+} and V^{3+} oxidation states.

The most commonly desired oxide is V_2O_5 due to its ability to undergo a semiconductor-metal transition phases.²⁰³ This transition changes gives the oxide

both electrochromic and thermochromic properties making it a desired material for applications such as smart windows.

Outlined in the following sections is a summary of precursors that have been reported to deposit vanadium oxide by atomic layer deposition.

Vanadyl acetylacetonate, $[\text{VO} (\text{C}_5\text{H}_7\text{O}_2)_2]$ was reported by Dagur *et al*²¹³ to deposit VO_x at 400-475°C with O_2 as its co-reactant. The resultant oxide was VO_2 with an oxidation state of 4+. However, high deposition temperatures were required to deposit the oxide in order to ensure that the non-reactive O_2 gas would react sufficiently with the precursor. As a result this process was closer to a CVD process.

Ostreng *et al*^{214, 215} reported deposition of VO_x using vanadyl tetratmethyl heptadionate, $[\text{VO} (\text{C}_{11}\text{H}_{19}\text{O}_2)_2]$ and ozone (O_3). The precursor exists in the V^{4+} oxidation state and thus it was expected to deposit VO_2 . However, it was reported that the co-reactant, O_3 drives further oxidation of the metal oxide forming the V^{5+} oxidation state forming either amorphous or crystalline V_2O_5 . In addition, the growth per cycle of deposited V_2O_5 was below one monolayer per cycle within the temperature range 162-235°C with a value of 0.02-0.09 nm/cycle. The low reactivity of $[\text{VO} (\text{C}_{11}\text{H}_{19}\text{O}_2)_2]$ makes it a poor candidate for the deposition of V_2O_5 and therefore little investigation in the precursor has been done.

One of the most commonly used vanadium precursor is vanadium oxy-tri-isopropoxide, $[\text{VO} (\text{OC}_3\text{H}_7)_3]$ (VTOP). VTOP can be used to deposit V_2O_5 using H_2O , O_2 or O_2 plasma as co-reactants. Badot *et al*²¹⁶ focused on depositing VO_x using H_2O as a co-reactant for energy storage applications. The growth rate was reported as being temperature-independent between 50-100°C at a rate of 0.017-0.02 nm/cycle. Above this temperature range the growth per cycle increased significantly however even at 190°C the growth rate remained below one monolayer per cycle. It was observed that due to the bulky iso-propoxide ligands blocking the vanadium-oxygen bonds the reaction with H_2O proceeded slowly resulting in a reduction in the growth rate.

Musschoot *et al*²¹⁷ reported on the deposition of V₂O₅ by plasma-enhanced ALD (PE-ALD) and thermal ALD using VTOP and either H₂O or O₂. The deposition proceeded between 50-100°C for both mechanisms. PE-ALD revealed a constant growth rate of 0.07 nm/cycle which was significantly higher than that obtained using thermal H₂O. However, PE-ALD resulted in films contaminated with a higher concentration of carbon when using water plasma than when thermal water was used. It was commented that when O₂ plasma was used the carbon concentration in the thin films was reduced.

Pure-phase crystalline V₂O₅ was deposited by Chen *et al*²¹⁸ using VTOP and O₃. The growth per cycle in the narrow ALD of 170-175°C was 0.027 nm/cycle. Due to the unfavourable kinetics due to steric hindrance the reaction between the precursor and the co-reactant was slow at lower temperatures.

Tetrakis dimethylaminovanadium (TEMAV) and H₂O or O₂ were used by Wang *et al* to deposit VO_x at 50-200°C. Temperature independent growth was observed for both co-reactants at 50-120°C. The growth per cycle increased significantly when the temperature was reduced below 120°C. However, it was observed that the growth rate for O₃ remained higher for H₂O than O₃. These methods both formed amorphous thin films with mixed oxidation states of V⁴⁺ and V⁵⁺. Both Wang *et al*²¹⁹ and Lv *et al*²²⁰ found that a post anneal formed VO₂ and using this precursor the desired V₂O₅ could not be achieved by this method.

An extensive study of vanadium oxide was carried out by Blanquart and his co-workers using tetrakis ethylmethyl amino vanadium (TEMAV) and either ozone (O₃) or H₂O as the co-reactant.²²¹ In both cases the deposition temperature range remained 100-175°C. It was observed that the growth rate of VO_x was higher when H₂O was used as a co-reactant and self-limiting growth was proven at 150°C for both processes. In order to obtain the desired V₂O₅ a post-growth anneal at 450°C was carried out in air or N₂. This post-anneal treatment was similarly used by Rampelberg who found that V₂O₅ could be obtained most reliably when using TEMAV and O₃ followed by a post-growth anneal treatment.^{222, 223, 224, 139}

Bibliography

- [1] A. M. Shevjakov, G. N. Kuznetsova, V. B. Aleskovskii, *Chemistry of High-Temperature Materials*, Proceedings of the Second USSR Conference on High-Temperature Chemistry of Oxides, Leningrad, USSR, (1965).
- [2] G. Sveshnikova, S. Kol'tov, V. B., Aleskovskii, *J. Appl. Chem. USSR*, **40**, 2644-2646, (1967).
- [3] A. A. Malygin, *J. Indust. Eng. Chem*, **12** (1), 1-11, (2006).
- [4] S. I. Kol'tsov, *J. Appl. Chem. USSR*, **42**, 1023, (1969).
- [5] G.V. Sveshnikova, S. I. Kol'tsov, V.B. Aleskovskii, *J. Appl. Chem. USSR*, 43, 1150, (1970).
- [6] G. V. Sveshnikova, S. I. Kol'tsov, V. B. Aleskovskii, *J. Appl. Chem. USSR*, 43, 432-434, (1970).
- [7] S. I. Kol'tsov, V. B. Aleskovskii, A. N. Volkova, V. M. Smirnov, *J. Appl. Chem. USSR*, 47, 1292-1295, (1975).
- [8] S. I. Kol'tsov, V. B. Kopylov, V. M. Smirnov, V. B. Aleskovskii, *J. Appl. Chem. USSR*, 49, 525-528, (1976).
- [9] A. P. Nechiporento, T. M. Sukhareva, A. A. Malygin, S. I. Kol'tsov, V. B. Aleskovskii, *J. Appl. Chem. USSR*, 52 (11), 2333-2337, (1978).
- [10] S. I. Kol'tsov, T. V. Tuz, T. N. Volkova, *J. Appl. Chem. USSR*, 52, 2074-20744, (1979).
- [11] R. L. Puurunen, *Chem. Vap. Deposition*, 20, 332-344, (2014).
- [12] T. Suntola, J. Anston, US Patent, No. 4,058,430, (1977).
- [13] T. Suntola, J. Anston, US Patent, No. 4,389,973, (1983).
- [14] V.-P. Tanninen, M. Oikkonen, T. Tuomi, *Thin Solid Films*, 109 (3), 283-291, (1983).

- [15] R. To, S. Korpela, J. of Cryst. Growth, 59 (1-2), 395-398, (1982).
- [16] S. M. George, Chem. Rev., 110, 111-131, (2010).
- [17] J. S. Ponraj, G. Attolini, M. Bosi, Critical Reviews in Solid State Mater. Sci., 38, 203-233, (2013)
- [18] C. Marichy, M. Bechelany, N. Pinna, Adv. Mater., 24, 1017-1032, (2012)
- [19] F. Zaera, J. Mater. Chem., 18, 3521-3526, (2008)
- [20] O. Sneh, R. B. Clark-Phelps, A. R. Londergan, J. Winkler, T. E. Seidel, Thin Solid Films, 402, 248-261, (2002)
- [21] M. Leskelä, M. Ritala, Angew. Chem. Int. Ed., 42, 5548-5554, (2003)
- [22] M. Knez, K. Nielsch, L. Niinistö, Adv. Mater., 19, 3425-3438, (2007)
- [23] V. Miikkulainen, M. Leskelä, M. Ritala, R. L. Puurunen, J. Appl. Phys., 113, 021301, (2013)
- [24] M. Leskelä, M. Ritala, Thin Solid Films, 409, 138-146, (2002)
- [25] X. Meng, X.-Q. Yang, X. Sun, Adv. Mater., 24, 3589-3615, (2012)
- [26] Y. S. Jung, A. S. Cavanagh, L. A. Riley, S.-H. Kang, A. C. Dillon, M. D. Groner, S. M. George, S.-H. Lee, Adv. Mater., 22, 2172-2176, (2010)
- [27] Y. S. Jung, A. S. Cavanagh, A. C. Dillon, M. D. Groner, S. M. George, S.-H. Lee, J. Electrochem. Soc., 157, A75-A81, (2010)
- [28] R. J. Narayan, N. A. Monteiro-Riviere, R. L. Brigmon, M. J. Pellin, J. W. Elam, JOM, 61, 12-16, (2009)
- [29] S. A. Skoog, J. W. Elam, R. J. Narayan, International Mater. Rev., 58, 113-129, (2013)
- [30] R. J. Narayan, S. P. Adiga, M. J. Pellin, L. A. Curtiss, S. Stafslie, B. Chisholm, N. A. Monteiro-Riviere, R. L. Brigmon, J. W. Elam, Mater. Today, 13, 60-64, (2010)

- [31] R. Francis, N. Istephanous, E. Bonde, M. Schugt, R. O'Brien, U.S. Patent Application, 11/278, 020, (2007)
- [32] N. K. R. Eswar, S. A. Singh, J. Heo, J. Mater. Chem. A., 7, 17703, (2019)
- [33] J. A. van Delft, D. Garcia-Alonso, W. M. M. Kessels, Semicond. Sci. Technol., 27, 074002, (2012)
- [34] N. Tétreault, L.-P. Heiniger, M. Stefik, P. P. Labouchère, É. Arsenault, N. K. Nazeeruddin, G. A. Ozin, M. Grätzel, ECS Trans., 41, 303-314, (2011)
- [35] N. Tétreault, É. Arsenault, L.-P. Heiniger, N. Soheilnia, J. Brillet, T. Moehl, S. Zakeeruddin, G. A. Ozin, M. Grätzel, Nano. Lett., 11, 4579-4584, (2011)
- [36] T. Feurer, P. Reinhard, E. Avancini, B. Bissig, J. Löckinger, P. Fuchs, R. Carron, T. P. Weiss, J. Perrenoud, S. Stutterheim, S. Buecheler, A. N. Tiwari, Prog. Photovolt: Res. Appl., 25, 645-667, (2017)
- [37] K. Ramanathan, J. Mann, S. Glynn, S. Christensen, J. Pankow, J. Li, J. Scharf, L. Mansfield, M. Contreras, R. Noufi, 38th IEEE Photovoltaic Specialists Conference, 001677-001681, (2012)
- [38] P. Saint-Cast, J. Benick, D. Kania, L. Weiss, M. Hofmann, J. Rentsch, R. Preu, S. W. Glunz, IEEE Electron Device Lett., 31, 695-697, (2010)
- [39] B. W. H. van de Loo, B. Macco, J. Melskens, M. A. Verheijen, W. M. M. Kessels, 43rd IEEE Photovoltaic Specialists Conference, 3655-3660, (2016)
- [40] W. Shockley, H. J. Queisser, J. Appl. Phys., 32, 510-519, (1961)
- [41] E. Langereis, S. B. S. Heil, H. C. M. Knoop, W. Keuning, M. C. M. van de Sanden, W. M. M. Kessels, Journal of Physics D: Applied Physics, 42(7): 073001, (2009)
- [42] A. W. Ott, J. W. Klaus, J. M. Johnson, S. M. George, Thin Solid Films, 292, 135-144, (1997)
- [43] M. Ritala, M. Leskela, E. Rauhala, Chem. Mater., 6 (4), 556-561, (1994)

- [44] M. Ylilammi, Thin Solid Films, 279, (1-2): 124-130, (1996)
- [45] R. L. Puurunen, Chem. Vap. Deposition, 9, (6), 327-332, (2003)
- [46] R. L. Puurunen, Chem. Vap. Deposition, 9, (5), 249-257, (2003).
- [47] R. L. Puurunen, J. Appl. Phys., 97, 121301, (2005).
- [48] H. B. Profijt, S. E. Potts, M. C. M. van de Sanden, W. M. M. Kessels, J. Vac. Sci. Technol. A 29(5), 050801, (2011)
- [49] A. Seweryn, R. Pietruszka, B. S. Witkowski, A. Wiezbicka, R. Jakiela, P. Sybilski, M. Godlewski, Crystals, 9(11), 554, (2019)
- [50] S. J. Ponraj, G. Attolini, M. Bosi, Critical Reviews in Solid State Mater. Sci., 38(1), 203-233, (2013)
- [51] G. N. Parsons, S. M. George, M. Knez, MRS Bull., 36, 865-871, (2011)
- [52] M. R. Saleem, R. Ali, M. B. Khan, S. Hnkanen, J. Turunen, Frontiers in Materials, 15, 1:18, (2014)
- [53] R. W. Johnson, A. Hultqvist, S. F. Bent, Materials Today, 17(5), 236-246, (2014)
- [54] G. Triani, J. Campbell, P. Evans, J. Davis, B. Latella, R. Burford, Thin Solid Films, 518, 3182-3189, (2010)
- [55] H. Im, N. J. Wittenberg, N. C. Lindquist, S. -H. Oh, J. Mater. Res., 27, 663-671, (2012)
- [56] E. Lanereis, S. B. S. Hil, H. C. M. Knoop, W. Keuning, M. C. M. van de Sanden, W. M. M. Kessels, J. Phys.D: Appl. Phys., 42, 073001, (2009)
- [57] M. Cho, H. B. Park, J. Park, S. W. Lee, C. S. Hwang, J. Jeong, H. S. Kang, Y. W. Kim, J. Electrochem. Soc., 152(5), F49-F53, (2005)
- [58] C. Detavernier, J. Dendooven, D. Deduytsche, J. Musschoot, ECS Trans., 16(4), 239-246, (2008)

- [59] W. M. M. Kessels, S. B. S. Heil, E. Langereis, J. L. van Hemmen, H. C. M. Knoops, W. Keuning, M. C. M. van de Sanden, *ECS Trans.*, 3(15), 183-190, (2007)
- [60] J. L. van Hemmen, S. B. S. Heil, J. H. Klootwijk, F. Roozeboom, C. J. Hodson, M. C. M. van de Sanden, W. M. M. Kessels, *J. Electrochem.*, 154(7), G165-G169, (2007)
- [61] S. B. Heil, P. Kudlacek, E. Langereis, R. Engeln, M. A. van de Sanden, W. M. M. Kessels, *Appl. Phys. Lett.*, 89(13), 131505, (2006)
- [62] V. Zardetto, B. L. Williams, A. Perotta, F. Di Giacomo, M. A. Verheijen, R. Andriessen, W. M. M. Kessels, M. Creatore, *Sustainable Energy Fuels*, 1, 30-55, (2017)
- [63] G. Luka, T. Krajewski, L. Wachnicki, B. Witkowski, E. Lusakowska, W. Paszkowicz, E. Guziewicz, M. Godlewski, *Phys. Status Sol. A*, 207, 1568-1571, (2010)
- [64] R. Jayakrishnan, K. Mohanachandran, R. Sreekumar, C. Sudha Kartha, K. P. Vijayakumar, *Mater. Sci. Semicond. Processing*, 16, 326-331, (2013)
- [65] B. A. Victor, *Nuclear Inst. Meth. Phys. Research B*, 413, 57-61, (2017)
- [66] R. Ayouchi, F. Martin, D. Leinen, J. R. Ramos-Barrado, *J. Crystal Growth*, 247, 497-504, (2003)
- [67] S. O'Brien, L. H. K. Koh, G. M. Crean, *Thin Solid Films*, 516, 1391-1395, (2008)
- [68] S. O'Brien, M. G. Nolan, M. Copuroglu, J. A. Hamilton, I. M. Povey, L. Pereira, R. Martins, E. Fortunato, M. E. Pemble, *Thin Solid Films*, 518, 4515-4519, (2010)
- [69] W. Tang, D. C. Cameron, *Thin Solid Films*, 238, 83-87, (1994)
- [70] Y. Wang, B. Chu, *Superlattices and Microstructures*, 44, 54-61, (2008)
- [71] D. Mendil, F. Challali, T. Touam, A. Chelouche, A. H. Souici, S. Ouhenia, D. Djouadi, *J. Luminescence*, 215, 116631, (2019)
- [72] R. S. Goncalves, P. Barrozo, G. L. Brito, B. C. Viana, F. Cunha, *Thin Solid Films*, 661, 40-45, (2018)

- [73] M. Purica, E. Budianu, E. Rusu, M. Danila, R. Gavrilă, Thin Solid Films, 403-404, 485-488, (2002)
- [74] V. K. Kaushik, C. Mukherjee, T. Ganguli, P. K. Sen, J. Alloys and Compounds, 696, 727-735, (2017)
- [75] A. Krämer, S. Engel, N. Sangiorgi, A. Sanson, J. F. Bartolomé, S. Gräf, F. A. Müller, Appl. Surf. Sci., 399, 282-287, (2017)
- [76] M. S. Al-Assiri, M. M. Mostafa, M. A. Ali, M. M. El-Desoky, Superlattices and Microstructures, 75, 127-135, (2014)
- [77] W. Zhao-Yang, H. Li-Zhong, Z. Jie, Sun, Jie, W. Zhi-Jun, Vacuum, 78, 53-57, (2005)
- [78] K. Black, A. C. Jones, P. R. Chalker, J. M. Gaskell, R. T. Murray, T. B. Joyce, S. A. Rushworth, J. Crystal Growth, 310, 1010-1014, (2008)
- [79] X.-L. Chen, X. Yang, J.-Ming, Liu, D.-K. Zhang, J.-J. Zhang, Y. Zhao, X.-D. Zhang, Vacuum, 109, 74-77, (2014)
- [80] S. Pati, P. Banerji, S. B. Majumder, Sensors and Actuators A: Physical, 213, 52-58, (2014)
- [81] T. Tynell, M. Karppinen, Semicond. Sci. Technol., 29, 043001, (2014)
- [82] A. Kumar, P. Kumar, K. Kumar, T. Singh, R. Singh, K. Asokan, D. Kanjilal, J. Alloys and Compounds, 649, 1205-1209, (2015)
- [83] A. Ashrafia, C. Jagadish, J. Appl. Phys., 102, 071101, (2007)
- [84] M. A. Johar, R. A. Afzal, A. A. Alazba, U. Manzoor, Adv. Mater. Sci. and Eng., 934587, (2015)
- [85] Z. Gao, P. Banerjee, J. Vacuum Sci. and Technol. A, 37, 050802, (2019)
- [86] V. Lujala, J. Skarp, M. Tammenmaa, T. Suntola, Appl. Surf. Sci., 82-83, 34, (1994)

- [87] E. Guziewicz, M. Godlewski, L. Wachnicki, T. A. Krajewski, G. Luka, S. Gieraltowska, R. Jakiela, A. Stonert, W. Lisowski, M. Krawczyk, *Semicond. Sci. Technol.*, 27, 074011, (2012)
- [88] M. Tammenmaa, T. Koskinen, L. Hiltunen, L. Niinisto, M. Leskala, *Thin Solid Films*, 124, 125-128, (1985)
- [89] S.-H. Ko Park, C.-S. Hwang, H.-S. Kwack, J.-H. Lee, H. Y. Chu, *Electrochem. Solid-State Lett.*, 9, G299, (2006)
- [90] Y. Kawamura, N. Hattori, N. Miyatake, M. Horita, Y. Uraoka, *Japan. J. Appl. Phys.*, 50, 04DF05, (2011)
- [91] S. M. Sultan, O. D. Clark, T. B. Masaud, Q. Fang, R. Gunn, M. M. Hakim, K. Sun, P. Ashburn, H. M. Chong, *Microelectron. Eng.*, 97, 162-165, (2012)
- [92] H. W. Huag, W. C. Chang, S. J. Lin, Y. L. Chueh, *J. Appl. Phys.*, 112, 124102, (2012)
- [93] H. Makino, A. Miyake, T. Yamada, N. Yamamoto, T. Yamamoto, *Thin Solid Films*, 517, 3138-3142, (2009)
- [94] E. Guziewicz, M. Godlewski, T. Krajewski, L. Wachnicki, A. Szczepanik, K. Kopalko, A. Wójcik-Głodowska, E. Przeździecka, W. Paszkowicz, E. Lusakowska, P. Kruszewski, N. Huby, G. Tallarida, S. Ferrari, *J. Appl. Phys.*, 105, 122413, (2009)
- [95] V. Lujala, J. Skarp, M. Tammenmaa, T. Suntola, *Appl. Surf. Sci.*, 82-83, 34-40, (1994)
- [96] B. Sang, M. Konagai, *Japan. J. Appl. Phys.*, 35, L602, (1996)
- [97] E. Guziwewica, I. A. Kowalik, M. Godlewski, K. Kopalko, V. Osinniy, A. Wójcik, S. Yatsunencko, E. Lusakowska, W. Paszkowicz, M. Guziewicz, *J. Appl. Phys.*, 103, 033515, (2008)
- [98] E. B. Yousfi, J. Fouache, D. Lincot, *Appl. Surf. Sci.*, 153, 223, (2000)
- [99] J. Lim, C. Lee, *Thin Solid Films*, 515, 3335, (2007)

- [100] S. Jeon, S. Bang, S. Lee, S. Kwon, W. Jeong, H. Jeon, H. J. Chang, H.-H. Park, J. Electrochem. Soc., 155, H738, (2008)
- [101] K. Saito, Y. Yamamoto, A. Matsuda, S. Izumi, K. Ishida, K. Takahashi, Phys. Stat. Solidi, B, 229, 925, (2002)
- [102] J. Malm, E. Sahramo, J. Perala, T. Sajavaara, M. Karppinen, Thin Solid Films, 519, 5319-5322, (2011)
- [103] S. Jeon, S. Bang, S. Lee, S. Kwon, W. Jeong, H. Jeon, H. J. Chang, H.-H. Park, J. Electrochem. Soc., 155, H738-H743, (2008)
- [104] B. Sang, M. Konagai, Jpn. J. Appl. Phys., 35, L602-L605, (1996)
- [105] A. Yamada, B. Sang, M. Konagai, Appl. Surf. Sci., 112, 216-222, (1997)
- [106] K. Saito, Y. Watanabe, K. Takahashi, T. Matsuzawa, B. Sang, M. Konagai, Solar Energy Mater. Solar Cells, 49, 187-193, (1997)
- [107] J. Lim, C. Lee, Thin Solid Films, 515, 3335-3338, (2007)
- [108] H. Makino, S. Kishimoto, T. Yamada, A. Miyake, N. Yamamoto, T. Yamamoto, Phys. Stat. Sol., 205, 8, 1971-1974, (2008)
- [109] S.-Y. Pung, K.-L. Choy, X. Hou, C. Shan, Nanotechnol., 19, 435609, (2008)
- [110] H. Makino, A. Miyake, T. Yamada, N. Yamamoto, T. Yamamoto, Thin Solid Films, 517, 3138-3142, (2009)
- [111] T. Krajewski, E. Guziewicz, M. Godlewski, L. Wachnicki, A. Wokcik-Glodowska, M. Lukasiewicz, K. Kopalko, V. Osinniy, M. Guziewicz, Microelectronics Journal, 40, 293-295, (2009)
- [112] E. Guziewicz, M. Godlewski, T. A. Krajewski, L. Wachnicki, G. Luka, J. Z. Domagala, W. Paszkowicz, B. J. Kowalski, B. S. Witkowski, A. Duzynska, A. Suchocki, Phys. Status Sol. A, 247, 1611-1615, (2010)

- [113] S. C. Gong, S. Bang, H. Jeon, H.-H. Park, Y. C. Chang, H. J. Chang, *Met. Mater. Int.*, 16, 953-958, (2010)
- [114] J.-E. Kim, S.-M. Bae, H.-S. Yang, J.-H. Hwang, *J. Korean Ceramic Soc.*, 47, 353-356, (2010)
- [115] Y.-S. Min, C.-J. An, S.-K. Kim, J.-W. Song, *Bull. Korean Chem. Soc.*, 31, 2503, (2010)
- [116] T.-Y. Chiang, C.-L. Dai, D.-M. Lian, *J. Alloys and Compounds*, 509, 5623-5626, (2011)
- [117] J. T. Tanskanen, J. R. Bakke, T. A. Pakkanen, S. F. Bent, *J. Vac. Sci. and Technol. A*, 29, 031507, (2011)
- [118] Y.-C. Cheng, Y.-S. Kuo, Y.-H. Li, J.-J. Shyue, M.-J. Chen, *Thin Solid Films*, 519, 5558-5561, (2011)
- [119] R. Kudrawiec, J. Misiewicz, L. Wachnicki, E. Guzewicz, M. Godlewski, *Semiconduct. Sci. and Technol.*, 26, 075012, (2011)
- [120] K. Tapily, D. Gu, H. Baumgart, G. Namkoong, D. Stegall, A. A. Elmustafa, *Semiconduct. Sci. and Technol.*, 26, 115005, (2011)
- [121] K. Pradhan, P. F. Lyman, *ECS Trans.*, 41, 247-253, (2011)
- [122] T. Wang, H. Wu, C. Chen, C. Liu, *Appl. Phys. Lett.*, 100, 011901, (2012)
- [123] A. Illiberi, F. Roozeboom, P. Poodt, *ACS, Appl. Mater. Interfaces*, 4, 268-272, (2012)
- [124] M. B. M. Moataz, C. J. Oldham, *J. Vac. Sci. Technol.*, 30, 01A155, (2012)
- [125] Z. Chai, L. Xinchun, D. He, *Surf. Coatings Technol.*, 207, 361-366, (2012)
- [126] Z. Baji, Z. Lábadí, Z. E. Horváth, G. Molnár, J. Volk, I. Bársony, P. Barna, *Cryst. Growth Des.*, 12, 5615-5620, (2012)
- [127] N. Y. Yuan, S. Y. Wang, C. B. Tan, X. Q. Wang, G. G. Chen, J. N. Ding, *J. Cryst. Growth*, 366, 43-46, (2013)

- [128] A. J. M. Mackus, C. MacIsaac, W.-H. Kim, S. F. Bent, J. Chem. Phys., 146, 052802, (2017)
- [129] H. K. Park, B. S. Yang, S. Park, M. S. Kim, J. C. Shin, J. Heo, J. Alloys and Compounds, 605, 124-130, (2014)
- [130] A. Afshar, K. C. Cadien, Appl. Phys. Lett., 103, 251906, (2013)
- [131] T. Singh, T. Lehnen, T. Leuning, D. Sahu, S. Mathur, Appl. Surf. Sci., 289, 27-32, (2014)
- [132] W.-J. Lee, S. Bera, Z. Wan, W. Dai, J.-S. Bae, T. E. Hong, K.-H. Kim, J.-H. Ahn, S.-H. Kwon, J. Am. Ceram. Soc., 102, 5881-5889, (2019)
- [133] J. Cai, Z. Ma, U. Wejinya, M. Zou, Y. Liu, H. Zhou, X. Meng, J. Mater. Sci., 54, 5236-5248, (2019)
- [134] C.-S. Ku, J.-M. Huang, C.-M. Lin, H.-Y. Lee, Thin Solid Films, 518, 1373-1376, (2009)
- [135] T. Nam, J.-M. Kim, M.-K. Kim, H. Kim, J. Korean Phys. Soc., 59, 452, (2011)
- [136] C.-H. Zhai, R.-J. Zhang, Y.-X. Zheng, S.-Y. Wang, J. Liu, N. Dai, L.-Y. Chen, Nanoscale Res. Lett., 11, 407, (2016)
- [137] P. Banerjee, W.-J. Lee, K.-R. Bae, S. B. Lee, G. W. Rubloff, J. Appl. Phys., 108, 043504, (2010)
- [138] J. W. Elam, D. Routkevitch, S. M. George, Chem. Mater. 15, 1020, (2003)
- [139] I. I. Kazadojev, Growth of V2O5 films for electrochromic and battery applications, (published doctoral dissertation), University College Cork, Ireland (2018)
- [140] Q. Hou, F. Meng, J. Sun, Nanoscale Res. Lett., 8, 144, (2013)
- [141] H. Sato, T. Minami, S. Takata, T. Miyata, M. Ishii, Thin Solid Films 236, 14-19, (1993)

- [142] Y. Wu, P. M. Hermkens, B. W. H. van de Loo, H. C. M. Knoops, S. E. Potts, M. A. Verheijen, F. Roozeboom, W. M. M. Kessels, *J. Appl. Phys.*, 114, 024308, (2013)
- [143] Y. Wu, A. D. Giddings, M. A. Verheijen, B. Macco, T. J. Prosa, D. J. Larson, F. Roozeboom, W. M. M. Kessels, *Chem. Mater.*, 30, 1209-1217, (2018)
- [144] D.-J. Lee, J.-Y. Kwon, S.-H. Kim, H.-M. Kim, K.-B. Kim, *J. Electrochem. Soc.*, 158, D277-D281, (2011)
- [145] D.-J. Lee, H.-M. Kim, J.-Y. Kwon, H. Choi, S.-H. Kim, K.-B. Kim, *Adv. Funct. Mater.*, 21, 448-455, (2011)
- [146] H. K. Park, J. Heo, *Appl. Surf. Sci.*, 309, 133-137, (2014)
- [147] Y. Wu, S. E. Potts, P. M. Hermkens, H. C. M. Knoops, F. Roozeboom, W. M. M. Kessels, *Chem. Mater.*, 25, 4619-4622, (2013)
- [148] J.-S. Na, Q. Ping, G. Scarel, G. N. Parsons, *Chem. Mater.*, 21, 5585, (2009)
- [149] S. C. Gong, J. G. Jang, H. J. Chang, J.-S. Park, *Synth. Met.*, 161, 823-827, (2011)
- [150] J.-S. Na, G. Scarel, G. N. Parsons, *J. Phys. Chem. C*, 114, 383-388, (2010)
- [151] J. Y. Kim, Y.-J. Choi, H.-H. Park, S. Golledge, D. C. Johnson, *J. Vac. Sci. Technol. A*, 28, 1111, (2010)
- [152] Z. Baji, Z. Lábadi, Z. E. Horváth, M. Fried, B. Szentpáli, I. Bársony, *J. Therm. Anal. Calorim.*, 105, 93-99, (2011)
- [153] M. Steglich, A. Bingel, G. Jia, F. Falk, *Sol. Energy Mater. Sol. Cells*, 103, 62-68, (2012)
- [154] Y.-J. Choi, S. C. Gong, D. C. Johnson, S. Golledge, G. Y. Yoem, H.-H. Park, *Appl. Surf. Sci.*, 269, 92, (2013)
- [155] Y. Geng, L. Guo, S.-S. Xu, Q.-Q. Sun, S.-J. Ding, H.-L. Lu, D. W. Zhang, *J. Phys. Chem. C*, 115, 12317, (2011)
- [156] R. Mundle, A. K. Pradhan, *J. Appl. Phys.*, 115, 183503, (2014)

- [157] P. K. Nayak, Z. Wang, H. N. Alshareef, *Adv. Mater.*, 28, 7736, (2016)
- [158] T. Dhakal, A. S. Nandur, R. Christiam, P. Vasekar, S. Desu, C. Westgate, D. Koukis, D. Arenas, D. Tanner, *Solar Energy*, 86, 1306, (2012)
- [159] C. H. Ahn, H. Kim, H. K. Cho, *Thin Solid Films*, 519, 747-750, (2010)
- [160] G. Luka, L. Wachnicki, B. S. Witkowski, T. A. Krajewski, R. Jakiela, E. Guziewicz, M. Godlewski, *Mater. Sci. Eng. B*, 176, 237-241, (2011)
- [161] N. P. Dasgupta, S. Neubert, W. Lee, O. Trejo, J.-R. Lee, F. B. Prinz, *Chem. Mater.*, 22, 4769-4775, (2010)
- [162] N.-J. Choi, K.-W. Kim, H.-S. Son, S.-N. Lee, *Electron. Mater. Lett.*, 10, 259-262, (2014)
- [163] C. H. Ahn, A. Y. Lee, H. K. Cho, *Thin Solid Films*, 545, 106-110, (2013)
- [164] W. J. Maeng, J.-W. Lee, J. H. Lee, K.-B. Chung, J.-S. Park, *J. Phys. D, Appl. Phys.*, 44, 445305, (2011)
- [165] V. Romanyuk, N. Dmitruk, V. Karpyna, G. Lashkarev, V. Popovych, M. Dranchuk, R. Pietruszka, M. Godlewski, G. Dovbeshko, I. Timofeeva, O. Kondratenko, M. Taborska, A. Ievtushenko, *Acta. Phys. Pol. A*, 129, A36, (2016)
- [166] S. J. Kwon, *Japan. J. Appl. Phys.*, 44, 1062-1066, (2005)
- [167] J. G. Lu, Z. Z. Ye, Y. J. Zeng, L. P. Zhu, L. Wang, J. Yuan, B. H. Zhao, *J. Appl. Phys.*, 100, 073714, (2006)
- [168] H. Saarenpää, T. Niemi, A. Tukiainen, H. Lemmetyinen, N. Tkachenko, *Solar Energy Mater. Sol. Cells*, 94, 1379-1383, (2010)
- [169] M. J. Maeng, *J. Vac. Sci. Technol. B*, 30, 031210, (2012)
- [170] M. Ritala, M. Leskela, E. Nykänen, P. Soininen, L. Niinistö, *Thin Solid Films*, 225, 288-295, (1993)

- [171] H. Döring, K. Hasimoto, A. Fujishima, *Berichte der Bunsengesellschaft für Physikalische Chemie*, 96, 620-622, (1992)
- [172] J. Aarik, A. Aidla, T. Uustare, M. Ritala, M. Leskelä, *Appl. Surf. Sci.*, 161, 385-395, (2000)
- [173] A. Rahtu, M. Ritala, *Chem. Vap. Dep.*, 8, 21-28, (2002)
- [174] H. Shin, D. K. Jeong, J. A. Lee, M. M. Sung, J. I. Kim, *Adv. Mater.*, 16, 1197-1200, (2004)
- [175] J. W. Lim, S. J. Yun, J. H. Lee, *Electrochem. Solid Stat. Lett.*, 7, F73-F76, (2004)
- [176] W. J. Maeng, H. Kim, *Electrochem. Solid Stat. Lett.*, 9, G191-G194, (2006)
- [177] R. Pheamhom, C. Sunwoo, D. H. Kim, *J. Vac. Sci. Technol. A*, 24, 1535-1539, (2006)
- [178] G. Torrisi, A. Di. Mauro, M. Scuderi, G. Nicotra, G. Impellizzeri, *RSC Adv.*, 6, 88886, (2016)
- [179] M. Ritala, M. Leskelä, L. Niinisto, P. Haussalo, *Chem. Mater.*, 5, 1174, (1993)
- [180] Z.-Y. Ye, H.-L. Lu, Y. Geng, Y.-Z. Gu, Y. Zhang, Q.-Q. Sun, S.-J. Ding, D. W. Zhang, *Nanoscale Res. Lett.*, 8, 108, (2013)
- [181] D.-J. Lee, K.-J. Kim, S.-H. Kim, J.-Y. Kwon, J. Xu, K.-B. Kim, *J. Mater. Chem., C*, 1, 4761, (2013)
- [182] K. Bergum, P.-A. Hansen, H. Fjellvag, O. Nilsen, *J. Alloys and Compounds*, 616, 618-624, (2014)
- [183] Z. Wan, W.-S. Kwack, W.-J. Lee, S.-H. Jang, H.-R. Kim, J.-W. Kim, K.-W. Jung, W.-J. Min, K.-S. Yu, S.-H. Park, E.-Y. Yun, J.-H. Kim, S.-H. Kwon, *Mater. Res. Bull.*, 57, 23-28, (2014)
- [184] K. Bergum, H. Fjellvag, O. Nilsen, *Appl. Surf. Sci.*, 332, 494-499, (2015)

- [185] M. Reiners, K. Xu, N. Aslam, A. Devi, R. Waser, S. Hoffmann-Eifert, *Chem. Mater.*, 25, 2934-2943, (2013)
- [186] C. Jin, B. Liu, Z. Lei, J. Sun, *Nanoscale Res. Lett.*, 10, 95, (2015)
- [187] Y. Geng, Z.-Y. Xie, W. Yang, S.-S. Xu, Q.-Q. Sun, S.-J. Ding, H.-L. Lu, D. W. Zhang, *Surf. Coatings Technol.*, 232, 41-45, (2013)
- [188] M. Sh. Muhammed, M. K. Kalaf, S. J. Mohammed, *Mater. Sci. Eng.*, 557, 012065, (2019)
- [189] C. Zhang, Z. Peng, X. Cui, E. Neil, Y. Li, S. Kasap, Q. Tang, *Appl. Surf. Sci.*, 433, 1094-1099, (2018)
- [190] C. R. Aita, Y. L. Liu, M. L. Kao, S. D. Hansen, *J. Appl. Phys.*, 60, 749, (1986)
- [191] D. Wruck, S. Ramamurthi, M. Rubin, *Thin Solid Films*, 182, 79-86, (1989)
- [192] L.J. Meng, R. A. Silva, H. N. Cui, V. Teixeira, M.P. dos Santos, Z. Xu, *Thin Solid Films*, 515, 195-200, (2006)
- [193] J. G. Zhang, J. M. McGraw, J. Turner, D. Ginley, *J. Electrochem. Soc.* 144.5, 1630-1634, (1997)
- [194] C. Julien, E. Haro-Pontiatowski, M. A. Camacho-López, L. Escobar-Alarcón, J. Jiménez-Jarquín, *Mater. Sci. and Eng. B*, 65, 170-176, (1999)
- [195] C. V. Ramana, R. J. Smith, O. M. Hussain, C. C. Chusuei, C. M. Julien, *Chem. Mater.*, 17, 1213-1219, (2005)
- [196] C. V. Ramana, R. J. Smith, O. m. Hussain, M. Massot, C. M. Julien, *Surf. Interface Anal.*, 37, 406-411, (2005)
- [197] C. V. Ramana, O. M. Hussain, R. Pinto, C. M. Julien, *Appl. Surf. Sci.*, 207, 135-138, (2003)
- [198] C. V. Ramana, O. M. Hussain, B. Srinivasu;u Naidu, P. J. Reddy, *Thin Solid Films*, 305, 219-226, (1997)

- [199] C. V. Ramana, O. M. Hussin, B. Srinivasulu Naidu, *Mater. Chem. Phys.*, 50, 195-199, (1997)
- [200] C. V. Ramana, O. M. Hussain, B. Srinivaulu Naidu, C. Julien, M. Balkanski, *Mater. Sci., Eng.*, B52, 32-39, (1998)
- [201] G. Groult, E. Balnois, A. Mantoux, K. Le Van, D. Lincot, *Appl. Surf. Sci.*, 252, 5917-5925, (2006)
- [202] C. Piccirillo, R. Binions, I. P. Parkin, *Chem. Vap. Deposition*, 13, 145-151, (2007)
- [203] H. Groult, K. Le Van, A. Mantoux, L. Perrigaud, P. Doppelt, *J. Power Sources*, 174, 312-320, (2007)
- [204] S. Beke, *Thin Solid Films*, 519, 1761-1771, (2011)
- [205] N. K. Nandakumar, E. G. Seebauer, *Thin Solid Films*, 519, 3663-3668, (2011)
- [206] I. I. Kazadojev, S. O'Brien, L. P. Ryan, M. Modreanu, P. Osiceanu, S. Somacescu, M. E. Pemble, I. M. Povey, *ECS Trans.*, 85, 83-94, (2018)
- [207] A. Nancy Anna Anasthasiya, K. Gowtham, R. Shruthi, R. Pandeewari, B. G. Jeyaprakash, *Intern. J. Nanoscience*, 17, 1760037, (2018)
- [208] R. Irani, S. M. Rozati, S. Beke, *Mater. Chem. Phys.*, 139, 489-493, (2013)
- [209] S. Gavalas, E. Gagaoudakis, D. Katerinopoulou, V. Petromichelaki, S. Wight, G. Wotring, E. Aperathitis, G. Kiriakidis, V. Binas, *Mater. Sci. in Semiconductor Processing*, 89, 116-120, (2019)
- [210] A. Boudi, N. Benramdane, A. Nakrela, Mathieu, B. Khelifa, R. Desfeux, A. Da Costa, *Mater. Sci. Eng. B95*, 141-147, (2002)
- [211] E. A. Meulenkaamp, W. van Klinken, A. R. Schlatmann, *Solid State Ionics*, 126, 235-244, (1999)
- [212] M. Benmoussa, A. Outzourhit, R. Joudani, A., Bennouna, E. L. Ameziane, *Active and Passive Elec. Comp.*, 26, 246-256, (2003)

- [213] Z. S. El Mandough, M. S. Selim, *Thin Solid Films*, 371, 259-263, (2000)
- [214] P. Dagur, A. U. Mane, S. A. Shrivashankar, *J. Cryst. Growth*, 275, 1223-1228, (2005)
- [215] E. Ostreng, K. B. Gandrud, Y. Hu, O. Nilen, H. Fjellvag, *J. Mater Chem. A*, 2, 15044, (2014)
- [216] E. Ostreng, O. Nilsen, H. Fjellvag, *J. Phys. Chem. C*, 116, 19444-19450, (2012)
- [217] J. C. Badot, S. Ribes, E. B. Yousfi, V. Vivier, J. P. Pereira-Ramos, N. Baffier, D. Lincotb, *Electrochem. Solid-State Lett.*, 3, 485-488, (2000)
- [218] J. Musschoot, D. Deduytsche, H. Poelman, J. Haemers, R. L. V. Meirhaeghe, S. V. den Berghe, C. Detavernier, *J. Electrochem. Soc.*, 156, 122-126, (2009)
- [219] X. Chen, E. Pomerantseva, P. Banerjee, K. Gregorczyk, R. Ghodssi, G. Rubloff, *Chem. Mater.*, 24, 1255-1261, (2012)
- [220] Y. Gao, Y Shao, L. Yan, H. Li, Y. Su, X. Wang, *Adv. Funct. Mater.*, 26, 4456-4463, (2016)
- [221] X. Lv, Y. Cao, L. Yan, Y. Li, L. Song, *Appl. Surf. Sci.*, 396, 214-220, (2017)
- [222] T. Blanquart, J. Niinisto, M. Gavagnin, V. Longo, M. Heikkila, E. Puukilainen, V. R. Pallem, C. Dussarrat, M. Ritala, M. Leskala, *RSC Adv.*, 3, 1179-1185, (2013)
- [223] G. Rampelberg, D. Deduytsche, B. De Schutter, P. A. Premkumar, M. Toeller, M. Scharkers, K. Martens, I. Radu, C. Detavernier, *Thin Solid Films*, 550, 59-64, (2014)
- [224] G. Rampelberg, M. Schaekers, K. Martens, Q. Xie, D. Deduytsche, B. De Schutter, N. Blasco, J. Kittl, C. Detavernier, *Appl. Phys. Lett.*, 98, 162902, (2011)

Chapter 2: Introduction to Perovskite Solar Cells

2.1 History of Perovskite Solar Cells

The term “perovskite” was coined in 1839 named after a Russian mineralogist, Perovski, when Gustav Rose discovered calcium titanate (CaTiO_3).^{1,2} Perovskites are materials that exist with the molecular formula ABX_3 or have the same crystal structure as CaTiO_3 .³ A commonly used perovskite material is a halide-based perovskite. In this case, A is a cation such as CH_3NH_3^+ (methylammonium, MA), $\text{HC}(\text{NH}_2)_2^+$ (formamidinium, FA), Cs^+ and Ru^+ . The anion, B are generally 3d, 4d or 5d transition metals in an octahedral formation such as Pb^{2+} , or Sn^{2+} and X is a halogen (Br^- , I^- or Cl^-) (see figure 2.1).⁴ It was found that the lead-based halide perovskite exhibited the most attractive features with good optical absorption, electrical properties including high electron and hole mobility and low surface recombination. The first halide-based perovskite was first reported by Müller in 1958 where he describes the structure of CsPbI_3 and CsPbBr_3 .⁵

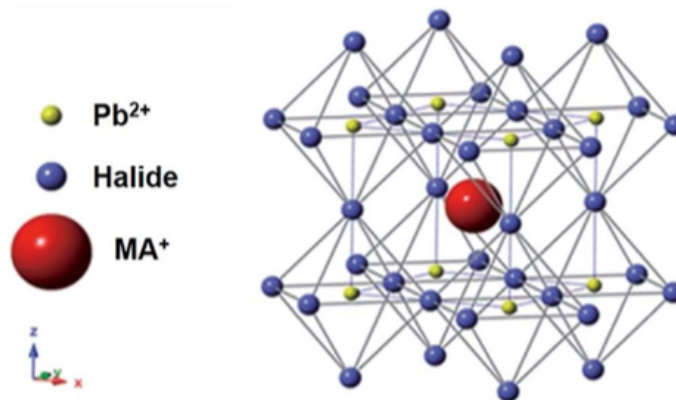


Figure 2.1: Crystal structure of an organometallic halide perovskite (MAPbX_3)^{6,7}

1991 is noted for the break-through fabrication of the dye-sensitised solar cell (DSSC) based on the mechanism of photosynthesis. O'Regan and Gratzel reported that using a DSSC sunlight could be converted into electrical energy. They reported power conversion efficiencies (PCEs) of roughly 7%.^{8,9} Inspired by the new method of

absorbing light, DSSC began incorporating perovskite materials into their cells to improve the PCEs.

The first photovoltaics fabricated using perovskite materials were reported by Miyasaka *et al* who replaced the dye pigment in DSSC with organic-inorganic hybrid perovskite halides, $\text{CH}_3\text{NH}_3\text{PbBr}_3$ resulting in power conversion efficiencies of 3.13%.^{3, 9-11} After further studies the PCE was found to increase by 0.68% once bromine was replaced by iodine.¹² However, a more extensive study of this area was not carried out due to low PCEs and instability caused by the liquid electrolytes used as hole transport materials.

Large advancements were made in 2012 by two separate research groups. Kim, Gratzel and Park fabricated a solid-state meso-structured perovskite solar cell using a perovskite absorber as the main photoactive layer. They were able to replace the liquid electrolyte with a solid hole transport material, Spiro-MeOTAD and used mesoporous- TiO_2 as its corresponding electron transport layer.¹³ Around the same time Snaith and co-workers also reported success using Spiro-MeOTAD as the hole transport material. Several other developments emerged from this success. Snaith *et al* concluded that mixed-halide perovskite materials such as $\text{CH}_3\text{NH}_3\text{PbI}_{3-x}\text{Cl}_x$ had improved stability and charge transport than previously used $\text{CH}_3\text{NH}_3\text{PbI}_3$. Extremely thin absorber cells were also created by coating nanoporous- TiO_2 with a thin perovskite layer. Open-circuit voltages of the cells were improved by replacing the nanoporous TiO_2 with an insulating Al_2O_3 network. These alterations showed increased PCEs to 10.9%.^{10, 14}

Since then perovskite solar cells have been fabricated as two different structures; mesoporous and planar structure.¹⁴ Mesoporous structures are produced by depositing the absorber PK layer on top of a porous TiO_2 layer. The absorber layer then self-assembles in the gaps of the TiO_2 . This method can prevent leakage in the cell. A planar structure is formed by deposited several hundred nanometres of PK in between the ETM and HTM layers. This was shown to improve the ease at which the device fabrication/configuration procedure occurs. Both methods can produce cells

in excess of 15% with the mesoporous structure still in more common use than the planar structure.^{6, 15}

Fabrication of perovskite solar cells has grown in photovoltaic research as power conversion efficiencies rapidly began to rise. To-date, the efficiencies of a single junction perovskite solar cell is in excess of 20%.^{9, 15}

2.2 Operating Principle of Solar Cell Devices

Light is made up of group of energised particles known as photons. The energy of a photon is dependent on the frequency (ν) or wavelength (λ) when the photon moves at the speed of light (c). The energy of a photon can be explained by equation 2.1 below where h is Planck's constant.

$$E = h\nu = \frac{hc}{\lambda} \quad \quad \quad \mathbf{2.1}$$

A solar cell's working mechanism is related to the *photovoltaic effect*. The photovoltaic effect occurs when a voltage or an electric current is generated when a material is exposed to light. Electrons in a materials valence band can become energised when exposed to electromagnetic radiation of greater energy than the band gap of the material. The electrons are then promoted from the valence band to the conduction band (leaving a hole behind in the valence band where the electron left from) where they are free to move freely through the material and conduct electricity. The photovoltaic effect is very similar to the photoelectric effect where electrons are released from a material exposed to light with a higher energy than the band gap of the material.

The photovoltaic effect occurs via three main processes.

(i) Absorption of light energy and generation of electron-hole pair

An ideal semiconductor is made up of a valence band and a conduction band which can be populated with electrons. The region between the two bands is known as the band gap where no electrons are able to populate. Relaxed electrons generally populate the low energy band of valence band. Absorbed energy causes the electrons to be promoted from the valence band to the conduction band if the amount of energy absorbed is greater than the band gap of the material. Once an electron is promoted to the conduction band, it leaves behind a void in the valence band. This void is known as a hole. A hole behaves like a positively charged ion and thus the exposure of a solar cell to light results in the generation of an electron-hole pair.

(ii) Separation of electron-hole pair

As soon as the electron-hole pair is generated, both carriers will soon want to recombine. If one wants to collect the energy generated by the formation of the electron-hole pair measures must be in place to keep the electrons and holes separated. The design of a solar cell generally includes the placement of a semi-permeable membrane or material on either side of the absorber (perovskite absorber layer) where only electrons can flow through one material and holes through another. For perovskite solar cells, a hole transport material (*p*-type) and an electron transport material (*n*-type) acts as this semi-permeable membrane to allow the flow of holes and electrons respectively.

(iii) Extraction of charge carriers to external load

Charge carriers are then transported from the perovskite cell via electrical contacts. Once the electrons have passed through the external circuit they recombine with the holes on the metal-absorber contact before the cycle begins again.

2.3 Electrical Characteristics of Solar Cell Devices

Photovoltaic devices operate based on photo generated current and voltage after exposure to light. When a cell is in the dark no photocurrent should be generated.

The voltage generated in the cell at zero current is known as the open-circuit voltage, (V_{oc}). This represents the maximum voltage that is available from the cell. The current generated by the solar cell when the voltage across the device is zero is known as the short-circuit current, (I_{sc}). As the I_{sc} is the maximum current that can be obtained from the cell it represents the light-generated current. In order to eliminate the dependency on the area of illumination when comparing with the state-of-the-art, the short-circuit current density, J_{sc} is more commonly used in literature. The J_{sc} is observed to decrease with increasing band gap whereas, the V_{oc} increases with increasing band gap. For any load resistance applied to the solar cell, R_L , the cell produces a voltage between 0 and V_{oc} . Similarly, it also produces a current, I , such that $V = IR_L$. The IV is calculated when the cell is under illumination.

The quantum efficiency, QE is the ratio of the amount of electrons that have been transferred to the external load that were produced by incident light at a given wavelength. J_{sc} can be derived from equation 2.2 below,

$$J_{sc} = q \int b_s(E) QE(E) dE \quad 2.2$$

Where $b_s(E)$ represents the number of photons of energy incident to an area at a given time within the range E to $E + dE$ and q is the electronic charge. QE describes the combined charge separation efficiency, absorption co-efficient of the solar cell material and the efficiency of charge extraction in the device. It is independent of the incident spectrum and thus is a standard quantity for comparing solar cell performance under various conditions.

For photovoltaic devices to efficiently prevent recombination of electrons and holes an asymmetric junction is required. The band gap, work function, spatial variation in electrical properties and density of states all aid in the formation of an asymmetric junction in the cell. As a result, when a load is present, the voltage produced between the terminals of the cell generates a current which acts in the opposite direction to the photo generated current. The net current is then used for the I_{sc} value. This

reverse current is called the dark current, J_{dark} . J_{dark} varies for an ideal diode, equation 2.3.

$$J_{\text{dark}}(V) = J_o \left(e^{\frac{qV}{k_B T}} - 1 \right) \quad 2.3$$

Where J_o is a constant, k_b is Boltzmann's constant and T is temperature in Kelvin. The total IV response of the cell is then calculated as the sum of the photo generated current (forward direction) and the dark current (reverse direction) (eqn. 2.4).

$$J = J_{sc} - J_{\text{dark}} \quad 2.4$$

The maximum voltage of the cell, open circuit voltage (V_o) is observed when the contacts are isolated. This I seen when the dark current and the open circuit photocurrent values cancel out.

$$V_{oc} = \frac{kT}{q} \ln \left(\frac{J_{sc}}{J_o} + 1 \right) \quad 2.5$$

From equation 2.5, it is evident that the V_{oc} increases with light intensity.

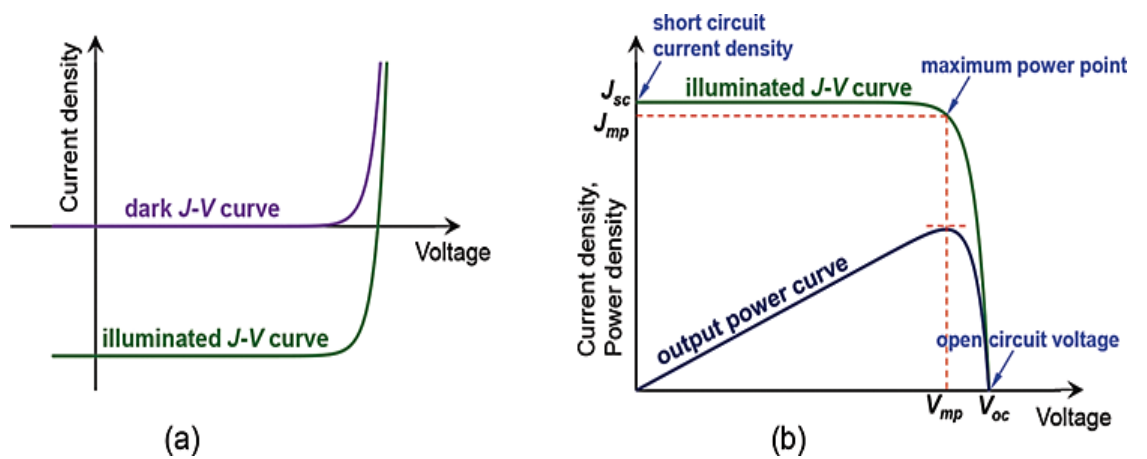


Figure 2.2: (a) Typical J - V curve of a photovoltaic cell when under illumination and in the dark, (b) Curve graphing the output power density against voltage indicating the

short-circuit density, (J_{sc}), open circuit voltage, (V_{oc}) and maximum power point, (V_{mp} , J_{mp})¹⁶

As mentioned earlier, open circuit voltage and short circuit current describe the output voltage and current of the solar cell respectively. The cell maximum power output or cell power density can be described by equation 2.6 below.

$$P = JV \quad 2.6$$

From figure 2.2(b), short circuit density, J_{sc} is calculated when voltage across the cell is zero. Similarly, the open circuit voltage, V_{oc} is obtained when the current density of the cell is zero. The maximum power output, (P_{mp}) of the cell occurs at a voltage, V_{mp} and respective current density, J_{mp} as illustrated in figure 2.2(b). The resulting fill factor (FF) describes the *squareness* of the J-V curve and is an important figure of the merit for the cell (eqn. 2.7).¹⁷

$$FF = \frac{I_{mp} V_{mp}}{I_{sc} V_{oc}} \quad 2.7$$

The power conversion efficiency (PCE) of a device is explained using η and is defined as the ratio of power input to power output of a solar cell device (eqn. 2.8).

$$PCE = \frac{P_{out}}{P_{in}} = \frac{J_{mp} V_{mp}}{P_{in}} = \frac{V_{oc} I_{sc} FF}{P_{in}} \quad 2.8$$

J_{sc} , V_{oc} , FF and η are the four main characteristics that described the quality of a solar cell device. In order to ensure a standard method for comparison amongst other solar cells a standard test condition has been developed where cells are illuminated using an incident power density of 1000 Wm^{-2} , an Air Mass (AM) 1.5 illumination spectrum at a temperature of 25°C .¹⁸

2.4 Working Mechanism of Perovskite Solar Cells

As previously mentioned a solar cell contains a light absorbing material that absorbs photons which cause the generation of electron-hole pairs which can be extracted from the cell via the hole transport material (HTM) and electron transport material (ETM) to the external load connected to the cell in an asymmetric manner.

There are a range of solar cell structures that are in use today such as the p - n junction solar cell, dye-sensitised solar cell and perovskite solar cell. Most solar cells are based upon the principles of a p - n junction.

A p - n junction forms when a p -type material and an n -type material come together. Excess electrons from the donor n -type material migrate across the depletion zone to recombine with the positive holes in the p -type material. The electrons that have migrated across have now left behind positively charged holes in their stead. As a result, the excess electrons that exist in the acceptor material will migrate across to recombine with the negatively charge electrons in the n -type material. This continues until enough electric field has been built up between the n -type and p -type materials preventing further migration across the depletion zone (figure 2.3).

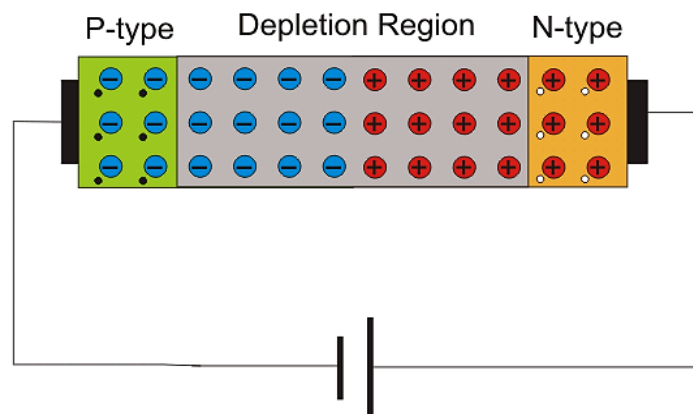


Figure 2.3: Schematic of a p - n junction outlining the depletion zone, n -type and p -type layers¹⁹

Dye-sensitised solar cells contain a photoactive dye that generates electrical energy once exposed to light. The dye absorbs photons from incident light and causes the excitation of electrons in the dye. The excited electrons then migrate to the conduction band of a semiconductor material (usually TiO_2) where they are transported to the conductive electrode. A liquid electrolyte closed the the circuit so that the oxidised dye can be regenerated to begin the circuit again (figure 2.4).

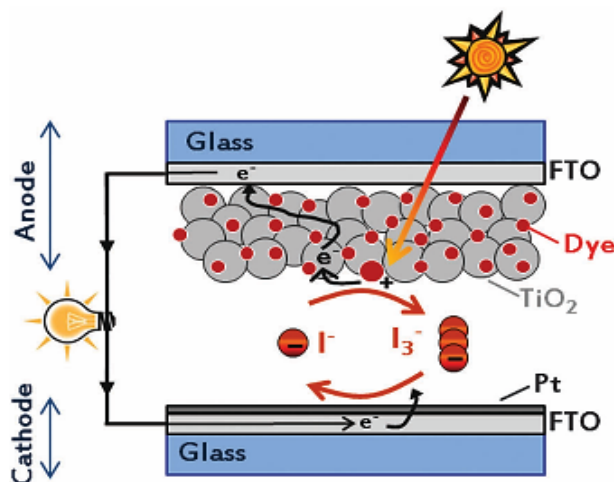


Figure 2.4: Illustration of the operating mechanism of dye-sensitised solar cells²⁰

Perovskite solar cell devices are made up of a perovskite absorber layer between an n -type semiconductor and a p -type semiconductor. The perovskite material absorbs photons and excites electrons in the material forming electron-hole pairs. The charges are then separated allowing the electrons to be extracted via the electron transport material to the external load. The charge separation and extraction can occur via two possible reactions: (a) photo generated electrons can be injected into ETM first with the injection of holes into the HTM subsequently or (b) the photo generated holes are injected into the HTM first and the photo generated electrons are injected into the ETM subsequently.²¹ These reaction mechanisms are illustrated by figure 2.5 below.

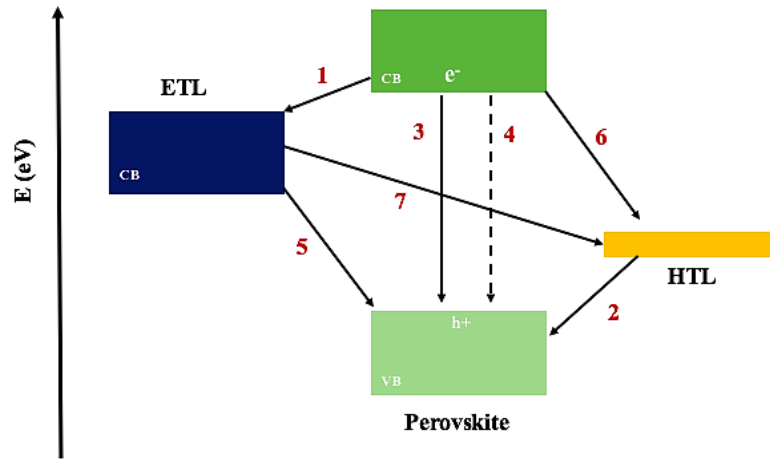
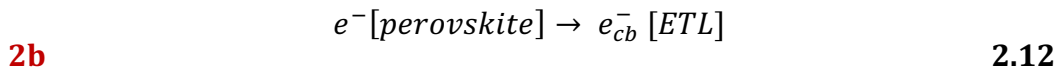
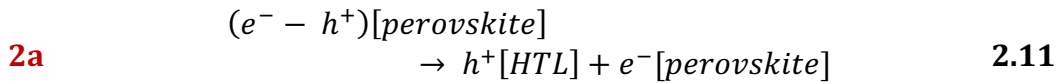
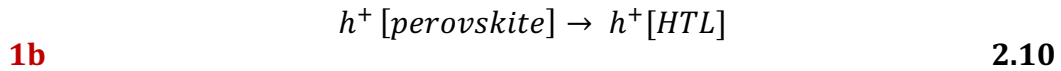
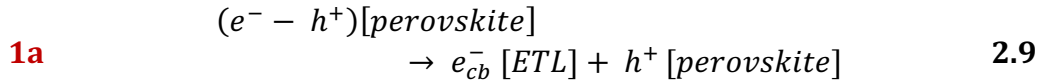


Figure 2.5: Schematic outlining the energy levels and electron transfer processes in p-i-n architecture perovskite solar cell. The charge transfer processes 1-7 are further explained by equations 2.9-2.17 below.²¹



Undesired reactions such as photoluminescence, non-radiated recombination and exciton elimination all compete with the extraction of the charge carriers (eqn. 2.13, 2.14)

$$\mathbf{3} \quad (e^- - h^+)[perovskite] \rightarrow h\nu \quad \mathbf{2.13}$$

$$\mathbf{4} \quad (e^- - h^+)[perovskite] \rightarrow \nabla \quad \mathbf{2.14}$$

The electrons are then transferred back to the ETL and the holes are transferred to the HTL before recombining at the interface between the electron and hole transport materials (eqn. 2.15-2.17).

$$\mathbf{5} \quad e_{cb}^- [ETL] + h^+ [perovskite] \rightarrow \nabla \quad \mathbf{2.15}$$

$$\mathbf{6} \quad h^+ [HTL] + e^- [perovskite] \rightarrow \nabla \quad \mathbf{2.16}$$

$$\mathbf{7} \quad h^+ [HTL] + e_{cb}^- [ETL] \rightarrow \nabla \quad \mathbf{2.17}$$

The power conversion efficiency (PCE) of the cell is dependent on the kinetics of these reactions.²²

2.5 Device Architecture

Due to the tuneable bandgap and optoelectronic properties of perovskites, it makes it possible to fabricate PK solar cells in a variety of architectures.¹⁴ There are two main structure previously mentioned in section 2.1, mesoporous and planar structures. Each structure can then be fabricated depending on which transport material is exposed to light first. Where the ETL is exposed to light first the configuration is known as an *n-i-p* architecture. Conversely, where the HTL is the first to encounter light the configuration is known as a *p-i-n* architecture.²³ The processing and fabrication requirements differ depending on the perovskite structures. As a result, different HTM, ETM and metal contacts are used depending on the configuration of the cell. The conventional and inverted structures are illustrated in figure 2.6.

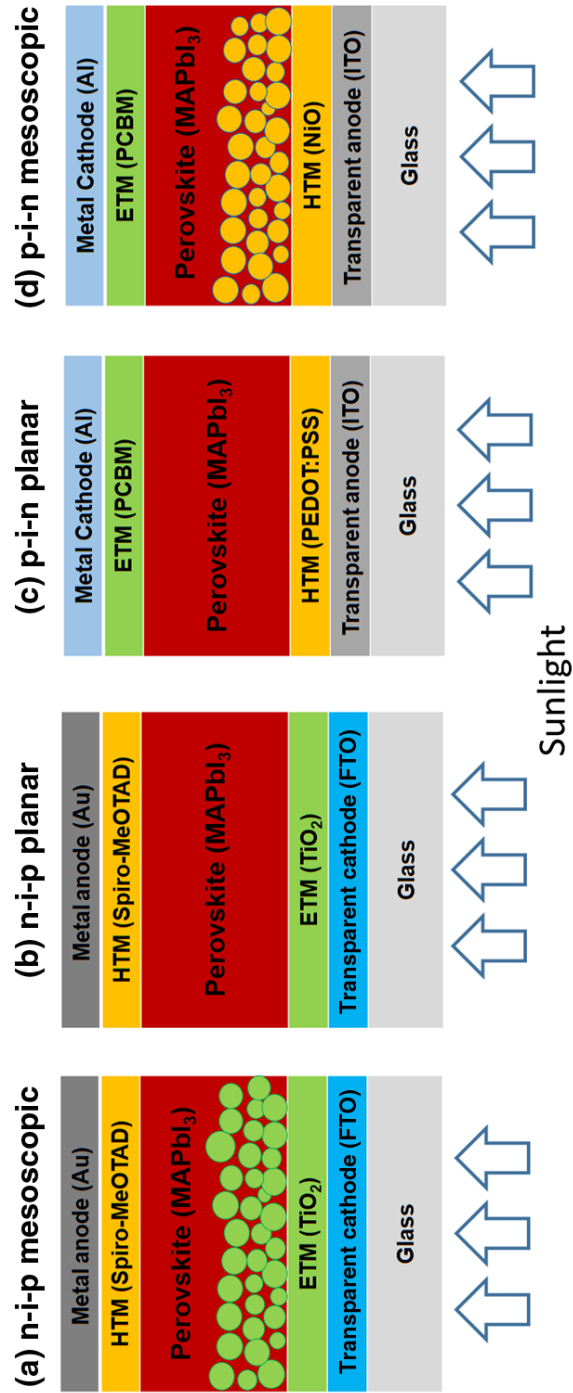


Figure 2.6: Schematics of conventional and inverted architectures of perovskite solar cells including (a) n-i-p mesoscopic, (b) n-i-p planar, (c) p-i-n inverted mesoscopic and (d) p-i-n inverted planar structure²⁴

2.5.1 Conventional *n-i-p* Configuration

The *n-i-p* configuration is the most commonly used for mesoscopic perovskite solar cells which have been reported to give one of the highest efficiency solar cells.^{25, 26} A mesoscopic *n-i-p* structure (figure 2.6 (a)) generally consists of a transparent conducting oxide cathode (usually FTO), an electron transport material, mesoporous metal oxide (TiO₂) filled with perovskite material, hole transport material and an anode (Au). The mesoscopic layer reduces the carrier length reducing the leakage current between the anode and the cathode. Light absorption improves due to light scattering in the porous structure. However, due to low open circuit voltages (V_{oc}) and short-circuit densities (J_{sc}) obtained due to limited grain growth of the perovskite in the pores of the m-TiO₂ other structures were also explored.²⁴

Planar *n-i-p* structures (figure 2.6 (b)), consist of an ETL and HTL sandwiching the perovskite absorber layer and does not use a mesoporous-TiO₂ layer. By improving the interface between each layer in the structure, similar efficiencies can be achieved using a planar *n-i-p* structure as mesoscopic *n-i-p*. Planar *n-i-p* structures have been reported to exhibit enhanced V_{oc} and J_{sc} values relative its mesoporous counterpart. However, due to pre-existing interface issues, planar *n-i-p* structures have been known to exhibit signs of hysteresis (see section 2.6).

2.5.2 Inverted *p-i-n* Configuration

The inverted planar *p-i-n* structure is fabricated by changing the deposition order where the HTM is the first transport material to be exposed to light. In this case, organic and inorganic hole transport materials have been used. Deposition methods used to deposit inorganic HTM are not often compatible with the *n-i-p* configuration and can result in the degradation of the underlying absorber layers. When the structure is inverted there are less limitations on the deposition methods available for deposition of the HTM. Most commonly used is polymer poly (3, 4-ethylenedioxythiophene) Poly (styrene-sulfonate) or PEDOT: PSS deposited on ITO.^{27, 28} Sputtered NiO has also been reported as a successful HTM for inverted *p-i-n* structures.²⁹ The use of inorganic oxides as a HTM has also made it possible for the

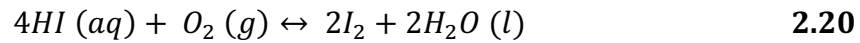
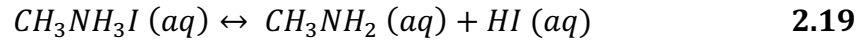
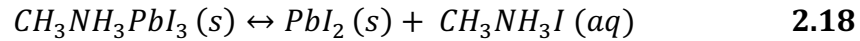
fabrication of the mesoscopic *p-i-n* architecture.³⁰ NiO/mp-Al₂O₃ or c-NiO/mp-NiO materials have been used to produce the mesoporous layers.^{24, 31, 32}

2.6 Challenges

2.6.1 Stability

Although the power conversion efficiencies of perovskite solar cells have risen to >20% in the last number of years, long-term stability remains an issue that needs to be overcome. It has been reported that exposure to high humidity and oxygen, moisture, UV radiation and high temperatures have caused the degradation of the perovskite solar cell.³

CH₃NH₃PbI₃ has been known to hydrolyse when exposed to moisture due to its sensitivity to water. The degradation of CH₃NH₃PbI₃ proceeds via the following reactions:

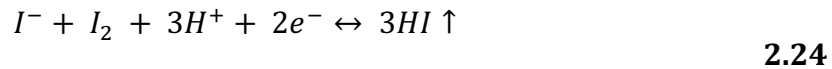
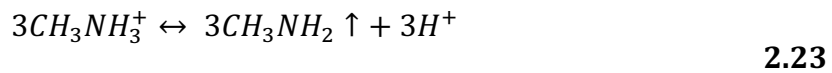
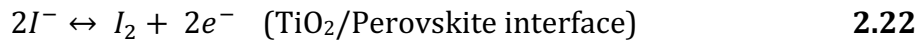


A photochemical reaction causes HI to degrade to H₂ and I₂ under UV radiation. It can also decompose via a redox reaction when in the presence of O₂ (eqn. 2.20). The degradation of HI drives the decomposition reactions to completion³³. As the perovskite material is apparently sensitive to moisture and oxygen many processing steps must be carried out in an inert environment such as a glove box.

It has also been well reported that perovskites are affected by highly humid conditions. Seok *et al*, describes that $\text{CH}_3\text{NH}_2\text{PbBr}_3$ begin to decompose at 55% humidity resulting in the perovskites colour changing from black to dark brown and finally to a yellow colour²⁶. However, they were able to show that $\text{CH}_3\text{NH}_2\text{PbI}_3$ was more sensitive to the humidity than its counterpart³⁴.

Thermal stability of the cell can also become a degrading factor when the solar cell device is illuminated. Much of the energy being generated from the cell is emitted through heat energy. If the cell is unable to handle the heat of the device the lifetime of the device can be reduced. $\text{CH}_3\text{NH}_2\text{PbI}_{3-x}\text{Cl}_x$ was also tested under high temperatures by Tan *et al* who annealed the perovskite at 100°C for 1 hour. Subsequently, the temperature was raised every 10 minutes in increments of 10°C. It was observed that large grains began to form on the perovskite surface, however, and PbI_3 crystals were also evident on the surface often forming islands. Large gaps in the film caused by the island formation caused reduced contact between the ETL and HTL further reducing the efficiency³⁵.

As explained in section 2.5, the most commonly fabricated perovskite solar cell is made up of compact and mesoporous TiO_2 used as an ETL. At the ETL/perovskite interface, degradation of the perovskite can occur when exposed to intense UV radiation. The mechanism for such decomposition is described as follows:



The structure of the perovskite is broken down as the TiO_2 extracts electrons from I^- (eqn. 2.22). The reaction is driven to completion by the elimination of H^+ and evaporation of CH_3NH_2 (b.p. 17°C) from equations 2.24 and 2.23. The electrons

previously extracted from the interface then reduce I_2 and the remaining HI evaporates.³³

Many methods have been studied in an attempt to improve the stability of the perovskite layer. Sb_2S_3 has been inserted into the interface between TiO_2 and perovskite as a surface blocking layer. It was observed that the stability of the perovskite increased significantly while maintaining its absorption properties and crystal structure.^{36, 37}

Encapsulation methods have also been successfully used for CIGS cells to improve the stability of the devices by protecting them from exposure to the elements. Double glass layers have been applied to front and back of CIGS cells to prevent exposure to air and moisture.³³ These encapsulation techniques have just started being applied to perovskite solar cell devices.³⁸⁻⁴⁰

2.6.2 Hysteresis

It is important to maintain a stable power output when fabricating efficient and stable perovskite solar cell devices. However, to date there has been evidence of J-V hysteresis in the PSCs. Hysteresis is observed when the direction or the rate of voltage sweep is altered giving different values when scanned in the forward and reverse bias. It has been reported that when a device is held in the forward bias before the measurement this can lead to a higher efficiency result than when the device is held in the reverse bias. This can put into question the integrity of the power conversion efficiencies calculated for each device.^{24, 41}

There are several causes that have been reported in literature including ferroelectricity, ion migration and charge trapping that have led to J-V hysteresis.⁴²

Small perovskite crystals formed in the absorber layer have been known to trap charges due to the presence of grain boundaries around the crystals.⁴³ These crystals have been reported as being in the interface layer between the perovskite and the transport layers. This charge trapping results in an unbalanced charge collection rate

at the transport layers. If the rate of charge transfer between the perovskite and the *n*- or *p*- type materials differ, charges will begin to gather at the interfaces reducing the charge collection rate. The grain boundaries can induce recombination of the electron-hole pairs further reducing the collection rate. Once the collection rate is reduced so does the efficiency of the device.^{44, 45}

Hysteresis is particularly pronounced in perovskites with the planar architecture. It has been found that perovskite solar cells with mp-TiO₂ in its structure have a reduced effect of hysteresis due to the presence of larger perovskite crystal grain sizes compared to cp-TiO₂ used in conventional *n-i-p* architectures. This has been attributed to better interfaces between the ETL and perovskite resulting in shorter diffusion lengths for carrier collection.⁴⁶ It has also been reported that thinning the mesoporous layer can also exacerbate the hysteresis observed in the device.⁴⁷ In order to reduce this effect PCBM has been incorporated into the grain boundaries, by combining the perovskite and PCBM solutions, to passivate the charge-traps reducing the effect of hysteresis. For conventional *n-i-p* devices that use cp-TiO₂, Snaith *et al*, began to passivate the ETL with C₆₀-SAM and PCBM where they concluded that the formation of charge traps were inhibited at the interface reducing the effect of hysteresis.⁴⁸

Another possible explanation of hysteresis can be explained by ion migration. When an external forward bias is applied to the device the ionic carriers are able to migrate against the direction of the electric field close to the electrodes. Here the positive ions can travel to the anode and the negative ions can travel to the cathode. When the field is lifted and the cell is illuminated the migrated ions allow for the stabilisation of the density of charges near each of the contacts. This method acts like *n*- or *p*-type doping at the charge collection contacts. Eventually the migrated ions will dissipate and redistribute across the perovskite absorber layer and the solar cell must function without the added doping near the electrodes.⁴⁹

Wei *et al* report that commonly used perovskite $\text{CH}_3\text{NH}_3\text{PbX}_3$ ($\text{X} = \text{I}, \text{Br}, \text{Cl}$) exhibits ferroelectric properties and has drawn a link between hysteresis and the presence of this ferroelectric component.⁵⁰ They showed the mixed halide $\text{CH}_3\text{NH}_3\text{PbI}_{3-x}\text{Cl}_x$ had signs of J-V hysteresis. The band structure at the interface of a perovskite material can be manipulated to change polarisation if the material contains ferroelectric character. The change in polarisation can result in varying the PCE output between the forward and reverse sweep. Negative poling has been shown to prevent charge separation in the device reducing the calculated PCE. This was particularly observed in perovskite cell devices with the planar architecture where the perovskite was especially sensitive to an external bias. In order to combat this anomaly in planar PSCs, C_{60} /fullerene molecules such as polystyrene sulfonate (PEDOT:PSS), phenyl-C61-butyric acid methyl ester (PCBM) and lithium fluoride (LiF) have been used as interlayers into planar devices using perovskite $\text{CH}_3\text{NH}_3\text{PbI}_3$.^{48,51,52} As mentioned earlier, the C_{60} molecules are able to passivate the trapped charges by interacting with the halide rich defective regions at the grain boundaries of the perovskite.

McGehee *et al*⁵³ reports that soaking the PSC device with light under a positive bias prior to electrical characterisation can lead to improved fill factor values, short circuit density, (J_{sc}) and PCE of the devices. However, it was also observed that light soaking the cells under a negative bias prior to electrical characterisation can degrade the PCE of the device. The PCEs of the devices are generally modulated by scanning the cells under forward and negative bias under dark conditions.⁴¹

2.7 Perovskite Tandem Devices

As previously noted, single-junction perovskite based solar cell devices have been able to achieve PCEs in excess of 20%. William Shockley and Hans J. Queisser calculated that a single *p-n* junction solar cell had a maximum theoretical PCE limit of 30% assuming the sun is blackbody radiation (6000 K), there is an absence of non-radiative recombination and the band gap of the material is between 1.1-1.4 eV.⁵⁴ As

the current single junction devices are approaching this theoretical efficiency limit, tandem solar cells have been proposed to replace single junction devices to enable to continuation of this progress.⁵⁵ A tandem cell with two electrical contacts (better known as a two terminal or monolithic tandem solar cell) has been calculated to potentially be able to achieve a PCE of 42% assuming the bandgaps of the materials are 1.0-1.9 eV.⁵⁶ Perovskite/Si tandem devices have been theoretically calculated to achieve 41% efficiency.⁵⁵ The perovskite sub cell acts to top up the efficiency of the c-Si solar cell and does not require to have power conversion efficiencies exceeding that of c-Si.

Due to their sharp absorption band edge and tuneable band gap, perovskite solar cells are the ideal candidate to incorporate into a tandem solar cell.

Tandem solar cells are made up of the combination of two solar cells. There are a wide variety of perovskite-tandem devices; perovskite-perovskite, perovskite-organic and perovskite-inorganic solar cells.⁵⁸ For the sake of this research, we focus on perovskite-inorganic tandem solar cells where PCEs of 20.5-25.5% have been achieved for perovskite/Si tandem cells.⁵⁹⁻⁶²

The majority of perovskite-inorganic solar cell devices are made up of a wide-bandgap perovskite solar cell and a low bandgap inorganic solar cell. Here the wide-bandgap material absorbs high energy photons and the bottom cells absorbs the low energy photons broadening the spectral range the cell can absorb.^{55, 63}

There is also an incentive to utilise already optimised or commercialised technology and combine it with the perovskite-based solar cell. Such commercialised technology includes silicon or copper indium gallium selenide (CIGS).⁵⁵ Most work has been done combining silicon solar cells and perovskite solar cells.

Tandem solar cells can be fabricated as either a 2T (two-terminal or monolithic) or 4T (four-terminal) tandem device. A 4T device requires four electrical contacts, where three of these must be semi-transparent to allow light absorption into the cell.

The 2T device requires only two electrical contacts where one must be semi-transparent. By placing two solar cells in tandem, the efficiency of the cell increases as each individual cell will be producing electrical energy and the power conversion efficiencies for these cells is additive.⁶⁴

Since the recombination layers are required to be transparent and most TCOs are not completely transparent it is more desirable to have two electrical contacts instead of four in the solar cell. Removing two of the contacts can result in higher PCEs. In addition, the fabrication of a monolithic solar cell device is cheaper due to a reduction in the number of required layers.⁶⁵ In this thesis we focus on a 2T monolithic perovskite-Si tandem solar cell.

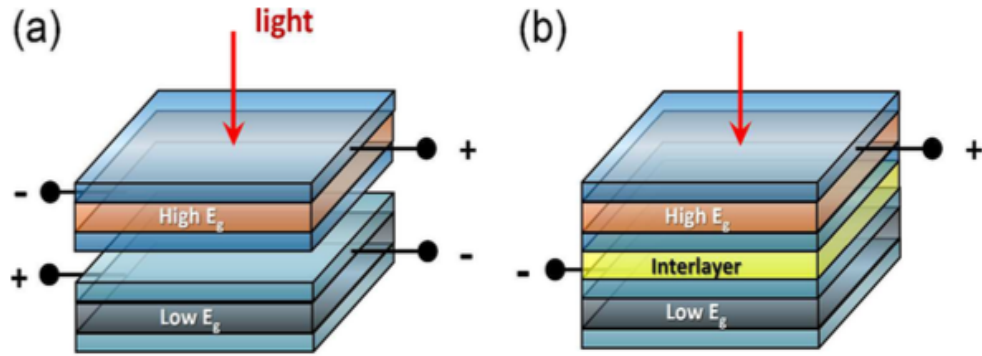


Figure 2.7: Schematic representing (a) 4T (four-terminal) and (b) 2T (two-terminal/monolithic) tandem solar cells showing the material with a high energy bandgap on top of the material with a low energy bandgap⁵⁵

The cells are generally connected by a recombination layer (illustrated by the interlayer in figure 2.7) or tunnel junction which is required to be of low resistance and have good optical transparency. This enables the hole current and the electron current to pass through the sub cells and recombine to maintain neutrality.

Indium-tin oxide (ITO) has been shown to be a good recombination layer due to its high transparency and good electrical properties. However, stacking solar cell devices can lead to processing challenges in particular for 2T tandems. Deposition

methods and conditions may need to be altered in order to prevent degradation of the sub cells.⁶⁴ The deposition of ITO has been optimised using a sputtering technique followed by a high temperature anneal ($>400^{\circ}\text{C}$).^{63, 66} For the fabrication process of a single-junction perovskite solar cell, ITO can be deposited as a TCO onto a glass substrate using sputtering as the material is the first layer of the structure. However, once the ITO is being used as a recombination layer between the perovskite and the Si solar cells, other deposition techniques or materials need to be used replacing the ITO as a recombination layer.

Other layers in the structure can also be affected by this transition into the tandem solar cell world. Mesoporous- TiO_2 a commonly used ETL in perovskite solar cells requires a 500°C temperature anneal. When incorporated in a monolithic perovskite/Si tandem device this high temperature anneal will degrade the underlying Si solar cell. In this case, perovskite-based tandem solar cells are often fabricated using a *p-i-n* configured perovskite top cell in tandem with a c-Si solar cell in order to prevent damage to the active layers. As a result, alternative ETLs such as SnO_2 deposited by low temperature ALD have been investigated as a replacement.^{67, 68} ALD deposits the metal oxide at low temperatures and as a low energy process enables the material to be deposited on top of the perovskite material, making the possibility of a *p-i-n* configured perovskite/Si tandem solar cell device more viable.

Bibliography

- [1] G. Rose, *Ann. Phys.*, **124**, 551-573, (1839) (in German)
- [2] G. Rose, *De Novis Quibusdam Fossilibus Quae in Montibus Uraliis Inveniuntur Scripsit*, (1839)
- [3] H. Tang, S. He, C. Peng, *Nanoscale Research Lett.*, **12**:410, (2017)
- [4] L. Singh, U. S. Rai, K. D. Mandal, N. B. Singh, *Progress Cryst. Character. Mater.*, **60**, 15-62, (2014)
- [5] C. K. Müller, *Nature*, 182, 1436, (1958)
- [6] T. B. Song, Q. Chen, H. Zhou, C. Jiang, H. H. Wang, Y. M. Yang, Y. Yiu, J. You, Y. Yang, *J. Mater. Chem., A*, 3, 9035-9050, (2015)
- [7] Z. Ku, Y. Rong, M. Xu, T. Liu, H. Han, *Sci. Rep.*, 3, 3132, (2013)
- [8] B. O'Regan, M. Grätzel, *Nature*, 353, 737-740, (1991)
- [9] M. K. Nazeeruddin, *Nature*, 538, 463-464, (2016)
- [10] M. M. Lee, J. Teuscher, T. Miyasaka, T. N. Murakami, H. J. Snaith, *Science*, 338, 643-647, (2012)
- [11] U. Bach, D. Lupo, P. Comte, J. E. Moser, F. Weissörtel, J. Salbeck, H. Spreitzer, M. Grätzel, *Nature*, 395, 583-585, (1998)
- [12] A. Kojima, K. Teshima, Y. Shirai, T. Miyasaka, *J. Am. Chem. Soc.*, 131, 6050-6051, (2009)
- [13] H. S. Kim, C. R. Lee, J. H. Im, K. B. Lee, T. Moehl, A. Marchioro, S. J. Moon, R. Humphrey-Baker, J. H. Yum, J. E. Moser, M. Grätzel, *Sci. Rep.*, 2, 591, (2012)
- [14] M. A. Green, A. Ho-Baillie, H. J. Snaith, *Nature Photonics*, 8, 506-514, (2014)
- [15] L. Yang, A. T. Barrows, D. G. Lidzey, T. Wamg, *Reports on Progress in Physics*, 79, 026501, (2016)

- [118] Y. Tao, Printed Electronics: Current Trends and Applications, Chapter 4, IntechOpen, (2016)
- [17] T. Markvart, L. Castaner, McEvoy's Handbook of Photovoltaics, Chapter 1, Elsevier, (2018)
- [18] J. Nelson, The Physics of Solar Cells, Imperial College Press, (2004)
- [19] Electrical4U. 2019, Forward and Reverse Bias of P-N Junctions, [ONLINE], Available at <https://www.electrical4u.com/pn-junction/>. [Accessed 3 September 2019]
- [20] F. Bella, C. Gerbaldi, C. Barolo, M. Grätzel, Chem. Soc. Rev., 44, 3431-3473, (2015)
- [21] A. Marchioro, J. Teuscher, D. Friedrich, M. Kunst, R. van de Krol, T. Moehl, M. Grätzel, J.-E. Moser, Nature Photonics, 8, 250-255, (2014)
- [22] T. Swetha, S. P. Singh, J. Mater. Chem. A., 3, 18329-18344, (2015)
- [23] S. S. Mali, C. K. Hong, Nanoscale, 8, 10528-10540, (2016)
- [24] Z. Song, S. C. Watthage, A. B. Phillips, M. J. Heben, J. Photonics for Energy, 6, 022001, (2016)
- [25] E. H. Jung, N. J. Jeon, E. Y. Park, C. S. Moon, T. J. Shin, T. Y. Yang, J. H. Noh, J. Seo, Nature, 567, 511, (2019)
- [26] S. Y. Woon, J. H. Noh, N. J. Jeon, Y. C. Kim, S. Ryu, J. Seo, S. Seok, Science, 348, 1234-1237, (2015)
- [27] O. Malinkiewicz, A. Yella, Y. H. Lee, G. M. Espallargas, M. Grätzel, M. K. Nazeeruddin, H. J. Bolink, Nature Photonics, 8, 128-132, (2013)
- [28] J.-Y. Jeng, Y.-F. Chiang, M.-H. Lee, S. -R. Peng, T.-F. Guo, P. Chen, T.-C. Wen, Adv. Mater., 25, 3727-3732, (2013)
- [29] K.-C. Wang, P.-S. Shen, M.-H. Li, S. Chen, M.-W. Lin, P. Chen, T.-F. Guo, ACS, Appl. Mater Interfaces, 6, 11851-11858, (2014)

- [30] K.-C. Wang, P.-S. Shen, M.-H. Li, S. Chen, M.-W. Lin, P. Chen, T.-F. Guo, *ACS, Appl. Mater. Interfaces*, 6, 11851-11858, (2014)
- [31] W. Chen, Y. Wu, J. Liu, C. Qin, X. Yang, A. Islam, Y.-B. Cheng, L. Han, *Energy and Environmental Sci.*, 8, 629-640, (2015)
- [32] K.-C. Wang, J.-Y. Jeng, P.-S. Shen, Y.-C. Chang, E. W.-G. Diau, C.-H. Tsai, T.-Y. Chao, H.-C. Hsu, P.-Y. Lin, P. Chen, T.-F. Guo, T.-C. Wen, *Sci. Rep.*, 4, 4756, (2014)
- [33] G. Niu, X. Guo, L. Wang, *J. Mater. Chem. A*, 3, 8970-8980, (2015)
- [34] J. H. Noh, S. H. Im, J. H. Heo, T. N. Mandal, S. I. Seok, *NanoLett.*, 13, (2013)
- [35] K. W. Tan, D. T. Moore, M. Saliba, H. Sai, L. A. Estroff, T. Hanrath, H. J. Snaith, U. Weisner, *ACS Nano*, 8, 4730-4739, (2014)
- [36] S. Ito, S. Tanaka, K. Manabe, H. Nishino, *J. Phys. Chem. C*, 118, 16995-17000, (2014)
- [37] K. Tsujimoto, D.-C. Nguyen, S. Ito, H. Nishino, H. Matsuyoshi, A. Konno, G. R. A. Kumara, K. Tennakone, *J. Phys. Chem. C*, 116, 13465-13471, (2012)
- [38] E. Ramasamy, V. Karthikeyan, K. Rameshkumar, G. Veerappen, *Mater. Lett.*, 250, (2019)
- [39] Z. Fu, M. Xu, Y. Sheng, Z. Yan, J. Meng, C. Tong, D. L. Z. Wan, A. Mei, Y. Hu, Y. Rong, H. Han, *Adv. Funct. Mater.*, 1809129, (2019)
- [40] J. Carolus, T. Merckx, Z. Purohit, B. Tripathi, H.-G. Boyen, T. Aernouts, W. de Ceuninck, B. Conings, M. Daenen, *Solar RRL*, 1900226, (2019)
- [41] B. Chen, M. Yang, S. Priya, K. Zhu, *J. Phys. Chem. Lett.*, 7, 907-917, (2016)
- [42] J. Xu, A. Buin, A. H. Ip, W. Li, O. Voznyy, R. Comin, M. Yuan, S. Jeon, Z. Ning, J. J. McDowell, P. Kanjanaboos, J.-P. Sun, Z. Lan, L. N. Quan, D. H. Kim, I. G. Hill, P. Maksymovych, E. H. Sargent, *Nat. Comm.*, 4, 7081, (2015)
- [43] H.-S. Kim, N.-G. Park, *J. Phys. Chem Lett.*, 5, 2927-2934, (2014)

- [44] S. van Reenen, M. Kemerink, H. J. Snaith, *J. Phys Chem. Lett.*, 6, 3908-3914, (2015)
- [45] J. Beilsten-Edmands, G. E. Eperon, R. D. Jonson, H. J. Snaith, P. G. Radaelli, *Appl. Phys. Lett.*, 106, 173502, (2015)
- [46] M. Grätzel, *Nature Materials*, 13, 838-842, (2014)
- [47] H. J. Snaith, A. Abate, J. M. Ball, G. E. Eperon, T. Leijtens, N. K. Noel, S. D. Stranks, J. T.-W. Wang, K. Wokciechowski, W. Zhang, *J. Phys. Chem. Lett.*, 5, 1511-1515, (2014)
- [48] K. Wokciechowski, S. D. Stranks, A. Abate, G. Sadoughi, A. Sadhanala, N. Kopidakis, G. Rumbles, C.-Z. Li, R. H. Friend, A. K.-Y. Jen, H. J. Snaith, *ACS Nano*, 8, 12701-12709, (2014)
- [49] Y. Zhang, M. Liu, G. E. Eperon, T. Leijtens, D. McMeekin, M. Saliba, W. Zhang, M. de Bastiani, A. M. Petrozza, L. M. Herz, M. B. Johnston, H. Lin, H. J. Snaith, *Materials Horizons*, 2, 315-322, (2015)
- [50] J. Wei, Y. Zhao, H. Li, G. Li, J. Pan, D. Xu, Q. Zhao, D. Yu, *J. Phys. Chem. Lett.*, 5, 3937-3945, (2014)
- [51] J. Seo, S. Park, Y. C. Kim, N. J. Jeon, J. H. Noh, S. C. Yoon, S. H. Seok, *Energy Environ. Sci.*, 7, 2642-2646, (2014)
- [52] H.-B. Kim, H. Choi, J. Jeong, S. Kim, B. Walker, S. Song, J. Y. Kim, *Nanoscale*, 6, 6679, (2014)
- [53] E. L. Unger, E. T. Hoke, C. D. Bailie, W. H. Nguyen, A. R. Bowring, T. Heumüller, M. G. Christoforo, M. D. McGehee, *Energy and Environ. Sci.*, 7(11), 3690-3698, (2014)
- [54] W. Shockley, H. J. Queisser, *J. Appl. Phys.*, 32, 510-519, (1961)
- [55] J.-W. Lee, Y.-T. Hsieh, N. DeMarco, S.-H. Bae, Q. Han, Y. Tan, *J. Phys. Chem. Lett.*, 8, 1999-2011, (2017)
- [56] A. D. Vos, *J. Phys. D: Appl. Phys.*, 13, 839-846, (1980)
- [57] M. H. Fitcher, B. Ehrler, *ACS Energy Lett.*, 1, 863-868, (2016)

- [58] N. Torabi, A. Behjat, Y. Zhou, P. Docampo, R. J. Stoddard, H. W. Hillhouse, T. Ameri, *Mater. Today Energy*, 12, 70-94, (2019)
- [59] J. P. Mailoa, C. D. Bailie, E. C. Johlin, E. T. Hoke, A. J. Akey, W. H. Nguyen, M. D. McGehee, T. Buonassisi, *App. Phys. Lett.*, 106, (2015)
- [60] J. Zheng, C. F. J. Lau, H. Mehrvarz, F.-J. Ma, Y. Jiang, X. Deng, A. Soeriyadi, J. Kim, M. Zhang, L. Hu, X. Cui, D. S. Lee, J. Bing, Y. Cho, C. Chen, M. A. Green, S. Huang, A. W. Y. Ho-Baillie, *Energy Environ. Sci.*, 11, 2432-2443, (2018)
- [61] F. Sahli, B. A. Kamino, J. Werner, M. Bräuninger, B. Paviet-Salomon, L. Barraud, R. Monnard, J. P. Seif, A. Tomasi, Q. Jeangros, A. Hesler-Wyser, S. Wolf, M. Despeisse, S. Nicolay, B. Niesen, C. Ballif, *Adv. Energy Mater.*, 8, 1702609, (2018)
- [62] Y. Wu, D. Yan, J. Peng, T. Duong, Y. Wan, S. P. Phang, H. Shen, N. Wu, C. Barugkin, X. Fu, S. Surve, D. Grant, D. Walter, T. P. White, K. R. Catchpole, K. Weber, *J. Energy, Environ. Sci.*, 10, 2472-2479, (2017)
- [63] N. N. Lal, Y. Dikhissi, W. Li, Q. Hou, Y.-B. Cheng, U. Bach, *Adv. Energy Mater.*, 7, 1602761, (2017)
- [64] B. Chen, X. Zheng, Y. Bai, N. P. Padture, J. Huang, *Adv. Energy Mater.*, 7, 1602400, (2017)
- [65] C. D. Bailie, M. D. McGehee, *MRS Bulletin*, 40, 681-686, (2015)
- [66] L. Kerkache, A. Layadi, E. Dogheche, D. Rémiens, *J. Phys. D: Appl. Phys.*, 39, 184-189, (2005)
- [67] J. Hu, Q. Cheng, R. Fan, H. Zhou, *Solar RRL*, 1, 1700045 (2017)
- [68] M. M. McCarthy, A. Walter, S. J. Moon, N. K. Noel, S. O'Brien, M. E. Pemble, S. Nicolay, B. Wenger, H. J. Snaith, I. M. Povey, *MRS Adv.*, 3, 3075-3084, (2018)

Chapter 3: Experimental Instrumentation

3.1 Deposition Systems

3.1.1 Cambridge Nanotech Fiji 200LLC ALD System

The Cambridge Nanotech Fiji 200LLC is an ALD system that consists of a single deposition chamber and an external load-lock chamber. The load-lock has the capability of loading up to a 200 mm wafer into the deposition chamber using a mechanical loading arm.



Figure 3.1: Image of Cambridge Nanotech Fiji 200LLC ALD System located in Tyndall National Institute

The deposition chamber can be heated to a maximum of 300°C, with a directly heated sample carrier and external heating jackets to prevent condensation on the reactor walls. The system uses two turbo pumps; one for the deposition chamber and one for the load-lock chamber. A gate valve connects the two chambers and maintains the integrity of the main deposition chamber. Once the load-lock pressure has reached equilibrium with the main chamber the gate valve can open and facilitate the loading of the samples.

The precursor manifold can maintain up to six precursor vessels at one time. Attached to the manifold are mass-flow controllers which aid in the regulation of the precursor delivery into the chamber. The precursor vapours are carried from their vessels into the main chamber using a direct draw system which is assisted by an argon gas flow. In order to prevent in-line condensation the manifold, inlet line, vapour trap, stop-valve and precursor vessels are all heated using controllable heating jackets.

Located above the deposition chamber is the plasma source created using an RF plasma generator which can be controlled using the central control box. The plasma requires a flow of argon gas to form, although the plasma can be altered by adding additional gas flows to the system (e.g. adding O₂ gas would form O₂ plasma).

The carrier gas has two functions; (i) The inert gas acts as a transportation system for source chemicals into the reaction chamber, (ii) acts as a purge gas in between ALD pulses to remove any unreacted precursor and by-products to the vapour trap. By-products and excess precursor accumulated during deposition is pumped from the chamber and delivered to the vapour trap. The trap consists of a heated large surface area of mesh material with a highly reactive surface where the by-products can be deposited. Without the trap the materials would otherwise deposit in the pumps which can reduce their working efficiency.

3.1.2 Picosun R200 ALD System

The Picosun R200 is an ALD system (figure 3.1) which works in a very similar way to the Cambridge Nanotech Fiji 200LLC. The system consists of a precursor delivery system, main chamber and external load-lock chamber.

The precursors are located under the main chamber and are connected to the chamber by a chemical delivery system. The gas lines are equipped with a mass-flow controllers (MFC), pressure transducers and pneumatic pulsing valves. The pneumatic pulsing valves attach the precursor vessels to the carrier gas valve and controls the flow of precursors into the reaction chamber. When a pulsing valve is

open source chemicals can be transferred into the carrier gas line and to the reaction chamber. However, when a pulsing valve is closed carrier gas will flow directly to the reaction chamber absent of source chemical. An added feature to the Picosun R200 is its boost function. When the boost function is activated and the pulsing valve is open, carrier gas is forced into the precursor bottle resulting in better transportation of the source chemical to the reaction chamber.



Figure 3.2: Image of the Picosun R200 ALD System located in Tyndall National Institute

The chamber has a dual chamber structure. The outer chamber acts as a vacuum chamber separating the main chamber from the outside air. The inner chamber or reaction chamber accommodates the chuck or the substrate holder and is where all deposition occurs. The reactions are contained by a chamber lid. This lid is situated on a pneumatic elevator that can be opened and closed to facilitate loading of wafers via the load-lock. All precursors are carried directly to the reaction chamber and the carrier gas lines and precursor vapour lines directly to the substrate and expelled

through a gas distributor. The gas distributor allows for uniform deposition by spreading the precursor evenly across the entirety of the substrates surface.

The vacuum system is located under the main chamber and is connected to the powder trap with after burner using vacuum piping. The after burner is situated at the pumping line before the powder trap. Excess chemical and by-products are transported to the after burner and are broken down by a series of controlled reactions using air or H₂O. The vapour trap below then collects the residual particles from the after burner preventing them from entering the pump.

3.2 Instrumentation for Analysis and Characterisation of Thin Films

3.2.1 X-ray Diffraction (XRD)

X-ray diffraction (XRD) is an analytical technique used to determine the crystal structure of materials by using electromagnetic rays of wavelengths between 1.0-1000 nm. A metal filament is heated and the electrons produced are accelerated by an electric field toward a metal target (Cu, Mo or Cr). The electrons bombard the target and produce electromagnetic radiation.

XRD requires a monochromatic x-ray source. A source that produces two wavelengths (K_{α} and K_{β}) gives two sets of reflections and two sets of interspersed reflections. This can make indexing difficult due to the wavelengths overlapping. Copper and molybdenum make good x-ray sources if the weaker K_{β} can be eliminated.

There are three types of x-ray sources; an x-ray tube, particle source rings and rotating anode tubes. The most widely used is an x-ray tube. Once the x-ray beam has been produced, the beam is directed through a collimator and mirrors in order to direct the beam toward the x-ray source.

When the electromagnetic rays hit an atom, the electrons surrounding the atom will oscillate at the same frequency as the electromagnetic beam. In most directions the waves should undergo destructive interference, where the waves that should combine are out of phase and thus no reflected energy will be emitted from the

sample. However, in crystalline materials the waves will undergo constructive interference in some directions due to combining in-phase waves. Thus some x-ray beams will be reflected from the sample at specific directions.

As XRD is based on scattering we can use Bragg's Law to describe how reflections occur when the x-ray beam comes in contact with a material.

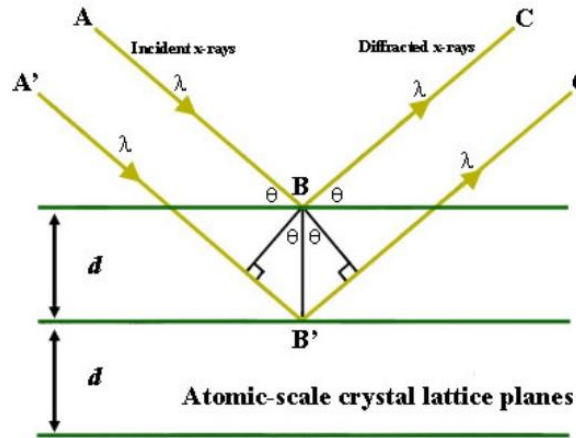


Figure 3.3: Schematic illustrating the application of Bragg's Law for X-ray Diffraction¹

Two parallel x-ray beams at wavelength, λ hit two parallel planes separated by spacing, d at an angle, θ and the rays are scattered as described above. The incident rays are in parallel and in phase until the beam reaches point, A. Here the second beam continues to the second layer where the beam is scattered by atom B. The beam thus must travel an extra distance $CB + BD$ assuming the beams are continuing adjacent and parallel. This extra distance is equal to $n\lambda$ where n is an integral multiple of the wavelength. Thus, $n\lambda = CB + BD$ for the two x-ray beams to remain the same.

In order to get the beam distance in terms of λ , the sine rule is used on the right-angled triangle ABC to determine:

$$d \sin \theta = CB \quad \mathbf{3.1}$$

$$2d \sin \theta = CBD \quad \mathbf{3.2}$$

Where, $CBD = n\lambda$

$$2d\sin\theta = n\lambda$$

3.3

Bragg's equation makes the distance between a set of atomic planes in a crystal and the angle at which the planes diffract x-rays relatable at a particular wavelength. Thus, when wavelength, λ and angle, θ are known, d_{hkl} can be calculated to determine the dimensions of the unit cell of a crystal lattice. All films analysed in this thesis were examined using a Phillips (PW3719) X'pert Materials Research X-ray diffractometer with a Cu K α radiation ($\lambda = 0.154056$ nm).

3.2.2 X-ray Photoelectron Spectroscopy

X-ray photoelectron spectroscopy (XPS) is a method used to quantify the elemental composition of a materials surface with the ability to detect all elements with the exception of H and He.

The analysis takes place under ultra-high vacuum (10^{-9} Torr). The sample is inserted into the pre-chamber first which can be exposed to the outside environment. The chamber is then pumped down to a low vacuum before being transferred to the main chamber under a high vacuum.

As illustrated in figure 3.4, the sample material is irradiated with monochromatic x-rays produced from an x-ray tube. To produce x-ray photons, a heated filament generates electrons that are then accelerated towards either an Al-K α or Mg-K α primary source. When the electrons hit the anode, a hole is created in its atoms. The hole is then filled by a relaxation of electrons from a higher energy level. This relaxation process causes x-ray fluorescence.

The electrons in the material absorb enough energy from the incident rays causing the emission of a photoelectrons with a certain kinetic energy. The emitted electrons then travel through an electrostatic transfer lens to an electrostatic hemispherical mirror analyser which measures the kinetic energy of the photoelectrons. The lens causes the deceleration of the photoelectrons and focuses them onto the entrance slit of the analyser (figure 3.3). The computer then produces a plot of the binding energy of the electrons versus the relative number of electrons ejected from the sample.

The method is based on Einstein's photo-chemical quantum equivalence law which is given by:

$$h\nu = E_b + E_k + \phi \quad 3.16$$

Where, $h\nu$ is the incident photon energy, E_b represents the binding energy of the electrons to the nucleus of the atom, E_k describes the kinetic energy of the emitted photoelectrons and ϕ is the work function or correction factor used by the instrument which represents the minimum amount of energy required for an electron to be emitted. It explains how when a material is irradiated with incident photons they have a high probability of emitting electrons from its orbital. In order to be ejected from its orbital the electron must exceed its binding energy and requires a minimum amount of energy (ϕ) to leave the target surface. The ejected photoelectron has a certain kinetic energy which is measured by the instrument.

Electrons with different kinetic energies travel different paths through the detector allowing the computer to differentiate the different electrons. As electrons further from the nucleus of the atom have less energy, they require less energy to be ejected and so the binding energy is lower for higher orbitals. Similarly electrons in different subshells such as s, p and d have different energies. XPS works to slow down the emission of the ejected photoelectrons in order to determine the composition of the sample material. X-ray photoelectron spectroscopy (XPS) was carried out using a Kratos AXIS_ULTRA with a monochromatized Al K α x-ray source of radiation of 1486.58 eV as the excitation source (10 mA, 15 kV).

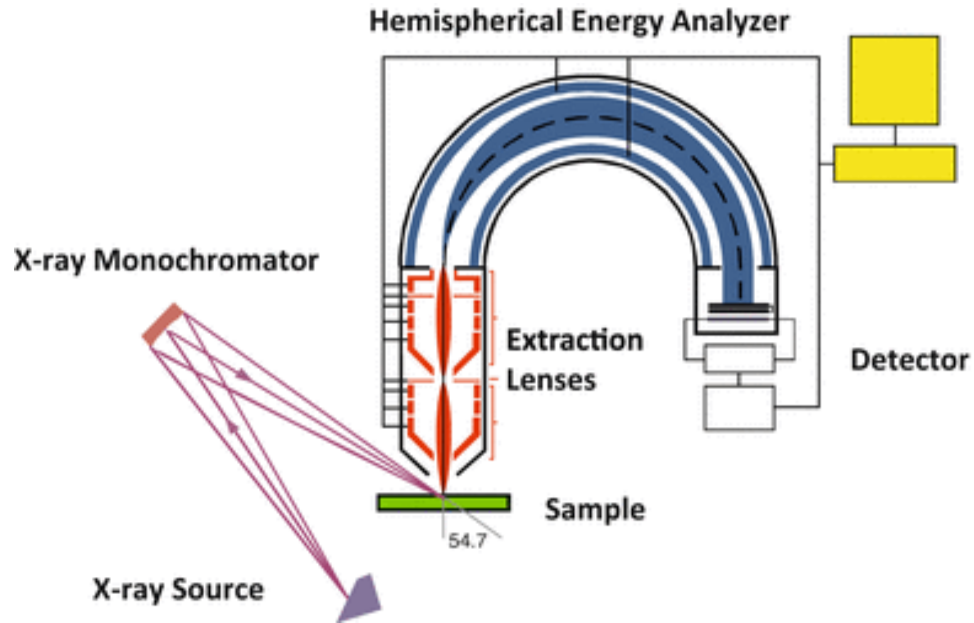


Figure 3.4: Schematic of X-ray Photoelectron Spectrometer²

3.2.3 Four Point Probe

A four-point probe can be used to measure the sheet resistance of semiconductor materials. The four-point probe consists of four equally spaced tungsten metal probe tips of a known radius. The probe tips are mounted on a spring-loaded mechanical stage that prevents damage of the tips during probing. A high impedance current source forces a current through the outer probes 1 and 4 and a voltmeter then measures the voltage drop between the inner probes 2 and 3. Using the values obtained from these measurements the sheet resistance of the samples can be determined. Highly resistive samples require low currents forced across the outer probes to ensure that voltages are not too high across the inner probes. For low resistive samples the current may need to be increased significantly.

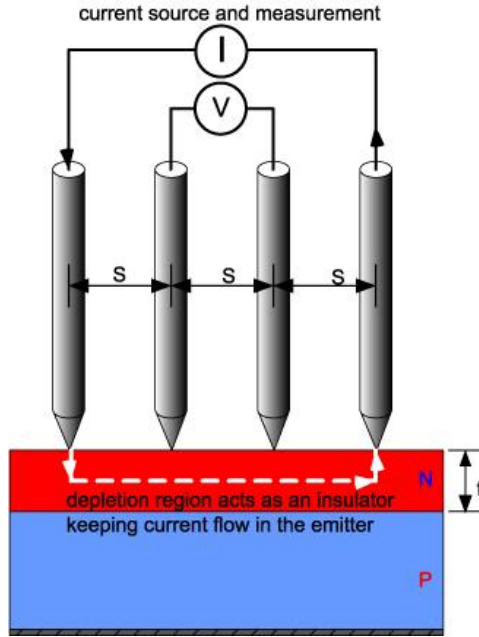


Figure 3.5: Schematic of four-point probe measurement set up³

For a four-point probe measurement on an infinite sheet equation 3.4 is used:

$$R_s = \frac{V}{I} \frac{\pi}{\ln \ln 2} \quad 3.4$$

When calculating the sheet resistivity of an infinite sample with finite thickness, w , the resistivity can be expressed as follows:

$$R_s = \frac{V}{I} \frac{\pi}{\ln \ln 2} F_c \quad 3.5$$

Where F_c is the correction factor where w is the length of the short edge of the sample in mm and s is the probe spacing. Most correction factors have been calculated and tabulated based on the size and geometry of the sample. For example, a rectangular sample has a long edge $l = 20$ mm and a short edge $w = 10$ mm and the probe spacing is 2 mm. Here $\frac{l}{w} = 2$ and $\frac{w}{s} = 5$. The tabulated correction factors must be searched

for the correction factor that meets these values. The sheet resistance must then be multiplied by this value in order to obtain an accurate sheet resistance for the sample. For thin films where the thickness of the sample, t , is much less than the probe spacing, s ($t \ll s$) $F_c = 1$. Thus the sheet resistance equation can be altered to:

$$R_s = 4.532 \frac{V}{I} \quad \mathbf{3.6}$$

For thick samples where the thickness of the samples is 40% more than the probe spacing an additional correction factor must be incorporated. This correction factor depends upon the ratio of the samples' thickness to the probe spacing and thus a different set of values are used for these sample sets. Samples in this thesis measured using a four point probe were examined using a Lucas Labs S-302-4 manual four point probe.

3.2.4 Hall Effect Measurement

Hall Effect measurements are used to determine the Hall voltage (V_H), carrier concentration (n), carrier mobility (μ_H), and conductivity type (N or P). The Hall Effect is observed when the current along the sample and the magnetic field through the same sample combine and produce an electrical current perpendicular to the magnetic field and the current. This results in a transverse voltage or Hall voltage. The force released from a magnetic field is called the Lorentz force. This force is the basis of the Hall Effect. By using the "Right Hand Rule" the sign on the charge carriers can be determined. Current flowing from left to right in a conductor indicates negative carriers moving from left to right or positive charges moving from right to left.

In order to measure the carrier mobility of a thin film the Hall voltage (V_H) must be determined by forcing a magnetic field and current perpendicular to the sample. This produces a transverse voltage also known as the Hall voltage. In addition to the Hall voltage, film thickness and resistivity are required for the calculation of Hall voltage.

The resistivity can be measured using a four-point probe method or a Van der Pauw technique (figure 3.6).

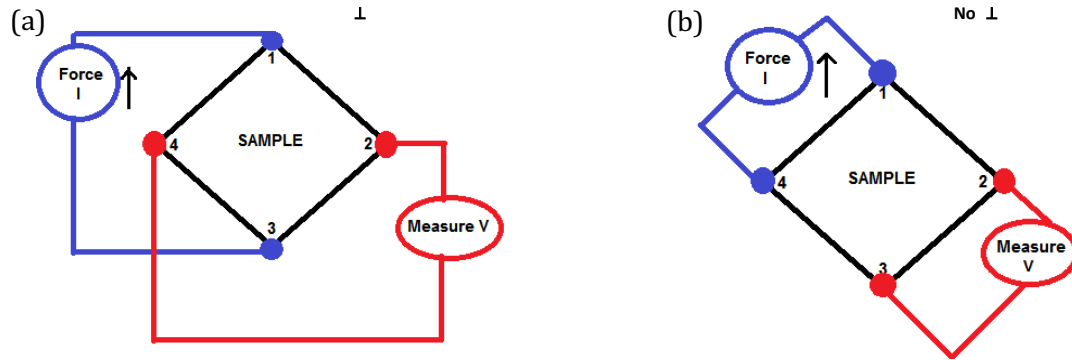


Figure 3.6: Illustrates the measurement configurations of (a) Hall Effect voltage measurement and (b) Van der Pauw measurement.

To measure the Hall voltage a current is forced through the opposite corners of the sample and the voltage is measured on the opposing opposite corners. Van der Pauw measurements require the current to be forced through the adjacent corners of the sample and the voltage is measured on the opposite adjacent corners. Van der Pauw measurements do not require a magnetic current to determine the voltage.

Mobility, (μ_H) can be measured using the formula:

$$\mu_H = \frac{|V_H t|}{BI\rho} \quad 3.7$$

Where, V_H , t , B , I and ρ are Hall voltage, thickness (cm), magnetic field, current and resistivity respectively.

To ensure that the values obtained from the measurements are reliable the source current polarity and magnetic field are reversed to undergo eight Hall Effect measurements and eight Van der Pauw measurements. Hall voltage is then

calculated when the current polarity is both positive (P) and negative (N) and the magnetic field is up and down giving equation 3.8 below.

$$V_H = \frac{(V_C + V_D + V_E + V_F)}{8} \quad 3.8$$

Where: $V_C = V_{24P} - V_{24N}$

$V_D = V_{42P} - V_{42N}$

$V_E = V_{13P} - V_{13N}$

$V_F = V_{31P} - V_{31N}$

In order to calculate the resistivity (ρ) accurately numerous Van der Pauw measurements are used where the source polarity is reversed similar to the Hall voltage measurement.

$$R_A = \frac{(R_{21.34} + R_{12.43} + R_{43.12} + R_{34.21})}{4} \quad 3.9$$

$$R_B = \frac{(R_{32.41} + R_{23.14} + R_{14.23} + R_{41.32})}{4} \quad 3.10$$

$$e^{\left(-\frac{\pi R_A}{R_s}\right)} + e^{\left(-\frac{\pi R_B}{R_s}\right)} = 1 \quad 3.11$$

$$\rho = R_s \cdot t \quad 3.12$$

The Hall mobility (μ_H) can then be calculated using the resistivity value from the Van der Pauw measurement and the Hall Effect voltage using equation 3.12 above. All samples in this thesis were measured using a LakeShore Model 8400 Series Hall effect measurement system.

3.2.5 Transmission Electron Microscopy (TEM)

Transmission Electron Microscopy (TEM) is a method that transmits electrons from an electron gun through a sample to create an image. Thermionic emission is the most widely used system to generate electrons. A tungsten wire bent into a hairpin shape is heated by an applied electrical current. When the tungsten reaches a temperature in excess of 2700 K electrons and light are generated from the wire. From the electron gun, electrons are then accelerated toward the anode. A beam of high energy electrons then pass through an aperture in the anode and into the microscope column.

The beam of electrons then passes through a series of condenser lenses which control the size of the electron beam hitting the sample ensuring that the samples is sufficiently illuminated. By limiting the size of the beam to slightly larger than the field of view a reduced number of electrons are then lost from the system resulting in a sharper image.

The sample is mounted below the condenser lenses in a specimen chamber. The chamber must allow the sample to be held in position above the objective lens securely and have the ability to mount the sample at a 45° angle in order for the electrons to strike the sample efficiently. The sample must also have the capability of moving or rotating in the horizontal plane in order to allow the operator to view the sample from various viewpoints.

The objective lens is used to focus the image being obtained from the sample. The lens consists of several apertures through which the beam can be focused. Without these apertures images of the sample would be without contrast and thus detail would be lost. Here an intermediate image is obtained. This image is then magnified by the projector lenses. Once final magnification is complete the image is displayed on a fluorescent screen for analysis.

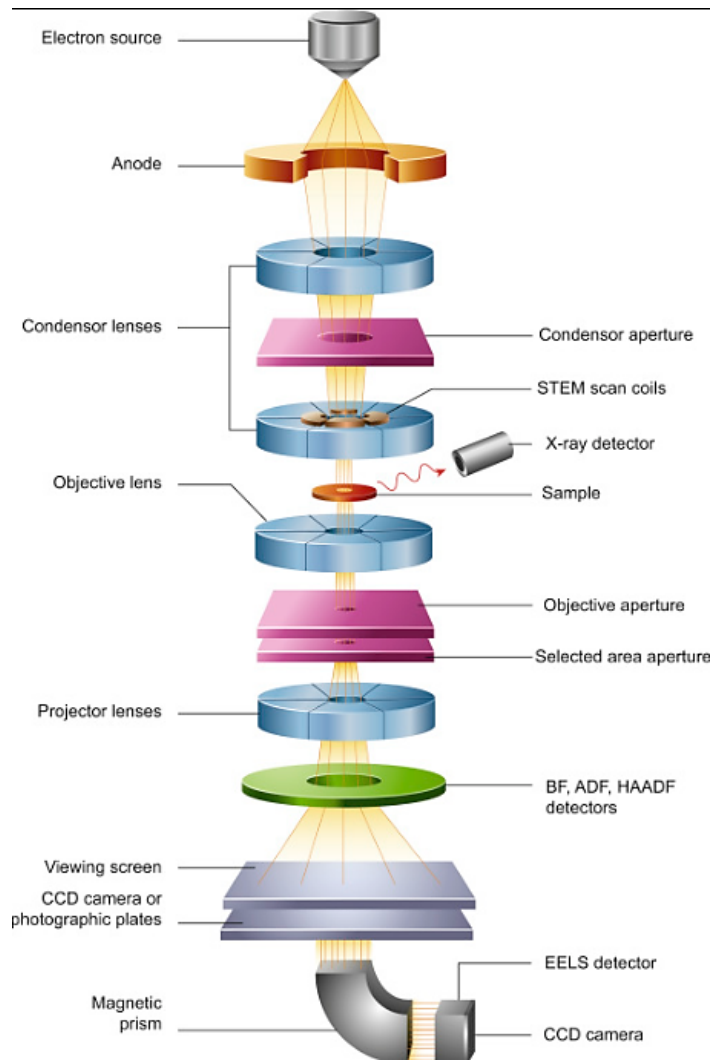


Figure 3.5: Schematic of the components that make up a Transmission Electron Microscope (TEM)⁴

3.2.6 Scanning Electron Microscopy (SEM)

Scanning electron microscopes (SEM) have similar components to that of the TEM. Both instruments perform analysis under vacuum, require an electron source such as an electron gun and use condenser lenses to control the size of the electron beam being accelerated toward the specimen. However, where TEM transmits electrons through the sample, SEM scans the surface of the sample and develops an image of that surface.

An electron gun produces a source of electrons which are accelerated toward an anode. The beam then passes through two or three condenser lenses which controls the size of the beam hitting the sample. The beam then passes through a coiled Cu wire or electromagnetic lens. A current passing through the Cu wire creates an electromagnetic field which causes convergence of the electron beam.

The now fine beam of electrons scans the surface of the sample in a raster sequence from left to right controlled by the deflector coils. The secondary electron detector counts the number of electrons given off the sample at each point. As the electron beam passes over features on the samples surface a cathode ray tube scans across its screen to form an image. The brightness of spots on the image is determined by the number of secondary electrons being detected at each point by the electron detector. The more electrons being detected the brighter the spot on the screen, thus applying contrast to any image obtained.

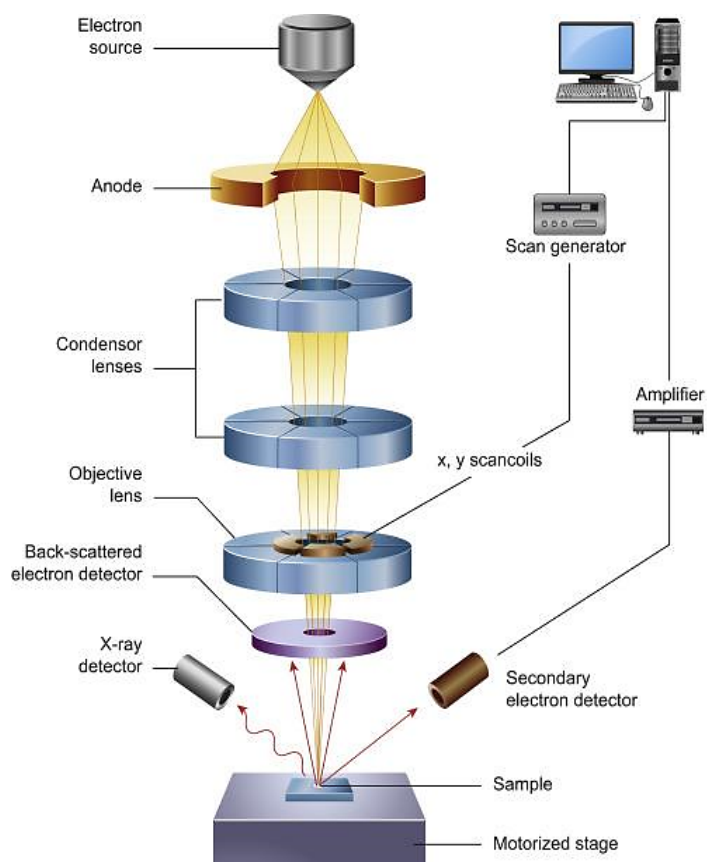


Figure 3.6: Schematic outlining the components of a Scanning Electron Microscope (SEM)⁴

3.2.7 UV/Visible/NIR Spectroscopy

The UV-visible-NIR region is characterised by the wavelength range of 200-3000 nm. During UV/visible spectrometry, incident light illuminates the surface of a sample at wavelength, λ . The sample will then absorb a quantity of energy from the incident light and the remainder will be transmitted through the sample. The transmitted light will then be detected by the photodetector a spectrum of the absorbed or transmitted light is graphed as a function of wavelength.

UV/visible spectroscopy is based on Beer-Lambert law which states that:

$$I = I_0 \times 10^{-kcl} \quad 3.13$$

Where I_0 = intensity of light illuminating the sample

I = intensity of light transmitted through the sample

k = proportionality constant

c = speed of light (m/s)

l = path length of the incident light (cm)

When applying Beer-Lambert law to optical spectroscopy,

$$\frac{I}{I_0} = \text{Transmittance (T)} \quad 3.14$$

$$\frac{I}{I_0} \times 100 = \text{Transmittance rate (\%T)} \quad 3.15$$

Absorbance (A) can similarly be calculated by rearranging the aforementioned equations 3.14 and 3.15 to give:

$$\log \left(\frac{1}{T} \right) = \log \left(\frac{I_0}{I} \right) = A \quad 3.16$$

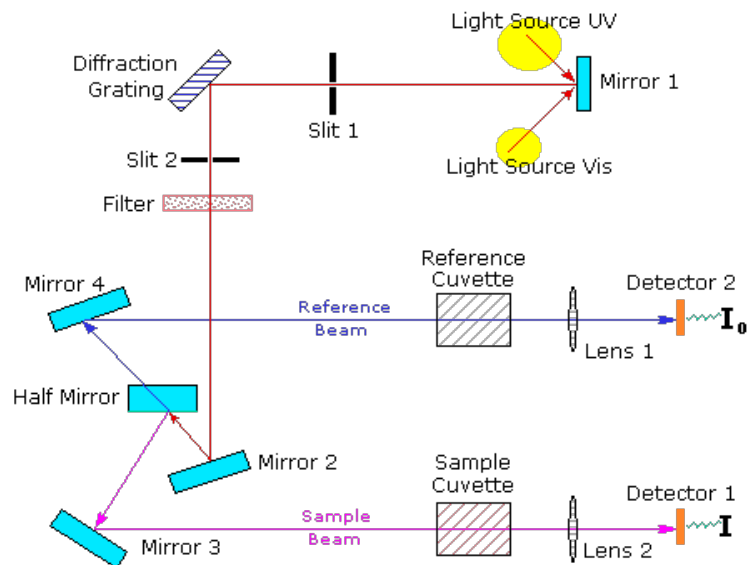


Figure 3.7: Schematic outlining the principle of UV-visible-NIR spectroscopy⁵

A UV/visible/NIR spectrometer is made up of several components including a light source, monochromator, sample holder, a photodetector and a signal processor. To

allow for analysis of the full spectral region the spectrometer requires two light sources. A deuterium arc lamp supplies light for the UV region whereas a tungsten-halogen lamp supplies light for the visible and near-IR region.

Light is emitted from the source and travels through a diffraction grating or prism which disperses the light into its integral wavelengths. By traveling through a monochromator or a slit a specific wavelength is directed toward the sample. A spectrometer can consist of a single beam monochromator or a double beam monochromator. A single beam monochromator allows for the reference sample and the test sample to enter the path of the incident light sequentially. However, a double beam monochromator splits the source light into two beams where two beam paths are formed; one to the reference sample and the other to the test sample. This allows the beam to pass through alternately the reference sample and the test sample.

The latter reduces the amount of stray light or scattered light in the system resulting in a higher quality spectrum.

Once the sample has absorbed or transmitted the incident light the light beam passes through a lens which focuses the beam on the detector. The detector then measures the intensity of the light transmitted through the sample. Over a period of time the spectrometer measures the intensity of the transmitted light over the desired range using the system outlined above. For the purpose of this work a Perkin Elmer Lambda 950 was used to analyse the % transmission of all samples.

Bibliography

- [1] Chemistry LibreTexts. 2019, *X-Ray Diffraction: Basics and Application*, [ONLINE], Available at <https://chem.libretexts.org/courses/Franklin> and Marshall College/Introduction to Materials Characterization - CHM 412 Collaborative Text/Diffraction Techniques/X-ray diffraction (XRD) basics and application. [Accessed 2 January 2019]
- [2] R. T. Haasch, *X-ray Photoelectron Spectroscopy (XPS) and Auger Electron Spectroscopy (AES)*, Practical Materials Characterisation, Springer, New York, NY, (2014)
- [3] PVEducation, 2019, Four Point Probe Resistivity Measurements, [ONLINE], Available at <https://www.pveducation.org/pvcdrom/characterisation/four-point-probe-resistivity-measurements>. [Accessed on 2 January 2019]
- [4] B. J. Inkson, Scanning electron microscopy (SEM) and transmission electron microscopy (TEM) for materials characterization, Materials Characterisation using Non Destructive Evaluation (NDE) Methods, University of Sheffield, Sheffield, UK. (2016)
- [5] Chemistry.msu.edu. 2019, UV-Visible Spectroscopy, [ONLINE], Available at <https://www2.chemistry.msu.edu/faculty/reusch/VirtTxtJml/Spectrpy/UV-Vis/uvspec.htm>. [Accessed on 2 January 2019]

Chapter 4: Fundamental Study of Atomic Layer Deposited ZnO and Doped ZnO

4.0 Experimental Details

4.1 Thermal ALD Processes

4.1.1 ALD of ZnO: Picosun R200

Deposition of ZnO was carried out using room temperature diethylzinc (DEZ) and H₂O. From previous studies and supporting literature, it was found that 200°C was the optimum temperature for ALD growth.^{1,2} The growth per cycle (GPC) observed on the Picosun used in this study matched the literature of values of ~0.2 nm/cycle (figure 4.1).³⁻⁵ This temperature was maintained for all growth in this chapter.

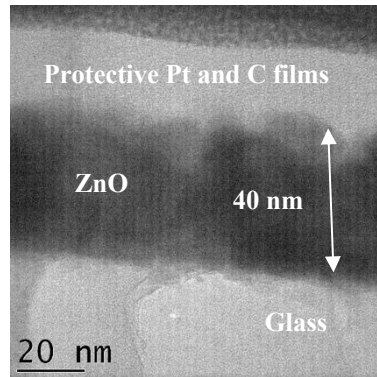


Figure 4.1: TEM image of 40 nm ZnO illustrating the growth rate of ZnO deposited at 200°C as ~0.2 nm/cycle

ZnO was deposited at various thicknesses (300-1000 ALD cycles) to determine how the electrical and optical properties changed with thickness. All growths were completed using the Picosun R200 and were deposited onto Corning® glass microscope slides and *p*-type Si substrates. All glass slides underwent a cleaning treatment of Decon 90, acetone and IPA prior to growth. *P*-type Si samples were cleaned using N₂ gas prior to oxide deposition as the samples were freshly fabricated. The growth parameters for the Picosun R200 are outlined in Table 4.1.

Substrates	Cycles	DEZ Pulse Time (s)	H ₂ O Pulse Time (s)	Purge Time (s)	Dep Temp (°C)
Glass/p-Si	300	0.05	0.1	6.0	200
Glass/p-Si	350	0.05	0.1	6.0	200
Glass/p-Si	500	0.05	0.1	6.0	200
Glass/p-Si	1000	0.05	0.1	6.0	200
Glass/p-Si	1500	0.05	0.1	6.0	200

Table 4.1: Growth conditions of ZnO for Picosun R200

4.1.2 ALD of Al-doped ZnO: Picosun R200

Deposition of Al-doped ZnO (AZO) was performed using the Picosun R200, doping was achieved by replacing a fraction of diethylzinc pulses with trimethylaluminium (TMA) using an ALD super-cycle methodology, with H₂O as co-reagent, as outlined in section 1.2. Both precursors were maintained at room temperature. From previous work it was determined that 19:1 ratio of ZnO:dopant contained the optimum amount of Al₂O₃ to obtain a good TCO.⁶ The GPC of Al₂O₃ was assumed to ~0.1 nm/cycle.^{7, 8} AZO was deposited on Corning® glass microscope slides and *p*-type Si substrates using Picosun R200. All glass substrates were precleaned using the same methodology as for the ZnO samples. In addition, to allow comparison with the nominally undoped samples the deposition temperature and range of thicknesses (300-1000 ALD cycles) matched those of the undoped ZnO as outlined in Table 4.2. Due to the growth rate of Al₂O₃ being slower than ZnO, and the potential for nucleation delays between laminates, the total thickness of the AZO films could not be assumed to be constant and hence sheet resistance was used to compare resistivity of the films.

Substrates	Cycles	Ratio of ZnO : Dopant	DEZ Pulse Time (s)	H ₂ O Pulse Time (s)	TMA Pulse Time (s)	Purge Time (s)
Glass/p-Si	300	19:1	0.05	0.1	0.1	6.0
Glass/p-Si	350	19:1	0.05	0.1	0.1	6.0
Glass/p-Si	500	19:1	0.05	0.1	0.1	6.0
Glass/p-Si	1000	19:1	0.05	0.1	0.1	6.0
Glass/p-Si	1500	19:1	0.05	0.1	0.1	6.0

Table 4.2: Growth conditions for AZO (19:1) deposited at 200°C for Picosun R200

4.1.3 ALD of Hf-doped ZnO: Picosun R200

For deposition of Hf-doped ZnO (HZO), tetrakis(ethylmethylanino)hafnium was heated to 70°C and the boost function on the Picosun R200 was activated. H₂O was maintained at room temperature. HZO was again deposited on Corning© glass microscope slides and *p*-type Si substrates. All glass substrates underwent the same pre-clean as the ZnO samples. The deposition temperature was maintained at 200°C to allow for comparison with ZnO and other doped ZnO samples. HZO was deposited at a dopant concentration of 19:1 at the same nominal thicknesses (pulse numbers) as other doped samples. The growth rate for HfO₂ was assumed to be ~0.1 nm/cycle.⁹
¹⁰ Growth parameters for the Hf- doped samples employing the Picosun R200 are outlined in Table 4.3.

Substrates	No. of Cycles	Ratio of ZnO:Dopant	DEZ Pulse Time (s)	H ₂ O Pulse Time (s)	TEMAH Pulse Time (s)	Purge Time (s)
Glass/p-Si	300	19:1	0.05	1.0	1.6	6.0
Glass/p-Si	350	19:1	0.05	1.0	1.6	6.0
Glass/p-Si	500	19:1	0.05	1.0	1.6	6.0
Glass/p-Si	1000	19:1	0.05	1.0	1.6	6.0
Glass/p-Si	1500	19:1	0.05	1.0	1.6	6.0

Table 4.3: Growth conditions of HZO (19:1) deposited at 200°C for Picosun R200

4.1.4 ALD of Ti-doped ZnO: Picosun R200

For the deposition of Ti-doped ZnO (TZO), tetrakis(dimethylamino)titanium was heated to 75°C and also required the activation of the boost function. H₂O was maintained at room temperature. TZO was deposited at 200°C on pre-cleaned Corning® glass microscope slides and *p*-type Si substrates. The same dopant pulse ratio of 19:1 was employed as the AZO and HZO to allow for comparison between dopants. The growth rate of TiO₂ was expected to be 0.05 nm per cycle.^{11, 12} Growth parameters of TZO on the Picosun R200 are outlined in Table 4.4.

Similar to section 4.1.2, the growth rate of TiO₂ is slower than ZnO the total thickness of the AZO films would vary slightly versus as-deposited ZnO.

Substrates	No. of Cycles	Ratio of ZnO : Dopant	DEZ Pulse Time (s)	H ₂ O Pulse Time (s)	TDMAT Pulse Time (s)	Purge Time (s)
Glass/p-Si	300	19:1	0.05	6.0	1.6	8.0
Glass/p-Si	350	19:1	0.05	6.0	1.6	8.0
Glass/p-Si	500	19:1	0.05	6.0	1.6	8.0
Glass/p-Si	1000	19:1	0.05	6.0	1.6	8.0
Glass/p-Si	1500	19:1	0.05	6.0	1.6	8.0

Table 4.4: Growth Parameters of TZO (19:1) deposited at 200°C for the Picosun R200

4.2 Results

4.2.1 Electrical Properties

Electrical conductivity was measured using a Lakeshore Hall Effect Measurement system as outlined in section 3.2.4. Here the sheet resistance (Ω/\square), Hall mobility (cm^2/Vs) and carrier concentration ($1/\text{cm}^3$) were obtained. Sheet resistance is measured as opposed to resistivity due to the potential for thickness variation due to differing growth rates of dopants and the potential for nucleation delays between laminate layers. The minimum and maximum excitation current applied for all films was 25 μA and 250 μA respectively. A summary of the electrical properties for ZnO and doped ZnO are outlined in Tables 4.5 - 4.8.

Film Thickness (nm)	Hall Mobility (cm^2/Vs)	Carrier Conc. ($1/\text{cm}^3$)	Sheet Resistance (Ω/\square)
60	15.3	2.02×10^{19}	3380.5
70	15.0	2.04×10^{19}	2912.9
100	25.0	3.05×10^{19}	809.0
180	27.7	2.78×10^{19}	449.9
200	17.3	4.52×10^{19}	399.8

Table 4.5: Electrical properties of ZnO deposited by thermal ALD at 200°C at a range of thicknesses (nominal values)

Film Thickness (nm)	Hall Mobility (cm^2/Vs)	Carrier Conc. ($1/\text{cm}^3$)	Sheet Resistance (Ω/\square)
60	9.86	1.88×10^{20}	559.4
70	7.46	2.15×10^{20}	554
100	9.15	3.39×10^{20}	200
200	8.76	4.26×10^{20}	83.5

Table 4.6: Electrical properties of AZO (19:1) deposited by thermal ALD at 200°C at a range of thicknesses (nominal values)

Film Thickness (nm)	Hall Mobility (cm²/Vs)	Carrier Conc. (1/cm³)	Sheet Resistance (Ω/□)
60	14.2	1.54 x 10 ²⁰	474
70	16.6	2.78 x 10 ²⁰	192.2
100	16.2	2.01 x 10 ²⁰	192
200	20.2	5.59 x 10 ²⁰	59.6

Table 4.7: Electrical properties of HZO (19:1) deposited by thermal ALD at 200°C at a range of thicknesses (nominal values)

Film Thickness (nm)	Hall Mobility (cm²/Vs)	Carrier Conc. (1/cm³)	Sheet Resistance (Ω/□)
60	5.7	1.74 x 10 ²⁰	1042.5
70	10	2.60 x 10 ²⁰	390
100	10.4	4.58 x 10 ²⁰	217.5
180	16.1	2.16 x 10 ²⁰	99.9
200	11.7	2.99 x 10 ²⁰	89.1

Table 4.8: Electrical properties of TZO (19:1) deposited by thermal ALD at 200°C at a range of thicknesses (nominal values)

An obvious trend was observed in the sheet resistance values of the as-grown ZnO and all the as grown doped ZnO thin films. It revealed that as the thickness of the films increased the sheet resistance decreased. Table 4.5 outlines the electrical properties of as-deposited ZnO at 200°C at a range of thicknesses. Although increasing the thickness from 60 nm to 100 nm reduced the sheet resistance to 399.8 Ω/□ this value could not compete with commercially available ITO thin films which can be obtained with values of 8-100 Ω/□.⁹ This suggests that doping at this growth temperature is vital to make the films electrically viable, an observation that is

confirmed by a distinct improvement in the sheet resistance values by the introduction of the dopants.

As thicker films (200 nm) gave the best electrical values discussion is focused on these samples. AZO and TZO revealed very similar sheet resistance values of $89.1 \Omega/\square$ and $83.5 \Omega/\square$ respectively (Tables 4.6 and 4.8). The main difference between the materials lay in the Hall mobility measurements where the values obtained for TZO were significantly improved as compared to AZO with a value of $11.7 \text{ cm}^2/\text{Vs}$ compared to $8.76 \text{ cm}^2/\text{Vs}$ for AZO. HZO was revealed to have the best sheet resistance value of $59.6 \Omega/\square$ and a Hall mobility value far superior to TZO of $20.2 \text{ cm}^2/\text{Vs}$.

Interestingly as grown ZnO reveals there appears to be no direct correlation between the Hall mobility value and low sheet resistance value. Table 4.5 show that the sheet resistance values for ZnO are far higher than any of the doped thin films and yet the Hall mobility values are on average higher than those obtained from HZO.

In order to compete with commercially available ITO the sheet resistance values must be as low as possible with a sufficient level of electron mobility. In addition to this the optical properties of the thin films must be comparable, or better, for the material to be a viable alternative to ITO.

4.2.2 Optical Properties

Figure 4.3 (a)-(d) shows the transmittance measurements of ZnO and doped ZnO thin films at 60-100 nm. The absorption edge for the samples was in between 275-370 nm due to the glass substrate. All samples had an optical transparency in excess of 70% in the visible range. It was clear that there were some changes in the transparency as the material increased in thickness however at 200 nm each film obtained a % transmittance in excess of 80% in the near IR and in excess of 70% in the UV/visible range. As the transparency was not degraded significantly by increasing the thickness of the films, it opened an avenue in which it was possible to

increase the thickness of the films further without compromising the device viability due to limitations in the optical properties of the TCO.

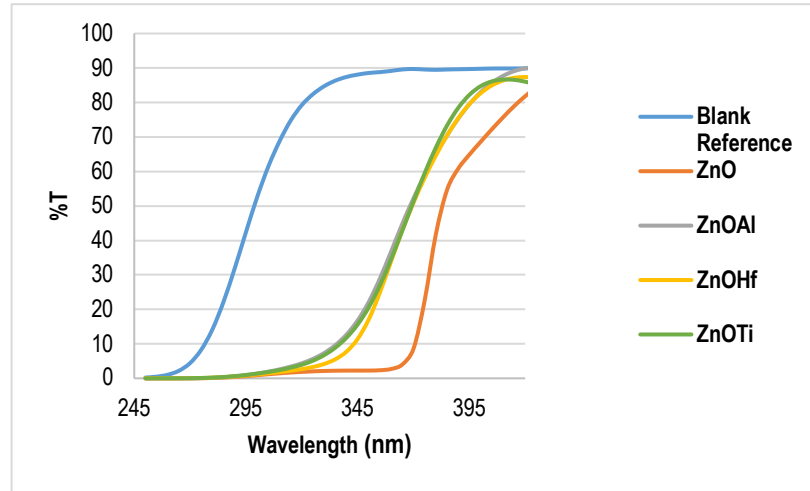


Figure 4.2: UV/Visible spectrum of 200 nm ZnO and doped ZnO deposited by thermal ALD with H_2O at $200^\circ C$ on glass showing the band gap shift due to the introduction of a dopant material

Figure 4.2 shows the UV/visible spectrum of ZnO and doped ZnO at 200 nm compared to a reference glass samples. It is evident that the incorporation of all the studied dopant material produces a blue shift in the wavelength of the absorption edge, with Al and Ti dopants having the greatest effect on the shift. Tseng *et al*¹, explains that the optical band gap of a semiconducting material with a direct band gap increases with increasing electron concentration as the conduction band is highly populated with excited electrons from shallow donor states. This implies that a blue-shift based on the Burstein-Moss theory can indicate an increase in the carrier concentration.^{1, 5}

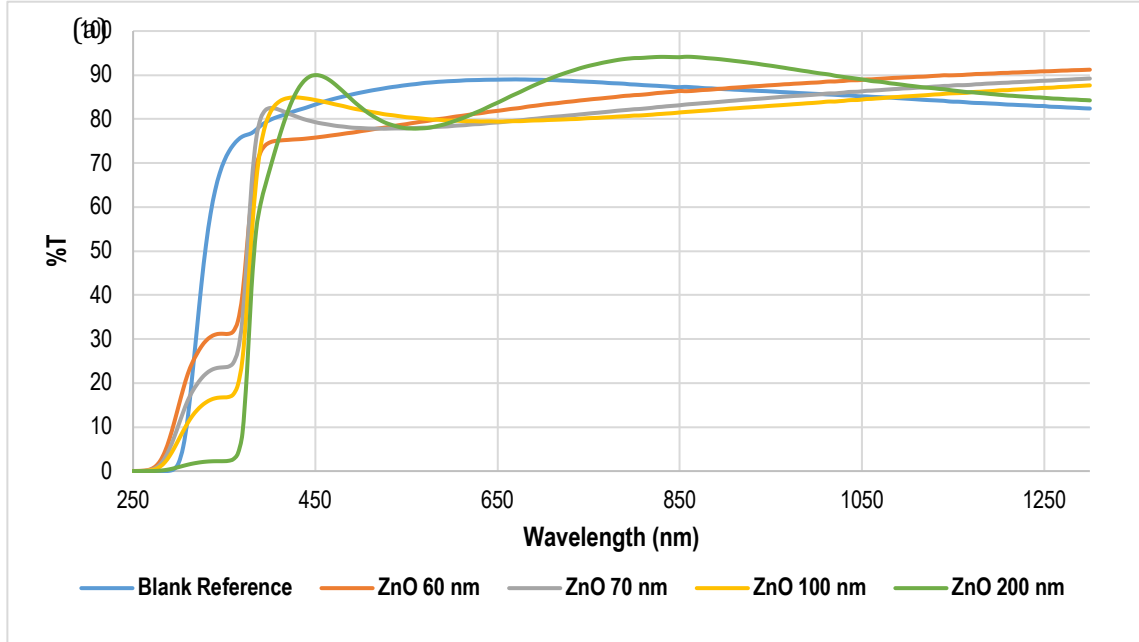


Figure 4.3 (a): shows the % transmittance of ZnO thin films deposited at 200°C by thermal ALD at a range of thicknesses (60-200 nm)

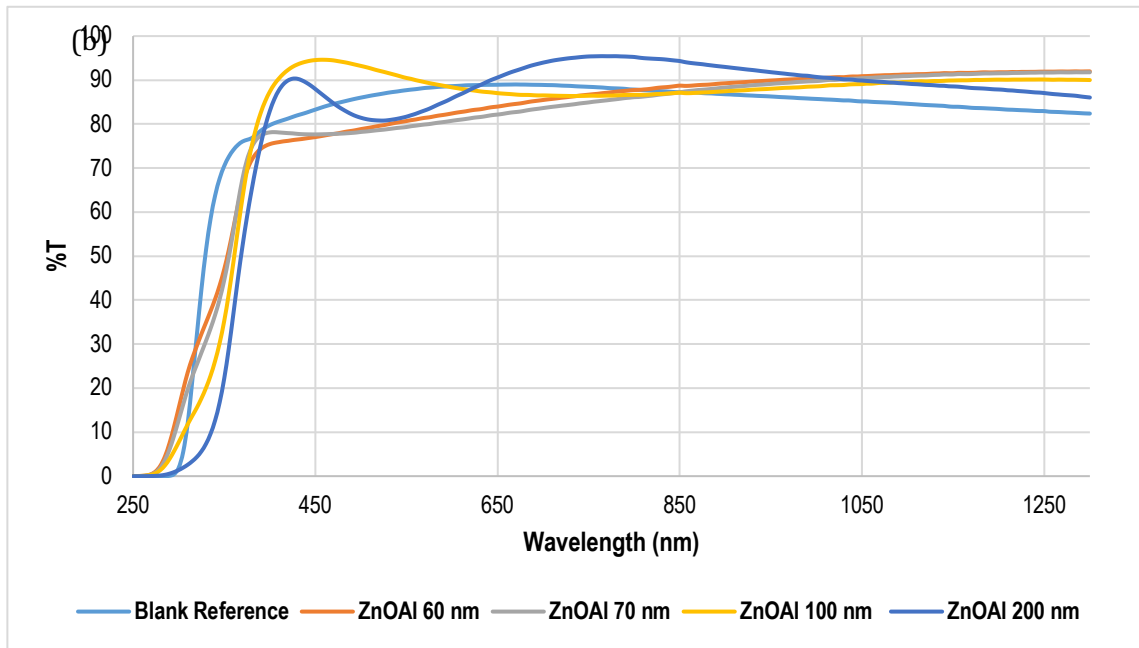


Figure 4.3 (b): shows the % transmittance of AZO (19:1) thin films deposited at 200°C by thermal ALD at a range of thicknesses (60-200 nm)

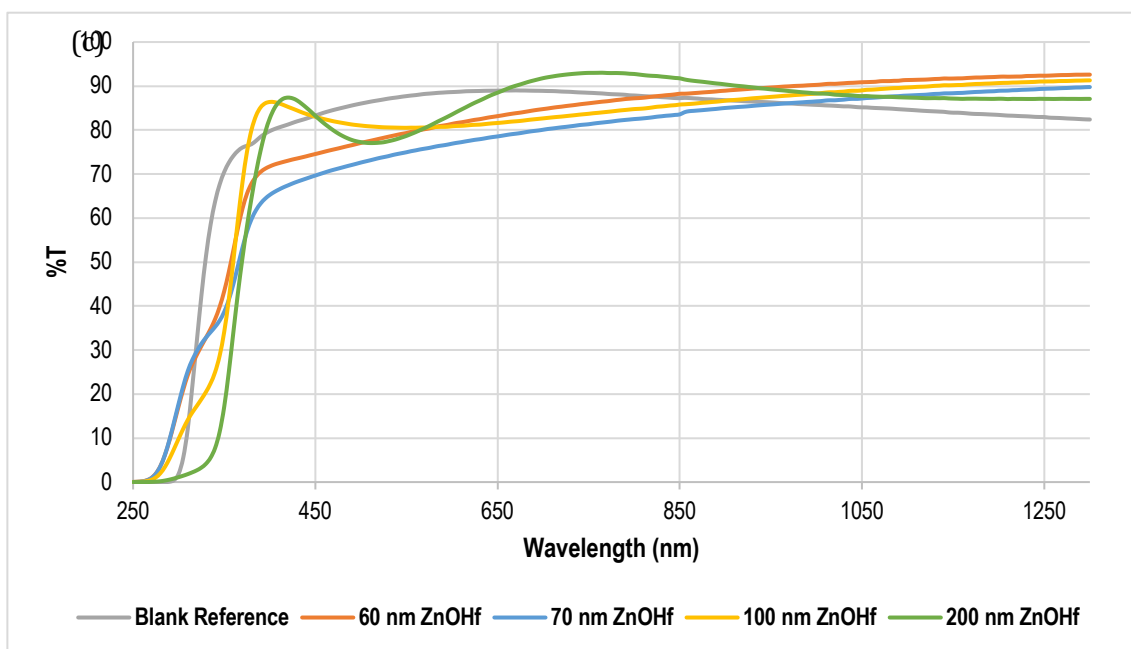


Figure 4.3 (c): shows the % transmittance of HZO (19:1) thin films deposited at 200°C by thermal ALD at a range of thicknesses (60-200 nm)

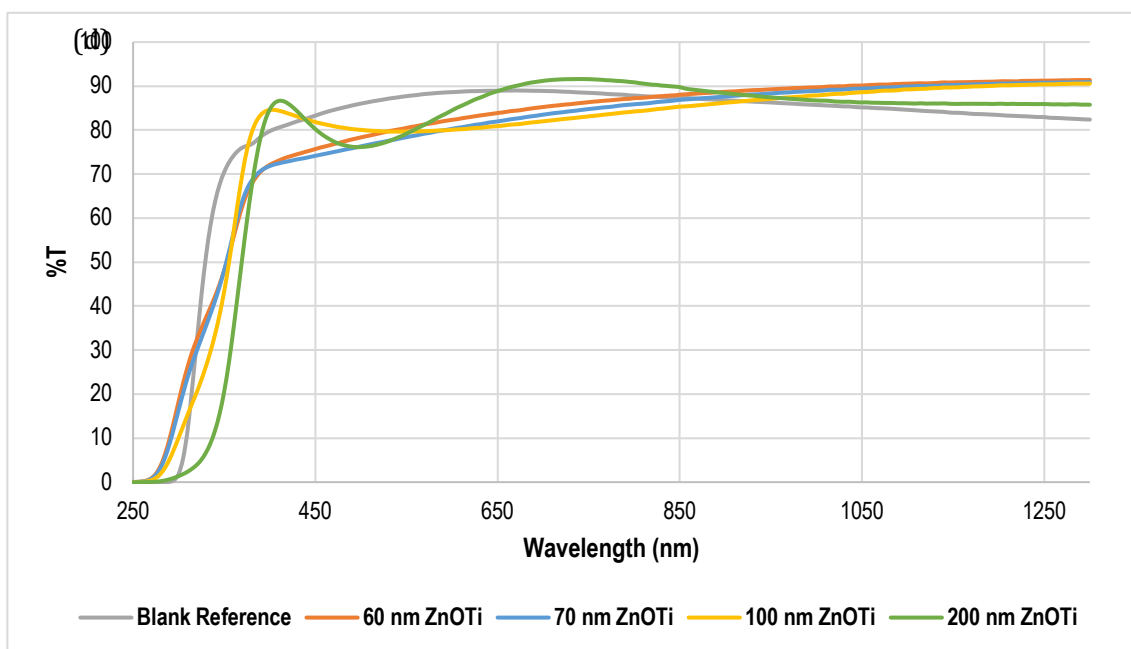


Figure 4.3 (d): shows the % transmittance of TZO (19:1) thin films deposited at 200°C by thermal ALD at a range of thicknesses (60-200 nm)

4.2.3 X-ray Diffraction

X-ray diffraction patterns of ZnO and doped ZnO are represented by figure 4.4(a-d). All films showed signs of crystallinity with the intensity of the peaks increasing with increasing thickness. The peak representing the [110] orientation was present in all films. ZnO (figure 4.4a) and HZO (figure 4.4c) revealed peaks of similar crystalline orientation at 31.8° , 34.4° , 56.7° which were assigned to [100], [002] and [110] respectively.^{2, 13-17} The preferred orientation for both films was in the [100] direction. AZO (figure 4.4b) was revealed to have a more ordered film with a distinct crystalline peak assigned to (100). TZO (figure 4.4d) had the most disordered thin film with peaks evident as positions 31.8° , 34.4° , 36° and 56.4° representing the [100], [002], [101] and [110] crystal orientations.^{1, 17, 18} TZO had a preferred orientation in the (100) direction and this peak increased in intensity as the thickness of the film increased.

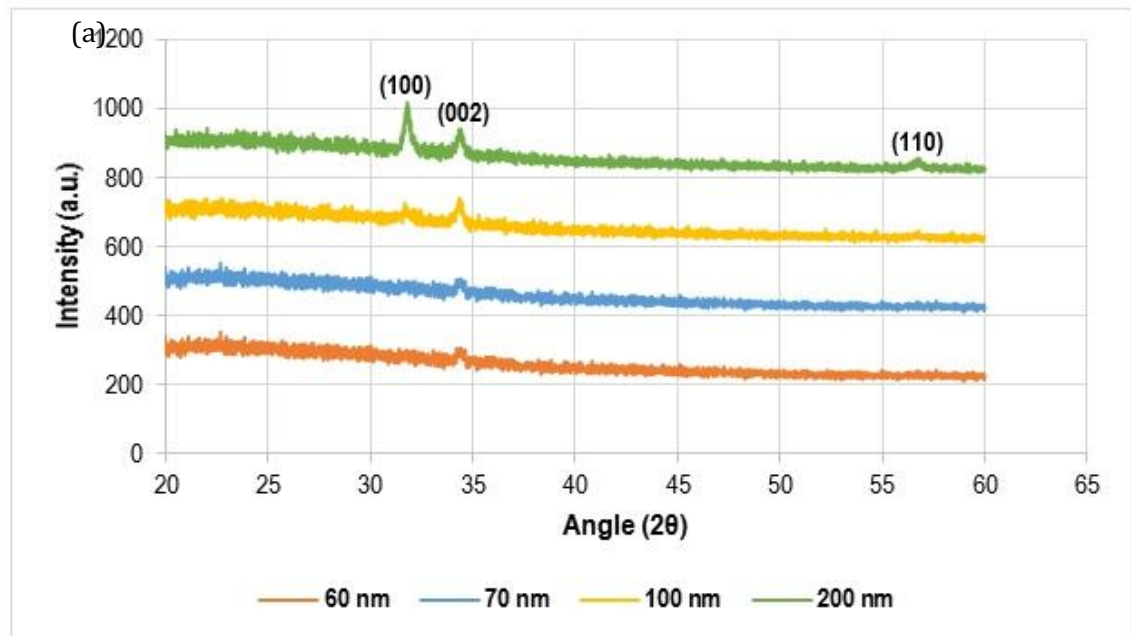


Figure 4.4: (a) XRD patterns of as-deposited ZnO at 200°C at a range of thicknesses (60-200 nm)

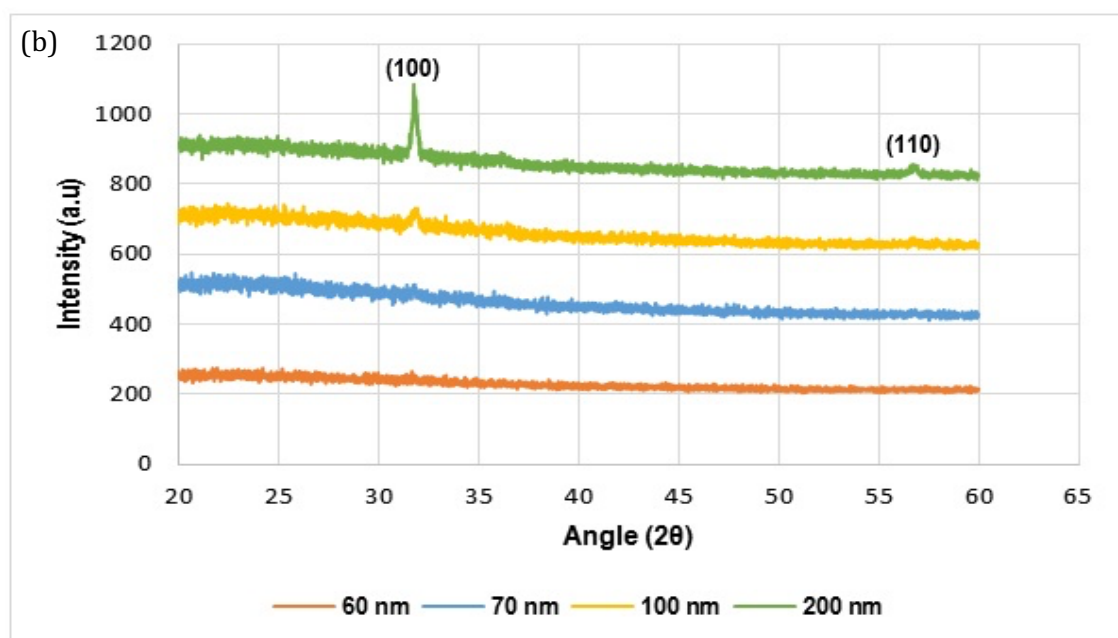


Figure 4.4: (b) XRD patterns of AZO (19:1) films deposited at 200°C at a range of thicknesses (60-200 nm)

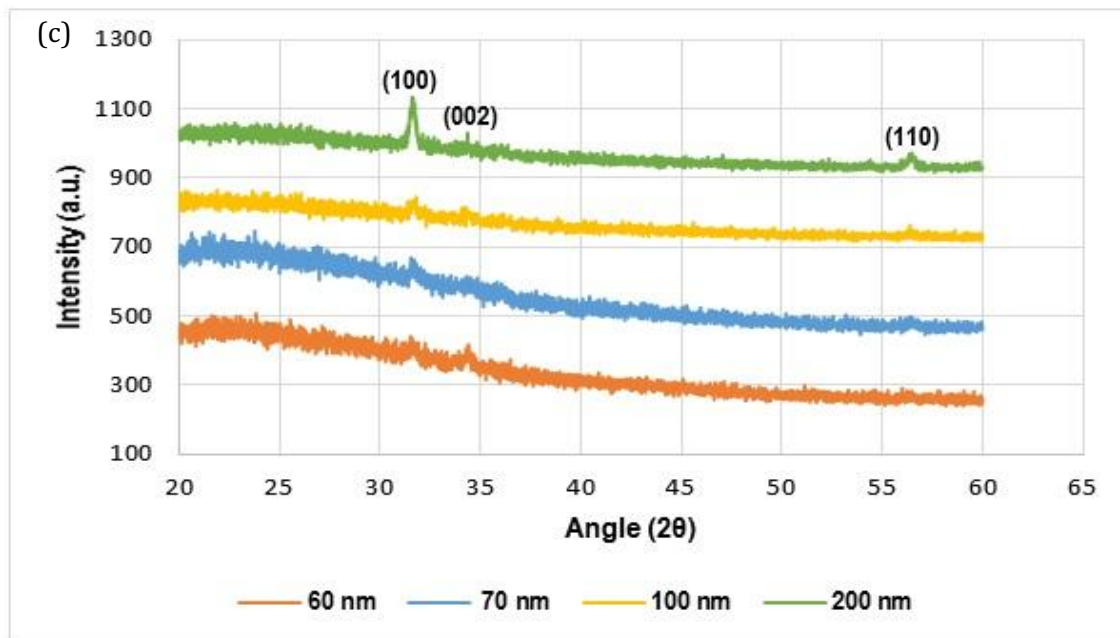


Figure 4.4: (c) XRD patterns of HZO (19:1) films deposited at 200°C at a range of thicknesses (60-200 nm)

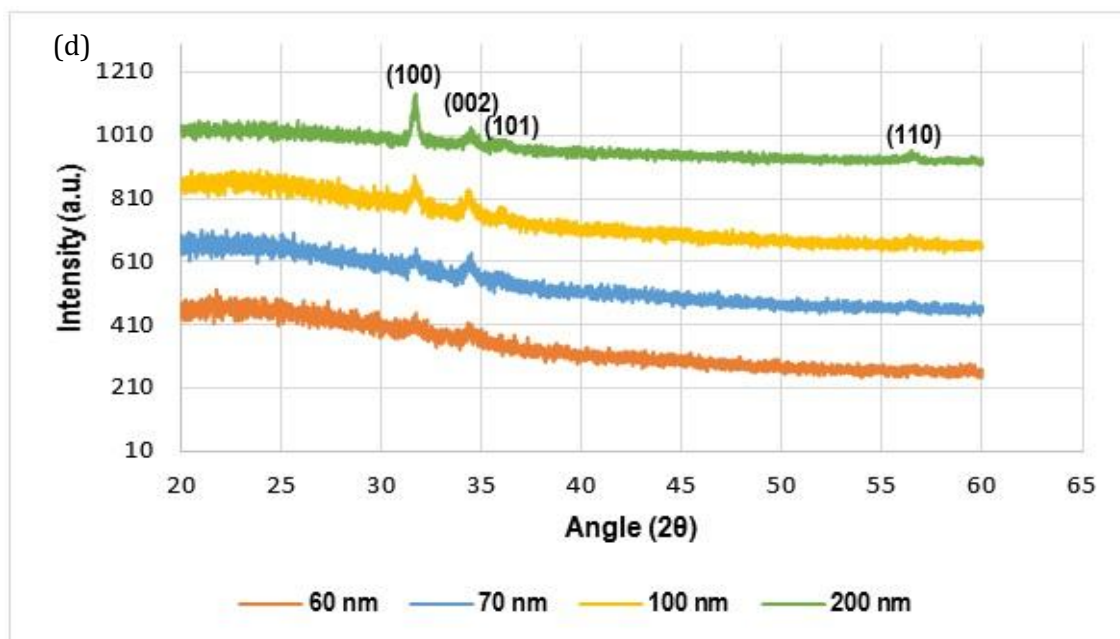


Figure 4.4: (d) XRD patterns of TZO (19:1) films deposited at 200°C at a range of thicknesses (60-200 nm)

4.2.4 X-ray Photoelectron Spectroscopy

Quantification values of ZnO and doped ZnO obtained from high resolution XPS are outlined in Table 4.9 below.

Sample	Name	Atomic %
ZnO	Zn 2p	42.2
	O 1s	50.1
	C 1s	7.7
HZO	Zn 2p	39.1
	O 1s	51.2
	C 1s	8.5
	Hf 4f	1.2
AZO	Zn 2p	36.9
	O 1s	51.1
	C 1s	7.9
	Al 2p	4.1
TZO	Zn 2p	38.5
	O 1s	50.3
	C 1s	9.6
	Ti 2p	1.6

Table 4.9: Quantification from high resolution XPS of atomic % of Hf, Al and Ti in ZnO films

It is clear from the data that the dopant elements were incorporated into the zinc oxide films. Aluminium doping was more effective as there was a greater atomic % of aluminium present (4.1 at. %) than in the case of hafnium (1.2 at. %) or titanium (1.6 at. %). It is also observed that due to the laminate deposition method that makes up atomic layer deposition the depth profile of the XPS system may penetrate different levels in each film and as a result the atomic % values obtained could be inconsistent. Residual carbon, arising from precursor ligands, was present in all films. This was expected, due to the low temperature ALD process conditions employed. See figures 1-4 in appendix II for high resolution spectra.

4.3 Discussion

This study of ZnO and doped ZnO revealed the potential for replacement of ITO and FTO currently being used in perovskite solar cells as the transparent contact. Although these materials are functional for single-junction devices, due to the high temperatures and high energy techniques used to deposit such materials an alternative material and deposition method is vital when fabricating a tandem solar device. Due to the thermal restrictions necessary to maintain the integrity of the perovskite cell in a tandem device, as grown ZnO and doped ZnO without post-growth annealing are studied.

It has been reported that the sheet resistance values and Hall mobility values depend on the film morphology and crystallinity.^{19, 20} Interpretation of data revealed that as the thickness of all thin films increased the sheet resistance reduced significantly and the Hall mobility values revealed a similar trend.

It can be seen in the XRD patterns measured in this work that the films become more orientated as the thickness increases and the peak intensities also increase. Figure 4.4 of the XRD patterns of ZnO and doped ZnO showed a preferred orientation in the [100] direction however in as-deposited ZnO, HZO and TZO a low intensity peak attributed to the [002] direction were also evident. ZnO samples that exhibit a strong (100) peak are generally those deposited on glass substrates.² It has been reported that the sheet resistivity of ZnO films is inversely proportional to the intensity of the (002) peak in XRD patterns.^{19, 21} This trend was also observed in figure 4.4. The intensity of the (002) peak became greater as the thickness of the film increased resulting in a reduction in the sheet resistance. Figure 4.4 (b) shows that the AZO thin film does not exhibit the (002) peak and shows a preferred orientation in the [100] direction. It has also been reported that the (002) peak present in as-deposited ZnO disappears once Al³⁺ ions have been incorporated into the film.^{2, 21, 22} Banerjee *et al.*³ proposed that the (100) plane is a neutrally charged surface caused by the presence of Zn²⁺ and O²⁻ ions existing in alternate rows on the surface. Once the Al₂O₃ is incorporated into the layer-by-layer structure the Al³⁺ ions upset the neutrality of the plane causing the preferential growth of the plane. This implies that the substrate

on which the material is deposited has an effect on the crystal structure of the thin film obtained.

In addition, it was clear that doping ZnO greatly improved the electrical characteristics of the ZnO. Figure 4.4 reveals that the most polycrystalline doped film resulted in the lowest sheet resistance value. Literature has reported that a more orientated film can result in greatly improved electrical characteristics.²⁴ Here, TZO appears to be more polycrystalline than AZO or HZO with the addition of a peak at 36° representing the [101] orientation. The crystallinity of the films varies depending on the dopant material introduced. This variation could be a consequence of how the material nucleates directly onto the substrate or how it nucleates on or around the dopant material. It was previously mentioned that the preferred orientation is influenced by the nature of the glass substrate onto which the films were deposited. It is also possible that the nucleation of the layers of ZnO material are being inhibited by the dopant and thus causing a difference in crystallinity depending on the dopant being introduced.^{20, 25}

Although improved crystallinity generally increases the electrical performance of the films, the presence of more crystallites in the thin films can result in the formation of large grains on the surface. ZnO has been reported to form large columnar features which can result in grain boundaries forming on the surface and cause ion scattering.^{26, 27} As the conductivity of the ZnO is mainly affected by the generation of electrons from oxygen vacancies and Zn interstitial atoms, large amount of charge can be lost in the grain boundaries. This phenomenon is known as charge trapping.^{26, 27}

The sheet resistance values of ZnO reduced significantly once the dopant material was introduced. ZnO reduced from $399.8 \Omega/\square$ to $83.5 \Omega/\square$ once Al^{3+} ions were introduced into the film. The same was observed for TZO and HZO where the sheet resistance values reduced to $89.1 \Omega/\square$ and $59.6 \Omega/\square$ respectively once Ti^{4+} and Hf^{4+} ions were introduced.

As the sheet resistance reduces with increasing thickness it is possible that the scattering in the films is being reduced as the film gets thicker due to improving the crystallinity in the film. The Hall mobility values are also known to be limited by these grain boundaries and ionized scattering.^{28, 29} Minami *et al*²⁸, mentions that a trend is usually seen between the Hall mobility values and the carrier concentration values where low carrier concentrations usually result in high Hall mobility values. From Tables 4.5-4.8, there seems to be a deviation in the data presented from this reported trend. Table 4.5 shows the electrical results of ZnO where the Hall mobility values reduces with increasing carrier concentration. However, once a dopant material is introduced, their ions influence the way in which the electrons migrate through the films. For both TZO and AZO (Tables 4.6 and 4.7) this trend is only observed for 200 nm thick films. HZO (Table 4.8) shows that the Hall mobility values are directly proportional to the carrier concentration. It is possible that for ZnO and HZO fewer grain boundaries are present in the film allowing for free movement of electrons through the film. Thus the dopant ions are having less of an influence on the resulting microstructure of the films. For AZO and TZO films charge trapping in the grain boundaries, due to large crystallites formed in the film, could have influenced the electrical data. Thus, it seems that there is a correlation between the crystallinity of the films and the electrical properties with a film with a smooth surface and few surface features reducing scattering and leading to a higher Hall mobility and a reduced sheet resistance value.⁵

The XPS data outlined in section 4.2.4 shows that the dopant elements were incorporated into the materials. However, due to the laminate deposition method employed by atomic layer deposition it is possible that the atomic percent obtained from the data is unreliable.²¹ As a result, the ALD cycle ratios are used to calculate nominal values for the atomic % in chapters 5-8.

4.4 Conclusion

ZnO was deposited by thermal ALD at 200°C using H₂O as the co-reactant at a range of thicknesses from 60 nm – 200 nm. ZnO was subsequently doped with Al, Hf and Ti under the same conditions for the same range of thicknesses using a nominal dopant concentration of 19:1 (ZnO:dopant). The films produced all gave an optical transparency in excess of 70% with the absorption band edge shifting once the dopants were introduced. ZnO and doped ZnO were polycrystalline and at 200 nm the films had a preferred orientation in the (002) direction. Doping the ZnO was observed to improve all electrical properties significantly with the best values achieved at the thickest film thickness 200 nm. HZO produced the best sheet resistance and Hall mobility values of 59.6 Ω/\square and 20.2 cm²/Vs respectively. AZO and TZO produced similar sheet resistance values to each other of 83.5 Ω/\square and 89.1 Ω/\square respectively, while their Hall mobility values were both significantly lower than those obtained for HZO.

Although, HZO seems to be the best material electrically when compared to AZO, TZO and as-deposited ZnO, in order to become a potential candidate to replace ITO/FTO in perovskite solar cells and later in tandem solar cells, the sheet resistance values need to be much lower. As the sheet resistivity decreases with increasing thickness and optical properties are not significantly degrade with thickness a further study of doped ZnO was carried out under the same growth conditions at 300 nm (chapter 5).

Bibliography

- [1] M. C. Tseng, D. S. Wu, C. L. Chen, H. Y. Lee, C. Y. Chien, P. L. Liu, R. H. Horng, *Appl. Surf. Sci.*, **491**, 535-543, (2019)
- [2] Z. Zhaochun, H. Baibiao, Y. Yongqin, C. Deliang, *Mater. Sci. Eng*, **B86**, 109-112, (2001)
- [3] D. J. Lee, H. M. Kim, J. Y. Kwon, H. Choi, S. H. Kim, K. B. Kim, *Adv. Funct. Mater.*, **21**, 448-455, (2011)
- [4] J. M. Jensen, A. B. Oelkers, R. Toivola, D. C. Johnson, J. W. Elam, S. M. George, *Chem Mater.*, **14**, 2276-2282, (2002)
- [5] P. Banerjee, W. J. Lee, K. R. Bae, S. B. Lee, G. W. Rubloff, *J. Appl. Phys.*, 108(4), 043504, (2010)
- [6] J. A. Hamilton, Chemical vapour deposition of zinc oxide and doped ZnO thin films, (Published doctoral dissertation), University College Cork, Ireland, (2012)
- [7] J. L. van Hemmen, S. B. S. Heil, J. H. Klootwijk, F. Roozeboom, C. J. Hodson, M. C. M. van de Sanden, W. M. M. Kessels, *J. Electrochem. Soc.*, 154 (7) G165-G169 (2007)
- [8] J. W. Elam, S. M. George, *Chem. Mater.*, 15, 1020-1028, (2003)
- [9] SPI Supplies. (2020) Available at: <https://www.2spi.com/ito-tech-data/> [ONLINE]. Accessed on 04/01/2020
- [10] K. Kukli, M. Ritala, J. Lu, A. Hårsta, M. Leskelä, *J. Electrochem. Soc.*, 151, F189-193, (2004)
- [11] B. A. Sperling, J. Hoang, W. A. kimes, J. E. Maslar, K. L. Steffens, N. V. Nguyen, *J. Vac. Sci. Technol. A: Vacuum, Surface and Films*, 32, 031513, (2014)
- [12] K. M. Gad, D. Vössing, A. Richter, B. Rayner, L. M. Reindl, S. E. Mohny, M. Kasemann, *IEEE J. Photovoltaics*, 6, 649-653, (2016)[29] K. Kukli, M. Ritala, T. Sajavaara, J. Keinonen, M. Leskelä, *Chem. Vap. Dep.*, 8, 199-204, (2002)

- [13] A. Wojcik, M. Godlewski, E. Guziewicz, R. Minikaev, W. Paszkowicz, *Jour. Cryst. Growth*, 310, 284-289, (2008)
- [14] S. Y. Pung, K. L. Choy, X. Hou, C. Shan, *Nanotech.*, 19(43), 435609, (2008)
- [15] D. Kim, H. Kang, J.M. Kim, H. Kim, *Appl. Surf. Sci.*, 257, 3776-3779, (2011)
- [16] Z. Wan, W. S. Kwack, W. J. Lee, S. I. Jang, J. W. Kim, K. W. Jung, W. J. Min, K. S. Yu, S. H. Park, E. Y. Yun, *Mater. Research Bull.*, 57, 23-28, (2014)
- [17] Z.-Y. Ye, H.-L. Lio, Y. Geng, Y.-Z. Gu, Z.-Y. Xie, Y. Zhng, Q.-Q. Sun, S.-J. Ding, D. W. Zhang, *Nanoscale Research Lett.*, 8, 108, (2013).
- [18] T. Minami, H. Sato, H. Nanto, S. Takata, *Jap. J. Appl. Phys.*, 24(10), 781-784, (1985)
- [19] J.-H. Lee, K.-H. Ko, B.-O. Park, *J. Crystal Growth*, 247, 119-125, (2003)
- [20] S. Bandyopadhyay, G. K. Paul, R. Roy, S. K. Sen, S. Sen, *Mater. Chem. Phys.*, 74, 83-91, (2002)
- [21] H. M. Zhou, D. Q. Yu, L. R. Xiao, J. Li, *Thin Solid Films*, 515, 6909-6914, (2007)
- [22] A. Yamada, S. Sang, M. Konagai, *Appl. Surf. Sci.*, 112, 216-222, (1997)
- [23] E. B. Yousfi, J. Fouache, D. Lincot, *Appl. Surf. Sci.*, 153, 223-234, (2000)
- [24] Y. Wu, P. M. Hermkens, B. W. H. van de Loo, H. C. M. Knoops, S. E Potts, M. A. Verheijen, F. Roozeboom, W. M. M. Kessels, *J. Appl. Phys.*, 114, 024308, (2013)
- [25] K. H. Kim, K. C. Park, D. Y. Ma, *J. Appl. Phys.*, 81, 7764, (1997)
- [26] Y. Igasaki, H. Saito, *J. Appl. Phys.*, 69, 2190, (1991)
- [27] F. R. Blom, F. C. M. Van de Pol, G. Bauhuis, Th. J. A. Popma, *Thin Solid Films*, 204, 365-376, (1991)
- [28] T. Minami, H. Sato, S. Takata, *Appl. Phys. Lett.*, 41, 958, (1982)
- [29] H. Nanto, T. Minami, S. Shooji, S. Takata, *J. Appl. Phys.*, 55, 1029, (1984)

Chapter 5: Optimisation of Transparent Conducting Oxide Layer for Incorporation into Perovskite Solar Cells

5.1 Experimental Details

5.1.1 ALD of ZnO and Doped ZnO: Picosun R200

Nominally undoped ZnO and 19:1 Al, Hf, Ti doped films were deposited by ALD using the Picosun R200 via the methodology detailed in Chapter 4. Growth was performed onto Corning glass microscope slides, quartz and Si(001) at 200°C for 1500 ALD cycles (nominally 300 nm). All glass slides and quartz substrates underwent a cleaning treatment of Decon 90, acetone and IPA prior to growth. P-type Si samples were cleaned using N₂ gas prior to oxide deposition as the samples were freshly fabricated. As the growth rates of Al₂O₃, TiO₂ and HfO₂ differ and are lower than that of ZnO the total thickness of the films after incorporation of the dopants would be variable as would the absolute concentrations. However, as with laminating doping it is often the vertical spacing of doping atoms that are significant the pulse ratio was maintained at 19:1 with no compensation for doping growth rates. The deposition parameters for each of the grown thin films are outlined in Table 5.1 below.

DEZ Pulse Time (s)	H ₂ O Pulse Time (s)	TMA Pulse Time (s)	TDMAT Pulse Time (s)	TEMAH Pulse Time (s)	Purge Time (s)	Deposition Temp (°C)
0.05	0.1	0.1	1.6	1.6	6.0	200

Table 5.1: Growth parameters of ZnO and doped ZnO thin films deposited at 200°C using a Picosun R200

5.2 Results

5.2.1 Surface Morphology

SEM images of ZnO and doped ZnO grown on both glass substrates and Si(001) are presented in figure 5.1. All films exhibited grains typical of polycrystalline films.

Figure 5.1 (a) Sample S, as-grown ZnO, revealed large grain sizes of 80 nm in length scattered across the surface. The cross-sectional SEM image of the film displayed a highly ordered film with columnar features in the bulk. Doping ZnO changes the microstructure of the films and causes the grains to increase in size. SEM of TZO exhibited similar features to those seen in AZO and HZO with large columnar grains evident on the surface. However, spherical features are also visible amongst the cylindrical features which are not seen on the surface of the other thin films. These features are similar to those seen in ZnO nanoparticles deposited by sol-gel or electrodeposition.^{1,2}

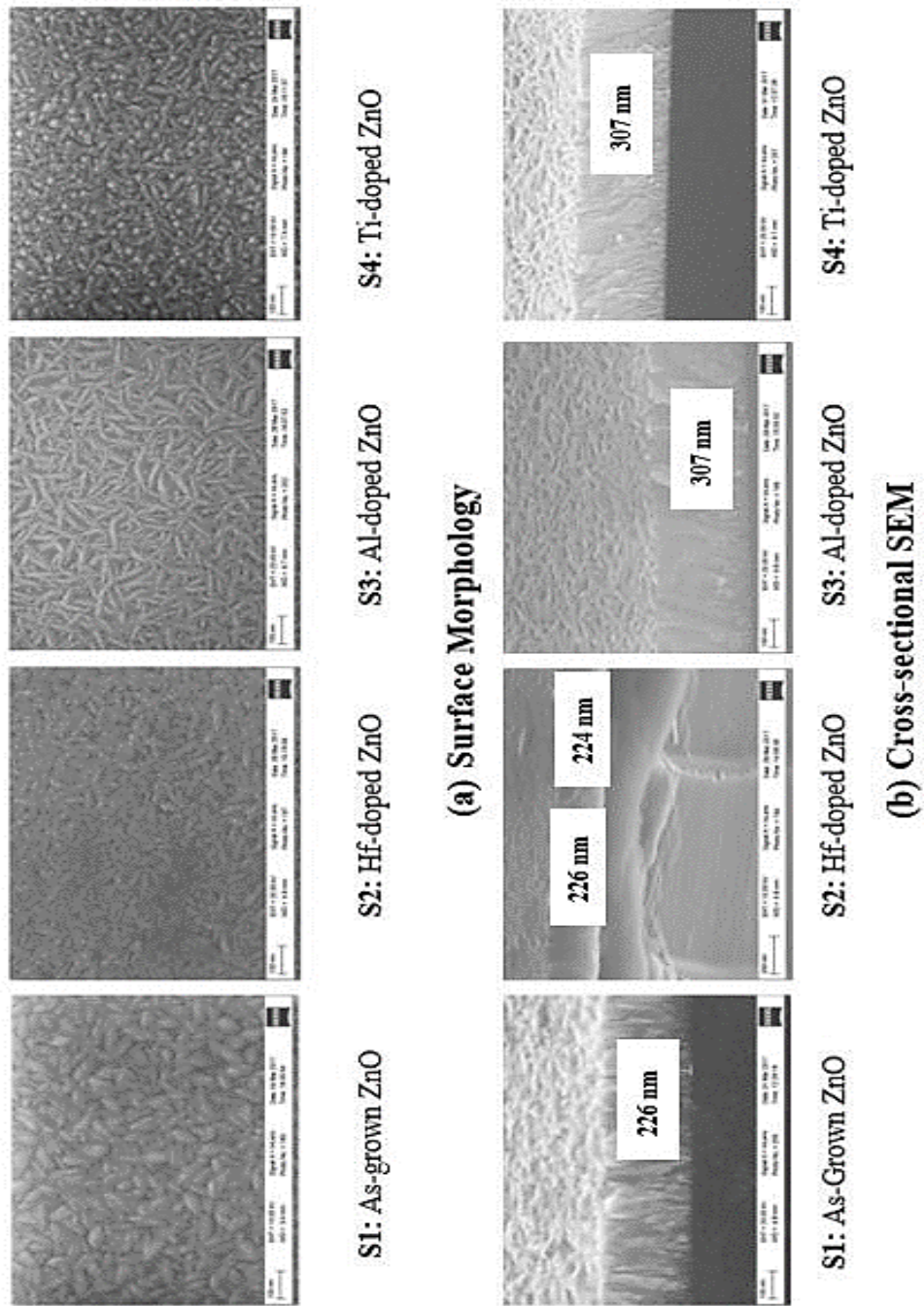


Figure 5.1: Shows images of (a) Surface SEM of ZnO and doped ZnO (Hf, Al and Ti) films on glass and (b) cross-sectional SEM of ZnO and doped ZnO (Hf, Al and Ti) films on Si(001)

The cross-sectional SEM represented by figure 5.1 (b) displays signs of a densely packed film with little sign of individual features. Based on a growth per cycle of 0.2 nm/cycle 1500 ALD cycles should deposit 300 nm of ZnO and doped ZnO. However, the cross-sectional SEM shows that there are discrepancies between the nominal thickness values and those observed. It is evident that there are nucleation delays when depositing the ZnO on the glass/Si(001) substrate and both delays and enhancements in growth on the doping layers. This variability in thickness underlines the need to consider sheet resistance values as opposed to resistivity.

5.2.2 X-ray Diffraction

Figure 5.2 show XRD patterns of (a) ZnO, (b) AZO, (c) HZO and (d) TZO. It is evident that all films are polycrystalline with a preferred orientation of [100]. Figure 5.2 (d) shows the TZO film where the (002) peak is of greater intensity than that seen in the as-grown ZnO and other doped ZnO films. In contrast to XRD patterns of the same materials at 200 nm explained in chapter 5, where the peak at 38° attributed to the [101] orientation was only evident in the TZO film at 200 nm, once the films had increased to 300 nm the (101) peak is now evident at the same position in each of the film doped or not. Similar to the patterns outlined in figure 5.2 AZO remained devoid of the (002) peak usually positioned at 34.4° .

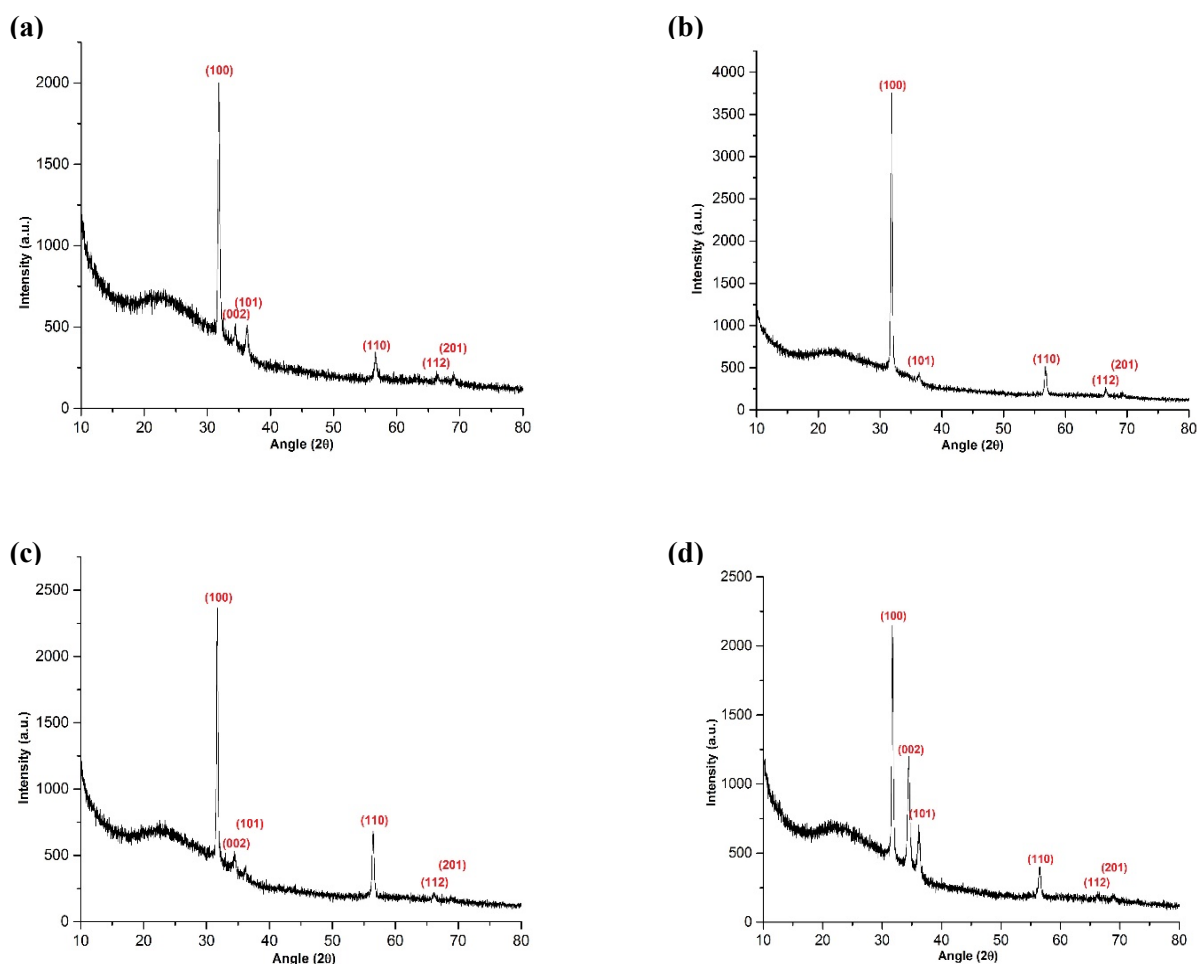


Figure 5.2: XRD patterns of 300 nm of (a) ZnO, (b) AZO (19:1), (c) HZO, (d) TZO (19:1) deposited by thermal ALD at 200°C

5.2.3 Optical Properties

It is established that TCOs in solar cells must have good optical transparency in order to allow light efficiently into the cell to be absorbed. Percentage transmission data is presented in figure 5.3. It was observed that all films were optically transparent in the UV/visible (400-600 nm) and near IR ranges with values in excess of 70%. HZO and TZO exhibited the highest percentage of transmission. The large decrease in transparency or absorption edge observed around 380 nm is characteristic of direct

band gap materials such as zinc oxide and can be exacerbated by the absorption spectrum exhibited by the glass substrate.

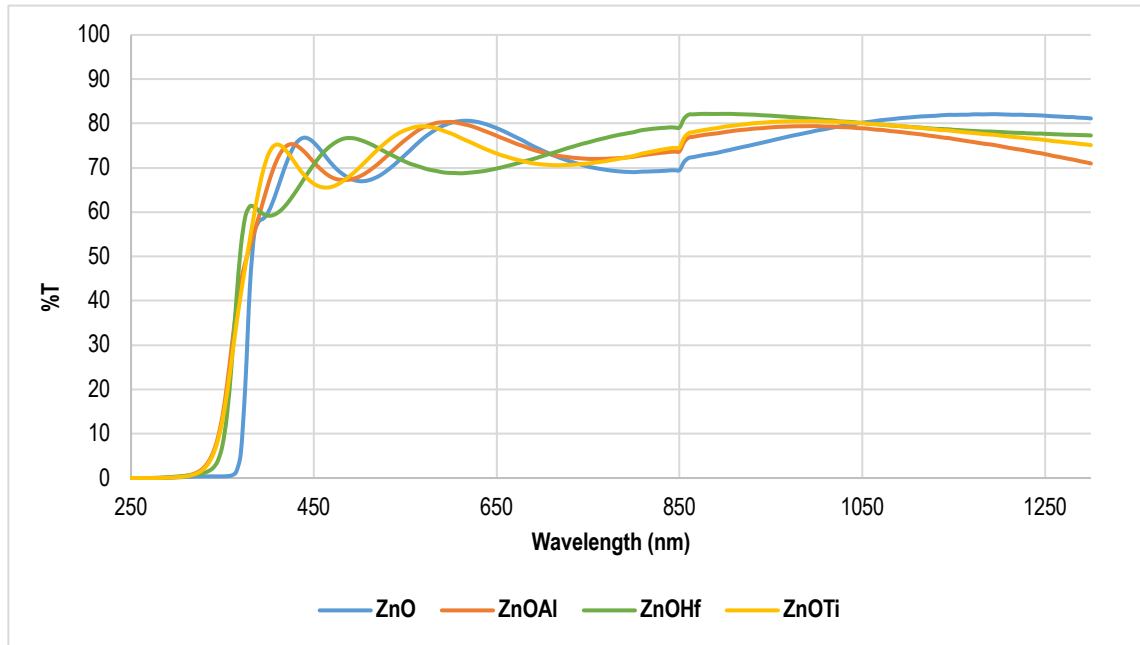


Figure 5.3: % transmission from UV/visible spectroscopy shows the optical properties of 300 nm (nominal) ZnO, AZO, HZO and TZO on glass

5.2.4 Electrical Properties

The electrical properties of the films were obtained using a Hall Effect measurement system as outlined in section 3.2.4 and are illustrated in Table 5.2. An ideal TCO would exhibit properties of high Hall mobility and low sheet resistance. As-grown ZnO films exhibited a high Hall mobility of 23 cm²/Vs and a sheet resistance of 230 Ω/□. As explained in chapter 4, obtaining a film that showed a sufficiently high Hall mobility while maintaining a sheet resistance similar to commercially available ITO and FTO was difficult. As a result, a compromise between Hall mobility and sheet resistance was required to determine the thin film closest to ideal.

Chapter 4 details that there is often a correlation between a films microstructure and its corresponding electrical properties. Films that are densely packed often exhibit high mobility values, however, when surface features are present, grain boundaries

formed can also reduce the electrical conductivity of the films resulting in the trade-off between Hall mobility and conductivity.

Film Description	Mobility (cm²/Vs)	Carrier Conc. (1/cm³)	Sheet Resistance (Ω/□)
S1 (ZnO)	23	3.7 x 10 ¹⁹	230
S2 (HZO)	15.4	1.6 x 10 ²⁰	60
S3 (AZO)	9.6	4.8 x 10 ²⁰	44.5
S4 (TZO)	12.7	2.9 x 10 ²⁰	41

Table 5.2: Electrical properties of ZnO and doped ZnO of 300 nm thickness

Increasing the thickness of the films by 100 nm saw a further reduction in the sheet resistance of the films. HZO exhibited the highest mobility of 15 cm²/Vs second only to as-deposited ZnO. Interestingly, the sheet resistance of HZO did not reduce further when the thickness was increased to 300 nm from 200 nm where it exhibited a sheet resistance of 59.6 Ω/□. Instead, a sheet resistance of 60 Ω/□ was obtained at 300 nm.

Where at 200 nm the sheet resistance of the HZO film was far lower than that of AZO and TZO at 300 nm AZO and TZO exhibited almost equally low sheet resistance values of 44.5 and 41 Ω/□ respectively. AZO produced a lower Hall mobility value than that of TZO of 9.6 cm²/Vs for AZO compared with 12.7 cm²/Vs for TZO. Thus TZO displayed properties closest to the commercially available ITO exhibiting low sheet resistance and good Hall mobility.

19:1 dopant ratio ZnO:dopant was chosen for this study based on previous work carried out on ZnO and literature, where 19:1 ratio produced films with the best electrical characteristics for AZO.³⁻⁷

To confirm that this dopant concentration is optimum for other dopant materials, the TZO Ti concentrations of 0.85 atomic %, 1.3 atomic % and 2.7 atomic %, calculated

based on formula outlined in equation 5.1, below representing 29:1, 19:1 and 9:1 respectively, were deposited at 200°C.

The 19:1 ZnO to dopant ratio used up to this point in the study were selected to correspond to the optimal dopant/laminate spacing observed in the literature for AZO.¹⁵ However, here it was observed that the other dopants employed (Hf and Ti) were electrically more promising as a consequence this doping ratio needs to be confirmed for these growth systems. With this in mind Ti doping ratios in ZnO were varied.

Note for these studies the Cambridge Nanotech Fiji 200LLC was employed due to maintenance issues with the Picosun R200. Although the growth recipes were similar and conditions aligned it should be acknowledged that absolute film properties will differ between reactors and hence this study is only valid in determining the optimal doping ratio and direct comparisons between samples from the two reactors should not be made.

TZO was deposited under the same conditions as outlined in section 5.1.1. In order to facilitate a good comparison study, the temperature was maintained at 200°C and the thickness of all samples was nominally 180 nm where 900 ALD cycles were used. The Ti concentrations, or more correctly pulse ratios, chosen were 9:1, 19:1 and 29:1. The growth parameters for the Cambridge Nanotech Fiji 200LLC are outlined in Table 5.3.

Substrate	No. of Cycle	Dopant ratio	DEZ Pulse Time (s)	H ₂ O Pulse Time (s)	TDMAT Pulse Time (s)	Purge Time (s)
Glass/p-Si	900	9:1	0.1	0.05	0.4	20.0
Glass/p-Si	900	19:1	0.1	0.05	0.4	20.0
Glass/p-Si	900	29:1	0.1	0.05	0.4	20.0

Table 5.3: Growth parameters for TZO at 200°C for Cambridge Nanotech Fiji

A variety of different equations have been used for calculating the atomic % however eqn. 5.1 was used for this comparison study.^{8,9} As mentioned in section 4.3, due to the laminate deposition methods used to deposit the thin films, all dopant concentration values reported in this study are based on nominal values calculated using the ALD cycle ratios. For the purpose of this study 180 nm of each film was deposited and the electrical properties were measured in the same way as for Table 5.3. See section 5.2.4 for more experimental details.

$$\frac{[Ti_{GPC}]}{[(Ti_{GPC})\text{No. of atoms of Ti} + (Zn_{GPC})\text{No. of atoms of Zn}]} \times 100 \quad 5.1^{4,10}$$

Table 5.4 shows the electrical properties of ZnO doped with 2.7 atomic %, 1.3 atomic % and 0.85 atomic % Ti concentrations at 180 nm. It is evident from the table that 1.3 atomic % gave the lowest sheet resistance value of 99.1 Ω/\square and the highest Hall mobility value of 16.4 cm^2/Vs . This implies that Ti concentration of 1.3 atomic % is the optimum at which to deposit TZO for use as a TCO.

Ti Conc. (ZnO:TiO₂)	Mobility (cm²/Vs)	Carrier Conc. (1/cm³)	Sheet Resistance (Ω/\square)
9:1 (2.7%)	6.78	1.71 x 10 ²⁰	297.9
19:1 (1.3%)	16.4	2.13 x 10 ²⁰	99.1
29:1 (0.85%)	14.0	1.59 x 10 ²⁰	155.6

Table 5.4: Electrical properties of TZO deposited by ALD with H₂O at 200°C for 900 ALD cycles (180 nm nominal) at a range of Ti concentrations

5.3 Discussion

The electrical data presented in table 5.2 shows that TZO is the best candidate for a replacement TCO for ITO/FTO in perovskite solar cells. The sheet resistance value, $41 \Omega/\square$ is within the sheet resistance range of commercially available ITO ($8\text{-}100 \Omega/\square$). It is low enough to allow current to flow freely throughout the film while still maintaining a sufficiently high Hall mobility value of $12.7 \text{ cm}^2/\text{Vs}$. It has been accepted that there is a link between the microstructure of the material and good optical and electrical properties¹¹. Polycrystalline materials have been known to produce low sheet resistance values. Similarly, as the density of the film increases a relative increase in electron mobility through the film is observed. Grain size can also influence the electrical properties. Large grains on the surface of the film can promote the movement of electrons as they can overlap each other. However, grain boundaries often form around these large features causing charge trapping and thus causing an increase in the sheet resistance¹²⁻¹⁴

As-deposited ZnO has a high mobility value of $23 \text{ cm}^2/\text{Vs}$, while its corresponding sheet resistance was also very high at $230 \Omega/\square$. This feature of high Hall mobility and high sheet resistance could be attributed to the large grains evident on the surface of the films observed in the SEM images in figure 5.1. In general, it has been shown that as the grain size of the material increases so too does the Hall mobility¹¹. SEM images of TZO revealed that the grain size was much smaller than that of ZnO and also displayed spherical features similar to those of ZnO nanoparticles¹⁻³.

Optical spectroscopy revealed that the HZO was the most optically transparent material in the near IR and TZO had the highest % transmission in the UV/visible region (figure 5.3). Although HZO exhibited good optical properties, in order for the materials to become a potential candidate for a TCO in perovskite solar cells it would require a massive improvement in the electrical properties.

As shown in chapter 4, there was a distinct trend where increasing the thickness of the film improved the electrical conductivity of the films. If HZO was deposited thicker it is possible this could improve the electrical properties of the material,

however HfO_2 is normally deposited between 200-350°C in order to deposit uniform, conformal thin films.¹⁵⁻¹⁸ Depositing the material at 200°C is depositing it at the lower end of the ALD window. As seen in section 5.2.1 a significant nucleation delay was observed causing the discrepancy of thicknesses between the materials. It was concluded that the nucleation delay was caused by the deposition temperature being at the lower limit for this precursor. For a transparent conducting oxide to be viable for a perovskite solar cell and tandem solar cell the material needs to be deposited at low temperatures (>200°C). As deposition of HfO_2 at 200°C already results in a nucleation delay depositing the same material at even lower temperatures was concluded as being outside the means of the Hf precursors. As a result, the remainder of this study focuses on TZO as the next most viable material.

Having determined that Ti was the best performing dopant used in this study the optimum concentration of dopant was explored. As outlined in Table 5.4 Ti concentration to produce a film with a 19:1 ratio does produce the best electrical properties which are sufficient to enable the replacement of ITO in perovskite solar cells. This observation is supported by the literature where a Ti concentration, to produce low sheet resistance values, 1.3 atomic % (19:1 ratio).³⁻⁷ 180 nm TZO deposited using at 0.85 atomic % Ti concentration produced a film with a Hall mobility value of 14.0 cm^2/Vs similar to the value 16.1 cm^2/Vs obtained from the film with 1.3 atomic % Ti concentration of the same thickness. However, the sheet resistance value of TZO film with 1.3 atomic % Ti concentration was 99.1 Ω/\square significantly lower than that of 0.85 atomic % Ti concentration with a value of 155.6 Ω/\square . The lower Ti concentration could not compete with the 1.3 atomic % Ti. When the film thickness is increased from 180 nm to 300 nm it is clear that the optimum thin film was obtained was ZnO deposited by thermal ALD at 200°C using a 1.3 atomic % Ti concentration (19:1 ratio).

5.4 Conclusion

ZnO was deposited by ALD at 200°C and subsequently doped with Hf, Al and Ti. The electrical and optical properties were investigated to determine which dopant material would be the most suitable candidate for TCO in perovskite solar cells to replace the expensive ITO. The presented results revealed that TZO was the most suitable TCO candidate with a sheet resistance value of $41 \Omega/\square$ and Hall mobility of $12.8 \text{ cm}^2/\text{Vs}$. In addition to promising electrical properties, TZO also exhibited high optical transparency of >80% in the UV/ visible and IR ranges. A further study was carried out to confirm which Ti concentration was the optimum, producing the best quality electrical properties. Doped ZnO with a 19:1 ZnO:dopant ratio (1.3 atomic %) was observed to exhibit the best electrical properties at 200°C. The properties of this as grown material were shown to be sufficient to be a viable alternative to ITO for the TCO layers in perovskite solar cells.

Bibliography

- [1] M. Copuroglu, L. H. Kelly Koh, S. O'Brien, G. M. Crean, *J. Sol-Gel Sci. Technol.*, **52**, 432-438, (2009)
- [2] L. Xu, Y. Guo, Q. Liao, J. Zhang, D. Xu, *J. Phys. Chem. B.*, **109**, 13519-13522, (2005)
- [3] X. Qian, Y. Cao, B. Guo, H. Zhai, A. Li, *Chem Vap Deposition*, **19**, 180-185, (2013)
- [4] D. J. Lee, H. M. Kim, J. Y. Kwon, H. Choi, S. H. Kim, K. B. Kim, *Adv. Funct. Mater.*, **21**, 448-455, (2011)
- [5] J. H. Lee, J. W. Lee, S. H. Wang, S. Y. Kim, H. K. Cho, J. Y. Lee, J. S. Park, *J. Nanoscale Nanotechnol.*, **12**, 5598, (2012)
- [6] T. Dhakal, D. Vanhart, R. Christian, A. Nandur, A. Sharma, C. R. Westgate, *J. Vac. Sci. Technol.*, **A 30**, 021202, (1998)
- [7] J. S. Na, Q. Peng, G. Scarel, G. N. Parsons, *Chem. Mater.*, **21**, 5585-5593, (2009)
- [8] P. Banerjee, W. J. Lee, K. R. Bae, S. B. Lee, G. W. Rubloff, *J. Appl. Phys.*, **108**, 043504, (2010)
- [9] Y. Wu, P. M. Hermkens, B. W. H. van de Loo, H. C. M. Knoop, S. E. Potts, M. A. Verheijen, F. Roozeboom, W. H. H. Kessels, *J. Appl. Phys.*, **114**, 024308, (2010)
- [10] J. W. Elam, D. Routkevitch, S. M. George, *J. Electrochem. Society*, **150**, G339-347, (2003)
- [11] S. Calnan, A. N. Tiwari, *Thin Solid Films*, **518**, 1839-1849, (2010)
- [12] N. P. Dasgupta, S. Neubert, W. Lee, O. Trejo, J. R. Lee, F. B. Prinz, *Chem Mater.*, **22**, 4769-4775, (2010)
- [13] H. M. Zhou, D. Q. Yu, L. R. Xiao, J. Li, *Thin Solid Films*, **515**, 6909-6914, (2007)
- [14] T. Minami, *Semiconduct. Sci. and Technol.*, **20**, S35, (2005)
- [15] Y. Wu, A. Devin Giddings, M. A. Verheijen, B. Macco, T. J. Prosa, D. J. Larson, F. Roozeboom, W. M. M. Kessels, *Chem. Mater.*, **30**, 1209-1217, (2018)

- [15] K. Kukli, M. Ritala, T. Sajavaara, J. Keinonen, M. Leskelä, Chem. Vap. Dep., 8, 199-204, (2002)
- [16] K. Kukli, M. Ritala, J. Lu, A. Hårsta, M. Leskelä, J. Electrochem. Soc., 151, F189-193, (2004)
- [17] J. Niinistö, M. Putkonen, L. Niinistö, S. L. Stoll, K. Kukli, T. Sajavaara, M. Ritala, M. Leskelä, J. Mater. Chem., 15, 2271-2275, (2005)
- [18] D. M. Hausmann, E. Kim, J. Becker, R. G. Gordon, Chem. Mater., 14, 4350-4358, (2002)

Chapter 6: Incorporation of Atomic Layer Deposited Ti-doped ZnO into Perovskite Solar Cells

6.1 Experimental Details

Transparent contacts: Planar perovskite solar cells were fabricated in the *p-i-n* configuration. Presented in this chapter are perovskite solar cells with atomic layer deposition TZO on glass substrates, these are compared with commercially bought ITO/glass substrate (Kinetic 12.4 Ω/\square). A Cambridge NanoTech Fiji F200 LLC ALD reactor was utilised for the growth of the TZO films. Growth was achieved using diethylzinc (DEZ) and H₂O in an argon carrier gas flow system as the metal precursor and oxygen sources respectively. Tetrakis(dimethylamido) titanium (TDMAT), with a growth rate of ~ 0.05 nm/cycle^{1,2} and Titanium tetraisopropoxide (TTIP), with a growth rate of ~ 0.02 nm/cycle^{3,4}, were used to dope the ZnO material in a 19:1 ratio (ZnO:TiO₂) for 1500 cycles. The Ti precursors were obtained from STREM Chemicals Inc. and the Zn precursor from Sigma Aldrich (Merck). TZO was deposited on Corning® glass microscope slides (0.9-1.10 mm thick) at 200°C and cut into 25 x 25mm samples. TDMAT was heated to 110°C while the DEZ and H₂O were held at room temperature.

As in the previous chapters, all glass substrates were ultra-sonicated in Decon-90, acetone and IPA thoroughly. The deposition routines for TDMAT and TTIP doping are outlined in Tables 6.1 and 6.2 below.

	Instruction	#	Value	Unit	Description
0	<i>wait</i>		3600	s	Substrate stabilisation time
1	<i>flow</i>	0	40	sccm	Carrier gas flow ON
2	<i>flow</i>	1	180	sccm	Plasma unit flow ON
3	<i>wait</i>		1	s	-
4	<i>pulse</i>	2	0.1	s	DEZ pulse time
5	<i>wait</i>		20	s	Purge time
6	<i>pulse</i>	5	0.05	s	H ₂ O pulse time

7	<i>wait</i>		19	s	Purge time
8	<i>go to</i>	4	10		Cycles until desired concentration has been reached
9	<i>wait</i>		1	s	-
10	<i>pulse</i>	0	0.5	s	TDMAT pulse time
11	<i>wait</i>		20	s	Purge time
12	<i>pulse</i>	5	0.05	s	H ₂ O pulse time
13	<i>Wait</i>		20	s	Purge time
14	<i>pulse</i>	2	0.1	s	DEZ pulse time
15	<i>wait</i>		20	s	Purge time
16	<i>Go to</i>	14	9		Cycle until desired concentration has been reached
17	<i>Go to</i>	4	-		Super cycle until desired thickness has been reached

Table 6.1: Outlines the experimental parameters used to deposit TZO (19:1 ZnO:TiO₂) using a Cambridge Nanotech Fiji F200LLC system using TDMAT as Ti precursor

	Instruction	#	Value	Unit	Description
0	<i>wait</i>		1	s	Substrate stabilisation time
1	<i>flow</i>	0	20	sccm	Carrier gas flow ON
2	<i>flow</i>	1	200	sccm	Plasma unit flow ON
3	<i>MFC Valve</i>	3	1	-	MFC Valve open. O ₂ flowing
4	<i>wait</i>		10	s	-
5	<i>wait</i>		2	s	-
6	<i>pulse</i>	2	0.05	s	DEZ pulse time
7	<i>wait</i>		20	s	Purge time
8	<i>pulse</i>	5	0.05	s	H ₂ O pulse time
9	<i>wait</i>		18	s	Purge time
10	<i>go to</i>	5	10	-	Cycles until desired concentration has been reached
11	<i>wait</i>		20	s	-
12	<i>pulse</i>	3	0.4	s	TTIP pulse time
13	<i>wait</i>		10	s	Purge time
14	<i>plasma</i>		300	W	Plasma powered on

15	<i>wait</i>		5		
16	<i>flow</i>	3	10	sccm	Oxygen gas flow ON
17	<i>wait</i>		4	s	Stablisation time
18	<i>Flow</i>	3	11	sccm	Oxygen gas flow ON
19	<i>wait</i>		2	sccm	
20	<i>flow</i>	3	12	sccm	Oxygen gas flow ON
21	<i>wait</i>		2	s	
22	<i>flow</i>	3	13	sccm	Oxygen gas flow ON
23	<i>wait</i>		2	s	
24	<i>flow</i>	3	14	sccm	Oxygen gas flow ON
25	<i>wait</i>		2	s	
26	<i>flow</i>	3	15	sccm	Oxygen gas flow ON
27	<i>wait</i>		20	s	
28	<i>flow</i>	3	0	sccm	Oxygen gas stopped flowing
29	<i>wait</i>		2	s	
30	<i>plasma</i>		0	W	Plasma powered off
31	<i>wait</i>		10	s	
32	<i>wait</i>		2	s	
33	<i>pulse</i>	2	0.05	s	DEZ pulse time
34	<i>wait</i>		10	s	Purge time
35	<i>pulse</i>	5	0.05	s	DEZ pulse time
36	<i>wait</i>		10	s	Purge time
37	<i>go to</i>	32	9	-	Cycle until desired concentration has been reached
38	<i>wait</i>		20	s	
39	<i>goto</i>	5	45	-	Super cycle until desired thickness has been reached

Table 6.2: Outlines the experimental parameters used to deposit TZO (19:1 ZnO:TiO₂) using a Cambridge Nanotech Fiji F200LLC system using TTIP as Ti Precursor

Post-deposition, in order to form electrode patterns the TZO substrates were laser ablated. The isolation of a TCO contact is achieved through the formation of a discontinuity in the TCO layer more commonly known as a P1 line. The P1 line was etched 5 mm from the edge of each 25 mm² samples using an UV ArF excimer laser

(193 nm Lasertechnik ATLEX 300i). At EPFL, a similar P1 line pattern was etched into the ITO coated glass substrates. A P2 line equivalent was then formed on the edge of the sample using Kapton tape opposite to the laser etched P1 line after the deposition of the active medium and prior to the formation of the hole transport material (see figure 6.1 for diagram of P1 and Kapton masking).

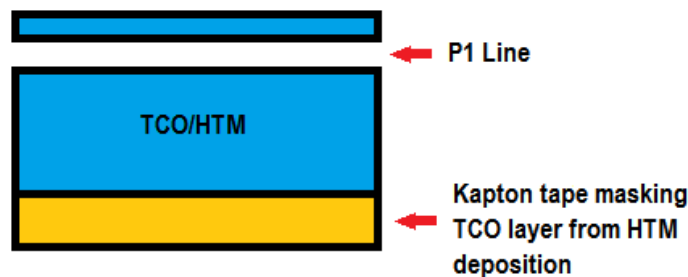


Figure 6.1: Schematic of the P1 line and Kapton masking of TZO or ITO in the fabrication of perovskite solar cells

Cell fabrication: At CSEM, a 20 nm layer of the hole selective material NiO was deposited by RF sputtering (ClusterLine 200 II from Evatec) on top of the ITO or Ti-doped ZnO substrate. The perovskite material was deposited on top of the NiO by a two-step process. Lead iodide (PbI_2) and cesium bromide (CsBr) were co-evaporated using a Kurt J. Lesker Minispectros evaporation machine at a base pressure of 1.5×10^{-5} Torr. A solution of FAI (formamidinium iodide) and FABr (formamidinium bromide) in ethanol was then spin-coated onto the PbI_2/CsBr layer at 4000 rpm for 33 seconds. The organohalide solution infiltrates the porous PbI_2/CsBr scaffold and the excess solution was ejected off during spin-coating. The $\text{Cs}_x\text{FA}_{1-x}\text{Pb}(\text{Br},\text{I})_3$ was then crystallised by annealing at 150°C in ambient air for 30 mins. C_{60} (19 nm) and electron selective layer TmPyPB (3 nm) were deposited subsequently using a home-built evaporation system at a rate of 0.04 nm/s and 0.02 nm/s respectively without breaking vacuum. The devices were completed by depositing 140 nm Ag using the home-built evaporation system at a deposition rate of 0.1 nm/s.⁵

Characterisation: Hall mobility and sheet resistance values of ITO and TZO were measured using a LakeShore Model 8404 AC/DC Hall Effect Measurement System. The crystalline orientation of the materials were obtained by x-ray diffraction (XRD) using a Phillips (PW3719) X'pert x-ray diffractometer with Cu K α radiation ($\lambda = 0.154056$ nm). The morphologies and thicknesses of the materials were examined using scanning electron microscopy (SEM, FEI Quanta FEG 650) and transmission electron spectroscopy (cross-section preparation, FEI Helios Nanolab; TEM, JEOL 2100). Optical analysis (UV-Vis-NIR) of the thin films were carried out using a Perkin Elmer Lambda 950 spectrometer. Performance of the fabricated perovskite cells was determined using a two-lamp class AAA WACOM sun simulator with an AM 1.5 G irradiance spectrum at 1000 W cm^{-2} . The cells active area of 0.25 cm^2 was defined using a metal mask. The J-V characteristics of the cells were obtained under reverse (V_{oc} to J_{sc}) and forward (J_{sc} to V_{oc}) conditions in order to extract the power conversion efficiency

6.2 Results and Discussion

The conductivity of the TZO was found to be dependent on the dopant precursor. Films grown with TTIP as the dopant precursor were found to be less conducting than those that used TDMAT (see Table 6.3). It is likely that the more reactive nature of TDMAT, as compared to TTIP, is key to this difference. Highly reactive precursors can improve the coverage and uniformity of the films by more efficiently filling reactive sites and removing residual ligands, thus promoting better conductivity. As a consequence of the better electrical performance it was decided that TDMAT and H₂O would be used as Ti doping precursor and co-reactant respectively for this study.

Dopant Precursor	Hall Mobility (cm²/Vs)	Carrier Concentration (1/cm³)	Sheet Resistance (Ω/□)
TTIP	0.914	2.11 x 10 ¹⁹	17905.0
TDMAT	16.4	2.30 x 10 ²⁰	99.1

Table 6.3: Electrical properties of 180 nm ALD-grown TZO deposited at 200°C using a ZnO:TiO₂ ratio 19:1

At 200°C ALD-grown TZO using TDMAT was found to be polycrystalline with a dominant orientation in the (100) direction (figure 6.2(a)). Plan view SEM of TZO shown in figure 6.2(b) shows evidence of large grains characteristic of crystalline films (explained in further detail in section 5.2.1.). The TEM image (figure 6.2(c)) of TZO deposited by 1500 ALD cycles shows the thickness to be 240 nm, less than the theoretical value of 300 nm. This is due to the nucleation delays between the laminates of dopant and matrix material which in turn is probably caused by physisorbed residual dopant ligands as they block growth sites. As a consequence, full monolayer growth of the desired material is not achieved reducing the thickness of the grown film. However, the SEM does provide evidence of plain hole free coverage and excellent uniformity of the thin films. This compares well with the ITO used by CSEM and EPFL in the fabrication of the control PK solar cells.

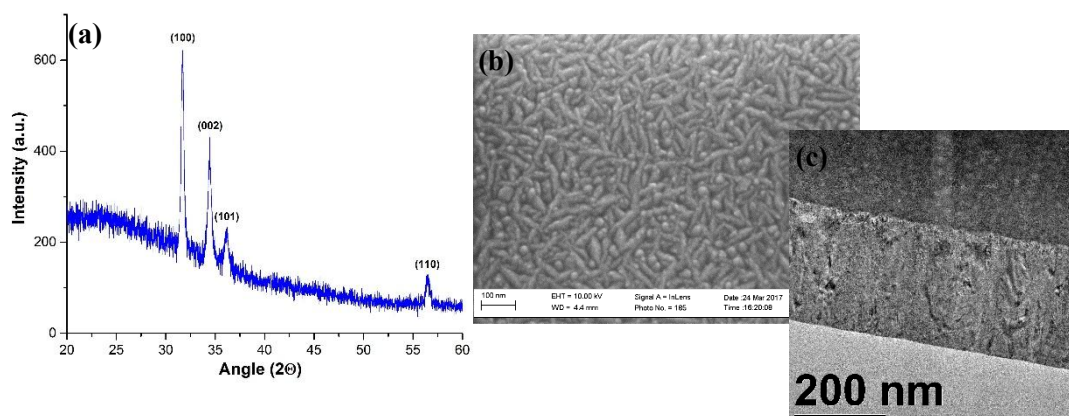


Figure 6.2: (a) XRD diffraction pattern illustrating polycrystalline features, (b) Plan-view SEM of showing surface morphology, (c) TEM image of 240 nm ALD-grown TZO at 200°C confirming its growth rate of 0.185 nm/cycle.

Optical performance of TZO and ITO are illustrated in figure 6.3 where an optical transparency in excess of 75%, for both films across the range 250-1300 nm, is observed. It should be noted that a target transparency of greater than 70% is required for viable transparent electrodes. It is evident that TZO is significantly more transparent than the reference ITO in the near IR region. However, the TZO absorbs more strongly in the UV/visible region than the ITO. This is a positive effect the Ti^{3+} ions have on the ZnO as it allows more light to enter the cell and be absorbed by the perovskite material.

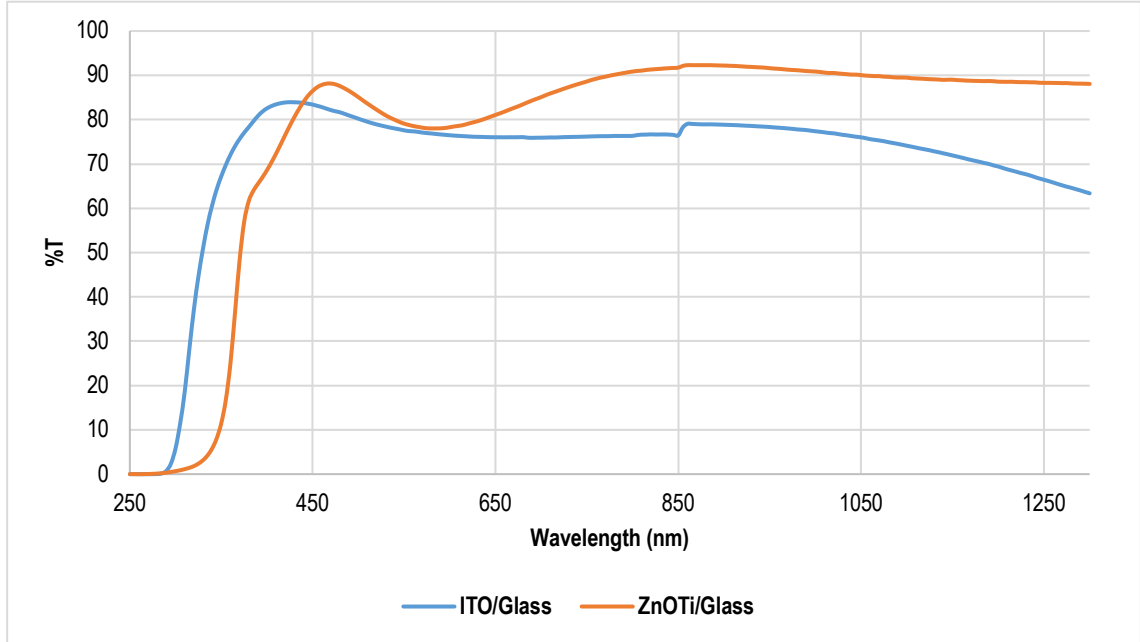


Figure 6.3: Transmission spectrum of TZO (300 nm nominal) deposited by ALD at 200°C (19:1) and ITO deposited on glass obtained from UV/visible spectroscopy

Electrical properties obtained using a Hall measurement system as detailed in section 3.2.4 of TZO and ITO are outlined in Table 6.4.

Sample Description	Hall Mobility (cm ² /Vs)	Carrier Concentration (1/cm ³)	Sheet Resistance (Ω/□)
130 nm ITO/glass substrate	25	1.5 x 10 ²¹	12.4
240 nm TZO/glass substrate	13.2	4.14 x 10 ²⁰	41.1

Table 6.4: Table comparing the electrical properties of ITO and TZO through Hall mobility, carrier concentration and sheet resistance

240 nm of TZO was the chosen thickness for fabrication of the PK solar cells due to its similarities in electrical and optical properties to that of ITO. Previous studies have shown that atomic layer deposited ZnO optimum growth temperature is 200°C

and results in promising electrical and optical properties rivalling ITO. Although TCOs in single junction perovskite solar cells are not limited by temperature, when transferred into tandem solar cells, a thermal budget of $<200^{\circ}\text{C}$ must be implemented in order to prevent degradation of the absorber layers. As a result, a maximum deposition temperature of 200°C was chosen for this study

The solar cells devices represented by figures 6.4(a) and 6.4(b), were composed of ITO or TZO on glass as transparent contacts, sputtered NiO hole transport layer, a $\text{Cs}_x\text{FA}_{1-x}\text{Pb}(\text{Br},\text{I})_3$ perovskite layer⁵, C60 buffer layer, 1,3,5-tri(*m*-pyrid-3-yl-phenyl)benzene, (TmPyPB)⁶ electron transport layer and evaporated Ag as the back electrode.

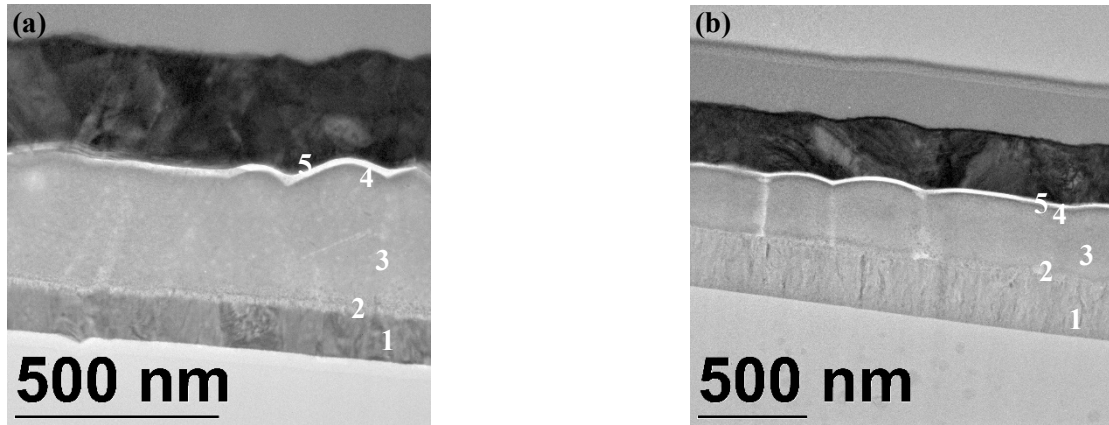


Figure 6.4: TEM images showing solar cell devices (a) Control state-of-the-art PK solar cell using ITO as TCO and (b) test cell using TZO as TCO; made up of a NiO hole transport layer (2a,b), a $\text{Cs}_x\text{FA}_{1-x}\text{Pb}(\text{Br},\text{I})_3$ perovskite layer (3a,b), C60 buffer layer (4a,b), TmPyPB electron transport layer (5a,b) and evaporated Ag as the back electrode and where (a) ITO (1a) acts as the transparent electrode and (b) TZO (1b) acts as the transparent electrode

Two device sets of four samples each were fabricated and electrically tested under a solar simulator. The best performing cells are presented here. Table 6.5 summarises the J-V cell results for each TCO perovskite solar cell system. Figures 6.5 (a) and (b)

show the J-V characteristics comparing the best PSC of the ITO sample set and TZO sample set under no light-soaking and light soaking conditions (where the device is exposed to light for several minutes prior to electrical characterization) and their corresponding external quantum efficiency is represented by figure 6.6.

Device 2, ALD-grown TZO resulted in a V_{oc} , J_{sc} and FF of 1027 mV, 18.03 mA/cm² and 39.01% respectively leading to a PCE of 7.22%. EQE displayed in figure 6.6 gives a current density of 18.54 mA/cm² without a light bias which is higher than what was predicted in the J-V results. When a light bias is applied to the cells the current density is decreased to 18.36 mA/cm² which is closer to the predicted value however still not in agreement with the J-V results. This effect is also exhibited in the device 1 which was fabricated using ITO as the transparent contact.

It is also observed in figure 6.6 that the EQE of ITO in the UV is better than that of TZO. This is expected as the UV cut off of TZO observed in figure 6.2 occurs at a longer wavelength than ITO. J-V curves reported V_{oc} , J_{sc} and FF of 1024 mV, 18.06 mA/cm² and 60.61% for PSC with ITO incorporated. The EQE displays a different value than predicted of 18.34 mA/cm² when no light bias was applied to the samples. When a light bias was implemented a reduction in current density to 18.33 mA/cm² was observed.

Transparent Contact Material	Aperture Area (cm ²)	Scan Direction	V_{oc} (mV)	J_{sc} (mA/cm ²)	FF (%)	Eff (%)
Device 1: ITO	0.25	Reverse	1023.8	18.06	60.61	11.03
		Forward	1062.9	18.03	60.57	11.61
Device 2: TZO	0.25	Reverse	1026.8	18.03	39.01	7.22
		Forward	1021.7	17.92	37.22	6.78

Table 6.5: Summary of IV parameters for p-i-n configured PK solar cells composed of two different transparent contacts. Device 1: Commercially bought ITO coated glass, Device 2: ALD TZO (19:1) glass substrates

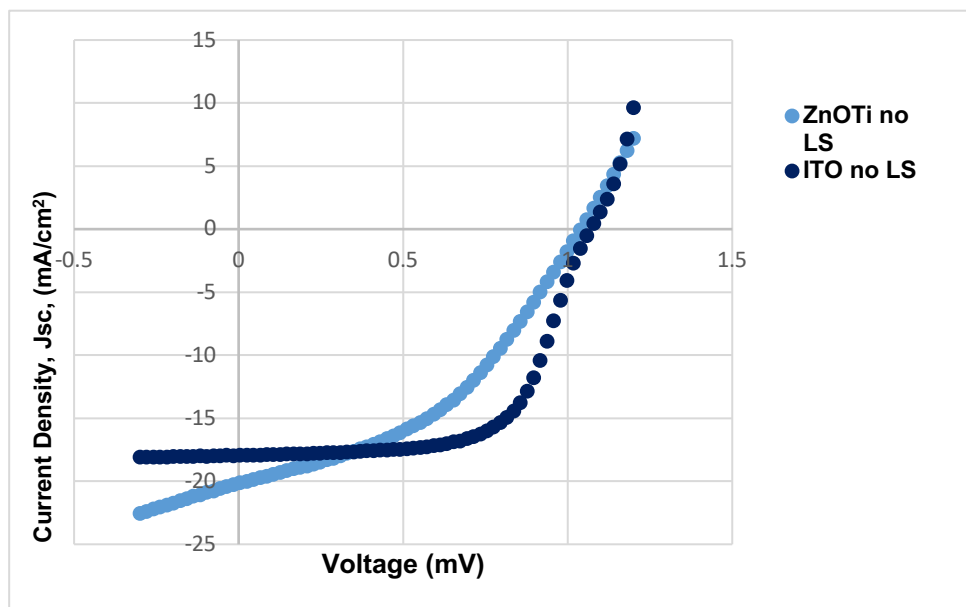


Figure 6.5 (a): J-V curve showing the electrical characteristics of the best PSC incorporating either ITO or TZO without light-soaking in a p-i-n configured PK solar cell

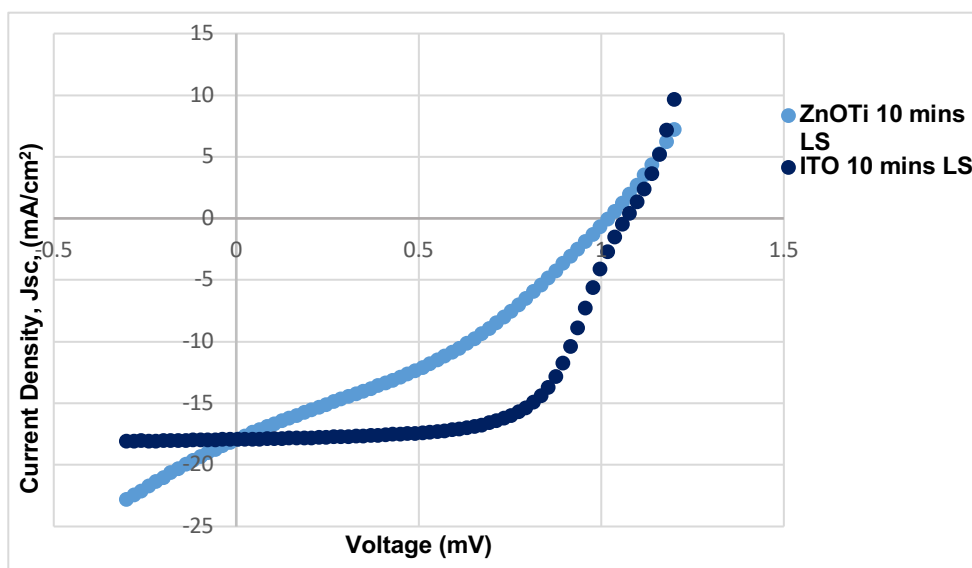


Figure 6.5 (b): J-V curve showing the electrical characteristics of the best PSC incorporating either ITO or TZO after 10 mins of light-soaking in a p-i-n configured PK solar cell

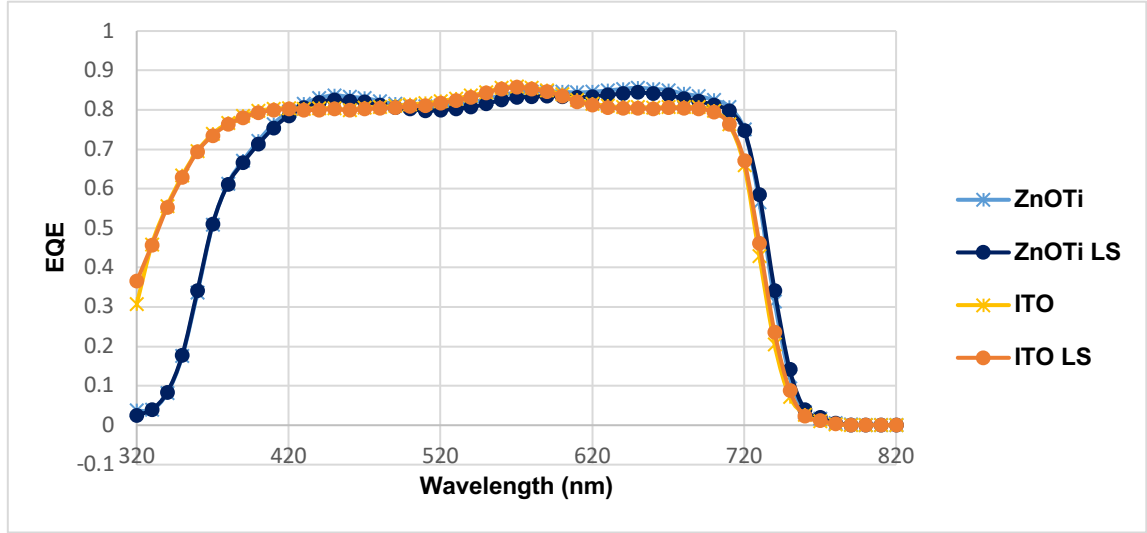


Figure 6.6: External quantum efficiency of best PSCs comparing ITO and TZO as a transparent electrode

6.3 Conclusion

As mentioned in section 2.7, tandem solar cells can be made up of a Si bottom cell and a perovskite top cell (*p-i-n* architecture). Here the Si bottom cell absorbs near IR and IR light and to date have reached efficiencies in excess of 24% for a crystalline silicon heterojunction solar cell.^{7,8} c-Si solar cells are slowly reaching their theoretical limits outlined by the Auger efficiency model so tandem solar cells where c-Si bottom cell and perovskite top cell are placed in tandem have drawn attention. In order to meet the thermal budgets required by tandem solar cells, a *p-i-n* architecture perovskite solar cell is placed on top of the c-Si solar cell. Here the perovskite solar cell tops up the efficiency of the c-Si cell. Thus the perovskite solar cell does not need to reach higher values than the state-of-the-art perovskite solar cell.

240 nm TZO was deposited at 200°C by ALD using a dopant concentration of 19:1 (ZnO:dopant). The electrical properties of the material were similar to that of the ITO currently used in state-of-the-art *p-i-n* perovskite solar cells with sheet resistance values of 41.1 Ω/\square and Hall mobility of 13.2 cm²/Vs. In order to demonstrate how well atomic layer deposited TZO compares to the state-of-the-art, two perovskite

solar cell devices were fabricated in collaboration with EPFL and CSEM. The test cell incorporated TZO as the TCO and a control cell was made up of the commercially available ITO.

J-V curves of the test cell show that the cells were producing a photocurrent efficiently. However, there was a discrepancy between the predicted maximum current density given by the J-V curves and the EQE. This disagreement was attributed to a reduced shunt resistance and increased series resistance in the cells which had a knock-on effect on the fill factor and overall cell efficiency.

Although not matching performance the TZO compared well to the state-of-the-art ITO with PCEs of 7.2% and 11.03% respectively. It should be recognized that this is the first attempt at fabrication using this type of TCO and hence it is expected that improvements in the fabrication methodology will likely reduce surface recombination, reduce the series resistance and increase the shunt resistance of the devices and as a consequence improve the PCE of the resulting cells.

Bibliography

- [1] A. G. Scheuermann, J. P. Lawrence, M. Gunji, C. E. Chidsey, P. C. McIntyre, *ECS Trans.*, **58(10)**, 75-86, (2013)
- [2] R. Katamreddy, V. Omarjee, B. Feist, C. Dussarrat, *ECS Trans.*, **16(4)**, 113-122, (2008)
- [3] G.-J. Choi, S. K. Kim, S.-J. Won, H. J. Kim, C. S. Hwang, *J. Electrochem. Soc.*, **156(9)**, G138-G143, (2009)
- [4] M. Tallarida, D. Fedrich, M. Städter, M. Michling, D. Schmeisser, *J. Nanosci. and Nanotechnol.*, **11(9)**, 8049-8053, (2011)
- [5] F. Sahli, J. Werner, B. A. Kamino, M. Bräuninger, R. Monnard, B. Paviet-Salomon, L. Barraud, L. Ding, J. J. Leon, D. Sacchetto, G. Cattaneo, *Nat. Mater.*, **17(9)**, 820, (2018)
- [6] C.-Y. Chen, J.-H. Chang, K.-M. Chiang, H.-L. Lin, S.-Y. Jsiao, H.-W. Lin, *Adv. Funct. Mater.*, **25**, 7064-7070, (2015)
- [7] K. Masuko, M. Shigematsu, T. Hashiguchi, D. Fujishima, M. Kai, N. Yoshimura, T. Yamaguchi, Y. Ichihashi, T. Mishima, N. Matsubara, T. Yamanishi, *IEEE Journal of Photovoltaics*, **4(6)**, 1433-1435, (2014).
- [8] M. Taguchi, A. Yano, S. Tohoda, K. Matsuyama, Y. Nakamura, T. Nishiwaki, K. Fujita, E. Maruyama, *IEEE Journal of Photovoltaics*, **4**, 96-99, (2013).

Chapter 7: Atomic Layer Deposition of Hole Transport Material, VO_x and Incorporation into Perovskite Solar Cells

7.0 Introduction

Many challenges are faced when fabricating a perovskite solar cells and perovskite tandem solar cells such as thermal restrictions (as will be discussed in chapter 8). Another major challenge discovered is in the scale up of the solar cell devices. Currently, hole transport materials are deposited using materials spin coated onto the perovskite in an *n-i-p* configuration (see chapter 2). This method is reliable only when depositing onto small sample areas. Another method deposits the hole transport material by electron beam evaporation which is a high energy process and can cause damage to the underlying tandem cell.

As the requirement to scale up tandem solar devices for commercial purposes becomes more pressing, the need to find an alternative deposition method and/or alternative material is required.

Here we discuss the deposition of VO_x by atomic layer deposition as a potential alternative hole transport material. The layer structure of V_2O_5 makes it a potential candidate for the insertion of Li^+ and Na^+ ions in Li-ion and Na-ion intercalation in batteries^{1, 2} highlighting the material's ability to transport holes.

This study analyses VO_x samples deposited under both thermal and plasma ALD conditions. In order to deposit a conformal film of high quality the material required deposition temperatures in excess of 250°C . Due to the thermal restrictions placed on perovskite based tandem solar cells, lower deposition temperatures are required to maintain the devices integrity. O_2 plasma is used to reduce the deposition temperature to within a suitable range. However, to protect the perovskite layer from the plasma a *p-i-n* solar device configuration is employed here.

7.1 Experimental Details

7.1.1 Thermal ALD of VO_x

VO_x was deposited using tetrakis (dimethylamino) vanadium (IV) (TDMAV) and H₂O as the metal precursor and oxygen source which were held at 80°C and room temperature respectively. Growth was performed on a Cambridge NanoTech Fiji F200LLC ALD reactor on Corning© glass microscope slides and p-Si at temperatures of 200°C and 250°C in an argon flow. The growth rate at these temperatures was previously determined to be 0.12 nm/cycle and 0.18 nm/cycle respectively.^{3,4} To generate films for analysis the VO_x was deposited for 333 cycles at each temperature. Prior to deposition, the glass substrates were ultra-sonicated in Decon 90, acetone and IPA thoroughly. Deposition parameters for each temperature are outlined in Table 7.1.

	Instruction	#	Value	Unit	Description
0	<i>wait</i>		3600	s	Substrate stabilisation time
1	<i>flow</i>	0	20	sccm	Carrier gas flow ON
2	<i>flow</i>	1	200	sccm	Plasma unit flow ON
3	<i>wait</i>		5	s	-
4	<i>pulse</i>	3	0.3	s	TDMAV pulse time
5	<i>wait</i>		20	s	Purge time
6	<i>pulse</i>	5	0.05	s	H ₂ O pulse time
7	<i>wait</i>		20	s	Purge time
8	<i>go to</i>	4	333		Cycles until desired thickness has been reached

Table 7.1: Outlines the growth parameters for the deposition of VO_x with H₂O at 200°C and 250°C

7.1.2 Plasma-Enhanced ALD VO_x

For the plasma process the Cambridge NanoTech Fiji F200 LLC ALD reactor was also employed. The VO_x was deposited at 200°C, the maximum temperature allowed by tandem solar cells, using TDMAV and O₂ plasma as the metal precursor and oxygen source respectively. TDMAV, as with the thermal process, was maintained at 80°C for

the deposition. Deposition was performed on Corning® glass microscope slides and p-Si, a significantly higher growth rate of 0.27 nm/cycle is observed for the plasma process.^{3,4} Consequently, 220 ALD cycles were required to match the thickness of the thermally deposited VO_x and allow comparison. As with the thermal ALD process the glass substrates were cleaned in Decon 90, acetone and IPA thoroughly. Deposition parameters of the PE-ALD VO_x are outlined in Table 7.2.

	Instruction	#	Value	Unit	Description
0	<i>wait</i>		3600	s	Substrate stabilisation time
1	<i>flow</i>	0	20	sccm	Carrier gas flow ON
2	<i>flow</i>	1	200	sccm	Plasma Unit flow ON
3	<i>MFC Valve</i>	3	1	-	Oxygen gas line activated
4	<i>wait</i>		5	s	-
5	<i>pulse</i>	3	0.3	s	TDMAV pulse time
6	<i>wait</i>		20	s	Purge time
7	<i>plasma</i>		300	W	Plasma power ON
8	<i>Wait</i>		5	s	
9	<i>Flow</i>	3	10	sccm	Oxygen gas flow ON
10	<i>Wait</i>		4	s	
11	<i>flow</i>	3	12	sccm	Oxygen gas flow ON
12	<i>wait</i>		1	s	
13	<i>Flow</i>	3	15	sccm	Oxygen gas flow ON
14	<i>Wait</i>		20	s	
15	<i>flow</i>	3	0	sccm	Oxygen gas flow OFF
16	<i>Wait</i>		2	s	
17	<i>plasma</i>		0	W	Plasma power OFF
18	<i>wait</i>		20	s	Purge time
19	<i>go to</i>	4	220	-	Cycles until desired thickness has been reached

Table 7.2: Outlines the growth parameters for the deposition of VO_x using O₂ plasma at 200°C

7.2 Results and Discussion

7.2.1 As grown VO_x

Figure 7.1 shows the x-ray diffraction of 20 nm (nominal) VO_x deposited by thermal ALD at 200°C and 250°C and O₂ plasma at 200°C without any post deposition treatment. It is clear from the XRD patterns that all VO_x films are amorphous. VO_x deposited using O₂ plasma at 200°C revealed two peaks at 12.11° and 30.54° which did not match any vanadium-based material and thus was attributed to a substrate feature. The amorphous nature of ALD films was also observed by Muschoot *et al* where VO_x films were deposited by VTIP and either thermal H₂O or plasma H₂O at 150°C. The films did not become crystalline until the films were annealed in O₂ at 450°C⁵. After the post-growth anneal the films revealed peaks attributed to (001) V₂O₅ and (002) V₂O₅.³ In a separate study however, Muschoot *et al* deposited VO_x films using O₂ plasma at 200°C and 250°C where the films were both deposited revealing peaks attributed to (001) V₂O₅ and (002) V₂O₅ without any post-growth treatment.⁶ This was not observed in the films discussed here, where even using O₂ plasma as a co-reactant did not induce crystallization.

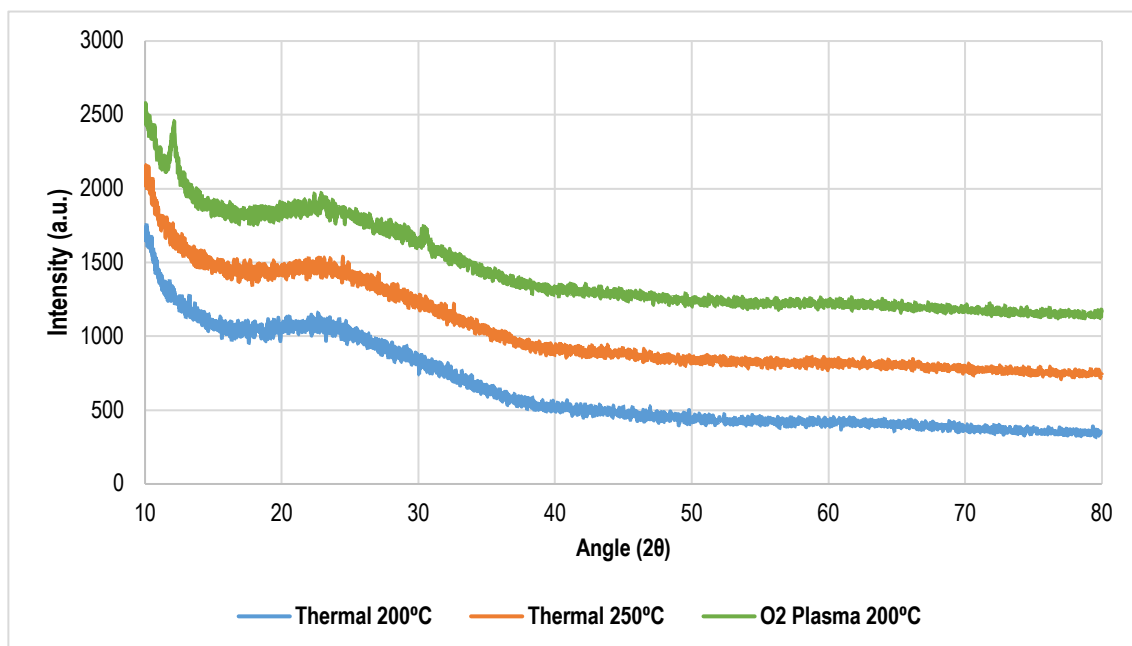


Figure 7.1: X-ray Diffraction pattern of 20 nm (nominal) as-grown VO_x deposited by thermal ALD at 200°C and 250°C using H₂O and by O₂ plasma at 200°C

Optical transmission properties of the thin films was gathered using UV/visible spectroscopy from 250-1200 nm. Figure 7.2 shows the % transmission of as-deposited VO_x by thermal H_2O at 200°C (blue), thermal H_2O at 250°C (orange), O_2 plasma at 200°C (green) and compared to a blank glass substrate (grey).

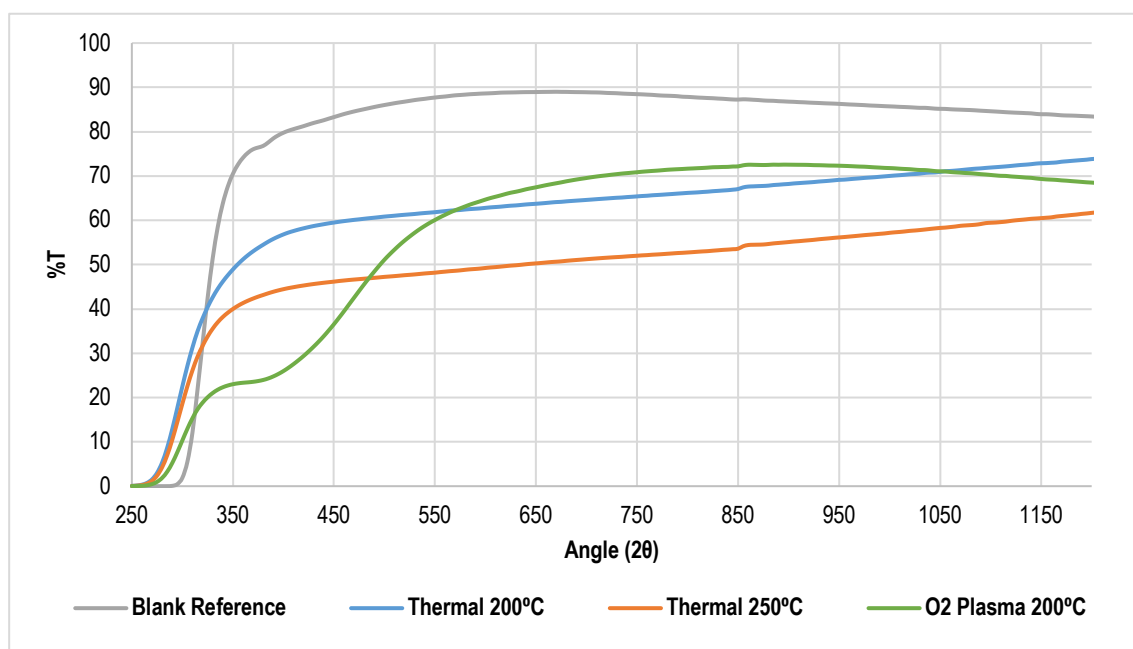


Figure 7.2: % transmission of 20 nm (nominal) as-grown VO_x deposited by thermal ALD at 200°C and 250°C using H_2O and by O_2 plasma at 200°C from UV/visible spectroscopy

It is evident from the data that all of the films absorb significantly, films deposited by O_2 plasma at 200°C were the most transparent in the near IR and visible than films deposited by thermal ALD. The plasma sample also appeared to absorb more strongly in the blue and UV range than either of the thermally deposited samples. From the two thermally deposited films, the %T deteriorated significantly with increasing the temperature however the absorption band edge of both samples did not seem to shift

significantly. The currently used inorganic hole transport material, NiO, has been reported as having a higher %T than any VO_x film giving values in excess of 83%.⁷

It was therefore concluded that as grown VO_x may not have the appropriate properties for an effective transparent hole transport medium, both in terms of transparency and the V₂O₅ layered structure required to facilitate the transport of holes. To induce a change from VO_x to V₂O₅ it was decided that an anneal would be necessary, a 450°C process in air for 1 hour, as outlined by Musschoot³, was chosen. Whilst it is recognized that such an anneal would negate the primary aim for a low temperature process for tandem cell integration the use of VO_x as a hole transport medium has yet to be demonstrated so was deemed still to be of interest.

7.2.2 Annealed VO_x

VO_x samples were annealed at 450°C for 1 hour under ambient conditions. XRD data of the samples revealed no change in crystallinity post-anneal.

Optical properties of the annealed films, in line with the colour change, improved significantly as illustrated by figure 7.3. where the transmission of thermal H₂O VO_x thin films at 200°C (blue), thermal H₂O at 250°C (orange), O₂ plasma at 200°C (green) are compared to a blank glass substrate (grey). It is evident that annealing the samples significantly improves the %T of all samples resulting in values of 80-90% in the visible and IR regions. Contrary to the observation in the as deposited films, figure 7.2, the most transparent film in the UV, visible and near IR range was that of VO_x deposited by thermal ALD at 200°C with the least transparent of the films having been deposited by O₂ plasma at 200°C. Although annealing does remove the strange visible absorption in the plasma film a more significant effect on the thermally deposited films is observed across the whole measured spectrum.

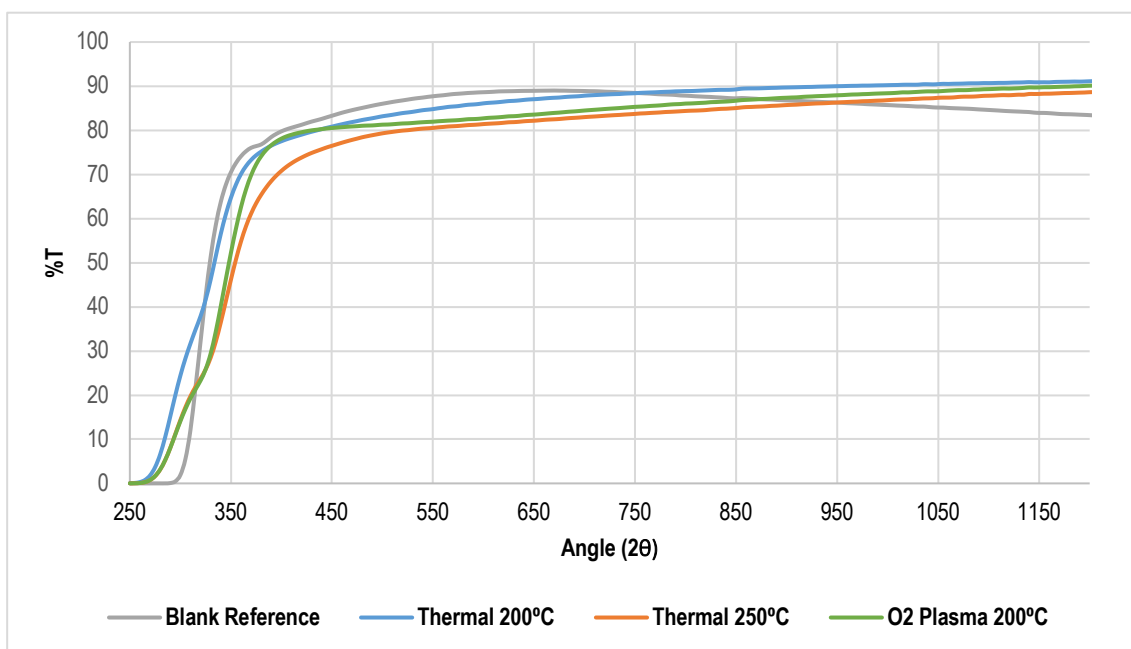


Figure 7.3: % transmission of 20 nm (nominal) VO_x deposited by thermal ALD at 200°C and 250°C using H_2O and by O_2 plasma at 200°C annealed at 450°C for 1hr from UV/visible spectroscopy

7.2.3 Surface Morphology of as grown and annealed samples

SEM images of VO_x thin films deposited by thermal H_2O ALD at 200°C and 250°C and O_2 Plasma at 200°C as-deposited and annealed at 450°C for 1 hour are shown in figure 7.4. Images (a)-(c) show the microstructure of the as-deposited VO_x and images (d)-(f) show the microstructure of the same samples annealed at 450°C for 1 hour.

VO_x deposited at 200°C by thermal H_2O ALD (figure 7.4 (a)), show randomly orientated grains of both cylindrical and spherical shapes. As the temperature increases to 250°C (figure 7.4 (b)), the grain size decreases, and the surface appears to be smoother and more conformal than when deposited at 200°C. The surface topography of VO_x samples deposited using O_2 plasma at 200°C (figure 7.4 (c)), shows a similar microstructure as those deposited by thermal H_2O at 200°C and has more randomly orientated grains.

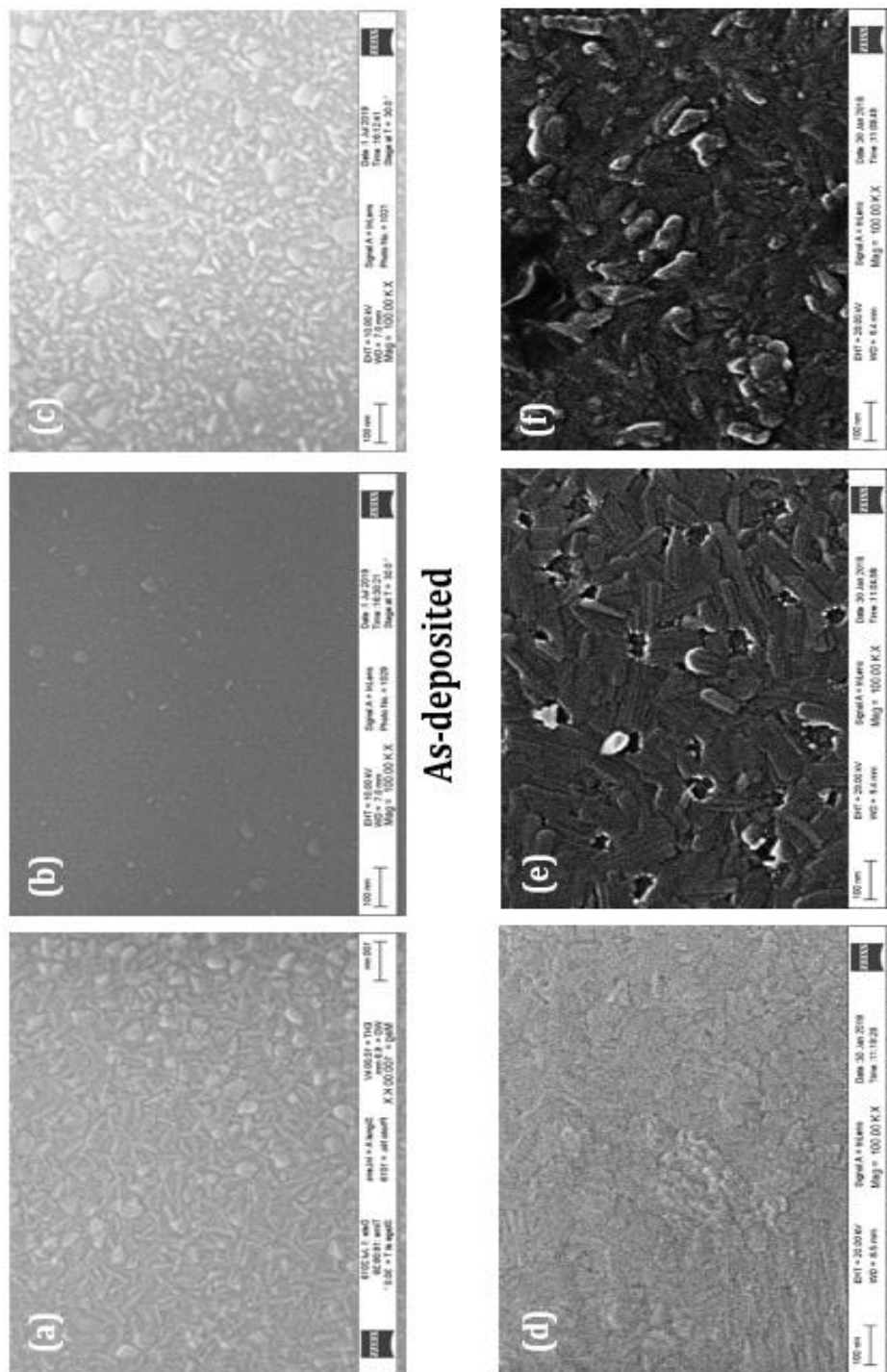


Figure 7.4: SEM images of as-deposited and annealed VO_x deposited by (a, d) O_2 plasma at 200°C, (b, e) thermal H_2O at 200°C and (c, f) thermal H_2O at 250°C on glass

Annealing the films at 450°C changes the microstructure of all the films dramatically. Comparing figure 7.4 (a) of as-deposited VO_x deposited by thermal H₂O at 200°C with (d) where the same sample is annealed shows that the surface grains are significantly reduced and leads to a smoother, more conformal film. As the temperature was increased to 250°C, the annealed sample shown in figure 7.4 (e) shows how the grain size increases significantly compared to its as-deposited counterpart in figure 7.4 (b). The grains have swollen and are randomly scattered across the surface however the films remain relatively smooth. When the sample was deposited by O₂ plasma at 200°C and annealed (figure 7.4 (f)) the grains also swell and increase in size. The film also is observed to become rougher compared to the as-deposited film in figure 7.4 (c). The increase in grain size post anneal is also reported by Singh *et al* as they revealed that exposure at high temperatures results in the enlargement of the surface grain size.⁸

7.3 Incorporation of VO_x into perovskite solar cells as a hole transport layer

7.3.1 Experimental Details

Hole transport material: Planar perovskite solar cells were fabricated in the *p-i-n* configuration. Here, standard hole transport layer, NiO is compared with atomic layer deposited (ALD) VO_x in perovskite solar cells based on power conversion efficiency (PCE). Cambridge NanoTech Fiji F200 LLC ALD reactor was used to deposit 20 nm VO_x at 200°C as described in section 7.1.2. TDMAV and O₂ plasma in an argon carrier gas flow system were used as the metal precursor and oxygen sources respectively. The growth rate for TDMAV at 200°C using O₂ plasma as a co-reactant was 0.27 nm/cycle.⁴ The precursors were obtained from STREM Chemicals Inc.

Prior to deposition, commercially bought ITO substrates (30-60 Ω/□) from Sigma-Aldrich (Merck) were ultra-sonicated in Decon 90, acetone and IPA thoroughly. The ITO was then etched using an excimer laser in order to form two separate electrode patterns. This isolation of the TCO is more commonly known as the P1 line. The line was etched 5 mm from the edge of each 25 mm² substrate using an UV ArF excimer

laser (193 nm Lasertechnik ATLEX 300i). A P2 line was then formed on the ITO substrates by masking 5 mm of the edge of the sample opposite to the laser etched P1 line prior to deposition of the hole transport material.

Three devices were fabricated and tested for power conversion efficiency (PCE) (Table 7.3). 20 nm NiO was used as the hole transport material in the control device. Device 1 used 20 nm as-deposited VO_x as the hole transport material and was compared to device 2 which incorporated 20 nm VO_x annealed at 450°C for 1 hour as the hole transport material.

At CSEM, a similar P1 and P2 line was made on their own ITO samples prior to NiO deposition. 20 nm NiO was deposited by RF sputtering (ClusterLine 200 II from Evatec) on top of commercial ITO (12.4 Ω/□) from Kintec.

Cell fabrication: At CSEM, to fabricate the solar cell, perovskite material Cs_xFA_{1-x}Pb(I,Br)₃ was deposited on top of NiO, as-grown VO_x or annealed VO_x hole transport material by spin-coating. 20 nm C₆₀ was thermally evaporated subsequently as the electron selective layer. The devices were completed by depositing 100 nm Cu by thermal evaporation as the back contact.

Performance of the fabricated perovskite cells was determined using a two-lamp class AAA WACOM sun simulator with an AM 1.5 G irradiance spectrum at 1000 W cm⁻². The cells active area of 0.25 cm² or 1.063 cm² was defined using a metal mask. The J-V characteristics of the cells were obtained under reverse (V_{oc} to J_{sc}) and forward (J_{sc} to V_{oc}) conditions in order to extract the power conversion efficiency.

	Hole Transport Material	Annealed at 450 °C
Control Device	20 nm PVD NiO	X
Device 1: Test Cell	20 nm Plasma ALD VO _x	X
Device 2: Test Cell	20 nm Plasma ALD VO _x	✓

Table 7.3: Summary of the hole transport materials incorporated into Control Device and devices 1 and 2

7.4 Results and Discussion

A control and two test device sets, each of four samples, were fabricated and electrically tested under a solar simulator as outlined in the experimental details. Table 7.4 summarises the cell results for each *p-i-n* configured perovskite solar cell device. The control device set was fabricated using RF sputtered NiO as the hole transport material, the standard in the state-of-the-art devices. Device 1 and device 2 sets were fabricated using the same methodology with the exception of the differing hole transport layers. Device 1 was produced using as-deposited VO_x at 200°C using O₂ plasma as the co-reactant, as the hole transport material. Device 2 set used the same recipe for VO_x but with the addition of a post anneal treatment of 450°C for 1 hour.

Full J-V characteristics comparing the RF sputtered NiO, as-deposited VO_x and annealed VO_x respectively in the reverse and forward bias are shown in Appendix II

Hole Transport Material	Aperture Area (cm ²)	Scan Direction	V _{oc} (mV)	J _{sc} (mA/cm ²)	FF (%)	Eff (%)
Control Device: NiO	1.06 cm ²	Forward	1010	18.66	53.97	10.17
Device 1: As-deposited VO _x	1.06 cm ²	Reverse	698	9.43	30.54	2.01
Device 2: Annealed VO _x	1.06 cm ²	Reverse	692	7.00	30.56	1.48

Table 7.4: Summary of best IV parameters for *p-i-n* configured PK solar cells composed of two test hole transport materials and a control sample. Control Device: 20 nm PVD NiO as-deposited/ ITO substrates, Device 1: 20 nm ALD VO_x as-deposited/ ITO substrates and Device 2: 20 nm ALD VO_x annealed at 450°C for 1 hr/ ITO substrates

As summarized in Table 7.4, the J_{sc} for the control device incorporating RF sputtered NiO gave a value of 18.66 mA/cm². Replacing the hole transport layer with VO_x shows a clear and significant reduction in the J_{sc} giving values of 9.43 mA/cm² for as-deposited VO_x in device 1 and 7.00 mA/cm² for annealed VO_x in device 2.

Refer to Appendix II for J-V curves. Figure 7.5 compares the open-circuit voltage (V_{oc}), current density (J_{sc}), fill factor (FF) and power conversion efficiency (PCE) of all test and control cells. It is evident from the box-graphs that the control device showed little variation from cell to cell indicating good reproducibility of the device. It is also clear that the V_{oc} and J_{sc} of both test devices are lower than those of the control device. The annealed samples resulted in a marginally lower V_{oc} on average of 692 mV from Table 7.4 compared to as-deposited samples 698 mV. However, from the box-graphs in figure 7.5, overall the annealed devices were slightly better than the as-deposited samples. The J_{sc} values for the both devices gave similar values with the average value of the as-deposited VO_x in device 1 were slightly higher with a value of 9.43 mA/cm² compared to 7.00 mA/cm² recorded for annealed samples of device 2 implying that the series resistance of the samples was much higher than that of the reference. This had a knock-on effect on the fill factor. The reference NiO gave a value of 53.97 and both device 1 and 2 gave values of 30.54 and 30.56. In order to improve these values the shunt resistance of the samples needs to be increased to aid the flow of the current throughout the device. As a result, the efficiency of device 1 and 2 were lower than the reference sample of 10.17% with values of 2.01% and 1.48% respectively.

Although these are low efficiencies working cells were fabricated that did yield a measurable power conversion efficiency demonstrating that this material may have some potential as a hole transport material. Additionally, as the values for V_{oc} and J_{sc} do not vary significantly when as-deposited or annealed it can be said that annealing the samples does not significantly improve the hole transport abilities of the VO_x in the cell.

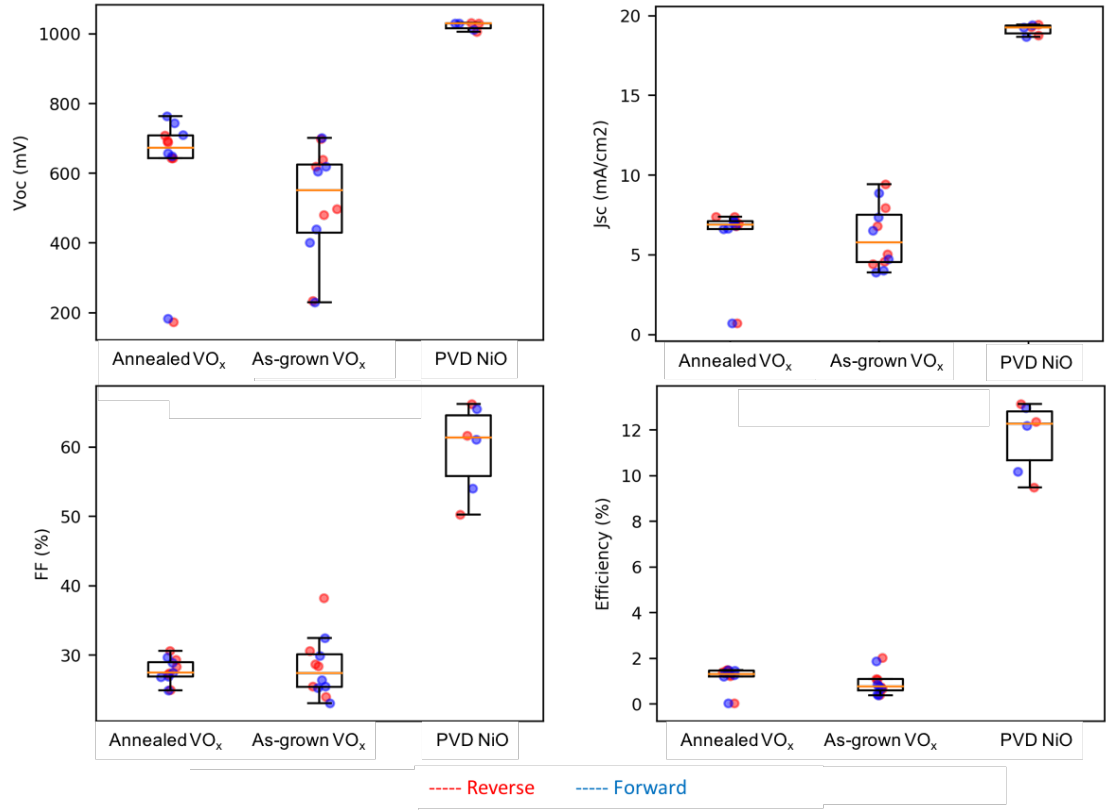


Figure 7.5: Summary of the (a) V_{oc} , (b) J_{sc} , (c) Fill Factor (FF) and (d) power conversion efficiency (PCE) of devices incorporating as-deposited and annealed ALD VO_x and control device incorporating PVD NiO as HTM in *p-i-n* configured PK solar cell

7.5 Conclusion

VO_x was deposited by thermal and plasma ALD and found to be XRD amorphous and with sub-optimal optical properties, particularly for the thermal ALD samples. To determine whether VO_x was a viable material system a post growth anneal was proposed, despite this not being ideal for the strict thermal budget restrictions for tandem cells. Two device sets were fabricated incorporating the VO_x as-deposited thin films and VO_x with a post-deposition anneal at 450°C for 1 hour. The samples were then compared to the standard device currently used in *p-i-n* configured perovskite solar cell devices where RF sputtered NiO is used as the hole transport

material. The devices were illuminated using a solar simulator and electrically characterized using open circuit voltage and current density to determine the fill factor and % efficiency of the cells.

Both device 1 and 2 produced a photo current and a PCE of 2.01% and 1.48% were obtained from the device respectively. Although both values were significantly lower than 10.17% obtained from the reference cell the fabrication and testing of the devices showed that VO_x has the ability to transport holes and has the potential to perform as a hole transport material. It is possible that modification of the hole transport medium thickness or the addition of interlayers could enhance the performance, however it is more likely that the ALD process selected is not ideal and an alternative process will need to be developed.

Bibliography

- [1] Y. Yang, Y. Tang, G. Fang, L. Shan, J. Guo, W. Zhang, C. Wang, L. Wang, J. Zhou, S. Liang, *Energy Environ. Sci.*, **11**, 3157, (2018)
- [2] J. S. Braithwaite, C. R. A. Catlow, J. D. Gale, J. H. Harding, *Chem. Mater.*, **11**, 1990-1998, (1999)
- [3] I. I. Kazadojev, S. O'Brien, L. P. Ryan, M. Modreanu, P. Osiceanu, S. Somacescu, M. E. Pemble, I. M. Povey, *ECS Trans.*, **85**, 83-94, (2018)
- [4] I. I. Kazadojev, Growth of V2O5 films for electrochromic and battery applications, (published doctoral dissertation), University College Cork, Ireland (2018)
- [5] J. Musschoot, D. Deduytsche, R. L. Van Meirhaeghe, C. Detavernier, *ECS Trans.*, **25**, 29-37, (2009)
- [6] J. Musschoot, D. Deduytsche, H. Poelman, J. Haemers, R. L. V. Meirhaeghe, S. V. den Berghe, C. Detavernier, *J. Electrochem. Soc.*, **156**, 122-126, (2009)
- [7] B. Islam, M. Yanagida, Y. Shirai, Y. Nabetani, K. Miyano, *ACS Omega*, **2**, 2291-2299, (2017)
- [8] T. Singh, S. Wang, N. Aslam, H. Zhang, S. Hoffmann-Eifert, S. Mathur, *Chem. Vap. Deposition*, **20**, 291-297, (2014)

Chapter 8: Low Temperature Atomic Layer Deposited Ti-doped ZnO for incorporation into Tandem Solar Cells

8.0 Introduction

In chapter 6 it was demonstrated that doped ZnO could be used in the fabrication of single junction solar cells and furthermore that this technology was compatible with the growth of a TCO contacts directly on a silicon sub cell in a tandem device. However, such an architecture is somewhat artificial as current device technology is more complex with multiple layers of TCO being required, some above more sensitive layers than the silicon sub cell; see figure 8.1.

For example, growth directly on to a perovskite layer would require a much lower thermal budget than 200°C over several hours to not degrade the active medium. As a consequence, for ALD ZnO to be widely incorporated into perovskite technology the growth temperature would need to be significantly reduced, in this chapter the material grown at lower temperatures is investigated in terms of its electrical and optical properties with a view to determining the feasibility.

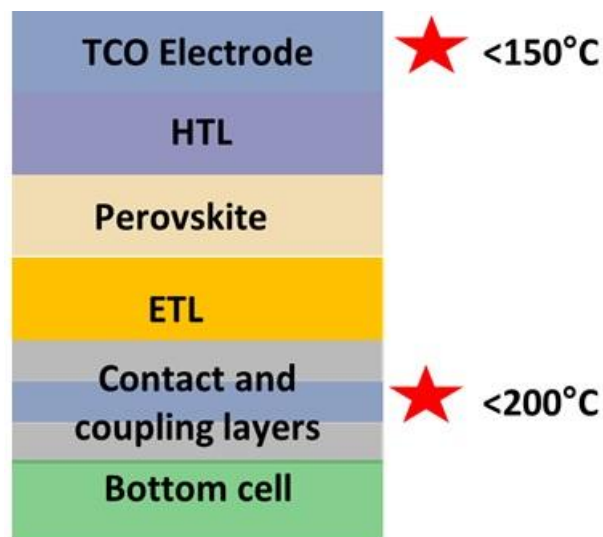


Figure 8.1: Schematic outlining the thermal restrictions required for tandem solar cells where the bottom cell is a c-Si subcell

8.1 Experimental

A Cambridge Nanotech Fiji 200LLC ALD reactor was used to grow nominally 180 nm thick films of TZO (19:1 ZnO:dopant) and nominally undoped ZnO using the same methodology as Chapters 4 and 5. Growth temperatures of 120°C and 150°C were selected to mimic the likely temperature requirements. The effect of deposition temperature on the electrical, structural and optical properties were then analysed and compared to those deposited at 200°C by thermal ALD.

The growth parameters for each growth system are outlined in Tables 8.1 and 8.2 for ZnO and TZO respectively. Refer to Chapter 4 and 5 for more details.

Substrate	DEZ Pulse Time (s)	H ₂ O Pulse Time (s)	Purge Time (s)	Deposition Temperature (°C)
Glass/p-Si	0.1	0.05	20.0	120
Glass/p-Si	0.1	0.05	20.0	150

Table 8.1: Growth parameters of (180 nm nominal) ZnO deposited by Cambridge Nanotech Fiji 200LLC by thermal ALD

Substrate	DEZ Pulse Time (s)	H ₂ O Pulse Time (s)	TDMAT Pulse Time (s)	Purge Time (s)	Deposition Temperature (°C)
Glass/p-Si	0.1	0.05	0.4	20.0	120
Glass/p-Si	0.1	0.05	0.4	20.0	150

Table 8.2: Growth parameters of (180 nm nominal) TZO (19:1) deposited by Cambridge Nanotech Fiji 200LLC by thermal ALD

8.2 Results and Discussion

8.2.1 Electrical Properties

Electrical conductivity was measured using a Lakeshore Hall Effect Measurement system as outlined in section 3.2.4. Here the sheet resistance (Ω/\square), Hall mobility (cm^2/Vs) and carrier concentration ($1/\text{cm}^3$) were obtained. The minimum and maximum excitation current applied for all films was 25 μA and 250 μA respectively.

A summary of the electrical properties for ZnO and TZO deposited at 120-200°C are outlined in Tables 8.3-8.5 below.

Description	Hall Mobility (cm²/Vs)	Carrier Conc. (1/cm³)	Sheet Resistance (Ω/□)
ZnO	9.94	3.33 x 10 ¹⁸	10400.0
TZO	3.99	8.81 x 10 ¹⁹	986.7

Table 8.3: Electrical properties of ZnO and TZO (19:1) deposited by ALD at 120°C for 900 cycles (nominal 180 nm)

Description	Hall Mobility (cm²/Vs)	Carrier Conc. (1/cm³)	Sheet Resistance (Ω/□)
ZnO	28.5	1.99 x 10 ¹⁹	610.8
TZO	9.57	1.31 x 10 ¹⁹	385.8

Table 8.4: Electrical properties of ZnO and TZO (19:1) deposited by ALD at 150°C for 900 cycles (nominal 180 nm)

Description	Mobility (cm²/Vs)	Carrier Conc. (1/cm³)	Sheet Resistance (Ω/□)
ZnO	27.7	2.78 x 10 ¹⁹	451.4
TZO	16.4	2.37 x 10 ²⁰	99.1

Table 8.5: Electrical properties of ZnO and TZO (19:1) deposited by ALD at 200°C for 900 cycles (nominal 180 nm)

At the lower deposition temperature 120°C, ZnO and TZO thin films produce high sheet resistivities compared to those deposited at the optimum temperature 200°C (Table 8.5). As a consequence, both the Hall mobility and carrier concentration

values are similarly low at 120°C. As the temperature increases to 150°C a dramatic decrease in sheet resistance is observed for ZnO and TZO films with TZO showing the lowest values 385.8 Ω/\square . As the carrier concentration of ZnO and TZO increase the Hall mobility values increase with ZnO exhibiting the highest value of 28.5 cm^2/Vs . However, at 150°C, Hall mobility and sheet resistivity values of TZO are substantially lower than those deposited at the optimum temperature. When the TZO is deposited at 200°C, the Hall mobility and carrier concentration values increase significantly. The sheet resistance values decrease far lower than that of ZnO deposited under the same conditions.

It was observed in chapter 4 that the electrical properties of the films improved as the thickness of the films increased. To determine if increasing the thickness to 300 nm would produce a film with viable values to those deposited at the same thickness at 200°C, TZO films were deposited for 1500 ALD cycles at 150°C again using the dopant ratio 19:1. The electrical properties were evaluated using the same Hall Effect measurement system. Increasing the thickness of the film reduced the sheet resistance from 385.8 Ω/\square to 125.1 Ω/\square . However, carrier concentration and Hall mobility values were similar to those of thinner TZO films showing values of 1.74×10^{20} and 9.6 cm^2/Vs respectively (see Table 1, Appendix II).

8.2.2 X-ray Diffraction

XRD patterns of 180 nm ZnO and TZO deposited by thermal ALD at 120°C, 150°C and 200°C are illustrated in figures 8.2-8.4 respectively. In the 120-200°C deposition temperature range, ZnO exhibits peaks attributed to wurtzite crystal orientations [100], [002], [101] and [110]. At 120°C, ZnO exhibits a preferred orientation in the [100] direction. As the deposition temperature increases to 150°C there is a change in the preferred orientation from [100] to [002]. Interestingly when ZnO is deposited at the optimum temperature, 200°C the preferred orientation reverts back to [100].

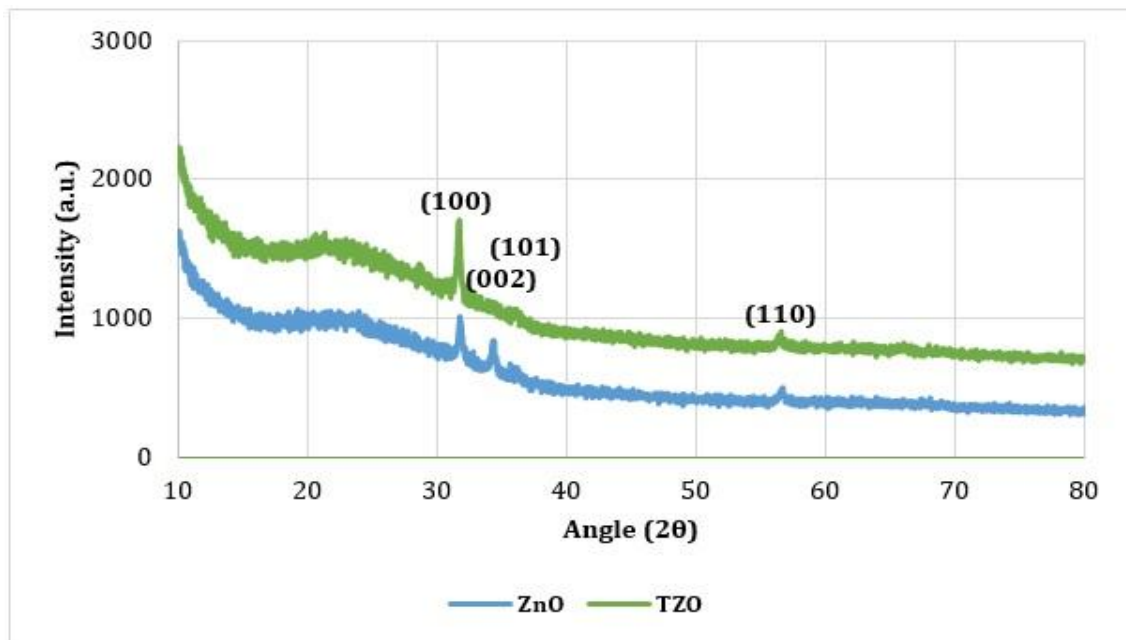


Figure 8.2: XRD Patterns of ZnO and TZO (19:1) deposited by ALD at 120°C for 900 cycles (nominal 180 nm)

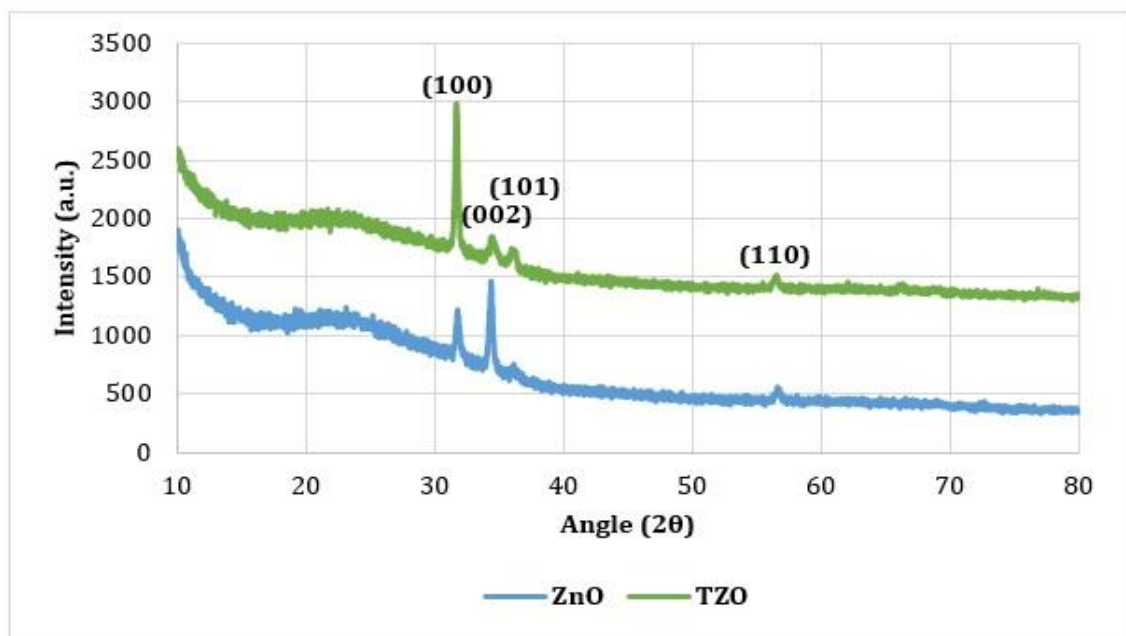


Figure 8.3: XRD Patterns of ZnO and TZO (19:1) deposited by ALD at 150°C for 900 cycles (nominal 180 nm)

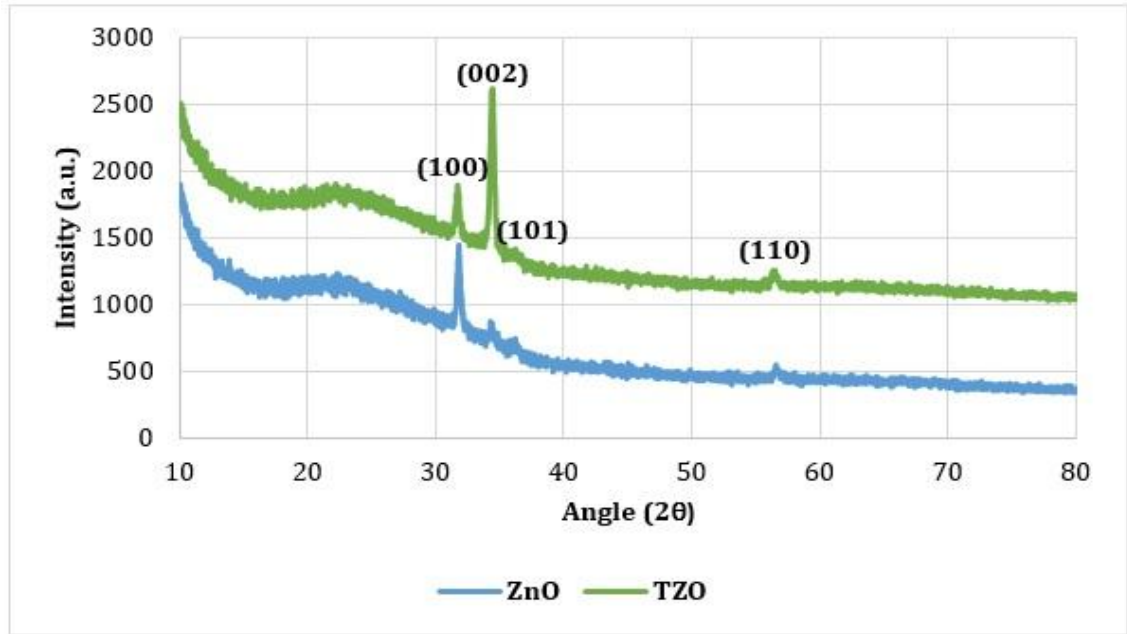


Figure 8.4: XRD Patterns of ZnO and TZO (19:1) deposited by ALD at 200°C for 900 cycles (nominal 180 nm)

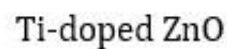
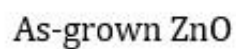
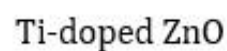
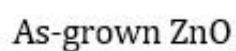
At 120°C when Ti is incorporated into the film the preferred crystalline orientation is maintained in the [100] direction. However, the peaks attributed to (002) and (101) disappear. These peaks then reappear once the deposition temperature is increased to 150°C. The [100] orientation increases in intensity at this temperature and is the most dominant crystalline direction. The preferred orientation then changes from [100] to [002] as the temperature increases further to 200°C. In addition, the (101) peak reduces in intensity at the higher deposition temperature. It is evident from the XRD patterns that the doping of ZnO with Ti changes the crystalline pattern significantly and is dependent on the deposition temperature.

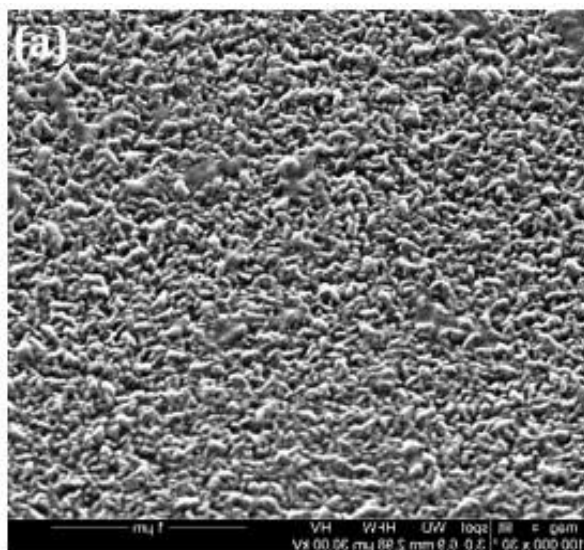
8.2.3 Surface Morphology

Surface and cross-sectional SEM images of ZnO and TZO are shown in figures 8.5 and 8.6. In the plan view, figure 8.5 (a), ZnO films deposited at 120°C, show signs of large cylindrical crystal grains on the films surface characteristic of ZnO films. When the

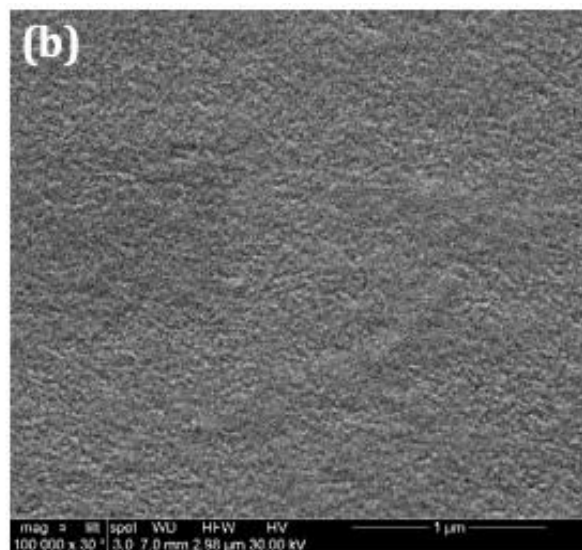
films are doped with Ti at the same temperature (Figure 8.5 (b)) the grains visibly reduce in size. Unlike the 300 nm TZO deposited at 200°C as outlined in section 6.2, the spherical features do not seem to appear at the lower temperatures. As the temperature increases to 150°C the films appear more conformal and the distinguishing features on the surface disappear.

The cross-sectional SEM of ZnO and TZO deposited at 120°C and 150°C are represented by figures 8.5 (c) and (d) and 8.6 (c) and (d). The images exhibit conformal uniform films with a smooth surface characteristic of ALD grown films. ZnO and TZO deposited at 120°C revealed a growth per cycle of 0.14 nm/cycle and 0.16 nm/cycle respectively. The growth per cycle increased when the deposition temperature increased to 150°C to 0.19 nm/cycle for ZnO which is close to the reported GPC for ZnO in the ALD window. Similar to the GPC of TZO deposited at 120°C, the GPC is far lower than ZnO for TZO deposited at 150°C with a GPC of 0.16 nm/cycle. In this case it seems TZO is not substantially affected by the deposition temperature.



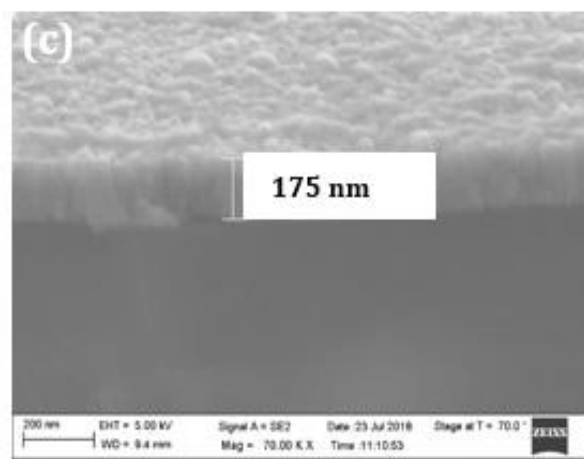


As-grown ZnO

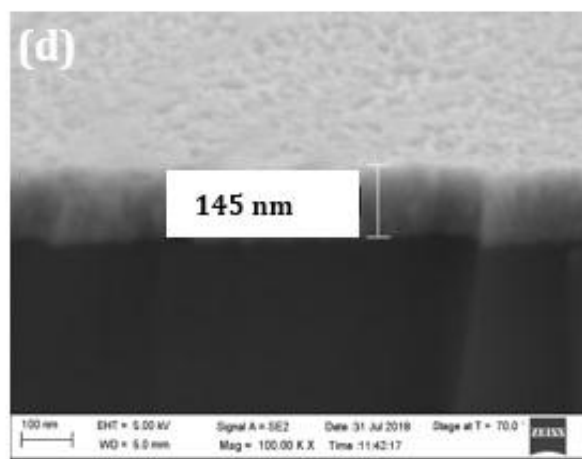


Ti-doped ZnO

Surface Morphology



As-grown ZnO



Ti-doped ZnO

Cross-sectional SEM

Figure 8.6: SEM images of (a) ZnO, (b) TZO (19:1) deposited by ALD for 900 cycles at 150°C

8.2.4 Optical Properties

The % transmission across the UV-visible spectrum of ZnO and TZO, deposited at 120°C, 150°C and 200°C, are shown in figures 8.7, 8.8 and 8.9 respectively. Films deposited at all temperatures exhibited transparencies in the range of 75-80% with a sharp absorption edge evident in all films that is characteristic of ZnO deposited on glass. At 120°C TZO films were substantially more transparent in the near IR range than ZnO. The films showed signs of similar transparency in the visible range however in the UV range the ZnO films exhibited a greater blue shift than TZO in the UV allowing greater transmittance in the blue UV.

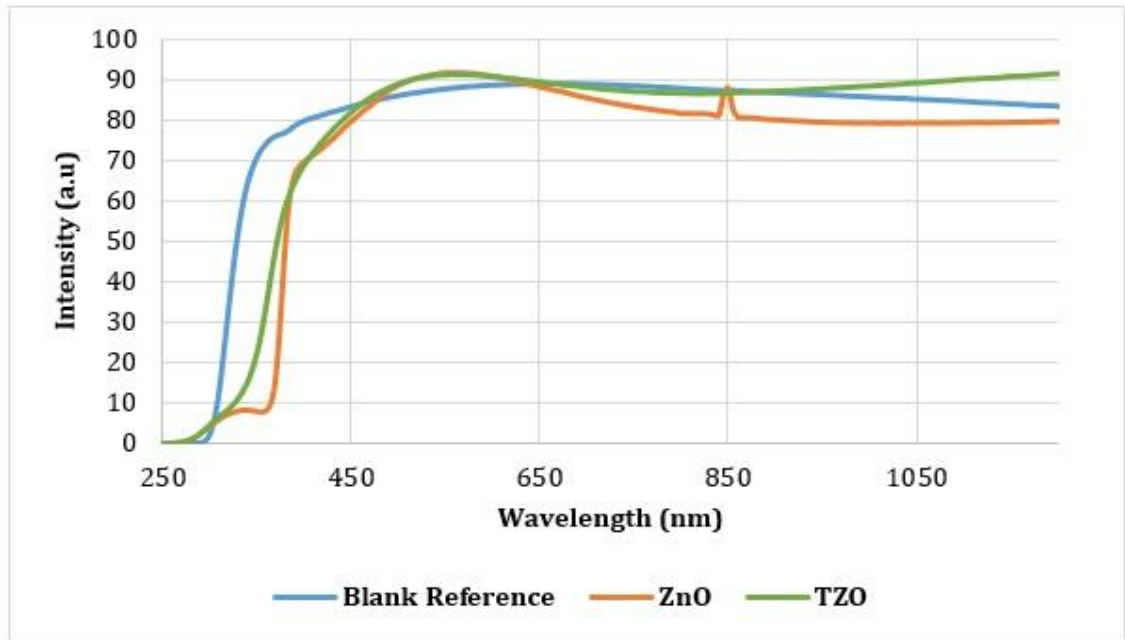


Figure 8.7: % Transmission spectrum of ZnO and TZO deposited by ALD at 120°C for 900 cycles (nominal 180 nm)

As the temperature increased to 150°C, TZO films became less transparent in the near IR, with ZnO films exhibiting more transparent films in the visible and near IR ranges. Similar to the films deposited at lower temperatures, ZnO films exhibited a greater blue shift than TZO in the UV allowing greater transmittance in the blue UV.

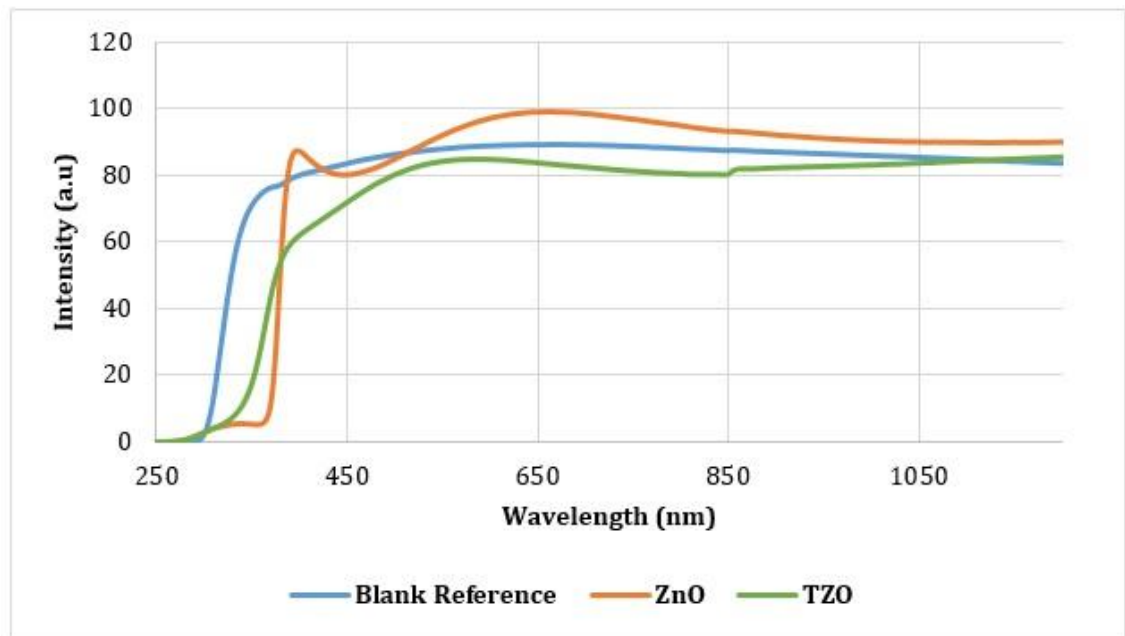


Figure 8.8: % Transmission spectrum of ZnO and TZO deposited by ALD at 150°C for 900 cycles (nominal 180 nm)

At the optimum deposition temperature for ZnO films, TZO and as-grown ZnO showed signs of similar transparency in the visible and near IR regions. TZO films absorbed strongly in the UV. This blue shift was more enhanced at the higher deposition temperatures.

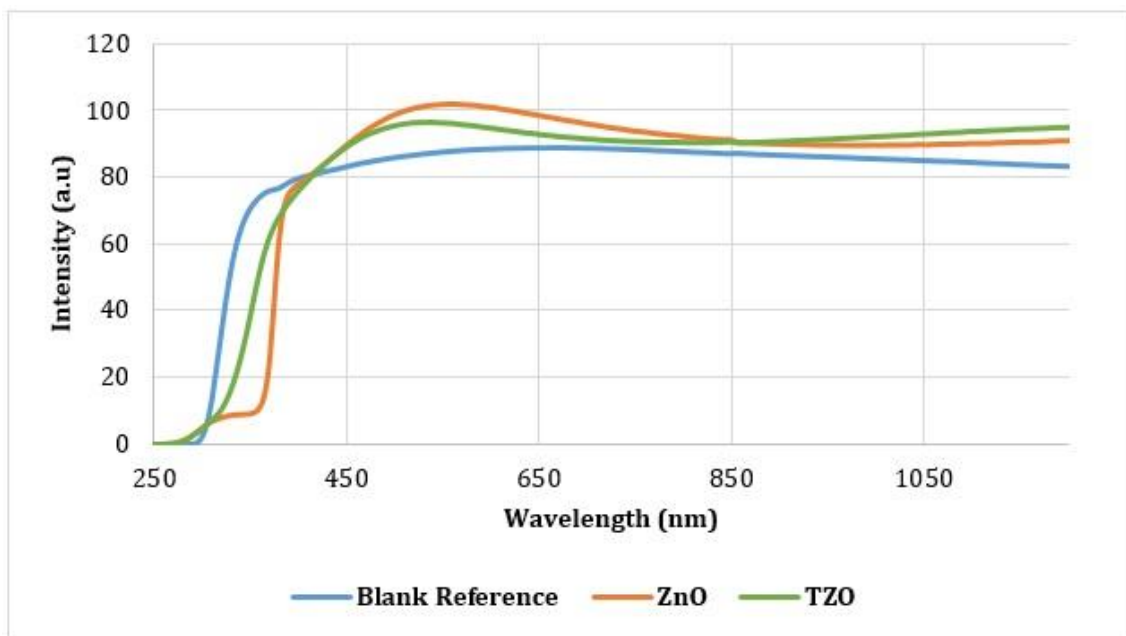


Figure 8.9: % Transmission spectrum of ZnO and TZO deposited by ALD at 200°C for 900 cycles (nominal 180 nm)

8.3 Discussion

The aim of this study was to determine how viable it is to use atomic layer deposited ZnO and TZO in tandem solar cells. The prerequisites for incorporation into a tandem include low temperature deposition conditions while still maintaining good optical and electrical characteristics. Here, we focus on deposited TZO (19:1) at 120°C and 150°C and compare them to the optimized deposition process at 200°C. For this study we deposited 180 nm (nominal values) for comparison purposes.

As seen in chapter 4, the incorporation of Ti into the ZnO films showed an improvement in the electrical properties of ZnO even at low temperatures. It has already been established that 19:1 ratio of ZnO:TiO₂ is the optimum Ti concentration to obtain low sheet resistance values for TZO. Further increasing the Ti concentration has been known to change the crystallinity of the films from polycrystalline to amorphous due to the build-up of TiO₂ at the grain boundaries¹. This implies that at 19:1 ratio the doping efficiency of Ti is at its most efficient.

The electrical properties of the films had a large dependence on deposition temperature. The sheet resistance values of both materials reduced with increasing temperature. The electrical properties of the as-grown ZnO maintained similar values at 150°C and 200°C with a reduction in sheet resistance being the only improvement when increased from 150°C to 200°C.

It has been reported that Hall mobility generally increases with decreasing carrier concentration and was attributed to ionized impurity scattering in the films.² However, in case of ZnO and TZO, the Hall mobility increased with increasing carrier concentration. It was hence theorized that improvements in the films crystallinity would improve the electron mobility in the films resulting in fewer grain boundaries in the films, therefore improving the overall electrical properties of the films.

From analysing the electrical properties of the films, it was evident that there is a correlation between the crystallinity of the thin films and their electrical properties. The best electrical results were obtained by films that exhibited a high intensity peak attributed to the (002) direction. At 200°C the films appear to be highly ordered and polycrystalline and appear to exhibit better quality electrical properties.

At low temperatures ALD films generally present with a high concentration of carbon due to incomplete desorption of ligands from the metal precursors remaining in the films^{3,4}. This has been known to increase the sheet resistance of thin films and could contribute to the high sheet resistance values observed at 120°C and 150°C.

XRD images showed that doped ZnO films change preferred orientation from c-axis to a-axis with increasing temperature. Banerjee *et al*⁵ similarly reported that Al-doped ZnO films exhibited a preferred orientation of the [100] direction at 150°C and when the deposition temperature was increased to 200°C the preferred orientation changed to the [002] direction. Figures 8.2-8.4 show similar changes when ZnO is doped with Ti. It is also observed that at 120°C the preferred orientation remains as the [100] direction. It is known that a material will grow to minimize the surface energy on the substrates surface.^{5,6} The c-axis plane is the most thermodynamically

stable plane. TZO films have been reported as depositing preferentially as c-axis orientated due to the higher nucleation rate of the lower energy plane.^{7,8} However, it is possible that the surface energy of the substrate changes at 200°C and thus causes the change from c-axis to a-axis plane.

Surface morphology analysis of the films offers an insight into how the material grows on the surface and how doping ZnO effects the deposition process. It is clear from figures 8.5 and 8.6 surface morphology images that all films exhibit columnar grains of random orientation and direction. These grains appear to change both size and shape when doped with Ti and when the temperature of the deposition is increased. Notably at 120°C the grain size is largest for as-grown ZnO. The electrical properties of the material reveal the highest sheet resistance values indicating the likely presence of charge trapping in the grain boundaries reducing the mobility of carriers within the films.⁷

The most interesting points are observed in the cross-sectional SEM images where the growth per cycle of the nominally undoped ZnO and TZO films are obtained at 120°C and 150°C. At 120°C both as-grown ZnO and TZO reveal to have a growth per cycle of 0.14 nm/cycle and 0.16 nm/cycle both below the reported ZnO GPC within the ALD window. Thus, it can be concluded that true ALD is not performed at this temperature. Based on literature 150°C is within the ALD window of ZnO and the GPC of ZnO is grown here is calculated as 0.19 nm/cycle characteristic of ALD ZnO.⁹⁻¹¹ However, the GPC calculated for TZO remained at 0.16 nm /cycle. This is indicative of a nucleation delay of DEZ on the dopant layers during deposition hindering the adsorption of ZnO on the TiO₂ laminate surfaces, most likely due to residual amine ligands.

In a perovskite-Si tandem solar cell the transparent conducting oxide in perovskite junction are required to maintain high transparency in the UV, visible and IR regions allowing for the UV/visible light to be absorbed by the perovskite cells and IR light to be absorbed by the Si cell. Even at low temperatures TZO maintains transparency between 75-80% which did not appear to vary as the temperature increased.

However, the sheet resistance of the material is not low enough to compete with ITO ($12.4 \Omega/\square$) which is currently being used as the standard TCO in perovskite solar cells. It was also established in section 8.2.1 that increasing the thickness of the material at low temperatures would not sufficiently improve the electrical properties for them to be viable in a tandem device.

8.4 Conclusion

180 nm (nominal values) of ZnO and TZO (19:1) were deposited by thermal ALD at 120°C and 150°C and compared to films deposited under the same conditions at 200°C . The electrical, optical and morphological characteristics were analysed and compared to determine the potential for use in tandem solar devices.

Electrical characteristics of the materials improved with increasing temperature with the best values being obtained at a deposition temperature of 200°C revealing a sheet resistance of $99.1 \Omega/\square$ for TZO. The crystallinity of the films improved as the temperature increased with the preferred orientation of TZO changing from [100] to [002] as the deposition temperature increased from 150°C to 200°C . A correlation was made between the low sheet resistance values and the highly ordered films in the [002] direction.

However, TZO films deposited at low temperatures did not exhibit the necessary electrical properties to compete with the commercially available ITO ($12.4 \Omega/\square$) with sheet resistance values of $986.7 \Omega/\square$ and $385.8 \Omega/\square$ for TZO deposited at 120°C and 150°C respectively.

Bibliography

- [1] S. Jakschik, U. Schroeder, T. Hecht, D. Krueger, G. Dollinger, A. Bergmaier, C. Luhmann, J. W. Bartha, *Appl. Surf. Sci.*, **211**, 352-359, (2003)
- [2] E. Ghiraldelli, C. Pelosi, E. Gombia, G. Chiavarotti, L. Vanzetti, *Thin Solid Films*, **517**, 434-436, (2008)
- [3] P. Banerjee, W.-J. Lee, K.-R. Bae, S. B. Lee, G. W. Rubloff, *J. Appl. Phys.*, 108, 043504, (2010)
- [4] J. Y. Kim, Y.-J. Choi, H.-H. Park, S. Golledge, D. C. Johnson, *J. Vac. Sci. Technol. A*, 28, 1111, (2010)
- [5] Z.-Y. Ye, H.-L. Lu, Y. Geng, Y.-Z. Gu, Y. Zhang, Q.-Q. Sun, S.-J. Ding, D. W. Zhang, *Nanoscale Res. Lett.*, 8, 108, (2013)
- [6] K. Bergum, H. Fjellvag, O. Nilsen, *Appl. Surf. Sci.*, 332, 494-499, (2015)
- [7] E. Guziwewica, I. A. Kowalik, M. Godlewski, K. Kopalko, V. Osinniy, A. Wójcik, S. Yatsunenko, E. Lusakowska, W. Paszkowicz, M. Guziewicz, *J. Appl. Phys.*, 103, 033515, (2008)
- [8] S.-Y. Pung, K.-L. Choy, X. Hou, C. Shan, *Nanotechnol.*, 19, 435609, (2008)
- [9] T. Krajewski, E. Guziewicz, M. Godlewski, L. Wachnicki, A. Wokcik-Glodowska, M. Lukasiewicz, K. Kopalko, V. Osinniy, M. Guziewicz, *Microelectronics Journal*, 40, 293-295, (2009)
- [10] D.-J. Lee, K.-J. Kim, S.-H. Kim, J.-Y. Kwon, J. Xu, K.-B. Kim, *J. Mater. Chem., C*, 1, 4761, (2013)
- [11] Z. Wan, W.-S. Kwack, W.-J. Lee, S.-H. Jang, H.-R. Kim, J.-W. Kim, K.-W. Jung, W.-J. Min, K.-S. Yu, S.-H. Park, E.-Y. Yun, J.-H. Kim, S.-H. Kwon, *Mater. Res. Bull.*, 57, 23-28, (2014)

Chapter 9: Conclusions and Future Work

9.1 Overall Conclusions

The aim of this work was to find a viable alternative transparent conducting oxide to replace indium-tin oxide (ITO) currently used in single junction solar cells. Due to the typically high temperature and high energy processes used to deposit this material in the commercial environment there is a potential short fall in the requirements of the solar industry. This is particularly pertinent in the field of perovskite solar cells where commercial viability is driving the progress from single junction solar devices to tandem multi-junction structures. In order to maintain the integrity of these relatively delicate device structures through complex fabrication methodologies, thermal and energetic restrictions are essential. This thesis has focused on investigating the potential of low temperature deposited zinc oxide, and doped zinc oxide as a replacement TCOs in solar devices.

The study in this thesis began as a fundamental investigation of atomic layer deposited zinc oxide at 200°C at a range of film thicknesses. All samples were grown using a thermal process with H₂O as the co-reactant. The samples were then analysed based on optical, electrical and morphological properties to determine how the change in thickness effected its properties. Analysis of the films determined that the increase in thickness changed the films crystallinity from amorphous to polycrystalline with peaks indicative of a wurtzite crystal structure. Interpretation of the electrical data revealed that increasing the films thickness reduced the sheet resistance values of the films significantly with the lowest values obtained at 200 nm. However, the resistance of the as grown films were still too high to compete with those of ITO. As a result, the elements Ti, Al and Hf were chosen to dope ZnO in an attempt to improve the electrical characteristics of the films. The films were deposited under the same conditions as ZnO and deposited at the same range of thicknesses. A 19:1 ratio (ZnO:dopant) was used to doped ZnO with Ti, Al and Hf.

The data revealed similar trends to ZnO, where increasing the thickness of the films changed the morphology from amorphous to a polycrystalline wurtzite crystal structure. The sheet resistance values of the films reduced with increasing thickness with the best values obtained from all of the films at 200 nm. Doping the ZnO revealed a significant reduction in sheet resistance at 200 nm compared with ZnO films of the same thickness, with Hf-doped ZnO, (HZO) obtaining the lowest sheet resistance of $59.6 \Omega/\square$ compared to $83.5 \Omega/\square$ and $89.1 \Omega/\square$ obtained for Al-doped ZnO, (AZO) and Ti-doped ZnO, (TZO) respectively. Hall mobility values of the films also revealed a significantly higher value of $20.2 \text{ cm}^2/\text{Vs}$ for HZO than ZnO, AZO or TZO. However, although doping the material improved the electrical properties significantly, the sheet resistance values were still quite high relative to ITO ($8\text{-}100 \Omega/\square$). It was theorized that due to the fact that the electrical properties improved with increasing thickness, an optimum sheet resistance value could be obtained by increasing the thickness to 300 nm.

Subsequently, 300 nm ZnO, TZO, AZO and HZO thin films were deposited at 200°C and with a 19:1 dopant ratio and compared. The growth analysis revealed that increasing the thickness did not significantly influence the optical properties of the films, maintaining the %T at $>70\%$. These thicker films were also examined by cross-sectional electron microscopy, from which it was evident that the thicknesses were not as expected from the calculated nominal literature growth rates. It was observed that nucleation delays occur when growing ZnO on both a glass substrate and onto dopant layers within the laminates. Crystallinity of the films increased with thickness which may have had a positive effect on the electrical properties which were determined to generally improve with a nominal thickness change of 200 to 300 nm. More specifically the AZO and TZO showed a reduction from $83.5 \Omega/\square$ to $44.5 \Omega/\square$ and $89.1 \Omega/\square$ to $41 \Omega/\square$. Hf-doped ZnO however demonstrated little change from $59.6 \Omega/\square$ to $60 \Omega/\square$. As both AZO and TZO exhibited a sheet resistance value closest to the commercially available ITO, Hall mobility measurements were carried out on the films. TZO exhibited a lower sheet resistance and higher Hall mobility of

12.7 cm²/Vs than AZO of 9.6 cm²/Vs. As a result, TZO was chosen as the most viable replacement for ITO in solar cell devices in this study.

As Ti was observed as being the best performing dopant, the optimum Ti concentration was investigated. A study comparing 19:1, 9:1 and 29:1 ZnO:dopant ratios were studied and verified that 19:1 dopant ratio was the optimum Ti concentration required to obtain highest quality TCO films.

The next step was to ensure that tetrakis(dimethylamido) titanium TDMAT was the best commercially readily available Ti precursor to deposit TZO films. In this case, TZO was deposited using titanium tetraisopropoxide (TTIP) using 19:1 ratio at 200°C. TTIP is grown using O₂ plasma as its co-reactant instead of thermally using H₂O as with TDMAT. The electrical characteristics of TTIP grown TZO were far inferior to TZO grown using TDMAT and thus going forward TDMAT remained the Ti precursor of choice.

Having ascertained that TZO had potential as a TCO, when grown under these restrictive conditions, the study then aimed to incorporate the optimized TZO film into a single junction perovskite solar cell device. As the solar industry is moving towards tandem solar cells the end goal was to ensure that the TZO film will be transferable to a tandem structure. Hence, the perovskite solar cell was designed in a *p-i-n* configuration that is more widely used in tandem devices. Perovskite solar cells were fabricated in collaboration with CSEM incorporating the 300 nm (nominal thickness) TZO film and comparing to control devices incorporating commercially sourced ITO (12.6 Ω/□). J-V curves of the devices revealed that the device was producing a photocurrent efficiently. However, there was evidence of a low shunt resistance and a high series resistance in the cell which ultimately resulted in a lower cell efficiency compared to the control cell. Although the test cell did not match the performance of the control, the cell compared well with a power conversion efficiency of 7.2% as opposed 11.03% with the state-of-the-art ITO technology.

As the solar industry moves toward tandem devices many challenges, in addition to the TCO, must be overcome to ensure scale up is possible. Presently, in single

junction devices hole transport materials are deposited on top of the perovskite material in an *n-i-p* configuration using spin coating techniques. As mentioned previously, in order to protect the integrity of the perovskite material in heterojunction systems the *p-i-n* device configuration is now being implemented. This allows researchers to look at replacing the currently used hole transport material with an alternative deposition method and material.

In this thesis vanadium oxide (VO_x) was selected as a possible hole transport medium. ALD growth of VO_x, under both thermal and plasma conditions, was incorporated into perovskite solar cells and initial viability studies made. Thermally as grown VO_x was deposited at 200°C and 250°C and compared to VO_x deposited at 200°C deposited using O₂ plasma. Optical properties revealed the material deposited by the plasma process produced the most transparent films. However, the transparency obtained was significantly inferior to the currently used inorganic hole transport layer sputtered NiO. As a result, it was determined that as grown VO_x did not have the appropriate properties as a viable hole transport material. As a result, a post growth anneal at 450°C was investigated. Optical properties of the annealed films were drastically improved, with those deposited using thermal ALD being the most transparent films.

In collaboration with CSEM, two test perovskite solar devices were fabricated incorporating the as grown films (200°C) and the annealed films. The devices were both compared to the CSEM's standard device incorporating RF sputtered NiO as the inorganic hole transport material. Both test devices produced a photocurrent with PCEs of 2.01% and 1.48% for the as grown and annealed films respectively. Although the values were low compared to the reference cell the demonstration of the VO_x samples ability to perform as a hole transport material is an important first step and worthy of further investigation.

Finally, although growth of TZO was demonstrated for the upper temperature limit for Si-perovskite heterojunctions to be viable, for more flexible integration of TCO layers into the heterostructures the material would be required to be deposited

below 200°C while maintaining good optical and electrical properties. In order to determine the lower limit TZO films were deposited at 120°C and 150°C and analysed. As expected, the electrical characteristics of the samples were negatively impacted by reducing the temperature. This was attributed to the fact that at low temperatures ALD films generally contain carbon due to unreacted ligands from the precursors remaining in the films. As a result, reducing the temperatures to 120°C and 150°C caused an increase in the sheet resistance values of the films. This implies that TZO films deposited at low temperatures did not exhibit required electrical properties necessary to compete with the commercially available ITO films.

To conclude, 300 nm (nominal) TZO films deposited by thermal ALD at 200°C have the potential to replace the currently used TCO in *p-i-n* configured perovskite solar devices competing with the state-of-the-art devices. ALD has the ability to deposit the material at low temperatures with good conformity making it a potential deposition method to deposit layers in single junction and tandem solar devices.

9.2 Future Work

There are some areas of this work which would warrant further investigation.

- Investigate other dopant elements such as gallium or indium to dope ZnO. The materials would be able to be deposited at low temperature by ALD. As both Ga and In have been previously used in other transparent conducting oxides they could provide the properties to help to achieve a low sheet resistance values close to commercial TCOs. Such studies may require precursor development as at these low temperatures the existing doping precursors are not ideal.
- Explore other Ti precursors to try and improve on the electrical and optical characteristics of the TZO films. Although TTIP proved to negatively impact on the properties of the ZnO films another precursor may have a more positive effect.

- VO_x films displayed potential as a hole transport material. Further work on deposition conditions by ALD and optimization of the film thickness could help to dissipate the shunting in the perovskite solar cells.
- A study of other inorganic hole transport materials deposited using atomic layer deposition should be investigated such as NiO and MoO_x which could work more efficiently than VO_x.

Appendix I

Publications and Conference Presentations

Publications

Igor I. Kazadojev, S. O'Brien, L. P. Ryan, M. Modreanu, P. Osiceanu, S. Somacescu, D. Vernardou, M. E. Pemble, I. M. Povey, *ECS Trans.*, **85**, 83-94, (2018)

Conference Presentations

L. P. Ryan, A. Walsh, M. M. McCarthy, S. O'Brien, M. E. Pemble, I. M. Povey, *Atomic Layer Deposition of ZnO for Transparent Conducting Electrodes in Solar Cells*
E-MRS Conference, Lille, France, 2016 (Oral Presentation)

L. P. Ryan, A. Walsh, M. M. McCarthy, S. O'Brien, M. E. Pemble, I. M. Povey, *Atomic Layer Deposition of Doped ZnO for Transparent Conducting Electrodes in Solar Cells*
ALD Conference, Dublin, Ireland, 2016 (Poster Presentation)

L. P. Ryan, A. Walsh, M. M. McCarthy, S. O'Brien, M. E. Pemble, I. M. Povey, *Atomic Layer Deposition of Doped Zinc Oxide for Transparent Conducting Layers in Solar Cells*
TCM Conference, Crete, Greece, 2016 (Oral Presentation)

L. P. Ryan, A. Walsh, M. M. McCarthy, S. Monaghan, M. Modreanu, S. O'Brien, M. E. Pemble, I. M. Povey, *Atomic Layer Deposition of Doped Zinc Oxide as an Alternative to Fluorine doped Tin Oxide for Transparent Contacts in Perovskite Solar Cells*
ALD Conference, Denver, Colorado, 2017 (Poster Presentation)

L. P. Ryan, A. Walsh, M. M. McCarthy, S. Monaghan, M. Modreanu, C. Romanitan, O. Chaix-Pluchery S. O'Brien, M. E. Pemble, I. M. Povey, *Atomic Layer Deposition of ZnO and Doped ZnO as Alternative Transparent Conducting Oxides for Photovoltaics*
ECS Conference, Seattle, Washington State, 2018 (Poster Presentation)

L. P. Ryan, A. Walsh, M. M. McCarthy, S. Monaghan, M. Modreanu, S. O'Brien, M. E. Pemble, I. M. Povey, *Efficient Perovskite Solar Cells using Atomic Layer Deposited Ti-doped ZnO as a Transparent Contact*
MRS Conference, Phoenix, Arizona, 2019 (Poster Presentation)

L. P. Ryan, A. Walsh, M. M. McCarthy, S. Monaghan, M. Modreanu, S. O'Brien, M. E. Pemble, I. M. Povey, *Perovskite Solar Cells Fabricated using Atomic Layer Deposited Doped ZnO as a Transparent Electrode*
ALD Conference, Seattle, Washington State, 2019 (Oral Presentation)

Appendix II

Additional Data

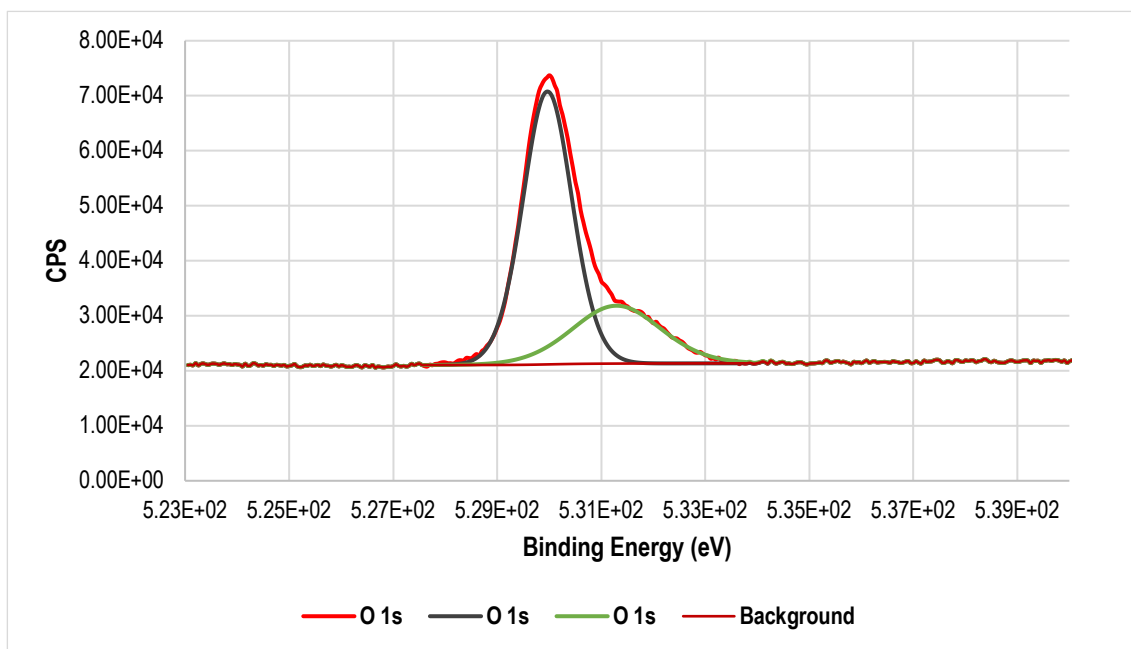


Figure 1: High resolution XPS of O 1s spectrum of 200 nm (nominal values) as-deposited ZnO deposited at 200°C

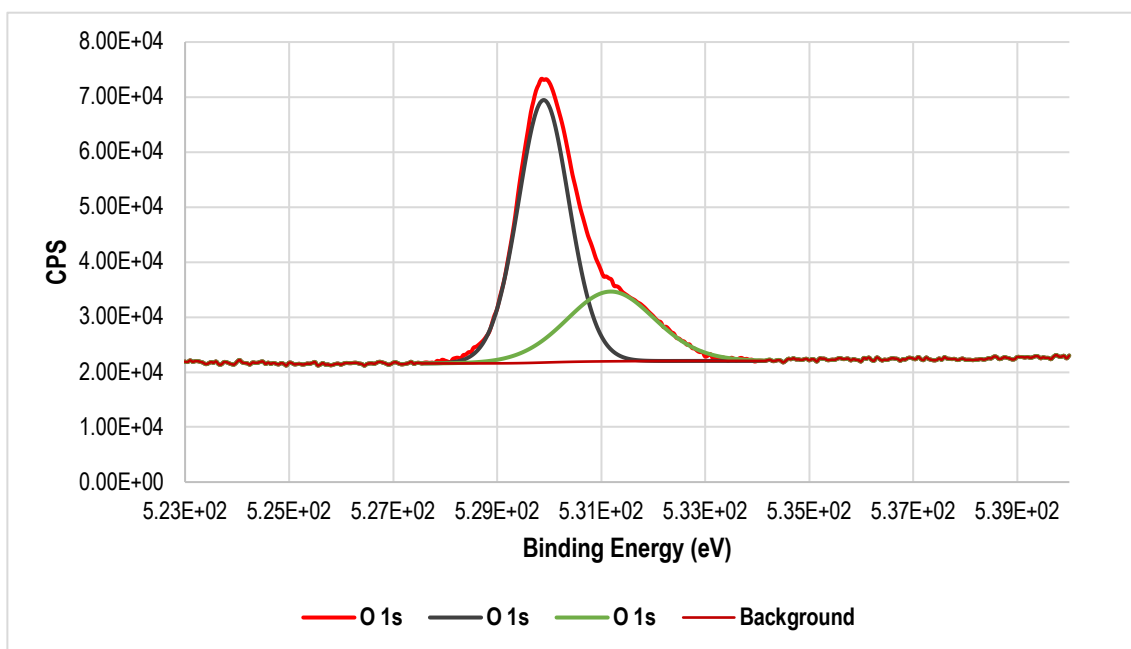


Figure 2: High resolution XPS of O 1s spectrum of 200 nm (nominal values) HZO (19:1) deposited at 200°C

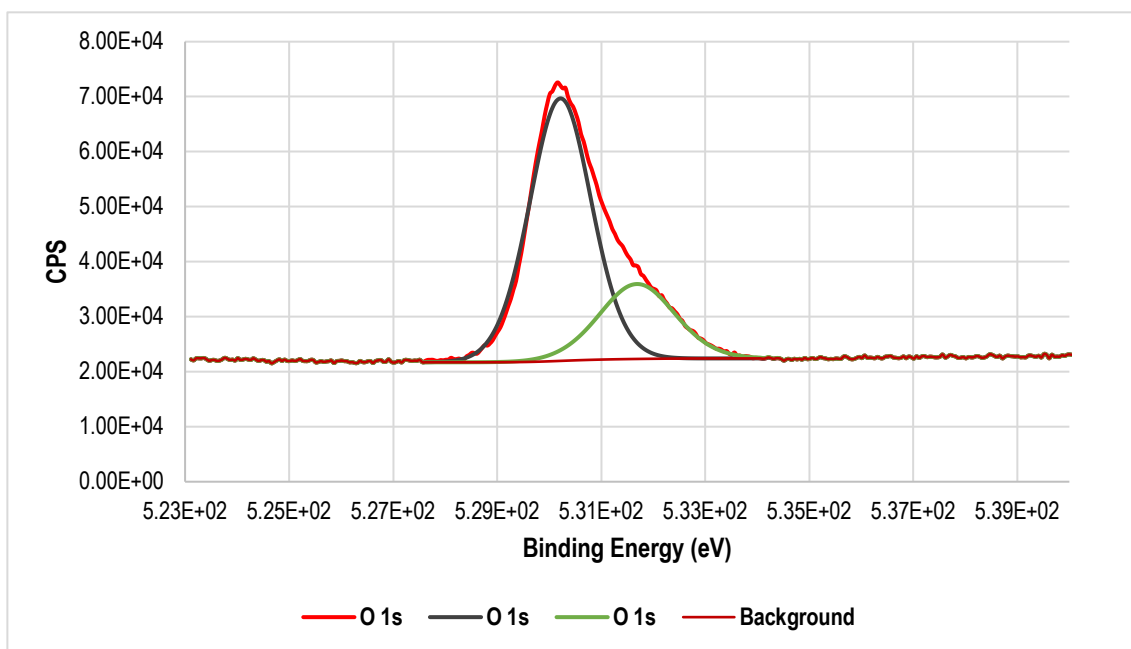


Figure 3: High resolution XPS of O 1s spectrum of 200 nm (nominal values) AZO (19:1) deposited at 200°C

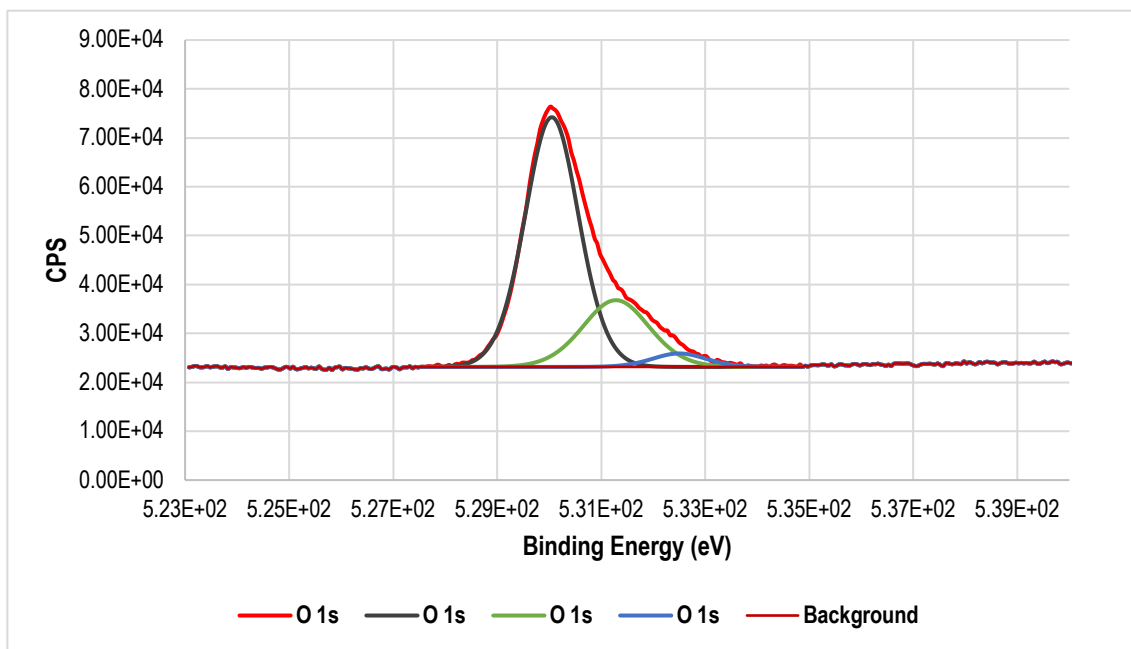


Figure 4: High resolution XPS of O 1s spectrum of 200 nm (nominal values) TZO (19:1) deposited at 200°C

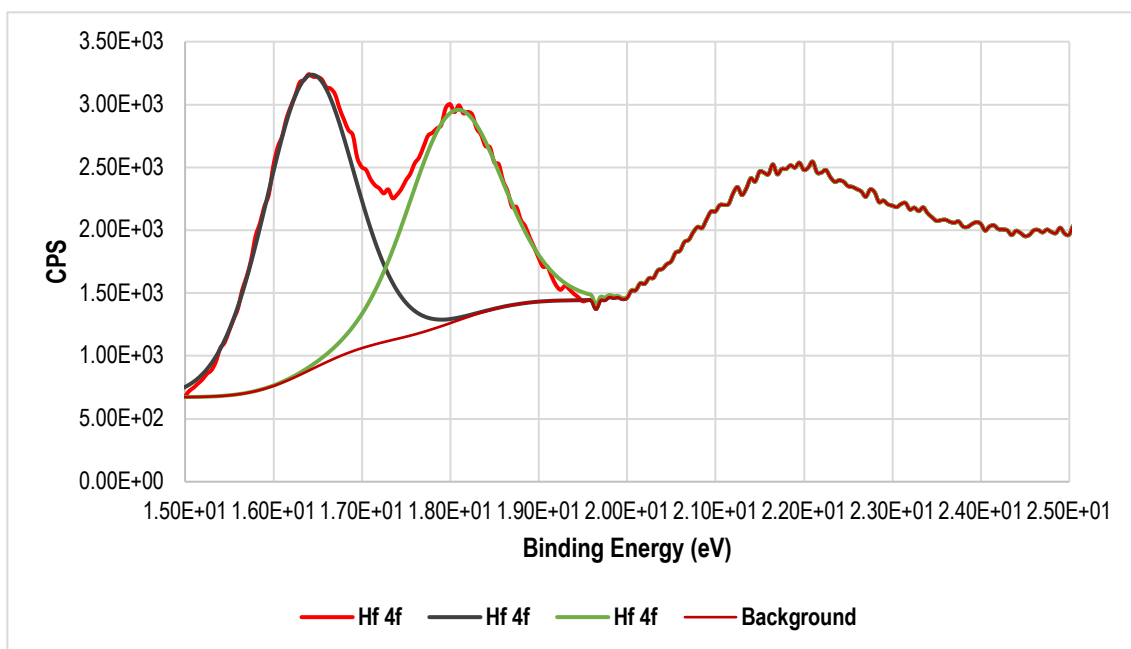


Figure 5: High resolution XPS of Hf 4f spectrum of 200 nm (nominal values) HZO (19:1) deposited at 200°C

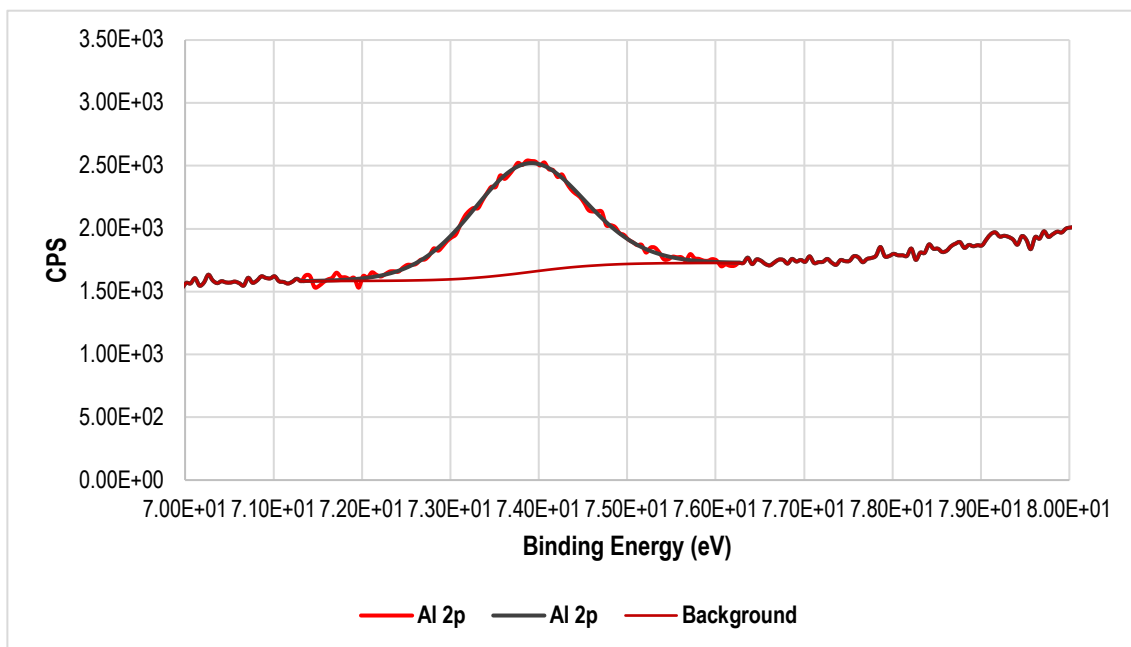


Figure 6: High resolution XPS of Al 2p spectrum of 200 nm (nominal values) AZO (19:1) deposited at 200°C

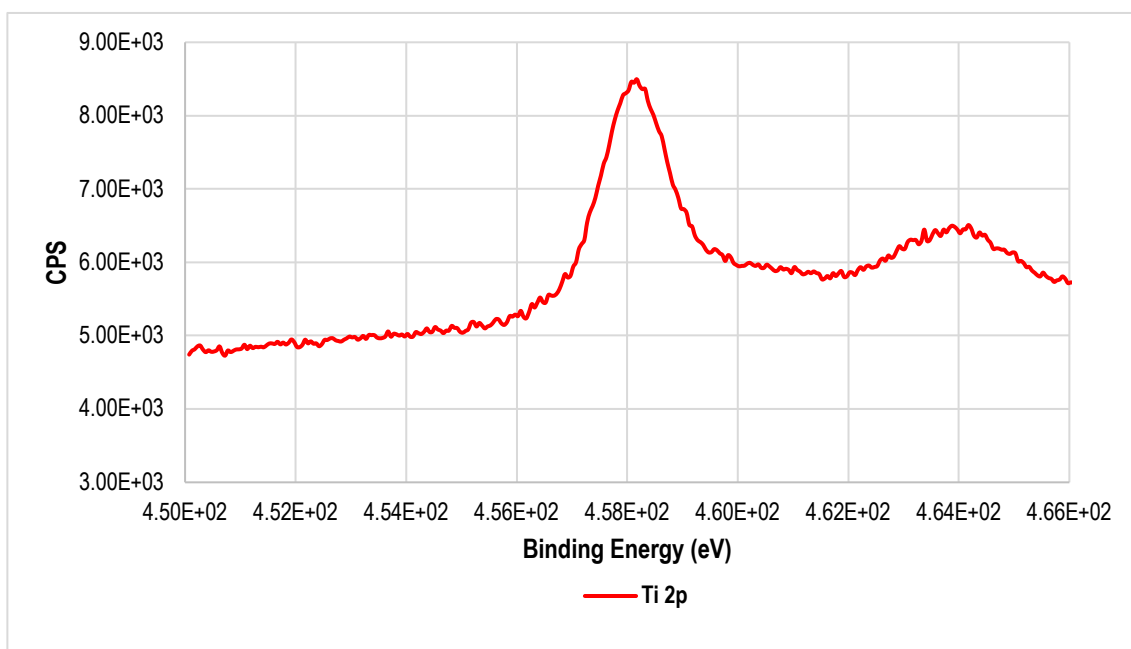


Figure 7: High resolution XPS of Ti 2p spectrum of 200 nm (nominal values) TZO (19:1) deposited at 200°C

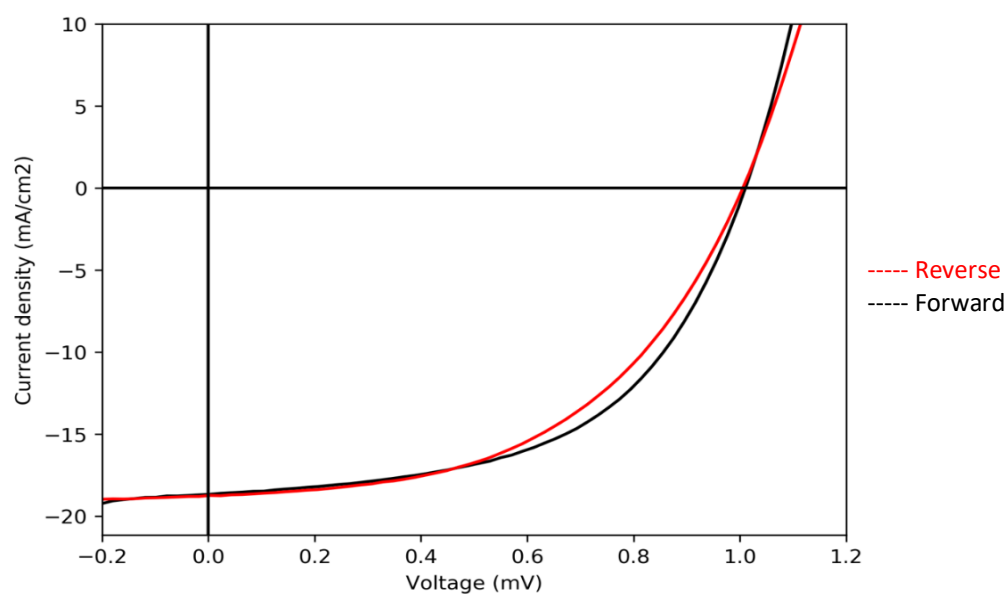


Figure 8: J-V curve showing the electrical characteristics of the best PSC of Control Device incorporating 20 nm RF sputtered NiO as HTM in a p-i-n configured PK solar cell

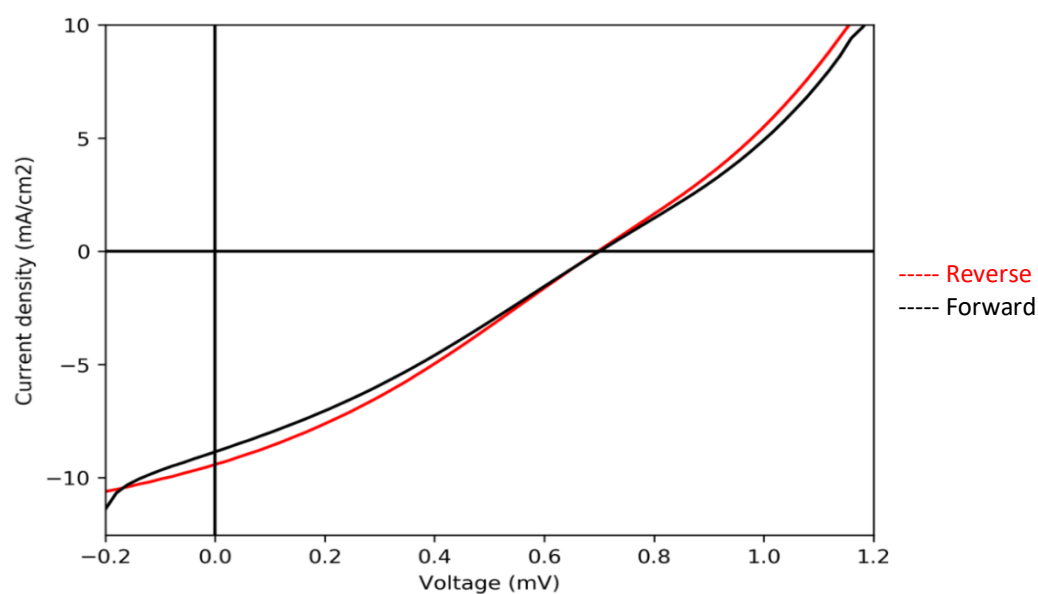


Figure 9: J-V curve showing the electrical characteristics of the best PSC of Device 1 incorporating 20 nm as-deposited VO_x as HTM in a p-i-n configured PK solar cell

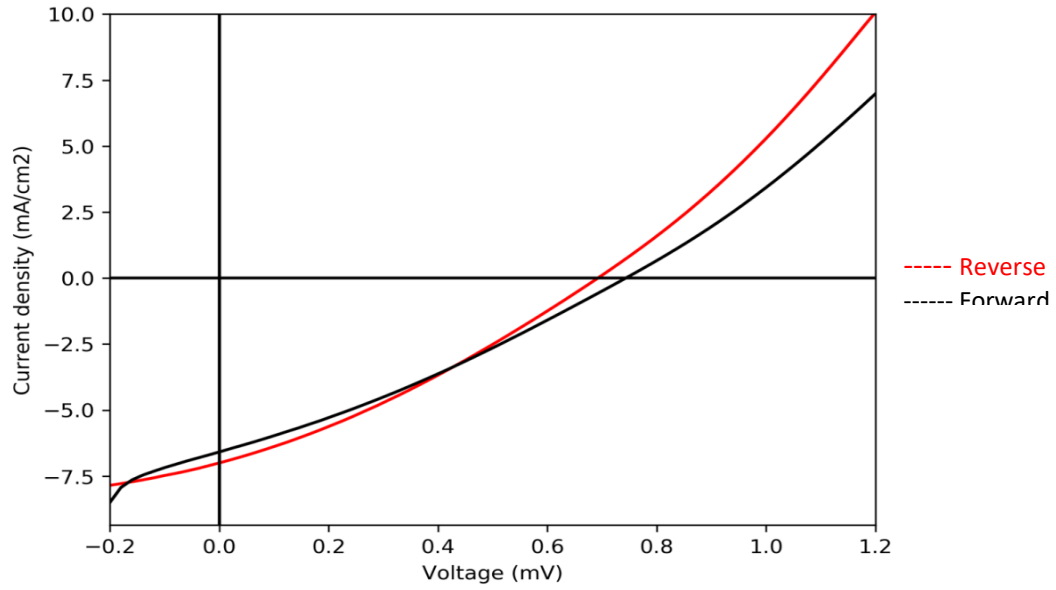


Figure 10: J-V curve showing the electrical characteristics of the best PSC of Device 1 incorporating 20 nm annealed VO_x as HTM in a p-i-n configured PK solar cell

Description	Hall Mobility (cm ² /Vs)	Carrier Conc. (1/cm ³)	Sheet Resistance (Ω/□)
ZnO (180 nm)	28.5	1.99 x 10 ¹⁹	610.8
TZO (180 nm)	9.57	1.31 x 10 ¹⁹	385.8
TZO (300 nm)	9.6	1.74 x 10 ²⁰	125.1

Table 1: Tabulated results of either nominally 180 nm or 300 nm (indicated) of TZO and ZnO deposited at 150°C using a 19:1 ratio

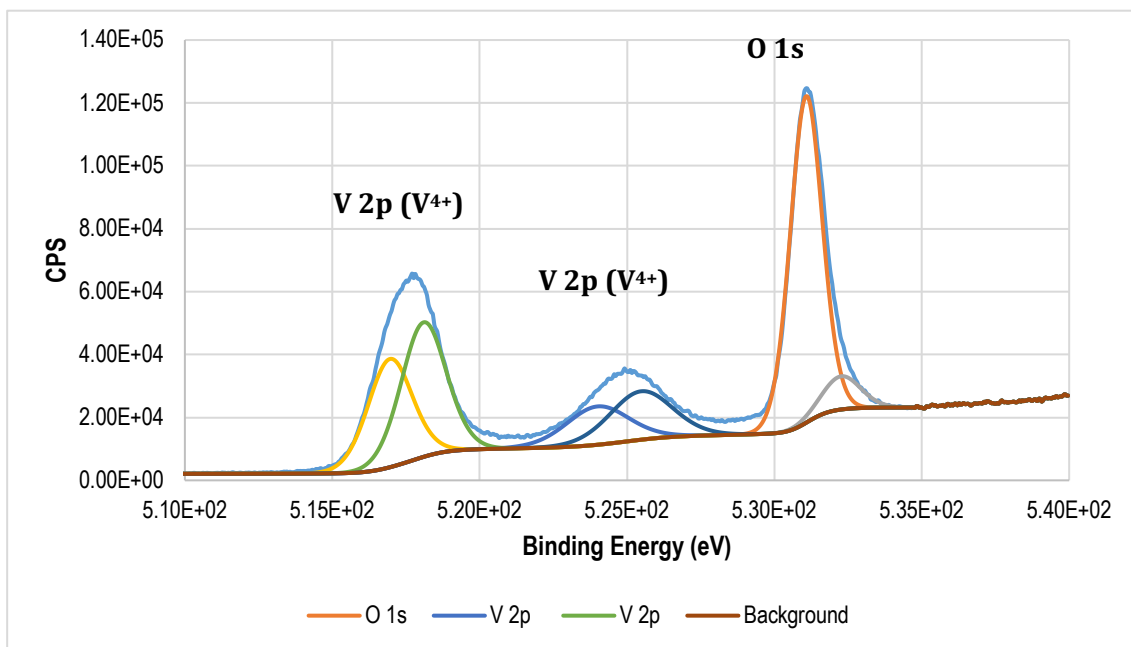


Figure 11: High resolution XPS of V 2p spectrum of 20 nm (nominal values) VO_x deposited by O₂ plasma ALD at 200°C